

University of Southampton Research Repository

Copyright © and Moral Rights for this thesis and, where applicable, any accompanying data are retained by the author and/or other copyright owners. A copy can be downloaded for personal non-commercial research or study, without prior permission or charge. This thesis and the accompanying data cannot be reproduced or quoted extensively from without first obtaining permission in writing from the copyright holder/s. The content of the thesis and accompanying research data (where applicable) must not be changed in any way or sold commercially in any format or medium without the formal permission of the copyright holder/s.

When referring to this thesis and any accompanying data, full bibliographic details must be given, e.g.

Thesis: Author (Year of Submission) "Full thesis title", University of Southampton, name of the University Faculty or School or Department, PhD Thesis, pagination.

Data: Author (Year) Title. URI [dataset]

SOME ADVANCES IN GAS PHASE PHOTOELECTRON SPECTROSCOPY

A thesis submitted to the
University of Southampton
for the degree of
Doctor of Philosophy
by
Jonathan David Mills

Department of Chemistry
The University
Southampton

May 1982

UNIVERSITY OF SOUTHAMPTON LIBRARY

A copy of this book is
deposited in the
University of Southampton
Library
for the use of
the Library
of the University of Southampton
Library

UNIVERSITY OF SOUTHAMPTON
LIBRARY

1971



Memorandum

This thesis documents original work carried out by the author over the period 1978 to 1981 and is submitted in partial fulfilment for the degree of Doctor of Philosophy. Where the work of other people has been used due reference has been given.

Acknowledgements

I am deeply indebted for the help, assistance and guidance I received in completing this research, and writing of this thesis, given by Professor Neville Jonathan, Dr John Dyke, Dr Alan Morris, Dr Nouredine Keddar and the other members of the PES research group, over the past three years, Simon Dunlavey, Ian Trickle, Noori Fayad, Marcus Winter, Graham Josland, Ann Lewis, Robert Lewis and Abed Ridha.

I would also like to pay tribute to the many friends I made whilst completing this research, all of whom contributed to making the period of my work in Southampton so vastly enjoyable. They are, to mention just a few, Bob Wyatt, Alan Fackerell, Geoff Abbot, Ian Cutting, Caroline Cook, Margaret "Mags" Philpot, Ian Moules, John Liddy, Tim Hopkirk and many others.

In addition, Peter Merrett and Roy Davis from the workshop and Julia deserve special mentions for superb standards of engineering and typing respectively.

In addition, and most sincerely, I would like to acknowledge the help and assistance I have received from Stella, for solace during melancholy, encouragement during languor and for exaltation during fruition.

Lastly and by no means least, I would like to thank my parents, for all that they have done throughout my life, and especially for being my most important tutors.

UNIVERSITY OF SOUTHAMPTON

ABSTRACT

FACULTY OF SCIENCE

CHEMISTRY

Doctor of Philosophy

SOME ADVANCES IN GAS PHASE PHOTOELECTRON SPECTROSCOPY

by Jonathan David Mills

The apparatus and techniques applicable to experimental Photoelectron Spectroscopy and theoretical Molecular Orbital calculations are described in detail.

The first three photoelectron bands of the fluorine monoxide (FO , $X^2\Pi$) radical have been identified experimentally. Analysis of the experimental data lead to accurate adiabatic ionization potentials and ionic state frequencies. Assignment of the bands was aided by the results of ab initio molecular orbital calculations.

The gas phase reaction of fluorine atoms with hydroisocyanic acid (HNCO) was investigated. No evidence could be found in the observed spectra for the isocyanate radical (NCO). However fluorine cyanate (FOCN) was proposed as the primary product of the radical quenching reaction.

Detailed theoretical calculations yielded accurate potential energy curves for hydrogen fluoride (HF) and its two lowest cationic states ($\text{HF}^+(X^2\Pi)$ and $\text{HF}^+(A^2\Sigma^+)$). Vibrational band envelopes in the HeI photoelectron spectrum were computed for ionization from various vibrationally excited states of HF .

In addition design details, and initial results, are given for a multidetector Photoelectron Spectrometer.

Commonly Used Notations

Ψ	Total electronic wavefunction which is a single determinant or a linear combination of determinants.
Ψ_{HF} or Ψ_0	Hartree Fock Wavefunction, usually a single determinant.
$\phi(x)$	Molecular orbital spatial function, usually a 2 electron function.
$\lambda(\sigma)$	One electron spin function.
$\chi(x)$	Atomic orbital.
Φ	Product of molecular spin orbitals.
ψ	Molecular spin orbital, product of space and spin functions.
x	Spatial coordinates.
σ	Spin coordinates.
τ	Space and spin coordinates.
\hat{A}	An operator, A.
\bar{A}	Expectation value of an operator a defined as: $\bar{A} = \langle \psi \hat{A} \psi \rangle.$
\underline{A}	A matrix or vector, A.
$\{a\}$	A set a.
$[a,b]$	Commutator, defined as $(ab - ba).$
\hat{F}	Fock operator.
\hat{h}	One electron operator.
\hat{g}	Two electron operator.
\hat{H} , \hat{H}	Hamiltonian operator.
\underline{A}^*	Complex conjugate of A.
$\text{Tr} \underline{A}$	Trace of matrix A.
\underline{A}^\dagger	Adjoint of matrix A.

Commonly Used Abbreviations

PES	Photo Electron Spectroscopy
UV	Ultra Violet
Ip	Ionization Potential
eV	Electron Volts
E_k	Kinetic Energy
CI	Configuration Interaction
HF	Hartree Fock
SCF	Self Consistent Field

III

CONTENTS

	Page
Preface	
Part I	
Chapter 1 Basic Principles of PES	1
Chapter 2 Theoretical Methods	13
Chapter 3 Instrument Details	68
Chapter 4 Photoelectron Spectroscopic Study of the $\text{FO}(\text{X}^2\Pi)$	82
Chapter 5 Photoelectron Spectroscopic Study of the reaction $\text{F} + \text{HNCO}$	98
Chapter 6 Theoretical Study of the First Two Ionic States of HF	117
Part II	
Chapter 1 Basic Principles of Multidetector Spectroscopy	147
Chapter 2 Multidetector Instrument: Design Details	157
Chapter 3 Initial Results	208

Preface

This thesis documents work carried out over a three year period in Gas Phase Photoelectron Spectroscopy. It is divided into two parts.

Part I is devoted mainly to studies with a single detector photoelectron spectrometer. Chapters 1-3 are devoted to introducing the basic principles of PES, outlining theoretical methods and describing instrument details. In addition two chapters (4 and 5) contain details of research projects investigating experimentally the radical species $\text{FO}(\text{X}^2\Pi)$ and the fast atom molecule reaction $\text{F} + \text{HNC}\text{O}$. Also a final chapter details theoretical results from an ab initio study of the HeI photoelectron spectrum of HF.

Part II deals exclusively with the work carried out during the development of a second generation photoelectron spectrometer. The first chapter in Part II introduces the principles of multidetector spectroscopy. The second chapter describes the design details of the multidetector photoelectron spectrometer developed for the PES group. Initial results are described in the final chapter with some conclusions and an assessment of the instrumental performance, compared to expected potential performance.

PART I

Chapter I
Introduction and
Basic Principles

Contents

Introduction

- I.1 Historical Origins of Photoelectron Spectroscopy
- I.2 Information derived from Photoelectron Spectra
- I.3 Selection Rules

Introduction

This chapter presents an introduction to Photoelectron Spectroscopy (PES), its developments and the basic principles of the ionization process. Many of the concepts will be used extensively in the later chapters of this thesis.

I.1 Historical Origins of Photoelectron Spectroscopy

Photoelectron Spectroscopy (PES) is a modern derivative of the phenomenon of the Photoelectric Effect. The first experimental observation of the Photoelectric Effect occurred when charged particles were emitted from metals when irradiated with ultraviolet light under vacuum [1,2,3]. Einstein [4] quantified the phenomenon, after the discovery of the electron [5] and the development of the quantum theory of light [6], in terms of a work function or binding energy of the electron in the metal. He proposed the following equation:

$$E_k = h\nu - \omega \quad \text{I-1-1}$$

Where E_k is the kinetic energy of the emitted electrons, $h\nu$ is the incident photon energy and ω is the work function or binding energy of the sample. This equation was not experimentally verified until 1916 [7]. Experiments by Robinson et al [8] revealed that photoelectrons emitted from metals irradiated with essentially monochromatic X-rays, had several binding energies and that these were related to the shell structure of the atom. Later the technique of measuring the velocities of photoelectrons emitted by X-rays was developed further [9] enabling precise determination of binding energies for solid samples. Robinson proposed an equation relating the kinetic energy of the ejected electron, E_k , to the photon energy as:

$$E_k = h\nu - h\nu_{\text{lim}} \quad \text{I-1-2}$$

Where $h\nu_{\text{lim}}$ is the energy of the photon corresponding to the absorption limit of the sample. This can be rewritten in terms of an ionization potential (I_p) as:

$$E_k = h\nu - I_p$$

I-1-3

This is the fundamental equation of photoelectron spectroscopy (PES), where I_p is the ionization potential of the sample.

PES as we know it today has divided into two separate fields. X-ray PES (XPS) was initially developed by Siegbahn [10] and ultra-violet PES (UVPES) by Turner et al [11]. In practice, XPS has almost exclusively been devoted to the study of solid samples, whereas UVPES is used mainly to study gaseous samples.

The work reported in this thesis is entirely devoted to UVPES, and all references of PES should be interpreted as meaning UVPES.

I.2 Information Derived from Photoelectron Spectra

Developments over the past decade have resulted in the kinetic energy of photoionized electrons being now measurable to an accuracy of approximately one part in a thousand. For UVPES, where the magnitude of the kinetic energies is of the order of a few electron volts (eV), this enables resolution of not only ionization of electrons in different shells, or orbitals, but also resolution of vibrational structure. However resolution of rotational structure is not yet routinely achieved due to the small separation of rotational states. Equation I-1-3 can be rewritten to include vibrational energy changes, on ionization as:

$$E_k = h\nu - I_p - E_{\text{vib}}$$

I-2-1

The photoelectron spectrum of a small molecule will in general show vibrational structure reflecting the change in vibrational energy on ionization.

Hence PES gives information pertaining to:

- (i) The accurate ionization potential of a molecular species to a particular ionic state, giving the ordering of ionic states.
- (ii) Some molecular spectroscopic parameters of the ionic state, such as vibrational frequencies and ionic equilibrium bond lengths (usually full analysis can only be achieved for diatomic molecules) for cases where vibrational structure is resolved.

The methods used in deriving these parameters from experimentally recorded spectra are covered in greater detail in Chapter IIb.

PES provides accurate ionization potentials that can be used in other branches of spectroscopy developed to study solely ionic species. The experimental ionization potentials can also be used to calculate ionic heats of formation and bond dissociation energies [12,13].

Also the ordering and relative intensities of photoelectron bands can be used to test the theoretical model which is used to predict these quantities, e.g. PES data provides a good test of molecular orbital theory.

The basic principles of PES given here can be found in greater detail in a number of excellent text books [14-16].

I.3 Selection Rules

As with all branches of spectroscopy, selection rules have been derived, that restrict, to first order, the possible changes in a set of quantum numbers. The selection rules for electronic and vibrational changes on ionization will now be derived specifically in terms of the ionization process. Changes in rotational energy will not be covered since resolution of rotational structure is not generally possible at present.

Consider a neutral atom/molecule, in a state characterized by a total wavefunction Ψ'' with orbital angular momentum quantum number L'' (Λ is appropriate for linear molecules), spin angular momentum quantum number S'' , and vibrational quantum number (for molecules) v'' , which is ionized to an ionic state characterized by a total wavefunction Ψ' , with quantum numbers $L'(\Lambda), S'$ and v' . The probability of photoionization is given by the square of the modulus of the dipole transition moment, where the transition moment integral is defined as:

$$M = \langle \Psi'(L', S', v') | \hat{\mu} | \Psi''(L'', S'', v'') \rangle \quad \text{I-3-1}$$

Where $\hat{\mu}$ is the dipole operator and is defined as a sum of electric and nuclear terms, i.e.:

$$\hat{\mu} = \sum_i \vec{r}_{Pe} + \sum_j \vec{r}_{Pn} \quad \text{I-3-2}$$

Where i sums over electrons and j sums over nuclei. Applying the Born-Oppenheimer Approximation to the wavefunction, i.e.:

$$\Psi(L, S, v) = \Psi_e(L, S) \Psi_n(v) \quad \text{I-3-3}$$

Substituting in I-3-1, and expanding \hat{u} , we obtain:

$$\begin{aligned} M = & \langle \Psi'_e(L', S') | \sum_i \vec{p}_e | \Psi''_e(L'', S'') \rangle \langle \Psi_n(v') | \Psi_n(v'') \rangle \\ & + \langle \Psi'_n(v') | \sum_j \vec{p}_n | \Psi''_n(v'') \rangle \langle \Psi'_e(L', S') | \Psi''_e(L'', S'') \rangle \end{aligned} \quad \text{I-3-4}$$

Since electronic eigenfunctions of different electronic states are orthogonal, the second product of integrals, in I-3-4, becomes zero. Hence the photoionization transition probability becomes proportional to:

$$\begin{aligned} |M|^2 = & |\langle \Psi'_e(L', S') | \sum_i \vec{p}_e | \Psi''_e(L'', S'') \rangle|^2 \\ & \times |\langle \Psi'_n(v') | \Psi''_n(v'') \rangle|^2 \end{aligned} \quad \text{I-3-5}$$

This is a product of the electronic transition moment, and the so called Frank Condon Factor (FCF). The selection rules are formulated to ensure a non-zero value for each of these integrals, and hence ensure a non-zero transition probability. In Chapter IIb the magnitude of the Frank Condon Factors will be discussed in greater detail. Since the transition, or ionization, probability is the product of two integrals, it is clearly non-zero when both of the integrals are non-zero. This leads to two selection rules which are based on the two integrals being non-zero. They are electronic selection rules and vibrational selection rules and shall be dealt with in turn.

(a) Electronic Selection Rules

Consider the first integral, of equation I-3-5, the electronic transition moment integral. This can be shown to be zero, to first order, when ionization occurs with an overall change in total spin angular momentum. Consider a two electron system being ionized by removal of an electron from a doubly occupied orbital. The final state electronic function would then consist of an antisymmetrized product of a one electron spin orbital function and a one electron continuum spin-orbital

function, usually a plane wave function. The initial electronic wavefunction is the usual antisymmetrized product of one electron spin orbital. In effect:

$$\Psi''_e = |\psi_i \bar{\psi}_i| \quad \text{I-3-6}$$

and the possible final state wavefunctions are:

$$^1\Psi'_e = \frac{1}{\sqrt{2}} [|\psi_i \bar{\psi}_c| - |\bar{\psi}_i \psi_c|] \quad \text{I-3-7}$$

$$^3\Psi'_e = |\psi_i \psi_c| \quad \text{I-3-8}$$

$$\text{or } |\bar{\psi}_i \bar{\psi}_c| \quad \text{I-3-9}$$

$$\text{or } \frac{1}{\sqrt{2}} [|\psi_i \bar{\psi}_c| + |\bar{\psi}_i \psi_c|] \quad \text{I-3-10}$$

Where ψ_i is a molecular spin orbital with α spin function and ψ_c is a continuum spin function with α spin. The bar in $\bar{\psi}_i$ and $\bar{\psi}_c$ denotes β spin functions for either case. The functions have been written using serial notation. (The first function is a function of electron 1 coordinates, second is a function of electron 2 coordinates).

Function I-3-7 represents a singlet function, where no change of total spin has occurred from the initial state and functions I-3-8 to I-3-10 are components of triplet state wavefunctions, representing a change in total spin of the system on ionization. Taking the singlet case first, substituting function I-3-6 and I-3-7, into the electronic transition moment integral, given as:

$$M_{e',e''} = \langle \Psi'_e(L',S') | \sum_i \vec{p}_{Pe} | \Psi''_e(L'',S'') \rangle \quad \text{I-3-11}$$

and expanding each determinant, leads to:

$$M_{e',e''} = \frac{1}{\sqrt{2}} \langle \frac{1}{\sqrt{2}} ((\psi_i \bar{\psi}_c) - (\bar{\psi}_i \psi_c) - (\bar{\psi}_i \psi_c) + (\psi_i \bar{\psi}_c)) | (\vec{p}_{Pe}(1) + \vec{p}_{Pe}(2)) | \frac{1}{\sqrt{2}} ((\psi_i \bar{\psi}_i) - (\bar{\psi}_i \psi_i)) \rangle \quad \text{I-3-12}$$

Expanding I-3-12 further, integrating over space and spin, for orthogonal orbitals ψ_i and ψ_c , gives:

$$M_{e',e''} = \frac{1}{2\sqrt{2}} \{2\langle\phi_c|\hat{p}_e(1)|\phi_i\rangle + 2\langle\phi_c|\hat{p}_e(2)|\phi_i\rangle\} \quad \text{I-3-13}$$

Putting:

$$m_i^c = \langle\phi_c|\hat{p}_e(1)|\phi_i\rangle = \langle\phi_c|\hat{p}_e(2)|\phi_i\rangle \quad \text{I-3-14}$$

gives:

$$M_{e',e''} = \sqrt{2} m_i^c \quad \text{I-3-15}$$

Hence for an ionization with no change in total spin, the electronic transition moment is non-zero. Consider the case for one of the triplet functions, one of equations I-3-8 \rightarrow 10, and proceeding as above. We find:

$$M_{e',e''} = \frac{1}{2\sqrt{2}} \{m_i^c - m_i^c - m_i^c + m_i^c\} = 0 \quad \text{I-3-16}$$

Hence ionization with a change in total spin reduces to a zero transition moment integral.

The treatment given here can be generalized to include ionization from a many electron system. The general selection rules, which are a consequence of the above results are:

- (1) Only ionizations which occur with no overall change of spin are allowed. Hence the change in spin angular momentum between the molecule and the ion must be $\pm\frac{1}{2}\hbar$, i.e. $\Delta S = \pm\frac{1}{2}$ between the molecule and the ion.
- (2) Only one electron ionizations are allowed because the electric dipole operator is a sum of one electron operators which each operate on the coordinates of a single electron.

These selection rules have been formulated from the results of evaluating the electronic transition moment integral and are valid only within the framework of the approximations used in deriving the results.

Selection rule breakdown might occur for cases where the molecule or ion are inadequately described by a single determinantal function. This inadequacy explains the observation of intensity for ionizations to ionic states which are not directly related to the neutral by a single electron removal, but are obtained from the neutral molecule formally by a more complex process of simultaneous ionization and excitation.

Intensity for these forbidden processes can be attributed through states which mix with either the molecular or ionic state. These states are often called "shake up states" and the "borrowed" intensity forms satellite lines in the spectrum, with intensities proportional to the square of the mixing coefficient in the multiconfigurational wavefunction.

It should be noted that intensity of the allowed ionizations assumes that m_i^c is non-zero. This is only true if the direct product of the irreducible representation of the wavefunctions ϕ_i and ϕ_c and any one of the components of \hat{p}_e contains the totally symmetric representation of the point group common to both the molecule and the ion. The irreducible representation of the free electron wavefunction is given from the direction (r, θ, ϕ) of its propagation vector, referenced to the molecule fixed axis system. Hence for a particular orbital ϕ_i , and for a particular component of the dipole operator \hat{p}_e , aligned with the electric vector of the incident photon beam, there will be a restricted direction of propagation (r, θ, ϕ) of the continuum function. This is given by the direction of the propagation vector that makes the direct product of the irreducible representations totally symmetric. These symmetry restrictions, on the direction of propagation of the ionized electrons, with respect to the incident photon beam, give rise to the angular dependence of the photoionization process. The angular dependence of photoelectrons emitted from an ensemble of randomly orientated molecules is characterized by an asymmetry parameter β . This parameter is dependent on the symmetry of the orbital being ionized (which governs the ionic state being produced), through group theoretical considerations given above. It is often used in the interpretation of photoelectron spectra as an aid to the assignment of the ionic state produced on ionization [16].

In addition to the spin selection rules discussed above, the electronic transition moment integral gives rise to orbital angular momentum selection rules. However, since the continuum function can adopt any value of orbital angular momentum to satisfy orbital angular momentum restrictions, the usual electric dipole selection rules, between the initial and final (ion plus free electron) states, can be satisfied for all ionic states produced by single electron ionization.

Hence it can be seen that the photoionization process obeys the standard optical electric dipole selection rules. But the final state wavefunction is characterized by the ionic state function and a continuum function for the free electron. Spin and orbital angular momentum are then partitioned, subject to quantum number restrictions, between the functions to satisfy symmetry and orthogonality restrictions.

(b) Vibrational Selection Rules

For cases where the electronic transition moment is non-zero, the vibrational component intensity is proportional to the Frank Condon Factor (FCF), which is the square of the modulus of the integral:

$$M_{v',v''} = \langle \Psi_n(v') | \Psi_n(v'') \rangle$$

Non-zero values of this integral are given when the direct product of the irreducible representations of the initial and final vibrational wavefunctions is totally symmetric. The irreducible representations of vibrational wavefunctions depends on the symmetry of the displacement coordinate (ξ), for a particular vibrational mode, and the vibrational quantum number for the particular vibrational state. A vibrational wavefunction, for a simple harmonic oscillator, contains a Hermite polynomial expansion in the displacement coordinate (ξ), which contains even powers of ξ for even values of v , and odd powers of ξ for odd values of v [17]. Hence symmetric vibrational modes have symmetric representations for all values of v , and asymmetric vibrations have antisymmetric representations for odd values of v and have symmetric representations for even values of v . The selection rules that restrict the allowed changes in vibrational quantum number for a non-zero FCF are:

- (1) For totally symmetric modes all values of Δv between the molecule and the ion are allowed.
- (2) For non totally symmetric vibrational modes changes in vibrational quantum number are restricted to $\Delta v = \pm 2n$. For transitions from $v'' = 0$ only even values of v' are allowed. Odd upper state vibrational levels are only accessible from odd lower state vibrational levels.

This analysis is for single mode excitation only, but can be

extended to treat combination bands (where excitation of two or more vibrational modes occurs) by considering the initial and final state vibration functions to be products of the individual vibrational wavefunctions for each mode. The rules derived above then apply to the total wavefunction. Also it must be noted that if ionization is accompanied with a change of equilibrium geometry (e.g. linear to bent) then only symmetry elements common to both species should be used in deriving the vibrational selection rules.

Hence it can be seen that vibrational selection rules are quite straightforward. For the case of diatomics, which have only one vibrational mode, all ionic state vibrational levels are accessible from any molecular vibrational level.

The basic principles of molecular PES, summarized here have been applied throughout this research. They have been used, along with the experimental and theoretical methods discussed in Chapters II and III in the interpretation of the photoelectron spectra of some transient species studied in the course of this research.

Chapter I

References

1. Hertz, H: Ann d Physik, 31, 983, (1887).
2. Elster, J and Geitel, H: Ann d Physik, 38, 40, (1889).
Elster, J and Geitel, H: ibid, 38, 497, (1889).
3. Lenard, P: Ann d Physik, 2, 359, (1900).
4. Einstein, A: Ann d Physik, 17, 132, (1905).
5. Thompson, J J: Phil Mag, 44, 293, (1897).
6. Planck, M: Ann d Physik, 4, 553, (1901).
7. Millikan, R A: Phys Rev, 7, 355, (1916).
8. Robinson, H and Rowlinson, W F: Phil Mag, 28, 277, (1914).
Robinson, H: Roy Soc Proc, 104, 455, (1923).
Robinson, H: Phil Mag, 50, 241, (1925).
Robinson, H and Cassie, A M: Roy Soc Proc, 113, 282, (1927).
Robinson, H and Young, C L: Roy Soc Proc, 128, 92, (1930).
9. Kretschmar, G C: Phys Rev, 43, 417, (1933).
10. Siegbahn, K and Edvanson, K: Nucl Phys, 1, 137, (1956).
11. Turner, D W and Al-Jobury, M I: J Chem Phys, 37, 3007, (1962).
12. Dyke, J M, Morris, A, Jonathan, N and Winter, M J: Mol Phys, 39, 629, (1980).
13. Dyke, J M, Morris, A, Jonathan N and Winter, M J: Molec Phys, to be published.
14. Eland, J H D: "Photoelectron Spectroscopy", Butterworths, London, (1974).
15. Turner, D W, Baker, C, Baker, C W and Brundle, C R: "Molecular Photoelectron Spectroscopy", Wiley-Interscience, London, (1970).
16. Rabalais, J W: "Principles of Ultra Violet Photoelectron Spectroscopy", Wiley-Interscience, New York, (1977).
17. Herzberg, G: "Molecular Spectra and Molecular Structure, Vol II, Infra Red and Raman Spectra of Polyatomic Molecules", D Van Nostrand, (1945).

Chapter II

Theoretical Methods in PES

Contents

Introduction

- IIa-1 The Variation Principle and the Virial Theorem
- IIa-2 Hartree Fock Roothaan Formalism for Closed Shell Molecules
- IIa-3 Koopmans' Theorem
- IIa-4 Open Shell Methods - ATMOL-3 Formalism
- IIa-5 Δ SCF Calculations
- IIa-6 Correlation Energy and Configuration Interaction - SPLICE Formalism
- IIa-7 Direct Methods for Calculation of Ionization Potentials
- IIb-1 Calculation of Molecular Spectroscopic Constants from Potential Curve Data
- IIb-2 Calculation of Frank Condon Factors from Spectroscopic Data

Introduction

In quantum chemistry we are interested in solutions of the time independent Schrodinger Wave equation [1-5].

$$\hat{H} \Psi_{TOT} = E_{TOT} \Psi_{TOT}$$

Where \hat{H} is the molecular Hamiltonian operator, Ψ_{TOT} is the total molecular wavefunction (a function of electronic and nuclear coordinates) and E_{TOT} is the total energy of the system. This outwardly simple expression has no exact solution for more than two charged particles (e.g. one nucleus and one electron as in the hydrogen atom). In the many electron case the use of simplifying approximations are required to make the wave equation mathematically tractable. A fundamental approximation is made by separating the total wavefunction into a product of functions dependent on electronic and nuclear coordinates, i.e.:

$$\Psi_{TOT}(r_e, \xi_n) = \Psi_{elec}(r_e) \Psi_{nucl}(\xi)$$

This is the Born Oppenheimer Approximation [6] and originates from the facile nature of the electronic motion around the much heavier and relatively static nuclei. The extent of this separation is reflected by the growth of an essentially separate branch of Quantum Chemistry, dealing solely with solutions of the molecular electronic wavefunction, called Molecular Orbital Theory.

In PES theoretical results are derived from all aspects of quantum chemistry. Molecular Orbital Theory is used extensively to predict molecular ionization potentials to near experimental accuracy. Also solutions of the nuclear wave equations are used to calculate vibrational spectroscopic parameters. This chapter is devoted to the theory involved in calculations used to interpret photoelectron spectra. The chapter is divided into two parts, the first is devoted to Molecular Orbital methods, the second is devoted to methods encountered in the calculation of spectroscopic constants. Extensive coverage is given to the techniques used directly in the derivation of results encountered in this thesis.

IIa-1 The Variation Principle and the Virial Theorem

The time independent Schrodinger wave equation, introduced previously, has only a limited number of exact solutions. In this section two important concepts are introduced, which form the cornerstone of Molecular Orbital (MO) Theory and appear in many texts [1-5].

(i) The Variation Principle

Consider an electronic system, described by a Hamiltonian \hat{H} , which has a complete set of exact orthogonal eigen functions $\{\psi_i\}$ and eigen values $\{E_i\}$, i.e.

$$\hat{H}\psi = E\psi \quad \text{IIa-1-1}$$

An approximate trial function, ξ , that satisfies the boundary conditions, can be expressed as a linear combination of the exact eigen functions, ψ_i , which remain undetermined, i.e.:

$$\xi = \sum_i \psi_i c_i \quad \text{IIa-1-2}$$

The expectation energy of the Hamiltonian, \hat{H} , is given by the energy functional:

$$e(\xi) = \frac{\langle \xi | \hat{H} | \xi \rangle}{\langle \xi | \xi \rangle} \quad \text{IIa-1-3}$$

Substituting equation IIa-1-2 into IIa-1-3 and expanding, the energy functional becomes:

$$e(\xi) = \frac{\sum_{ij} c_i^* c_j \langle \psi_i | \hat{H} | \psi_j \rangle}{\sum_{ij} c_i^* c_j \langle \psi_i | \psi_j \rangle} \quad \text{IIa-1-4}$$

Applying orthogonality restraints and putting:

$$\begin{aligned} E_i &= \langle \psi_i | \hat{H} | \psi_i \rangle \quad \text{and} \quad H_{ij} = \langle \psi_i | \hat{H} | \psi_j \rangle \\ \delta_{ij} &= \langle \psi_i | \psi_j \rangle \end{aligned} \quad \text{IIa-1-5}$$

Equation IIa-1-4 becomes:

$$e(\xi) = \frac{\sum_i (|c_i|^2 E_i + \sum_{j \neq i} c_i^* c_j H_{ij})}{\sum_i |c_i|^2} \quad \text{IIa-1-6}$$

Equation IIa-1-6 is the basic working equation of the Variation Principle.

It can be seen that $e(\xi)$ will be always less than any E_i , since $|c_i|^2$ is greater than or equal to zero, and always less than 1.

This very important result, first proved by Eckart [7], is the essence of the Variation Principle, which states that:

The expectation energy of a trial function will always be greater than the true eigen value and the lowest trial expectation energy will be the closest to the true eigen value. Also the trial function will be the closest approximation to the true eigen function when the expectation energy of the trial function is a minimum.

It can be seen that as ξ tends to the i^{th} exact eigen function, ψ_i , then c_i tends to unity and the expectation energy tends to the i^{th} exact eigen value, E_i . The expectation energy functional contains matrix elements between eigen functions ψ_i and ψ_j , which are non-zero for eigen functions of the same symmetry. Hence the energy functional is a weighted average of the energy expressions. This can never be lower than the lowest contributing term, which occurs for the lowest eigen value of that symmetry. The Variation Principle is therefore only applicable to the lowest eigen function of a particular symmetry.

The usefulness of the Variation Principle is that it provides a criterion for the choice of the "best" wavefunction as the trial function that gives the lowest energy. However, the Variation Principle applies only to the ground state of a given symmetry in a molecule.

(ii) The Virial Theorem

Consider an n particle wavefunction, with particle coordinates given by r_i , as:

$$\Psi(r_1, r_2, r_3, \dots, r_n) \quad \text{IIa-1-7}$$

The kinetic energy and potential energy of the system is given as the expectation values of the respective operators, i.e.:

$$\begin{aligned}\bar{V} &= \langle \Psi | \hat{V} | \Psi \rangle \\ \bar{T} &= \langle \Psi | \hat{T} | \Psi \rangle\end{aligned}\quad \text{IIa-1-8}$$

Consider now the change in the expectation values of the function, if the n particle vectors are linearly scaled by a factor, c . The renormalized scaled function would then be:

$$\Psi_c = c^{\frac{3n}{2}} \Psi(cr_1, cr_2, cr_3, \dots, cr_n) \quad \text{IIa-1-9}$$

and:

$$\begin{aligned}\bar{V}_c &= \langle \Psi_c | \hat{V} | \Psi_c \rangle \\ \bar{T}_c &= \langle \Psi_c | \hat{T} | \Psi_c \rangle\end{aligned}\quad \text{IIa-1-10}$$

Where, for an n electron atom:

$$\hat{V} = - \sum_{i=1}^n \left(\frac{Z}{r_i} \right) + \sum_{i=1}^n \sum_{j>i}^n \frac{1}{r_{ij}} \quad \text{IIa-1-11}$$

$$\hat{T} = -\frac{1}{2} \sum_{i=1}^n \nabla_i^2, \text{ in atomic units} \quad \text{IIa-1-12}$$

Then, expanding the bra-ket, IIa-1-10, for \bar{V}_c , we obtain:

$$\bar{V}_c = \int \Psi_c^* \left[\sum_{i=1}^n \left(\frac{-Z}{r_i} \right) + \sum_{i=1}^n \sum_{j<i}^n \frac{1}{r_{ij}} \right] \Psi_c d(cv) \quad \text{IIa-1-13}$$

Complete scaling of coordinates is achieved by multiplying the operator by $\frac{1}{c}$, and the whole integral by c , to give:

$$\bar{V}_c = c \int \Psi_c^* \left[\sum_{i=1}^n \left(\frac{-Z}{cr_i} \right) + \sum_{i=1}^n \sum_{j<i}^n \frac{1}{cr_{ij}} \right] \Psi_c \delta(cv) \quad \text{IIa-1-14}$$

Since [4]:

$$\int_a^b f(x) dx = \int_a^b f(cx) d(cx) \quad \text{IIa-1-15}$$

Then IIa-1-14, reduces to:

$$\bar{V}_c = c\bar{V} \quad \text{IIa-1-16}$$

The same approach for \bar{T} , which involves $\frac{1}{r_{ij}^2}$ terms, gives:

$$\bar{T}_c = c^2\bar{T} \quad \text{IIa-1-16}$$

We now seek the value of the scale factor which minimizes the total energy, given for the scaled function as:

$$\bar{E}_c = \bar{T}_c + \bar{V}_c = c^2\bar{T} + c\bar{V} \quad \text{IIa-1-17}$$

Differentiating with respect to c with \bar{T} and \bar{V} constants:

$$\frac{\delta \bar{E}_c}{\delta c} = 2c\bar{T} + \bar{V} = 0 \quad \text{IIa-1-17}$$

This gives the values of c which minimize the total energy, and is the basis of the Virial Theorem.

Consider the case when Ψ is an exact wavefunction, no further energy lowering would result from rescaling, hence c is unity, and IIa-1-17 becomes:

$$2\bar{T} + \bar{V} = 0$$

$$\text{or: } \bar{V} = -2\bar{T}$$

It follows that the Hartree Fock wavefunctions must satisfy the Virial relation through linear and non-linear scaling inherent in the Hartree Fock method. If the basis set is extensive enough, and the Hartree Fock limit is approached, then \bar{V}/\bar{T} will approach -2. This useful application of the Virial Theorem, as an indicator of closeness of approach to the Hartree Fock solution, must be considered a necessary but not a sufficient condition for convergence.

IIa-2 Hartree Fock Roothaan Formalism for Closed Shell Molecules

This section is based on Roothaan's derivation of the Hartree Fock SCF equations including the Linear Combination of Atomic Orbitals

(LCAO) approximation [8]. The section is divided into two parts. The first part contains a development of the formula for the expectation value of the molecular Hamiltonian, for the case where the wavefunction is a single determinantal antisymmetrized product. In the second part a derivation of the Hartree Fock Roothaan (HFR) equations will be given, by requiring the energy to be stationary with respect to variations in the molecular orbitals.

The discussion will be limited to a closed shell system of $2n$ electrons.

(i) The antisymmetrized product (AP) wavefunction for a $2n$ electron closed shell system is given by the Slater determinant [9]:

$$\Psi(2n) = (2n!)^{-\frac{1}{2}} |\psi_1(1)\bar{\psi}_1(2)\psi_2(3)\bar{\psi}_2(4)\dots\psi_n(2n-1)\bar{\psi}_n(2n)|$$

IIa-2-1

Where ψ_i is a one electron molecular spin orbital (MSO). The bar denotes spin function of β spin, no bar denotes an α spin function.

The set of n MSO's form an orthonormal set, i.e. for the μ^{th} electron:

$$\langle \psi_i(\mu) | \psi_j(\mu) \rangle = \delta_{ij}$$

IIa-2-2

The electronic energy of the $2n$ electron system is given by the expectation value:

$$\bar{E} = \langle \Psi(2n) | \hat{H} | \Psi(2n) \rangle$$

IIa-2-3

Substitution of the wavefunction into this expression and enumeration of the integrals will then give an expression for the energy.

Before equation IIa-2-3 can be evaluated, the determinantal wavefunctions have to be expanded. Expressing the determinants with the use of the antisymmetrizing operator:

$$\Psi(2n) = \hat{A}(\psi_1(1)\bar{\psi}_1(2)\dots\psi_n(2n-1)\bar{\psi}_n(2n))$$

IIa-2-4

For a $2n$ particle system, the antisymmetrizing operator has the form:

$$\hat{Q} = (2n!)^{-\frac{1}{2}} \sum_{\hat{P}} (-1)^P \hat{P} \quad \text{IIa-2-5}$$

$$= (2n!)^{-\frac{1}{2}} (1 - \sum_{ij} \hat{P}_{ij} + \sum_{ijk} \hat{P}_{ijk} \dots) \quad \text{IIa-2-6}$$

Where \hat{P} is the permutation operator carrying out all permutations, and \hat{P}_{ij} and \hat{P}_{ijk} etc, are 2 and 3 particle permutation operators, and P is the parity of each n particle permutation. Some useful properties of the antisymmetrization and permutation operators (which will be used later) are available in Pilar [5] Chapter 11.5.

Writing out \mathcal{H} more explicitly, using atomic units:

$$\mathcal{H} = \sum_{\mu=1}^{2n} \left(-\frac{1}{2} \nabla_{\mu}^2 - \sum_{\alpha=1}^{\text{nuclei}} \frac{Z_{\alpha}}{r_{\mu\alpha}} \right) + \sum_{\mu=1}^{2n} \sum_{\nu=\mu+1}^{2n} \frac{1}{r_{\mu\nu}} \quad \text{IIa-2-7}$$

This expression can be simplified into one electron and two electron terms. The kinetic energy and nuclear-electron attraction energies appearing in the first summation depend on one electron coordinate and the second summation over 2 electron coordinates represents the electron-electron interaction terms. The contribution to the energy from nuclear-nuclear repulsion terms has been omitted since a fixed geometry is being considered and hence the contribution is constant and can simply be added to the electronic energy.

Hence \mathcal{H} can be expressed as:

$$\mathcal{H} = \sum_{\mu=1}^{2n} \hat{h}_{\mu} + \sum_{\mu < \nu} \frac{1}{r_{\mu\nu}} \quad \text{IIa-2-8}$$

Equation IIa-2-3 can now be expressed as:

$$\begin{aligned} E = & \sum_{\hat{P}} (-1)^P \langle \psi_1(1) \bar{\psi}_1(2) \dots \psi_n(2n-1) \bar{\psi}_n(2n) | \sum_{\mu=1}^{2n} \hat{h}_{\mu} \\ & + \sum_{\mu < \nu} \frac{1}{r_{\mu\nu}} | \hat{P} \psi_1(1) \bar{\psi}_1(2) \dots \psi_n(2n-1) \bar{\psi}_n(2n) \rangle \end{aligned} \quad \text{IIa-2-9}$$

Taking each term of the Hamiltonian in turn, the contribution from the one electron term is:

$$\sum_{\hat{P}} (-1)^P \langle \psi_1(1) \bar{\psi}_1(2) \dots \psi_n(2n-1) \bar{\psi}_n(2n) | \sum_{\mu=1}^{2n} \hat{h}_{\mu} | \hat{P} \psi_1(1) \bar{\psi}_1(2) \dots \psi_n(2n-1) \bar{\psi}_n(2n) \rangle \quad \text{IIa-2-10}$$

By virtue of the space/spin orthogonality of each MSO the summation over all permutations, P, is restricted to the identity permutation only, equation IIa-2-10 reduces to:

$$\langle \psi_1(1) \bar{\psi}_1(2) \dots \psi_n(2n-1) \bar{\psi}_n(2n) | \sum_{\mu=1}^{2n} \hat{h}_{\mu} | \psi_1(1) \bar{\psi}_1(2) \dots \psi_n(2n-1) \bar{\psi}_n(2n) \rangle \quad \text{IIa-2-11}$$

Because \hat{h}_{μ} is independent of electron spin, and that each spatial orbital can be occupied by an electron of α or β spin, i.e.:

$$\psi_i(\mu) = \phi_i(x_{\mu}) \lambda(\alpha_{\mu}) \quad \text{IIa-2-12}$$

$$\psi_i(\mu) = \phi_i(x_{\mu}) \lambda(\beta_{\mu}) \quad \text{IIa-2-13}$$

Integration over spin reduces equation IIa-2-11 to:

$$\sum_{\mu=1}^n \langle \phi_1(1) \phi_2(2) \dots \phi_n(n) | \hat{h}_{\mu} | \phi_1(1) \phi_2(2) \dots \phi_n(n) \rangle \quad \text{IIa-2-14}$$

Which becomes:

$$\sum_{i=1}^n \langle \phi_i | \hat{h} | \phi_i \rangle = \sum_{i=1}^n H_{ii} \quad \text{IIa-2-15}$$

The integral in IIa-2-15 is defined as the one electron energy of the system, and represents the total one electron contribution.

Let us now return to equation IIa-2-9 and consider the contribution from the two electron portion, i.e.:

$$\sum_{\hat{P}} (-1)^P \langle \psi_1(1) \bar{\psi}_1(2) \dots \psi_n(2n-1) \bar{\psi}_n(2n) | \sum_{\mu < \nu} \frac{1}{r_{\mu\nu}} | \hat{P} \psi_1(1) \bar{\psi}_1(2) \dots \psi_n(2n-1) \bar{\psi}_n(2n) \rangle \quad \text{IIa-2-16}$$

Firstly consider the identity permutation. Separation of the integral into a product of integrals and using the orthonormality of the MSO's then the only non-zero integrals are those represented by:

$$\sum_{ij}^n \sum_{\mu < \nu}^{2n} \langle \psi_i(\mu) \psi_j(\nu) | \frac{1}{r_{\mu\nu}} | \psi_i(\mu) \psi_j(\nu) \rangle \quad \text{IIa-2-17}$$

This general expression can be simplified, by integration over spin, into terms arising from when electrons μ and ν occupy the same spatial orbital, and when they occupy different spatial orbitals. In the case when electrons μ and ν occupy different spatial orbitals there is four occurrences of the same integral since either spatial orbital can be associated with either α or β spin.

Hence IIa-2-17 becomes:

$$\begin{aligned} & \sum_{i=1}^n \langle \phi_i(\mu=2i-1) \phi_i(\nu=2i) | \frac{1}{r_{\mu\nu}} | \phi_i(\mu=2i-1) \phi_i(\nu=2i) \rangle \\ & + 4 \sum_{i < j}^n \langle \phi_i(\mu) \phi_j(\nu) | \frac{1}{r_{\mu\nu}} | \phi_i(\mu) \phi_j(\nu) \rangle \end{aligned} \quad \text{IIa-2-18}$$

These integrals represent coulomb interaction between 2 electrons in two spatial orbitals. They are given the symbol J with subscripts denoting the spatial orbitals.

Hence IIa-2-18 becomes:

$$\sum_{i=1}^n J_{ii} + 4 \sum_{i < j}^n J_{ij} \quad \text{IIa-2-19}$$

Returning to the two electron terms and considering the contribution after a single permutation. A permutation of two particles has a parity of -1 so all contributions are negative. Due to spin orthogonality only the permutation of 2 particles of like spin leads to non-zero integrals, with the operator operating on the 2 electrons that have been exchanged. This leads to 2 integrals of the same type, after integration over spin, for each spatial orbital. Integrals of the type:

$$-2 \sum_{i < j}^n \langle \phi_i(\mu) \phi_j(\nu) | \frac{1}{r_{\mu\nu}} | \phi_j(\mu) \phi_i(\nu) \rangle \quad \text{IIa-2-20}$$

are the only non-zero values. These integrals represent interaction between electrons of like spin in different spatial orbitals, and for this reason they have been called exchange integrals and are given the symbol K_{ij} .

Hence IIa-2-20 becomes:

$$-2 \sum_{i < j}^n K_{ij} \quad \text{IIa-2-21}$$

Permutations of more than 2 electrons leads to no non-zero integrals, hence there are no further contributions to equation IIa-2-9.

Summing up all the contributions, equations IIa-2-15, 19 and 21, the expectation energy for a closed shell system becomes:

$$\bar{E} = \sum_{i=1}^n H_{ii} + \sum_{i=1}^n J_{ii} + \sum_{i < j}^n (4J_{ij} - 2K_{ij}) \quad \text{IIa-2-22}$$

Using the relations:

$$J_{ij} = J_{ji}, \quad K_{ij} = K_{ji}, \quad J_{ii} = K_{ii} \quad \text{IIa-2-23}$$

and relaxing the restrictions on the double index summation, equation IIa-2-22 becomes:

$$\bar{E} = \sum_{i=1}^n H_{ii} + \sum_{i,j}^n (2J_{ij} - K_{ij}) \quad \text{IIa-2-24}$$

This is the familiar expression for the energy of a $2n$ electron closed shell system, for a wavefunction written as a single determinant of doubly occupied molecular orbitals.

(ii) From the previous section we see that the total energy associated with a $2n$ electron antisymmetrized product (AP) wavefunction is:

$$\bar{E} = 2 \sum_{i=1}^n H_{ii} + \sum_{i,j}^n (2J_{ij} - K_{ij}) \quad \text{IIa-2-25}$$

We now require to find the best possible orbitals to use in a wavefunction restricted to a single determinant. Using the Variation Method, we wish to find those orbitals which lead to a minimum value of the energy given by IIa-2-25, subject to the restriction that these orbitals remain orthonormal [8].

The Variational problem can be defined by the functional:

$$f = \bar{E} - \sum_{ij}^n \lambda_{ij} (S_{ij} - \delta_{ij}) \quad \text{IIa-2-26}$$

$$\text{Where: } \bar{E} = \langle \Psi(2n) | \mathcal{H} | \Psi(2n) \rangle \quad \text{IIa-2-27}$$

$$\text{and: } S_{ij} = \langle \phi_i | \phi_j \rangle \quad \text{IIa-2-28}$$

λ_{ij} is a set of Lagrangian undetermined multipliers and δ_{ij} is the Kroeneker delta function. \bar{E} , the expectation energy, and S_{ij} , the overlap integral, have their usual definitions as in IIa-2-27 and 28. The stationary values of f will be those for which δf vanishes, and provided Ψ is normalized, then $\delta \bar{E} = 0$ is also satisfied, i.e. it is necessary for \bar{E} to be stationary with respect to variations in Ψ .

Substituting IIa-2-25 and IIa-2-28 into IIa-2-26 gives:

$$f = 2 \sum_{i=1}^n H_{ii} + \sum_{i,j}^n (2J_{ij} - K_{ij}) - \sum_{ij}^n \lambda_{ij} (S_{ij} - \delta_{ij}) \quad \text{IIa-2-29}$$

In the following treatment only the spatial component of the molecular orbitals will be considered. It is also convenient to redefine the coulomb and exchange integrals in terms of coulomb and exchange operators [8].

Coulomb and exchange operators (denoted by a single subscript) are defined as:

$$\hat{J}_i(\mu)\phi_j(\mu) = \langle \phi_i(v) | \frac{1}{r_{\mu v}} | \phi_i(v) \rangle \phi_j(\mu) \quad \text{IIa-2-30}$$

$$\hat{K}_i(\mu)\phi_j(\mu) = \langle \phi_i(v) | \frac{1}{r_{\mu v}} | \phi_j(v) \rangle \phi_i(\mu) \quad \text{IIa-2-31}$$

respectively.

And, using these operators:

$$J_{ij} = \langle \phi_i(\mu) | \hat{J}_j(\mu) | \phi_i(\mu) \rangle = \langle \phi_j(\nu) | J_i(\nu) | \phi_j(\nu) \rangle \quad \text{IIa-2-32}$$

$$K_{ij} = \langle \phi_j(\nu) | \hat{K}_i(\nu) | \phi_j(\nu) \rangle = \langle \phi_i(\mu) | K_j(\mu) | \phi_i(\mu) \rangle \quad \text{IIa-2-33}$$

We now wish to find conditions which the orbitals ϕ_i must satisfy in order for the functional f to have a stationary value, i.e. $\delta f = 0$ for small variations $\delta\phi_i$. The first order variation in the functional f for a variation in ϕ_i by $\delta\phi_i$, is given as:

$$\delta f = 2 \sum_{i=1}^n \delta H_{ii} + \sum_{i,j}^n (2\delta J_{ij} - \delta K_{ij}) - \sum_{i,j}^n \lambda_{ij} \delta S_{ij} \quad \text{IIa-2-34}$$

Expanding H_{ii} , J_{ij} , K_{ij} and S_{ij} , equation IIa-2-34 becomes:

$$\begin{aligned} \delta f = & 2 \sum_{i=1}^n (\langle \delta\phi_i | \hat{h}_i | \phi_i \rangle + \langle \phi_i | \hat{h}_i | \delta\phi_i \rangle) \\ & + \sum_{i,j}^n (\langle \delta\phi_i | 2\hat{J}_j - \hat{K}_j | \phi_i \rangle + \langle \phi_i | 2\hat{J}_j - \hat{K}_j | \delta\phi_i \rangle) \\ & + \sum_{i,j}^n (\langle \delta\phi_j | 2\hat{J}_i - \hat{K}_i | \phi_j \rangle + \langle \phi_j | 2\hat{J}_i - \hat{K}_i | \delta\phi_j \rangle) \\ & - \sum_{i,j}^n \lambda_{ij} (\langle \delta\phi_i | \phi_j \rangle + \langle \phi_i | \delta\phi_j \rangle) \end{aligned} \quad \text{IIa-2-35}$$

Where \hat{h}_i is the one electron term in the Hamiltonian. The first and second double summations are symmetric in their indices, and lead to the same final sums. Thus equation IIa-2-35 can be rewritten:

$$\begin{aligned} \delta f = & 2 \sum_{i=1}^n [\langle \delta\phi_i | \hat{h}_i + \sum_j (2\hat{J}_j - \hat{K}_j) | \phi_i \rangle] \\ & + 2 \sum_{i=1}^n [\langle \phi_i | \hat{h}_i + \sum_j (2\hat{J}_j - \hat{K}_j) | \delta\phi_i \rangle] \\ & - \sum_{i,j}^n (\lambda_{ij} \langle \delta\phi_i | \phi_j \rangle + \lambda_{ij} \langle \phi_i | \delta\phi_j \rangle) \end{aligned} \quad \text{IIa-2-36}$$

Using the Hermitian properties of \hat{h}_i , \hat{J}_j and \hat{K}_j and noting that:

$$\sum_{i,j} \lambda_{ij} \langle \phi_i | \delta \phi_j \rangle = \sum_{i,j} \lambda_{ji} \langle \delta \phi_i | \phi_j \rangle^*$$

through being adjoints of each other, then IIa-2-36 can be rearranged to give:

$$\begin{aligned} \delta f = & 2 \sum_{i=1}^n [\langle \delta \phi_i | \hat{h}_i + \sum_j (2\hat{J}_j - \hat{K}_j) | \phi_i \rangle - \sum_j \lambda_{ij} \langle \delta \phi_i | \phi_j \rangle] \\ & + 2 \sum_{i=1}^n [\langle \delta \phi_i | \hat{h}_i + \sum_j (2\hat{J}_j - \hat{K}_j) | \phi_i \rangle^* - \sum_j \lambda_{ji} \langle \delta \phi_i | \phi_j \rangle^*] \end{aligned}$$

IIa-2-37

If δf is to vanish for an arbitrary variation of $\delta \phi_i$ then each summation in IIa-2-37 must be independently zero. The summation of integrals can only equal zero if they are all individually zero or they are finite but cancel. The latter equality would not hold for an arbitrary variation in $\delta \phi_i$ for all i , therefore we must conclude that each integral vanishes. For an integral to be zero requires that the integrand be identically zero.

Hence:

$$[h_i + \sum_j (2\hat{J}_j - \hat{K}_j)] \phi_i = \sum_j \lambda_{ij} \phi_j \quad \text{IIa-2-38}$$

and:

$$[h_i + \sum_j (2\hat{J}_j - \hat{K}_j)] \phi_i^* = \sum_j \lambda_{ji}^* \phi_j^* \quad \text{IIa-2-39}$$

Taking the complex conjugate of IIa-2-39 from IIa-2-38 we obtain:

$$\sum_j \lambda_{ji}^* (\lambda_{ij} - \lambda_{ji}^*) = 0 \quad \text{IIa-2-40}$$

Since the orbitals ϕ_j are linearly independent, it follows that:

$$\lambda_{ij} = \lambda_{ji}^* \quad \text{IIa-2-41}$$

Hence the Lagrangian multipliers are the elements of a hermitian matrix, and equations IIa-2-38 and IIa-2-39 are complex conjugates of each other. Hence equations IIa-2-38 and IIa-2-39 represent all the conditions for stationary energy and for optimized ϕ_i .

Using IIa-2-38 as the final equation for ϕ_i we can now define the operators:

$$\hat{G} = \sum_j (2\hat{J}_j - \hat{K}_j) \quad \text{IIa-2-42}$$

and:

$$\hat{H} = \hat{h}_i$$

and:

$$\hat{F} = \hat{H} + \hat{G}$$

Equation IIa-2-38 can now be written as:

$$\hat{F}\phi_i = \sum_j \phi_j \lambda_{ij} \quad \text{IIa-2-43}$$

Equation IIa-2-43 is a differential equation for each orbital ϕ_i and must not be confused with an eigen value equation.

The operators \hat{F} , \hat{G} and \hat{H} have become known as the Fock operator, the total electron interaction operator and the one electron operator respectively.

It is possible to choose a unitary transformation such that the matrix λ_{ij} is diagonalized and equation IIa-2-43 becomes an eigen value equation.

Expressing IIa-2-43 in matrix form we obtain:

$$\underline{F} \underline{\Phi} = \underline{\Phi} \underline{\Lambda} \quad (\underline{\Lambda})_{ij} = \lambda_{ij} \quad \text{IIa-2-44}$$

Also if the set of orbitals, $\underline{\Phi}$, is subject to a transformation by means of a unitary matrix \underline{U} , i.e.:

$$\underline{\Phi}' = \underline{\Phi} \underline{U} \quad \text{IIa-2-45}$$

With:

$$\underline{U} \underline{U}^* = \underline{U}^* \underline{U} = \underline{E} \quad \text{IIa-2-46}$$

And if IIa-2-44 is multiplied from the right by \underline{U} , we obtain:

$$\underline{F} \underline{\Phi} \underline{U} = \underline{\Phi} \underline{\Lambda} \underline{U} \quad \text{IIa-2-47}$$

If we premultiply $\underline{\Lambda}$ by the unit matrix in IIa-2-46 and use IIa-2-45, we

obtain from IIa-2-47:

$$\underline{F} \underline{\phi}' = \underline{\phi} \underline{U} \underline{U}^* \underline{\Lambda} \underline{U} \quad \text{IIa-2-48}$$

$$= \underline{\phi}' \underline{U}^* \underline{\Lambda} \underline{U} \quad \text{IIa-2-49}$$

Since $\underline{\Lambda}$ has been shown to be Hermitian (see IIa-2-41) then a unitary transformation can be chosen so as to make $\underline{\Lambda}$ diagonal. i.e.:

$$\underline{U}^* \underline{\Lambda} \underline{U} = \underline{\epsilon} \quad \text{and} \quad (\underline{\epsilon})_{ij} = \epsilon_i \delta_{ij} \quad \text{IIa-2-50}$$

Resulting in IIa-2-49 becoming:

$$\underline{F} \underline{\phi}' = \underline{\phi}' \underline{\epsilon} \quad \text{IIa-2-51}$$

However, the operator \underline{F} is defined in terms of the original orbitals $\underline{\phi}$, and not in terms of the transformed orbitals, ϕ' . Application of the unitary transformation matrix, \underline{U} , results in the transformed operators being equivalent to the original operator (see ref [5], page 344). As a result we may rewrite equation IIa-2-51, in pseudo eigen value form:

$$\underline{F} \underline{\phi} = \underline{\phi} \underline{\epsilon} \quad \text{or} \quad \hat{F}\phi_i = \epsilon_i \phi_i \quad \text{IIa-2-52}$$

The above equation has become generally known as the Hartree-Fock equation, and has as eigen values the energies ϵ_i associated with the one electron Hartree Fock orbitals ϕ_i . The origin of the orbital energies can be traced back to the Lagrangian multipliers λ_{ij} used in formulating the variational problem. (See equation IIa-2-26).

The approach outlined above leads to integro-differential equations that are unweildy and can not be easily solved for systems with more than one nucleus. This lead to Roothaan [8] introducing the LCAO approximation.

In the LCAO approximation each Hartree Fock orbital ϕ_i is expanded in terms of a basis set of atomic orbitals, i.e.:

$$\phi_i = \sum_p \chi_p c_{pi} \quad \text{IIa-2-53}$$

The set, $\{\chi_p\}$, is known as the atomic orbital basis set, where the atomic functions are linearly independent and normalized. If we

substitute for ϕ_i in equation IIa-1-52, we obtain:

$$\hat{F} \sum_p \chi_p c_{pi} = \epsilon_i \sum_p \chi_p c_{pi} \quad \text{IIa-2-54}$$

Multiplying from the left by χ_q and integrating gives:

$$\sum_p c_{pi} \langle \chi_q | \hat{F} | \chi_p \rangle = \epsilon_i \sum_p c_{pi} \langle \chi_q | \chi_p \rangle \quad \text{IIa-2-55}$$

Rearranging IIa-2-55, gives:

$$\sum_p c_{pi} (F_{pq} - S_{pq} \epsilon_i) = 0 \quad \text{IIa-2-56}$$

Where:

$$F_{pq} = \langle \chi_q | \hat{F} | \chi_p \rangle \quad \text{IIa-2-57}$$

$$S_{pq} = \langle \chi_q | \chi_p \rangle \quad \text{IIa-2-58}$$

Equations IIa-2-56 are simultaneous equations for the unknown c_{pi} , the non trivial solutions are obtained from the m roots of the secular determinant, i.e.:

$$\det | F_{pq} - S_{pq} \epsilon_i | = 0 \quad \text{IIa-2-59}$$

Since the operator \hat{F} depends on the values of c_{ip} , through ϕ_i , then these secular equations are non linear and must be solved by an iterative process. Equation IIa-2-59 has become known as the Hartree-Fock-Roothaan equation (HFR), and has become the accepted method of molecular orbital calculation.

IIa-3 Koopmans' Theorem

Koopmans' Theorem [10] states:

"If $\Psi(2n)$ is the "best" single determinantal wavefunction of a $2n$ electron closed shell system, and ϕ_k and ϕ_m are eigen functions of the Fock operator, \hat{F} , then $\Psi^{(k)}(2n-1)$ and $\Psi^{(m)}(2n+1)$ are also stationary with respect to further variations in the orbitals ϕ_k and ϕ_m respectively".

The physical interpretation of Koopmans' Theorem is that, for a calculation performed at the Hartree Fock limit, the ionization potential of a closed shell atom or molecule is given by the negative of the orbital energy of the orbital, ϕ_k , from where the electron was ionized. Also the electron affinity of a closed shell atom or molecule is given as the orbital energy of the orbital, ϕ_m , into which the electron will enter.

To demonstrate this, consider the total electronic wavefunction for a closed shell ground state configuration as a Slater determinant, i.e.:

$$^1\Psi(2n) = (2n)^{-\frac{1}{2}} |\psi_1(1)\bar{\psi}_1(2)\psi_2(3)\dots\psi_n(2n-1)\bar{\psi}_n(2n)| \quad \text{IIa-3-1}$$

where $\psi_i(\mu)$ are MSO's with α spin functions and $\bar{\psi}_i(\nu)$ are MSO's with β spin functions. Consider ionization of an electron from orbital ϕ_k of this system producing a $(2n-1)$ electron system whose wavefunction is constructed from orbitals in $\Psi(2n)$, i.e.:

$$^2\Psi^{(k)}(2n-1) = |\psi_1(1)\bar{\psi}_1(2)\dots\psi_k(2k-1)\dots\psi_n(2n-1)\bar{\psi}_n(2n)| \quad \text{IIa-3-2}$$

(Note: An electron with spin β is shown to be ionized here, equally likely would be ionization of the spin paired α spin electron. The distinction is inappropriate here and either occurrence leads to the same result in the case of restricted Hartree Fock orbitals).

Similarly, consider a $(2n+1)$ electron system, whose wavefunction is constructed from the orbitals of $\Psi(2n)$ plus an additional orbital, namely ψ_m , i.e.:

$$^2\Psi^{(m)}(2n+1) = |\psi_1(1)\bar{\psi}_1(2)\dots\psi_n(2n-1)\bar{\psi}_n(2n)\psi_m(2n+1)| \quad \text{IIa-3-3}$$

The determinantal functions IIa-3-2 and IIa-3-3 can be said to be approximate wavefunctions of the cation and anion respectively, of the system described by $\Psi(2n)$.

As described in section II(ii), the Hartree-Fock equations for the 'best' orbitals of a closed shell system can be written in pseudoeigen value form (equation IIa-2-52):

$$\hat{F}\phi_i = \epsilon_i \phi_i \quad \text{IIa-3-4}$$

where \hat{F} is the Fock operator.

The eigen value for orbital, ϕ_i , ϵ_i , is given as:

$$\begin{aligned} \epsilon_i &= \langle \phi_i | \hat{F} | \phi_i \rangle = \langle \phi_i | \hat{h}_i + \sum_j (2\hat{J}_j - \hat{K}_j) | \phi_i \rangle \\ &= \langle \phi_i | \hat{h}_i | \phi_i \rangle + \sum_j \langle \phi_i | (2\hat{J}_j - \hat{K}_j) | \phi_i \rangle \end{aligned} \quad \text{IIa-3-4}$$

Substituting:

$$\begin{aligned} \epsilon_i^0 &= \langle \phi_i | \hat{h}_i | \phi_i \rangle \\ J_{ij} &= \langle \phi_i | \hat{J}_j | \phi_i \rangle \quad \text{and} \quad K_{ij} = \langle \phi_i | \hat{K}_j | \phi_i \rangle \end{aligned}$$

into IIa-3-4, gives:

$$\epsilon_i = \epsilon_i^0 + \sum_j (2J_{ij} - K_{ij}) \quad \text{IIa-3-5}$$

Adding ϵ_i^0 to both sides of IIa-3-5 and summing over all n orbitals in the $2n$ electron system, IIa-3-5 becomes:

$$\sum_{i=1}^n (\epsilon_i + \epsilon_i^0) = 2 \sum_{i=1}^n \epsilon_i^0 + \sum_{i,j}^n (2J_{ij} - K_{ij}) \quad \text{IIa-3-6}$$

The right hand side of IIa-3-6 is equivalent to the energy of a $2n$ electron closed shell system. (See equation IIa-2-24). Hence the energy of a closed shell $2n$ electron system is given as the sum of the occupied orbital energies (ϵ_i) plus the one electron energies of each electron (ϵ_i^0). Using IIa-3-6 the energies of the neutral, anion and cation are:

$$E^0(2n) = \sum_{i=1}^n (\epsilon_i^0 + \epsilon_i) \quad \text{IIa-3-7}$$

$$E^-(2n+1) = \sum_{i=1}^n (\epsilon_i^0 + \epsilon_i) + \epsilon_m \quad \text{IIa-3-8}$$

$$E^+(2n-1) = \sum_{i=1}^n (\epsilon_i^0 + \epsilon_i) - \epsilon_k \quad \text{IIa-3-9}$$

Hence it follows that the ionization energy is given as:

$$E^+(2n-1) - E^0(2n) = -\epsilon_k \quad \text{IIa-3-10}$$

And the electron affinity is given as:

$$E^-(2n+1) - E^0(2n) = \epsilon_m \quad \text{IIa-3-11}$$

Equations IIa-3-8 and IIa-3-9 show that Koopmans' Theorem allows the expression of the energies of the cation and anion, of a $2n$ closed shell neutral system, in terms of the optimized orbitals of the neutral system. The energy differences, in equation IIa-3-10 and IIa-3-11, the ionization energy and electron affinity, are related to the eigen values of the Fock operator after Koopmans' Theorem has been applied.

In general Koopmans' Theorem yields reasonably good values for ionization potentials for the highest occupied orbitals of a closed shell molecules. However it is less successful, in practice, for electron affinities and higher ionization potentials. One reason for these errors is that we assumed that doubly occupied SCF orbitals, produced by a variational procedure on the neutral $2n$ electron system, will be suitable doubly occupied orbitals for the ion. In effect we are assuming that there is no reorganization of the electron distribution on addition or removal of an electron.

The use of the orbitals that minimise the energy of the $2n$ electron system for the ions will result in an energy for the cation or anion that is higher than that produced by an independent variational calculation on the ions. The lowering of energy of the ion, produced by an independent calculation, is called the Reorganization Energy, given the symbol R , and is positive which accounts for the Koopmans' Theorem result being an over-estimate of the experimental quantity.

Another contribution to the inaccuracy in the Koopmans' Theorem values, is the neglect of change in correlation energy between the neutral and the ion. It has been shown [11] that correlation effects can largely be accounted for as sums of electron pair interactions in the system. Hence the correlation energy of the neutral, the cation and the anion will differ because of different numbers of electron pair interactions in each

system.

In the case of ionization the Koopmans' Theorem value would usually be lower than experimental because the correlation energy of the neutral is usually greater than that of the cation. Whereas in the case of electron affinities the Koopmans' Theorem value would usually be higher than experimental because the correlation energy of the anion would usually be greater than that of the neutral.

The experimental ionization potentials and electron affinities associated with orbital ϕ_k and ϕ_m respectively can be related to the Koopmans' Theorem value [12] by the expressions:

$$I_p = -\epsilon_k - R + C \quad \text{IIa-3-12}$$

$$E_A = \epsilon_m - R - C \quad \text{IIa-3-13}$$

Where R is the reorganization energy of the ion and C is the absolute correlation energy difference between the neutral and the ion.

For the case of ionization potentials it can be seen that R and C contribute in an opposite sense and tend to cancel out. Koopmans' Theorem often works well in predicting correct ionic state ordering, especially if the ionic states are well separated, by 2-3 eV, and are low lying.

For the case of electron affinities it can be seen that R and C contribute in the same sense, resulting in the Koopmans' Theorem value for the electron affinities of a neutral molecule being much too large. It is for this reason that Koopmans' Theorem has found wide application in the prediction of ionization potentials and has been virtually neglected for the case of electron affinities.

II-4 Open Shell Methods - ATMOL-3 Formalism

In this section the open shell problem will be discussed, with a brief mention of the methods applied to its solution. In the later stages the formulation of the ATMOL SCF method will be expounded and its major features discussed in comparison with previous methods.

The initial approach to the open shell problem was to introduce the concept of different spatial orbitals for electrons of different

spins [13-15]. This method removes the limitation of spin pairing which leads to open and closed shell definitions. This method has become known as the Unrestricted Hartree Fock (UHF) method and has a major deficiency in the fact that the total wavefunction is not an eigen function of the operator \hat{S}^2 . However it is possible to use spin projection operators to remove contaminating spin functions [16]. Another approach was that of Nesbet [17,18], called the method of Symmetry and Equivalence restrictions. The method is uncomplicated and quite general but has a drawback in being a method which formulates the problem in terms of an effective Hamiltonian which is chosen by the user, and does not use the general electronic Hamiltonian.

The conditions for stationary energy were derived, for an open shell determinantal wavefunction, by Roothaan [19] using the Hartree Fock LCAO approach. Initially the paper outlined a method that formulated sets of SCF equations for the orbitals of the closed shell and open shell separately, by use of two Hamiltonians. This method has become known as the Roothaan Double Hamiltonian method and is limited in that the method does not treat virtual orbitals and does not converge to self consistency very rapidly. To circumvent these problems Roothaan, in the same paper, extended the treatment to convert his double Hamiltonian method, by use of coupling operators, to a single Hamiltonian approach. This had the advantage of being able to encompass virtual orbitals but the convergence characteristics of this approach were unsatisfactory in practice. Huzinaga [20] extended Roothaan's method to include two or more open shells for all spin multiplicities and the convergence properties of Roothaan's methods have also been studied further [21,22]. An alternative approach to the open shell problem was proposed by McWeeny [23-26] which entailed seeking a stationary energy with respect to changes in the first order density matrix rather than setting up an eigen value problem. The method has become known as the Density Matrix or Steepest Decents Method. Berthier [27] extended the method to include general open shell configurations using Hamiltonians that were analogous to Roothaan's, but suffered from poor convergence characteristics [28] and was too slow in practice. A further advance was made by the formulation of the Combined Hamiltonian method [29] by McWeeny, which

was the first to propose the use of three basic Hamiltonians. The method has the advantage that it is applicable to any open shell configuration but the initial canonicalisation scheme left the orbital energies poorly defined. However, this has been overcome [30] by redefining the orbital energies in terms of certain energy expectation values.

The next derivation of an open shell SCF procedure was what has now become known as the ATMOL method [31-34]. In this method the Combined Hamiltonian method of McWeeny is reformulated in the molecular orbital basis. This renders the blocks of the Hamiltonian, representing the closed, open and virtual shells, completely independent. It is this independence of the blocks within the molecular Hamiltonian that makes the ATMOL method unrivaled by any other ab-initio open shell method.

The ATMOL method will now be described in detail.

The ATMOL-3 SCF Method:

The ATMOL SCF procedure is designed to minimize the energy of a single determinantal wavefunction constructed from a set of orthonormal molecular orbitals, grouped into shells and approximated as a linear combination of a set of m atomic orbitals, $\{\chi\}$. The number of shells defined depends on the configuration under consideration, but here for simplicity we shall consider an open shell configuration with the open shell orbitals of the same symmetry. The discussion presented is easily extended to cover more complicated configurations where more shells have to be defined.

The molecular wavefunction is constructed from a set of m_1 doubly occupied molecular orbitals (DOMO's), a set of m_2 partial occupied molecular orbitals (POMO's) and a set of m_3 virtual orbitals (VMO's). Hence we have the condition, $m_1 + m_2 + m_3 = m$, the complete set of basis functions. The row matrices of DOMO's, POMO's and VMO's and the basis functions will be denoted thus:

$$\underline{\chi} = (\chi_1 \chi_2 \chi_3 \dots \chi_m) \quad \text{IIa-4-1}$$

$$\underline{\psi}_1 = \underline{\chi} \underline{T}_1 \text{ for DOMO's} \quad \text{IIa-4-2}$$

$$\underline{\psi}_2 = \underline{\chi} \underline{T}_2 \text{ for POMO's} \quad \text{IIa-4-3}$$

$$\underline{\Psi}_3 = \underline{X} \underline{T}_3 \text{ for VMO's} \quad \text{IIa-4-4}$$

Where the matrices \underline{T}_1 , \underline{T}_2 and \underline{T}_3 are $m \times m_1$, $m \times m_2$ and $m \times m_3$ matrices respectively, each containing the basis function coefficients in the LCAO expansion of a given molecular orbital in a particular shell. Combining equations IIa-4-1 \rightarrow IIa-4-4 into a single matrix expression:

$$\underline{\Psi} = (\underline{\Psi}_1 | \underline{\Psi}_2 | \underline{\Psi}_3) = \underline{X}(\underline{T}_1 | \underline{T}_2 | \underline{T}_3) = \underline{X} \underline{T} \quad \text{IIa-4-5}$$

Defining the first order spinless density matrices, for the various shells, as:

$$\begin{aligned} \underline{R}_1 &= \underline{T}_1 \underline{T}_1^\dagger \\ \underline{R}_2 &= \underline{T}_2 \underline{T}_2^\dagger \\ \underline{R}_3 &= \underline{T}_3 \underline{T}_3^\dagger \end{aligned} \quad \text{IIa-4-6}$$

The total wavefunction can now be uniquely defined by \underline{R}_1 and \underline{R}_2 , and is invariant against unitary mixing since it is a determinant, therefore equations IIa-4-6 are invariant to such unitary transformations.

Using the previously defined fixed nucleus Hamiltonian operator, \hat{H} , we may write the electron energy expression, following Roothaan [19], as:

$$\begin{aligned} E &= 2\text{Tr}\underline{R}_1 \underline{H} + 2\text{Tr}\underline{R}_1 \underline{J} | \underline{R}_1 | - \text{Tr}\underline{R}_1 \underline{K} | \underline{R}_1 | \\ &+ w\text{Tr}\underline{R}_2 \underline{H} + x\text{Tr}\underline{R}_2 \underline{J} | \underline{R}_2 | - y\text{Tr}\underline{R}_2 \underline{K} | \underline{R}_2 | \\ &+ 2w\text{Tr}\underline{R}_2 \underline{J} | \underline{R}_1 | - w\text{Tr}\underline{R}_2 \underline{K} | \underline{R}_1 | \end{aligned} \quad \text{IIa-4-7}$$

where \underline{H} is a matrix representation of the one electron operator, in basis function representation, with matrix elements:

$$(\underline{H})_{pq} = \langle \chi_p | \hat{h} | \chi_q \rangle \quad \text{IIa-4-8}$$

$\underline{J} | \underline{R}_i |$ and $\underline{K} | \underline{R}_i |$ are matrix representations of the coulomb and exchange operators respectively, with matrix elements:

$$(\underline{J} | \underline{R}_i |)_{pq} = \sum_{r,s}^{m_i} (\underline{R}_i)_{r,s} \langle \chi_p \chi_s | \hat{g} | \chi_q \chi_r \rangle \quad \text{IIa-4-9}$$

$$(\underline{K}|\underline{R}_i|)_{pq} = \sum_{r,s}^{m_i} (\underline{R}_i)_{r,s} \langle x_p x_s | \hat{g} | x_r x_q \rangle \quad \text{IIa-4-10}$$

where \hat{h} and \hat{g} are the one and two electron operator components of the Hamiltonian, \hat{H} .

The parameters, w , x and y appearing in IIa-4-8 are numerical constants which will depend on the particular open shell problem being studied. There is not a complete unified scheme for the calculation of such parameters, except that w is the fractional occupation of the set of m_2 POMO's. For most commonly occurring configurations and states the values of x , y and w are tabulated for input into the SCF program [35]. The parameters w , x and y are related to Roothaan's f , a and b parameters [19] by the expressions:

$$\begin{aligned} w &= 2f \\ x &= 2af^2 \\ y &= bf^2 \end{aligned} \quad \text{IIa-4-11}$$

The energy expression IIa-4-8 is now made stationary with respect to arbitrary variations in the molecular orbital, subject to orthonormality constraints. Unique specification of self consistency occurs when the matrix of the molecular Hamiltonian, in molecular orbital basis, is diagonalized, which requires $m(m-1)/2$ conditions to be satisfied.

The first $m_1(m_1-1)/2$, $m_2(m_2-1)/2$ and $m_3(m_3-1)/2$ conditions are satisfied for the DOMO's, POMO's and VMO's respectively by the following transformations:

$$\begin{aligned} \underline{T}_1^\dagger \underline{Z}_1 \underline{T}_1 &= \underline{\Lambda} \\ \underline{T}_2^\dagger \underline{Z}_2 \underline{T}_2 &= \underline{\Lambda} \\ \underline{T}_3^\dagger \underline{Z}_3 \underline{T}_3 &= \underline{\Lambda} \end{aligned} \quad \text{IIa-4-12}$$

where \underline{Z}_i are arbitrary hermitian matrices of order m_i and $\underline{\Lambda}$ is a diagonal matrix. Equations IIa-4-12 represent canonicalisation conditions for a given set of MO's. The diagonal elements of $\underline{\Lambda}$ represent orbital energies of the orbitals of a particular shell of MO's and \underline{Z}_i is

constructed from a one particle Fock operator, \hat{F}_n , in basis function representation. The Fock operator used to canonicalize the orbitals of a particular shell arbitrarily effects the magnitude of the orbital energies of the MO's and does not effect the total energy. This is because the SCF wavefunction is a determinant and is invariant to unitary transformation and hence the energy is constant. Hence provided the transformations in IIa-4-12 are unitary transformations then the choice of canonicalization operator is arbitrary. Sets of one particle Fock operators, \hat{F}_n , can now be defined, in basis function representation as:

$$\underline{F}_n = \underline{H} + 2\underline{J}|\underline{R}_1| - \underline{K}|\underline{R}_1| + c_n \underline{J}|\underline{R}_2| - \frac{1}{2}d_n \underline{K}|\underline{R}_2| \quad \text{IIa-4-13}$$

where c_n and d_n are functions of w , x and y . A few examples are listed in Table 1, and represent forms of F_n that have been successfully used in the past.

Each of the Fock operators can be expressed in terms of the trial molecular orbital basis, denoted by F_n^{MO} , by the similarity transformation:

$$\underline{F}_n^{\text{MO}} = \underline{T}_i^{-1} \underline{F}_n \underline{T}_i \quad \text{IIa-4-14}$$

Provided the matrix \underline{T} is real and orthogonal then the unitary transformations in equations IIa-4-12 become special cases of a similarity transformation. Hence the first sets of conditions for self consistency occur when \underline{T}_i become unitary matrices that diagonalize the matrix basis function representation of Fock operator, F_n , chosen for shell i .

Additional conditions for self consistency are satisfied by allowing unitary mixing of the molecular orbitals between shells. Given orthogonal sets of trial molecular orbitals, Ψ_1 , Ψ_2 and Ψ_3 we now require to derive expressions for the change in energy for significant variations in the trial molecular orbitals. We classify physically significant variations in the trial MO's as being one of the following:

- (1) Mixing between the DOMO's and VMO's
- (2) Mixing between the POMO's and VMO's
- (3) Mixing between the DOMO's and POMO's

Small variations, which conform to orthogonality constraints, are represented, for each of the above cases, as:

TABLE 1

	n	c_n	d_n
F_1	1	w	w
F_2	2	$\frac{2x}{w}$	$\frac{4y}{w}$
F_3	3	$\frac{2(w-x)}{(2-w)}$	$\frac{2(w-2y)}{(2-w)}$
F_4	4	$\frac{(4w^2-w^3-4x)}{w(2-w)}$	$\frac{(4w^2-w^3-8y)}{w(2-w)}$
F_5	5	$\frac{(w^3-4xw+4x)}{w(2-w)}$	$\frac{(w^3-8yw+8y)}{w(2-w)}$
F_6	6	$\frac{(4x-w^3)}{w(2-w)}$	$\frac{(8y-w^3)}{w(2-w)}$

The values of c_n and d_n for classes of Fock operators, nF_n , as n defined by equation IIa-4-13.

$$\begin{aligned}
 \Psi_1 &\rightarrow \Psi_1 + \Psi_{3-a} \Delta_a \\
 \Psi_2 &\rightarrow \Psi_2 + \Psi_{3-b} \Delta_b \\
 \Psi_2 &\rightarrow \Psi_1 + \Psi_{2-c} \Delta_c \quad \text{or} \quad \Psi_2 \rightarrow \Psi_2 - \Psi_{1-c} \Delta_c^\dagger
 \end{aligned}
 \tag{IIa-4-15}$$

Where Δ_a , Δ_b and Δ_c are arbitrary $m_3 \times m_1$, $m_3 \times m_2$ and $m_2 \times m_1$ matrices respectively with small elements. These are analogous to the Lagrangian multipliers used in section 2 of this chapter.

The corresponding change in the T matrices is represented as:

$$\begin{aligned}
 T_1 &\rightarrow T_1 + T_{3-a} \Delta_a \\
 T_2 &\rightarrow T_2 + T_{3-b} \Delta_b \\
 T_1 &\rightarrow T_1 + T_{2-c} \Delta_c \quad \text{or} \quad T_2 \rightarrow T_2 - T_{1-c} \Delta_c^\dagger
 \end{aligned}
 \tag{IIa-4-16}$$

From the definition of the first order density matrices (IIa-4-6) the variations in the R matrices are: (To first order in Δ only)

$$\begin{aligned}
 R_1 &\rightarrow R_1 + (T_{3-a} \Delta_a T_1^\dagger + T_{1-a} \Delta_a^\dagger T_3^\dagger) \\
 R_2 &\rightarrow R_2 + (T_{3-b} \Delta_b T_2^\dagger + T_{2-b} \Delta_b^\dagger T_3^\dagger) \\
 R_1 &\rightarrow R_1 + (T_{2-c} \Delta_c T_1^\dagger + T_{1-c} \Delta_c^\dagger T_2^\dagger) \\
 \text{or} \quad R_2 &\rightarrow R_2 + (T_{2-c} \Delta_c T_1^\dagger + T_{1-c} \Delta_c^\dagger T_2^\dagger)
 \end{aligned}
 \tag{IIa-4-17}$$

The variation in energy is then calculated for each Hamiltonian used for each shell. Assuming F_1 , F_2 and F_3 are used to canonicalize the DOMO's, POMO's and VMO's respectively, then the variations in the energies, to first order in Δ , are:

$$\begin{aligned}
 E_{\text{DOMO/VMO}} &\rightarrow E_{\text{DOMO/VMO}} + \text{Tr} F_1 (T_{3-a} \Delta_a T_1^\dagger + T_{1-a} \Delta_a^\dagger T_3^\dagger) \\
 E_{\text{POMO/VMO}} &\rightarrow E_{\text{POMO/VMO}} + \text{Tr} F_2 (T_{3-b} \Delta_b T_2^\dagger + T_{2-b} \Delta_b^\dagger T_3^\dagger) \\
 E_{\text{DOMO/POMO}} &\rightarrow E_{\text{DOMO/POMO}} + \text{Tr} F_3 (T_{2-c} \Delta_c T_1^\dagger + T_{1-c} \Delta_c^\dagger T_2^\dagger)
 \end{aligned}
 \tag{IIa-4-18}$$

Since F_1 , F_2 , F_3 are Hermitian, we find:

$$E_{\text{DOMO/VMO}} \rightarrow E_{\text{DOMO/VMO}} + 2\text{Tr} F_1 T_{3-a} \Delta_a T_1^\dagger$$

$$E_{\text{POMO/VMO}} \rightarrow E_{\text{POMO/VMO}} + 2\text{Tr} \underline{T}_{-2-3} \underline{\Delta}_{-b} \underline{T}_{-2}^{\dagger} \quad \text{IIa-4-19}$$

$$E_{\text{DOMO/POMO}} \rightarrow E_{\text{DOMO/POMO}} + 2\text{Tr} \underline{T}_{-3-2} \underline{\Delta}_{-c} \underline{T}_{-1}^{\dagger}$$

Using the property that the trace of a matrix product is invariant to the order of matrix multiplication, and rearranging equations IIa-4-19 we obtain:

$$\begin{aligned} E_{\text{DOMO/VMO}} &\rightarrow E_{\text{DOMO/VMO}} + 2\text{Tr} (\underline{T}_{-1}^{\dagger} \underline{F}_{-1-3}) \underline{\Delta}_{-a} \\ E_{\text{POMO/VMO}} &\rightarrow E_{\text{POMO/VMO}} + 2\text{Tr} (\underline{T}_{-2}^{\dagger} \underline{F}_{-2-3}) \underline{\Delta}_{-b} \\ E_{\text{DOMO/POMO}} &\rightarrow E_{\text{DOMO/POMO}} + 2\text{Tr} (\underline{T}_{-1}^{\dagger} \underline{F}_{-3-2}) \underline{\Delta}_{-c} \end{aligned} \quad \text{IIa-4-20}$$

For stationary energy then the change in the energy has to be zero. Hence for non trivial cases, the following conditions must be satisfied:

$$\begin{aligned} \underline{T}_{-1}^{\dagger} \underline{F}_{-1-3} &= \underline{0} \\ \underline{T}_{-2}^{\dagger} \underline{F}_{-2-3} &= \underline{0} \\ \underline{T}_{-1}^{\dagger} \underline{F}_{-3-2} &= \underline{0} \end{aligned} \quad \text{IIa-4-21}$$

Where $\underline{0}$ is a zero matrix of appropriate order.

Equations IIa-4-21 satisfy the remaining $m_1 m_3$, $m_2 m_3$ and $m_1 m_3$ conditions for unique self consistency for the set of m molecular orbitals.

Equations IIa-4-14, and IIa-4-21 can be seen to represent blocks of the molecular Fock operator in the molecular orbital basis. Blocks defined in equation IIa-4-14 occur on the diagonal and the off-diagonal blocks are represented by equations IIa-4-21 (upper triangle blocks are specified, lower triangle blocks are given as the adjoints of equations IIa-4-21). The Fock operator in the molecular orbital basis can then be written as:

$$\underline{F} = \begin{bmatrix} \underline{T}_{-1}^{\dagger} \underline{F}_{-s-1} & \lambda_{12} \underline{T}_{-1}^{\dagger} \underline{F}_{-3-2} & \lambda_{13} \underline{T}_{-1}^{\dagger} \underline{F}_{-1-3} \\ \lambda_{12} \underline{T}_{-2}^{\dagger} \underline{F}_{-3-1} & \underline{T}_{-2}^{\dagger} \underline{F}_{-p-2} + \alpha \underline{I}_{-2} & \lambda_{23} \underline{T}_{-2}^{\dagger} \underline{F}_{-2-3} \\ \lambda_{13} \underline{T}_{-3}^{\dagger} \underline{F}_{-1-1} & \lambda_{23} \underline{T}_{-3}^{\dagger} \underline{F}_{-2-2} & \underline{T}_{-3}^{\dagger} \underline{F}_{-v-3} + (\alpha + \beta) \underline{I}_{-3} \end{bmatrix} \quad \text{IIa-4-22}$$

Where:

α and β are scalars, called level shifters.

\underline{I}_2 and \underline{I}_3 are identity matrices of order m_2 and m_3 respectively.

$\lambda_{12}, \lambda_{13}, \lambda_{23}$ are scalars whose values are normally chosen to be unity, called damp factors.

$\underline{F}_D, \underline{F}_P, \underline{F}_V$ are the matrix basis set representations of the Fock operators used to canonicalize the DOMO, POMO and VMO shells respectively.

As can be seen the operator is blocked according to the shell definitions and has vanishing matrix elements connecting molecular orbitals of different categories, as self consistency approaches and the matrix becomes diagonal. The matrix elements between molecular orbitals of the same shell, may in principle adopt arbitrary values, depending on the canonicalization parameters chosen. It is clear that when \underline{F} is diagonal the conditions for self consistency, equations IIa-4-12 and IIa-4-21 will be satisfied.

The introduction of the parameters α , β and λ as level shifters and damp factors respectively is as an aid to achieving convergence, and is unique to the ATMOL method. Rayleigh-Schroedinger Perturbation Theory has been used to show that [32] the magnitude of elements of the $\underline{\Delta}$ matrices, in equations IIa-4-15 \rightarrow IIa-4-20, for the general case, is given by:

$$\begin{aligned} (\underline{\Delta}_a)_{ki} &= \lambda_{13}(\underline{F}_1)_{ki} / ((\underline{F}_P)_{ii} - (\underline{F}_V)_{kk} - \alpha - \beta) \\ (\underline{\Delta}_b)_{kj} &= \lambda_{23}(\underline{F}_2)_{kj} / ((\underline{F}_P)_{jj} - (\underline{F}_V)_{kk} - \beta) \\ (\underline{\Delta}_c)_{ji} &= \lambda_{12}(\underline{F}_3)_{ji} / ((\underline{F}_D)_{ii} - (\underline{F}_V)_{jj} - \alpha) \end{aligned} \quad \text{IIa-4-23}$$

From equations IIa-4-23 we can see that if α and β are chosen positive and sufficiently large then the elements of $\underline{\Delta}$ will be sufficiently small to make the first order analysis, in equations IIa-4-15 \rightarrow IIa-4-20, valid. Also the $\underline{\Delta}$ elements will be of opposite sign to the matrix elements of the relevant Fock operator, and hence will ensure an energy lowering (see equations IIa-4-18 \rightarrow IIa-4-20) on unitary mixing of molecular orbitals between shells. They are called level shifters because they effect the

diagonal elements of the Fock operator, see equation IIa-4-22, shifting the relative levels of the shells. The factors λ_{ij} are also introduced to control the magnitude of the $\underline{\Delta}$ matrix elements, by scaling the entire $\underline{\Delta}$ matrix, and are called damping factors. The use of the level shifters, damping factors, and choice of canonicalization parameters makes the ATMOL method highly adaptable and able to find convergence for any molecular electronic configuration and state.

The iterative scheme implemented in the ATMOL-3 SCF programs is as follows:

- (1) Construct trial vectors for the k^{th} iterative cycle, \underline{T}^k and compute density matrices, \underline{R}_1 and \underline{R}_2 according to equations IIa-4-6.
- (2) Using the density matrices and the file of the two electron integrals, in basis function representation, compute the matrices \underline{A} , \underline{B} and \underline{C} from:

$$\underline{A} = \underline{H} + 2\underline{J}[\underline{R}_1] - \underline{K}[\underline{R}_1] \quad \text{IIa-2-24}$$

$$\underline{B} = \underline{J}[\underline{R}_2] \quad \text{IIa-4-25}$$

$$\underline{C} = \underline{K}[\underline{R}_2] \quad \text{IIa-4-26}$$

Evaluate the electronic energy, from equation IIa-4-7, for the state under consideration.

- (3) Linearly transform matrices \underline{A} , \underline{B} and \underline{C} into the trial molecular orbital basis, and construct the blocks of \underline{F} , as defined in equation IIa-4-22, according to the canonicalization parameters chosen.
- (4) The matrix \underline{F} is diagonalized, and, after suitable ordering of the columns, the eigen vector array \underline{Q}^k is obtained. \underline{Q}^k defines the iterated molecular orbitals as linear combinations of the trial molecular orbitals, \underline{T}^k .
- (5) The iterated molecular orbitals are constructed as linear combinations of basis functions, as the vector array \underline{T}^{k+1} , from:

$$\underline{T}^{k+1} = \underline{T}^k \underline{Q}^k \quad \text{IIa-4-27}$$

- (6) Orthonormality of the columns of the vector array, \underline{T}^{k+1} , is

refreshed by means of a Schmidt procedure. The iterated vector array is now presented for input for the next cycle at state (1). The process is repeated until the magnitude of the off diagonal elements, in F , is below a present threshold, and self consistency is achieved.

The ATMOL method, as discussed here, has been used extensively in the research described in later chapters of this thesis. The main advantages of ATMOL are its general applicability, lack of complication, excellent convergence properties and extensive adaptability. These features are almost entirely due to the direct diagonalization of the matrix representation of the molecular Hamiltonian in molecular orbital basis rather than solving a complex pseudo eigen value equation. The representation of the Hamiltonian in molecular orbital basis partitions the Hamiltonian into independent blocks, which leads to the enhanced flexibility of the method.

II-5 Δ SCF calculations

As discussed in section 3 of this chapter, Koopmans' Theorem can only be applied to closed shell molecules and atoms, for the prediction of ionization potentials. Also one of the principle errors encountered when using Koopmans' Theorem, is the neglect of reorganization energy, arising from relaxation effects on ionization. However, both these drawbacks can be overcome by predicting ionization potentials as a direct energy difference between the neutral and the ion state, at SCF level. This method has become known as the Δ SCF method, and was first used by Bagus in the study of the electron hole states of closed shell atoms [36]. The Δ SCF method has major advantages in that it is applicable to both open and closed shell systems, and full account of electronic reorganization effects is made, since separate calculations are performed on the neutral and the ion and a simple energy difference is taken as the ionization energy. For the prediction of ionization potentials of open shell species the Δ SCF method is often the only method available, but it can prove computationally expensive for systems where several ion states are produced from a single ionization. The calculated SCF energies used to obtain the Δ SCF ionization potentials

directly influence the accuracy of the result, with sophisticated lengthy SCF calculations on both the ion and the neutral giving highly accurate predictions.

The Δ SCF method allows for reorganization of the orbitals on ionization, but makes no attempt to allow, generally, for changes in correlation energy or relativistic effects on ionization. The method is also restricted to cases where the molecular or ionic state, is well defined by a single determinantal wavefunction [37]. A greater degree of accuracy in the theoretical prediction of I_p 's will be by methods that account for correlation energy of the neutral and ionic states explicitly.

IIa-6 Correlation Energy and Configuration interaction - SPLICE Formalism

The form of the Hamiltonian used in HFR-SCF calculations is composed of two parts (see equation IIa-2-8), a one electron and a two electron part. The two electron term treats electron interaction in an approximate way and this leads to the correlation energy error. Disregarding the correlated motions of the electrons brings about the difference between the exact non relativistic energy and the SCF energy calculated in a near Hartree Fock calculation. This difference is called the Correlation Energy [38].

The correlation energy of a system is usually a very small fraction of the total energy ($\sim 0.5\%$ typically) but this may be a significant error when considering small differences in total energies. Particularly serious errors occur for physical problems where the correlation energy corrections do not cancel, e.g. for dissociation energies of molecules. The large variations of correlation energy encountered leads to the concept of two types of contributions to the definition of the correlation energy. Firstly dynamical correlation, which includes the concept of correlated electron motion, and non dynamical correlation, which accounts for correlation energy contributions due to near degeneracy and rearrangements of electron orbitals within the Hartree Fock model [39]. This duplicity can be overcome by redefining correlation energy with reference to an appropriate multiconfigurational SCF (MC-SCF) wave function rather

than with reference to the Hartree Fock limit [40].

Many schemes have been developed to recover the correlation energy deficiency and improve the Hartree Fock result, ranging from empirical and semiempirical estimates to extensive and elaborate methods of Configuration Interaction (CI) and Pair Theories. Of these the CI method appears to be the most generally applicable and the most straightforward, though it is a major computational task.

In this section a detailed account of the method of CI, which has been used extensively in this work, will be given, along with a brief review of the other correlation energy methods.

Review of Correlation Energy Methods:

(i) Empirical and Semiempirical Methods.

These methods include the empirical parameterization of bonding and lone pair contributions [41,42] and semiempirical parameterizations of many Electron Theory such as the Effective Pair Correlation Energy [43,44,45] and the Pair Population Method [46]. Other methods include the Population Analysis Method [47] and the United Atom Method for first and second row hydrides [48].

(ii) Pair Correlation Theories.

The use in general electron pair theory of the cluster expansion approach [49] has lead to numerous derivations of working equations, which differ in the approximations used. Some of the more popular methods are:

The Independent Electron Pair Approximation (IEPA) [50,51],
the Many Electron Theory (MET) [52],
the Coupled Electron Pair Approximation (CEPA) [53,54,55],
and the Coupled Pair Many Electron Theory (CP-MET) [56,57].

(iii) Perturbation Calculations.

The methods have evolved by the treatment of the electron correlation effect as a perturbation of the HF Hamiltonian. The most widely used approach has become known as the Many Body Rayleigh Schrodinger Perturbation Theory (MB-RSPT) and represents the greatest degree of sophistication and accuracy [58,59,60,61].

Configuration Interaction:

The method of CI is a straightforward variational solution of the

Ritz [62] linear expansion of electronic wavefunctions. This method employs a linear expansion of the trial functions, expressed as:

$$\Psi_{CI} = \sum_{s=1}^n c_s \Psi_s \quad \text{IIa-6-1}$$

where the Ψ_s are predetermined expansion functions and the linear expansion coefficients, c_s , are varied to make E_{CI} stationary. This leads to the generalized matrix eigen value equation:

$$\underline{H} \underline{c} = \underline{E} \underline{S} \underline{c} \quad \text{IIa-6-2}$$

where \underline{H} and \underline{S} are Hermitian matrices of order n , with matrix elements defined as:

$$(\underline{H})_{ij} = \langle \Psi_i | \hat{H} | \Psi_j \rangle \quad \text{IIa-6-3}$$

$$(\underline{S})_{ij} = \langle \Psi_i | \Psi_j \rangle \quad \text{IIa-6-4}$$

and \underline{c} is a column vector of the expansion coefficients. The set of expansion functions $\{\Psi_s\}$ is in general chosen to be orthonormal, hence \underline{S} becomes a unit matrix and IIa-6-2 reduces to:

$$\underline{H} \underline{c} = \underline{E} \underline{c} \quad \text{IIa-6-5}$$

The n linearly independent eigen vectors \underline{c}_p with eigen values, E_p , can be chosen to be orthonormal and will be numbered so that:

$$E_1 \leq E_2 \leq E_3 \dots \leq E_n \quad \text{IIa-6-6}$$

Each eigen value E_p of IIa-6-5 is an upper bound to the corresponding eigen value of \hat{H} , and extending the range of the linear expansion of the wavefunction (IIa-6-2) will lower the eigen values to approach the exact eigen values of the time independent, fixed nucleus, non relativistic Schrodinger equation [63].

The application of the variational principle to a trial function which is written as a linear combination of many predetermined terms is conceptually simple and quite general. The CI method can be applied, in principle, to any stationary state of an atomic or molecular system, be it open shell, closed shell, ground state or excited state, near the

equilibrium geometry or far from the equilibrium geometry. These characteristics of the CI methods are overshadowed by the magnitude of the computational effort encountered in implementing the CI method for physically realistic systems.

Computational problems arise from the large number of configuration functions that can be generated for a realistic molecule, with a basis set near the Hartree Fock limit. Also the number of configuration functions required in the expansion of the trial wavefunction is found to be of the order of hundreds, often exceeding thousands, before convergence of the eigen values to the true non-relativistic energy, and recovery of most of the correlation energy is realized. The size of the configuration space required, to recover a certain proportion of the correlation energy, is dependent on the orbital space used in constructing the configuration functions. It has been shown that the use of Natural orbitals (NO's) [64,65,66] and Pair Natural Orbitals (also called Pseudonatural Orbitals) (PNO's) [67], leads to recovery of a greater proportion of the correlation energy, for a fixed number of configuration functions, than the use of Hartree Fock virtual orbitals. However the discussion presented here will be limited to an orbital space constructed from Hartree Fock molecular orbitals.

The computational approach to a CI calculation proceeds through five distinct stages. These are: Construction of Configuration Functions, Selection of Configuration Functions, Matrix element evaluation, CI Matrix eigen value evaluation, and Wavefunction analysis. The computational details for each of these stages will now be discussed, with particular reference to the SPLICE CI program [68] used extensively in the research described in this thesis. Each stage will be discussed in turn.

(A) Construction of Configuration Functions

Configuration functions (CF's) used in the expansion of the wavefunction must be antisymmetrized functions that obey the Exclusion Principle. Several considerations play an important role in choosing a method for constructing CF's which satisfy spin or space and spin symmetry requirements. Major factors are: (1) the ease of computation of matrix elements between CF's; (2) ability to generate a complete and

linearly independent set of CF's for any one configuration, that are preferably orthonormal; (3) it is preferable to construct the CF's such that important contributions to the wavefunction, for any one configuration, are concentrated in as few CF's as possible. Since the Hamiltonian is spin free it is advantageous to choose the CF's to be eigen functions of the spin operators, \hat{S}^2 and \hat{S}_Z , so that only functions with spin eigen functions corresponding to the desired solution need be considered. The problem of constructing spin adapted CF's has been approached in basically two methods. Firstly the straightforward approach is to use Lowdin spin projection operators to project the desired spin components from a function constructed of primitive spin functions [69]. Secondly geneological construction schemes have been devised in order to impose a hierarchical structure of spin functions to take account of double occupancy restrictions. Such functions have become known as geminally antisymmetric spin functions [70]. The principle construction schemes, for such functions, are the Kotani-Yamanouchi scheme [71,72], the Gelfand-Tsetlin [73], the Serber Scheme [74] and the Rumer Valence bond or Bonded Function scheme [75].

The SPLICE program uses an implementation of the bonded function scheme, as formulated by Boys and Reeves [76], Reeves [77], Cooper and McWeeny [78] and Sutcliffe [79]. The bonded functions are constructed with the aid of strict rules, for a common orbital product, to produce a linearly independent canonical set. The rules are:

- (1) Bracket all doubly occupied orbitals together.
- (2) From the remaining orbitals construct all bracket patterns that preserve an excess, if any, of left brackets.

Bracketed pairs of orbitals are defined as:

$$\begin{aligned} [\phi_i \phi_j] &= \phi_i(i) \phi_j(j) \frac{1}{\sqrt{2}} \{ \alpha(i) \beta(j) - \beta(i) \alpha(j) \} \text{ if } \phi_i \neq \phi_j \\ &= \phi_i(i) \phi_j(j) \alpha(i) \beta(j) \text{ if } \phi_i = \phi_j \end{aligned} \quad \text{IIa-6-7}$$

and the unpaired brackets are defined as:

$$[\phi_i] = \phi_i(i) \alpha(i) \quad \text{IIa-6-8}$$

The second rule corresponds to the traditional Rumer rules [75] and is

analogous to the Path Diagram rule [71] used to ensure linear independence among spin functions. The bonded functions in a canonical set, obtained for a single orbital product, according to the rules above, are normalized (assuming orthonormal orbitals ϕ_i), but are not orthogonal. (The bonded functions within a canonical set obtained from one orbital product will be orthogonal to those obtained from another). The bonded functions of a canonical set can, however, be orthogonalized with a Schmidt orthogonalization which will reduce the number of off diagonal matrix elements in the final CI matrix. The use of bonded functions as CF's gives the advantages of ease of matrix element evaluation, and reduced storage requirements for the configuration list, since all permutations are implicit within the canonical set. However they have the disadvantage that they are not all orthogonal.

The configuration generation section of SPLICE proceeds to generate a list of canonical sets of bonded functions, referenced through the orbital product that imparts the largest number of spin coupled pairs. The list is constructed by considering all possible double and/or single orbital excitations from a list of reference functions (or root functions) by replacing orbitals in the reference functions by members of an orbital pool. The orbital pool defines those orbitals which are available for substitution and usually comprises the virtual SCF orbitals. Flexibility in configuration list generation is provided for with facilities to consider separate classes of excitations, restricting the set of orbitals in the pool, restricting replacement of any of the occupied set of orbitals and the use of molecular symmetry to classify sets within the orbital pool. However in many calculations on realistic systems it is found that the initially generated configuration list is too large for complete use in the construction of the CI matrix. In such cases it is then necessary to select the important configurations for construction of the final CI matrix.

(B) Selection of Configurations

The reduction of the full configuration list, generated by consideration of all single and double replacements of a reference function, is invariably necessary, and can be achieved by two major selection schemes. Firstly there is preselection, which reduces the size of the

orbital space, and secondly there is individual selection, which scans the initial configuration list to remove individual configurations. Both of these schemes are implemented in SPLICE and will be discussed in turn in terms of the options available in SPLICE.

Preselection of configurations can be achieved in two ways. One is truncation of the virtual orbital space, usually to exclude the uppermost SCF virtual orbitals from the orbital pool. The second, usually applied in conjunction with the first, is to specify that the inner shell orbitals remain unavailable for replacement. This inner shell "freezing" completely neglects inner shell correlation effects, hence truncation of the uppermost virtual orbitals will have little accumulative effect. Since these orbitals correlate the inner shell orbitals most strongly, it is for this reason that both restrictions are applied simultaneously. These approaches are often obligatory first steps in reducing the initial configuration list.

Individual configuration selection is the screening of the initial configuration list to select those CF's which make the most significant contributions to the final CI wavefunction. This can be done either by estimating the CI coefficient of an individual CF in the final CI wavefunction or by estimating the contribution to the lowering of the energy for each CF. Through perturbation theory the CI coefficients, c_s , and the energy contribution, ΔE_s , of a CF, Ψ_s , are [80]:

$$c_s = \frac{\langle \Psi_s | \hat{H} | \Psi_0 \rangle}{\langle \Psi_0 | \hat{H} | \Psi_0 \rangle - \langle \Psi_s | \hat{H} | \Psi_s \rangle} \quad \text{IIa-6-9}$$

$$\Delta E_s = \frac{|\langle \Psi_s | \hat{H} | \Psi_0 \rangle|^2}{\langle \Psi_0 | \hat{H} | \Psi_0 \rangle - \langle \Psi_s | \hat{H} | \Psi_s \rangle} \quad \text{IIa-6-10}$$

These formulae are quite adequate for CF selection, provided Ψ_0 is a good zero order wavefunction and that the principal contribution of Ψ_s to the correlation energy is through first order interaction with Ψ_0 . In cases where Ψ_0 is not a good zero order wavefunction, where multiple root functions are required, then the method must be extended to treat the interaction between each of the root configurations, and the

replacement CF's. This has given rise to the so called A_k and B_k procedures [81]. The method implemented in SPLICE is that of Buenker and Peyerimhoff [82], and is intermediate between the A_k and B_k approaches in its selection technique. The test configurations are screened individually by considering interactions with the complete set of root configurations. This leads to small eigen value equations, which are diagonalized and rearranged, giving the contribution to the energy lowering of the k^{th} canonical set.

The scheme for performing configuration selection on an initial list of configurations constructed at the configuration generation stage is:

- (1) Choose a reference, or main, set of configurations, or canonical sets of configurations, to comprise the set $\{\Psi_m\}$. This is often best achieved by performing a small full CI calculation and treating all configurations with a coefficient in the final CI wavefunction of greater than 0.1, as a member of the set $\{\Psi_m\}$. The set $\{\Psi_m\}$ should also contain configurations which play a leading role in the representation of any desired higher roots.
- (2) Selection of the configurations remaining, comprising the set $\{\Psi_R\}$ is then performed to yield a selected set $\{\Psi_S\}$ and a discarded set $\{\Psi_D\}$. This partitioning can be accomplished by either threshold selection or cumulative selection. Threshold selection is accomplished by specifying an energy threshold, and all configurations with contributions to the energy lowering less than the threshold are discarded. Cumulative selection is achieved by specifying the number of configurations required to be selected and those with the largest contribution to the energy lowering are retained. Of these alternatives threshold selection represents the method of greatest control with typical values for the threshold energy of the order of 100-10 micro AU. The dependence of the final energy on the threshold value, E_T , [82,83] makes the choice of E_T very critical. However in the calculation of relative energy differences the use of selection techniques can very effectively reduce the amount of calculation without

severe loss of accuracy [84]. Once the selected list, or initial list (if not too extensive), has been finalized then the CI Hamiltonian matrix is constructed.

(C) Matrix Element Calculation

The next stage is to evaluate the matrix elements of the CI Hamiltonian between the bonded functions in the final configuration list. In SPLICE this process is segmented into primary generation of a list of symbolic matrix elements, that reference one and two electron integrals by the method of Projective Reduction, and secondly the numerical evaluation of the symbolic references. This approach has evolved because it is unlikely that a complete list of one and two electron integrals is able to be held in computer memory simultaneously, hence the symbolic list can be sorted to reference a "core" load of integrals in sequence, with the least amount of peripheral activity [85].

The use of bonded functions, as CF's, entails a concomitant treatment for the Projective Reduction of the corresponding matrix elements. The matrix element between two general bonded functions, Ψ_S and Ψ_T is given by the formula [68,76-79]:

$$\langle \Psi_S | \hat{H} | \Psi_T \rangle = \sum_{ij} a_{ij}^{ST} \langle \phi_i | \hat{h} | \phi_j \rangle + \sum_{ijkl} b_{ijkl}^{ST} \langle \phi_i \phi_j | \hat{g} | \phi_k \phi_l \rangle$$

Where the coefficients a_{ij}^{ST} and b_{ijkl}^{ST} are evaluated by the method of Projective Reduction and they make up the symbolic matrix element list. The computational realization of this method is described in more detail in references [85] and [77] and contains detailed algorithms for the implementation of Projective Reduction formulae on a computer.

Once the CI Hamiltonian matrix has been constructed the next step is to calculate the eigen values and eigen vectors of the matrix.

(D) CI Matrix Eigen Value Evaluation

The size of the CI matrix has prompted the investigation of many methods to efficiently diagonalize a sparse diagonally dominant matrix. The SPLICE program is capable of implementing two methods of solving generalized eigen value equations (IIa-6-5) both of which are iterative in nature. Firstly the standard diagonalizer is an implementation of the

Shavitts Method of Optimal Relaxations (MOR) [86]. The second alternative method is through Davidsons implementation of Lanczos algorithm [87].

The MOR method gives the lowest, or highest, root of \underline{H} . However to evaluate a few of the lowest, or highest, roots in order the method must be adapted. The most successful of these adaptations appears to be the "root shifting method" [86], in which each root is found in turn and the matrix, \underline{H} , is modified to make the next desired root the lowest. The calculation of several roots by the MOR method adds to the computational task because the modified matrix has to be calculated and stored, which requires as much storage and computation as any of the previous roots. The convergence of the MOR method to a stationary vector is generally good for diagonally dominant matrices with well separated eigen values. However the use of the root shifting technique, for higher roots, reduces the diagonal dominance of \underline{H} , hence increasing the number of iterative cycles required to reach convergence for higher roots. Some methods are however available to accelerate the rate of convergence. One is the Aitken δ^2 process [86] and another is the over relaxation method [88]. The most serious convergence difficulties of MOR occur in the case of near degenerate eigen values, and it was to circumvent these problems that Davidson's method was implemented.

Davidson's method is a reformulation of Lanczos Method [87] for the tridiagonalization of a matrix. The advantages of the Davidson scheme compared to Shavitts MOR procedure is that a complete set of roots can be generated simultaneously, with even selective convergence on higher vectors conceivable, and near degenerate roots do not cause convergence difficulties.

Comparison of the two methods shows that the number of multiplications, for both methods, is proportional to n^2 , where n is the order of the final CI matrix, for each root.

In conclusion the Davidson method is more powerful for calculating higher roots, or multiple roots of the CI matrix, than Shavitts MOR method, and should always be used for cases where near degenerate roots are present.

(E) Wavefunction Analysis

Once the desired eigen vectors of the CI matrix have been calculated the wavefunction can then be analysed to evaluate physically meaningful quantities and to express the wavefunction in alternative representations. In SPLICE, wavefunction analysis is performed to evaluate pair correlation energies and to express the final wavefunction in terms of natural orbitals.

Pair correlation energies are the contributions to the total correlation energy from pairs of electrons in the root configuration. The pair correlation energy, connecting pairs i and j is defined as:

$$E_{i,j}^P = - \frac{c_{ij}^{kab}}{c_{oo}^1} \sum_{a,b,k} \left[\langle \psi_{oo} | \hat{H} | \psi_{ij}^{kab} \rangle - \langle \psi_{oo} | \hat{S} | \psi_{ij}^{kab} \rangle E_{CI} \right] \quad \text{IIa-6-12}$$

where i and j denote occupied orbitals, a and b ($a \leq b$) are vacant orbitals in the orbital pool which replace i and j . The index k distinguishes the k^{th} member of a multidimensional canonical set associated with a single orbital product, c_{oo}^1 is the coefficient of the first member of the root canonical set in the final CI wavefunction. Parameters c_{ij}^{kab} are the coefficients of the replacement functions ψ_{ij}^{ab} , where i and j have been replaced by a and b respectively, in the final CI wavefunction, and E_{CI} is the final CI energy. From IIa-6-12, the correlation energy, E_{CORR} , is given by:

$$E_{\text{CORR}} = E_{CI} - E_{\text{HF}} = \sum_{i \leq j} E_{ij}^P \quad \text{IIa-6-13}$$

Pair energy analysis thus enables a clear analysis of the individual contributions to the correlation energy, from each pair, which can be used to enumerate many properties of chemical interest.

Analysis of the wavefunction in terms of natural orbitals proceeds with the calculation of the one and two particle spin and spin less (spin free) density matrices in MO and AO basis representations. The natural orbitals, in any representation, are obtained as eigen vectors of the respective density matrices, with the eigen values being occupation

numbers of the orbitals. In SPLICE the natural orbitals are output to data sets that interface to the ATMOL suite of programs, for graphical or population analysis. Also the data sets can be used as input to further CI calculations, thus allowing iterative natural orbital CI (INO-CI) or natural orbital CI(NO-CI) calculations to be carried out.

The SPLICE package is a series of modules which implements the stages of a CI calculation, as discussed above. The precise computational details and card input specifications can be found in the SPLICE Users Manual, [68]. It is hoped that the discussion in this section introduces some of the techniques required to perform CI calculations and gives an insight into the computational problems encountered in CI calculations.

Ila-7 Direct Methods for Ionization Potentials

The methods described so far for the calculation of ionization potentials have been based on calculations that yield total energies of electronic states of molecules and molecular ions, with the ionization potential being given by the energy difference between the ionic and molecular states. However ionization potentials, for valence electrons, represent only a small fraction of the total molecular energy, for systems of interest. It is for this reason that theoretical methods leading to the direct calculation of ionization potentials, and excitation energies, have been developed. For the case of ionization potentials a brief summary of the more widely established direct methods will be given here. They are:

- (1) The Rayleigh Schrodinger Perturbation approach, expressing the ionization potential as a sum of perturbation terms [89] and perturbative corrections to Koopmans' Theorem [90].
- (2) The Equations of Motion Method (EOM) [91-95].
- (3) The Many Body Greens Function, or Electron Propagator Method [96-104].
- (4) The Open Shell Cluster Expansion Method [105,106].
- (5) The Common Unitary Operator Method [107].

- (6) The Multiple Scattering X alpha (MS-X α) Transition State Method [108-110].

The summary presented here is not a complete list of theoretical techniques, but represents many of the methods most commonly used. Each method is identical in that the ionization potential of a system, for a particular ionization, is given by a single calculation. The method, except for the MS-X α method, are closely related [111,112] and are all formulated in terms of second quantization using fermion statistics. The two methods which are the most computationally tractable are the EOM method and Greens Function method. The use of these methods is becoming more widespread and will soon be available to the experimentalist via "black box" computer programs.

IIb-1 Calculation of Molecular Spectroscopic Constants from Potential Curve Data

Ab Initio MO calculations carried out for a series of bond lengths, for diatomic molecules, give values of the total electronic energy as a function of bond length. The data points of this potential function can then be fitted to a model potential in order to evaluate the spectroscopic constants associated with the potential. Analysis of calculated potential curves is possible by use of the computer program, "VIBROT".

The program fits the energy/bond length data to a five constant fourth order polynomial in $(r - r_e)$ of the form:

$$E_{el}(r) = E_{el}(r=\infty) - D_e^o + \frac{1}{2}k_e(r-r_e)^2 + \frac{1}{3!}c_3(r-r_e)^3 + \frac{1}{4!}c_4(r-r_e)^4 \quad \text{IIb-1-1}$$

This function is related to the Dunham expression [113,114]:

$$E_{el}(r) = E_{min} + a_0 \left(\frac{r-r_e}{r_e}\right)^2 \left[1 + a_1 \left(\frac{r-r_e}{r_e}\right) + a_2 \left(\frac{r-r_e}{r_e}\right)^2\right] \quad \text{IIb-1-2}$$

$$\text{where: } a_0 = \frac{k_e r_e^2}{2} \quad \text{IIb-1-3}$$

$$a_0 a_1 = \frac{1}{3!} c_3 r_e^3 \quad a_1 = \frac{c_3 r_e}{3k_e} \quad \text{IIb-1-4}$$

$$a_0 a_2 = \frac{1}{4!} c_4 r_e^4 \quad a_2 = \frac{c_4 r_e^2}{12k_e} \quad \text{IIb-1-5}$$

$$E_{\min} = E_{el}(r=\infty) - D_e^0 \quad \text{IIb-1-6}$$

Here, r_e , is the equilibrium bond length, D_e^0 is the dissociation energy, k_e is the bond force constant and c_3 and c_4 are constants. The determination of the five unknown parameters requires 5 energy/bond length data points. The method of solution implemented is basically that of Varshni [115], using a Newton Raphson linearization of five simultaneous equations. These are solved iteratively using a Scarborough procedure [116] with the stationary values of D_e^0 , r_e , k_e , c_3 and c_4 being found iteratively. Once converged values of the five constants have been found, the various spectroscopic constants are evaluated from the following identities:

$$\alpha_e = -\left[\left(\frac{c_3}{3k_e}\right)r_e + 1\right] \frac{6B_e^2}{\omega_e} \quad \text{IIb-1-7}$$

$$\omega_e x_e = \frac{h}{64\pi^2 c \mu} \left[\frac{5}{3} \left(\frac{c_3}{k_e}\right)^2 - \frac{c_4}{k_e} \right] \quad \text{IIb-1-8}$$

$$\omega_e = \frac{1}{2\pi} \sqrt{\frac{k_e}{\mu}} \quad \text{IIb-1-9}$$

$$B_e = \frac{h}{8\pi^2 c \mu r_e^2} \quad \text{IIb-1-10}$$

$$D_e = \frac{4B_e^2}{\omega_e^2} \quad \text{IIb-1-11}$$

where h is Planks constant, c the velocity of light and μ is the reduced mass of the diatomic.

This analysis is a means of evaluating from a calculated potential curve a number of the standard spectroscopic constants. These constants can then be used for comparison with experimentally determined spectroscopic constants, or as input to the Franck Condon Factor program to calculate Franck Condon Factors from theoretically derived data.

IIb-2 Calculation of Frank Condon Factors from Spectroscopic Constants

For small molecules resolution of vibrational components is possible in most PES experiments. The analysis of the separations yields vibrational spectroscopic constants for the ionic state. The recorded spectra will also show a vibrational intensity distribution, with the overall shape of the band being dependent on the change in bond length and vibrational frequency experienced on ionization. The analysis of this intensity distribution is only possible through calculation of the Frank Condon Factors (FCF's) associated with each level. For a given potential function in the upper and lower state the change in bond length on ionization, Δr , can be deduced by comparing experimental and calculated component intensities, for all components in the band, for various fixed values of Δr . The value of Δr that correctly reproduces the experimental band envelope will then be the value of the actual bond length change for that ionization. This value can then be used with the known bond length of the neutral to evaluate the ionic state bond length. This analysis assumes that the electronic transition moment for the ionization is constant for all vibrational levels, i.e. the vibrational component intensity is directly proportional to the FCF for all components. Provided each vibrational component is well resolved and no additional intensity from overlapping bands is present, then the change in bond length can usually be estimated to $\pm 0.01 \text{ \AA}$. This accuracy has been confirmed by extensive studies of the PE spectra of several species with well characterized spectroscopic constants available for the neutral and ionic species [117,118].

FCF's can also be evaluated using spectroscopic parameters derived from computed potential curves (see IIb-1). This enables the complete simulation of the experimental spectrum from theoretical data. This has

been used to completely predict the vibrational band envelopes in the PE spectrum of HF, as described in Chapter VI of this thesis.

The FCF's are evaluated using the computer program "FCF". The program proceeds by constructing Morse potential functions, for the upper and lower state, from input spectroscopic constants. Vibrational wavefunctions are then evaluated for several levels of each state, using the constructed potential, by solving the radial Schrodinger wave equation. The method used is that of Cooley [119,120,121]. Overlap integrals between upper and lower state vibrational functions are evaluated, for the required levels, by Simpsons rule, between specified limits. Finally the FCF's are output along with the calculated term values.

The use of calculated FCF's in the analysis of experimentally recorded spectra enables the extension of the characterization of the ionic state to include estimates of ionic equilibrium bond lengths. Also they provide a valuable way of presenting theoretically calculated data in an experimentally tangible form.

Chapter II

References

1. Eyring, H, Walter, J and Kimball, G E, Quantum Chemistry, John Wiley, New York, (1944).
2. Coulson, C A, Valence (2nd Edition), Clarendon Press, Oxford, (1961).
3. Murrell, J N, Kettle, S F A, and Tedder, J M, Valence Theory, John Wiley and Sons Limited, London, (1970).
4. Lowe, J P, Quantum Chemistry, Academic Press, New York and London, (1978).
5. Pilar, F L, Elementary Quantum Chemistry, McGraw-Hill Book Company, New York, (1968).
6. Born, M, and Oppenheimer, R, Ann Phys, 84, 457, (1927).
7. Eckart, C E, Phys Rev, 36, 878, (1930).
8. Roothaan, C C J, Rev Mod Phys, 23, 69, (1951).
9. Slater, J C, Phys Rev, 35, 210, (1930).
10. Koopmans, T A, Physica, 1, 104, (1933).
11. Clementi, E, J Chem Phys, 38, 2248, (1963).
Clementi, E, *ibid*, 39, 175, (1963).
Clementi, E, *ibid*, 42, 2783, (1965).
Clementi, E and Viellard, A, *ibid*, 44, 3050, (1966).
12. Richards, W G, Int J Mass Spec and Ion Phys, 2, 419, (1969).
13. Pople, J A, and Nesbet, R K, J Chem Phys, 22, 571, (1954).
14. Berthier, G, Comp Rend Acad Sci, 238, 91, (1954).
15. Pople, J A, and Longuet-Higgins, L C, Proc Phys Soc, A68, 591, (1955).
16. Amos, A T and Hall, G C, Proc Roy Soc (London), A263, 483, (1961).
17. Nesbet, R K, Proc Roy Soc (London), A230, 312, (1955).
18. Nesbet, R K, Rev Mod Phys, 35, 552, (1963).
19. Roothaan, C C J, Rev Mod Phys, 32, 179, (1960).

20. Huzinaga, S, Phys Rev, 120, 866, (1960).
21. Guest, M F, and Saunders, V R, Molec Phys, 28, 819, (1974).
22. Grabenstetter, J E, and Grein, F, Molec Phys, 31, 1469, (1976).
23. McWeeny, R, Proc Roy Soc (London), A235, 496, (1956).
24. McWeeny, R, Proc Roy Soc (London), A241, 239, (1957).
25. McWeeny, R, Uppsala University, Uppsala, Sweden, Quantum Chemistry Group Preprint, 98, May 1, (1963).
26. McWeeny, R, Phys Rev, 126, 1028, (1962).
27. Berthier, G, "Molecular Orbitals in Chemistry, Physics and Biology", page 64, Ed: P-O Lowdin and B Pullman, Academic Press, New York, (1964).
28. Sleeman, D H, Theor Chim Acta, 11, 135, (1968).
29. McWeeny, R, "Molecular Orbitals in Chemistry, Physics and Biology", page 305, Ed: P-O Lowdin and B Pullman, Academic Press, New York, (1964).
30. Dodds, J L, and McWeeny, R, Chem Phys Letts, 13, 9, (1972).
31. Hillier, I H, and Saunders, V R, Proc Roy Soc A, 320, 161, (1970).
32. Hillier, I H, and Saunders, V R, Int Jnl of Quantum Chem, 4, 503, (1970).
33. Hillier, I H, and Saunders, V R, Int Jnl of Quantum Chem, 7, 699, (1973).
34. Guest, M F, and Saunders, V R, Molec Phys, 28, 819, (1974).
35. ATMOL-3 Users Manual: Rutherford Laboratory, Didcot, Oxford.
36. Bagus, P S, Phys Rev A, 139, 619, (1965).
37. Bulgin, D, Dyke, J M, and Morris, A, J Chem Soc Faraday II, 73, 983, (1977).
38. Lowdin, P-O, Adv Chem Phys, 2, 207, (1959).
39. Shavitt, I: "Methods of Electronic Structure Theory", Chapter 6, "The Method of Configuration Interaction", Ed: H Schaefer III, Plenum Press, New York and London, (1977).
40. Horsteng, R P, Dunning Jr, T H, Gilman, R R, Pipano, A, and Shavitt, I, J Chem Phys, 62, 4764, (1975).

41. George, P, Trochtman, M, Brett, A M, and Back, C W, Int J Quantum Chem, 12, 61, (1977).
42. Moffat, J B, J Mol Structure, 15, 325, (1973).
43. Pamuk, H O, Theor Chim Acta, 28, 85, (1972).
44. Sinanoğlu, O, and Pamuk, H O, J Amer Chem Soc, 95, 5435, (1973).
45. Lie, G C, and Clementi, E, J Chem Phys, 60, 1275, (1974).
46. Hollister, C, and Sinanoğlu, O, J Amer Chem Soc, 88, 13, (1966).
47. Liu, H P D, and Verhaegen, G, J Chem Phys, 53, 735, (1970).
48. Cade, P E, and Huo, W E, J Chem Phys, 47, 614, (1967).
49. Coester, F, Nucl Phys, 22, 177, (1961).
50. Ahlrichs, R, Lischka, H, Staemmler, V, and Kutzelnigg, W, J Chem Phys, 62, 1255, (1975).
51. Jungen, M, Ahlrichs, R, Theor Chim Acta, 17, 339, (1970).
52. Sinanoğlu, O, J Chem Phys, 6, 706, (1962).
53. Kelly, H P, Phys Rev, A134, 1450, (1964).
Kelly, H P, ibid, B136, 896, (1964).
54. Kutzelnigg, W, "Methods of Electronic Structure Theory", Ch 5, "Pair Correlation Theories", Ed: H F Schaefer III, Plenum Press, New York and London, (1977).
55. Meyer, W, Theor Chim Acta, 35, 277, (1974).
56. Paldus, J, and Cizek, J, Adv Quantum Chem, 9, 105, (1975).
57. Paldus, J, Cizek, J, and Shavitt, I, Phys Rev, A5, 50, (1972).
58. Robb, M A, "Computational Techniques in Quantum Chemistry and Molecular Physics", Eds: G H F Dierckson, B T Sutcliffe and A Veillard, D Reidel, Dordrecht, (1975).
59. Bartlett, R J, and Silver, D M, Int J Quantum Chem, 9, 183, (1975).
60. Manne, R, Int J Quantum Chem, 11, 175, (1977).
61. Freeman, D L, and Karplus, M, J Chem Phys, 64, 2641, (1976).
62. Ritz, W, J Reine Angew Math, 135, 1, (1909).
63. Hylleraas, E A, and Undheim, B, Z Phys, 65, 759, (1930).

64. Lowdin, P-O, Phys Rev, 97, 1474, (1975).
65. Bender, C F, and Davidson, E R, Phys Rev, 183, 23, (1969).
Bender, C F, and Davidson, E R, J Phys Chem, 70, 2675, (1967).
66. Shavitt, I, Rosenberg, B J, Palalikit, S, Int J Quantum Chem, 10, 33, (1976).
67. Meyer, W, "Methods of Electronic Structure Theory", Ch II, "Configuration Expansions by Means of Pseudonatural Orbitals", Ed: H Schaefer III, Plenum Press, New York and London, (1977).
68. Guest, M F, and Rodwell, W R, "SPLICE, The Bonded Function CI Program", Users Manual, Parts 1-4. Science Research Council, Daresbury Laboratory, Daresbury, Warrington, WA4 4AD.
69. Harris, F E, Adv Quantum Chem, 1, 59, (1964).
70. Salmon, W I, and Ruedenberg, K, J Chem Phys, 57, 2776, (1972).
71. Kotani, M, Ohno, K, and Kagama, , "Encyclopaedia of Physics", Ed: S Flugge, Vol 37/2, page 1, Springer Verlag, Berlin, 1961.
Kotaini, M, Amerniya, A, Ishiguro, E, and Kimura, T, "Tables of Molecular Integrals", 2nd Edition, Maruzen, Tokyo, (1963).
72. Yamanouchi, T, Proc Phys-Math Soc Japan, 20, 547, (1938).
73. Gelfand, I L, and Tsetlin, M L, Dokl Akad Nauk SSSR, 71, 825, (1950); *ibid*, 71, 1017, (1950).
74. Serber, R, J Chem Phys, 2, 697, (1934).
75. Heitler, W, and Rumer, G, Z Phys, 68, 12, (1931).
Rumer, G, Gottinger Nachr, 337, (1932).
Slater, J C, Phys Rev, 38, 1109, (1931).
76. Boys, S F, Reeves, C M, and Shavitt, I, Nature, 178, 1207, (1956).
77. Reeves, C M, Ph.D. Thesis, Cambridge, (1957).
Reeves, C M, Commun ACM, 9 276, (1966).
78. Cooper, I L, and McWeeny, R, J Chem Phys, 45, 226, (1966);
errata; *ibid*, 45, 3484, (1966).
79. Sutcliffe, B T, J Chem Phys, 45, 235, (1966).
80. Bender, C F, and Davidson, E R, Phys Rev, 183, 23, (1969).
81. Gershgorin, Z, and Shavitt, I, Int J Quantum Chem, 2, 751, (1968).
82. Buenker, R J, and Peyerimhoff, S D, Theoret Chim Acta, 35, 33, (1974).

83. Buenker, R J, and Peyerimhoff, S D, Theoret Chim Acta, 39, 217, (1975).
84. Ruffenetti, R C, Hsu, K, and Shavitt, I, Theoret Chim Acta, 45, 33, (1977).
85. Diercksen, G H F, and Sutcliffe, B T, Theoret Chim Acta, 34, 105, (1974).
86. Shavitt, I, Bender, C F, Pipano, A, and Hosteny, R P, J Comput Phys, 11, 90, (1973).
87. Davidson, E R, J Comput Phys, 17, 87, (1975).
88. Ruhe, A, Math Comput, 28, 695, (1974).
89. Kvensnicka, V, and Hubac, I, J Chem Phys, 60, 4483, (1974).
90. Chong, D P, Herring, G, and McWilliams, D, J Chem Phys, 61, 78, (1974).
91. Rowe, D J, Rev Mod Phys, 40, 153, (1968).
92. Shiluya, T, and McKoy, V, Phys Rev A, 2, 2208, (1970).
93. Simmons, J, and Smith, W D, J Chem Phys, 58, 4899, (1973).
94. Smith, W D, Chen, T, and Simmons, J, Chem Phys Letts, 26, 296, (1974).
Smith, W D, Chen, T, and Simmons, J, J Chem Phys, 61, 2670, (1974).
95. McCurdy Jr, C W, Rescigno, T N, Yeager, D L, and McKoy, V, "Methods of Electronic Structure Theory", Ch 9, "The Equations of Motion Method, An Approach to the Dynamical Properties of Atoms and Molecules", Ed: H Schaefer III, Plenum Press, New York and London, (1977).
96. Roman, P, "Introduction to Quantum Field Theory", John Wiley and Sons, New York, (1969).
97. Doll, J D, and Reinhardt, W P, J Chem Phys, 57, 1169, (1972).
98. Linderberg, J, and Ohrn, Y, J Chem Phys, 49, 716, (1968).
99. Linderberg, J, and Ohrn, Y, "Propagators in Quantum Chemistry", Academic Press, London, (1973).
100. Pickup, B T, and Goscinski, O, Mol Phys, 26, 1013, (1973).
101. Purvis, G D, and Ohrn, Y, J Chem Phys, 60, 4063, (1974).
102. Cederbaum, L S, Theor Chim Acta, 31, 239, (1973).

103. Cederbaum, L S, and Domcke, W, Adv Chem Phys, 36, 205, (1977).
104. Cederbaum, L S, Domcke, W, Von Niessen, W, and Schirmer, J, "Computational Methods in Chemistry", Ch 4, "Phenomena in Photoelectron Spectroscopy and Their Theoretical Calculation", Ed: J Bargon, Plenum Press, New York and London, (1980).
105. Paldus, J, Cizek, J, Saute, M, and Lafargue, A, Phys Rev A, 17, 805, (1978).
106. Mukhopodhgay, A, Moitra, R, and Mukherjee, D, J Phys B: Atom and Molecular Phys, 12, 1, (1979).
107. Reitz, H, and Kutzelnigg, W, Chem Phys Letts, 60, 111, (1979).
108. Slater, J C, "Computational Methods in Bond Theory", Plenum Press, New York, (1971).
109. Slater, J C, Adv Quantum Chem, 4, 203, (1970).
110. Beebe, N H F, Chem Phys Letts, 19, 290, (1973).
111. Purvis, G D, and Ohrn, J Chem Phys, 65, 917, (1976).
112. Herman, M F, Yeager, D L, and Freed, K F, Chem Phys, 29, 77, (1978).
113. Dunham, L, Phys Rev, 41, 713, (1932).
114. Dunham, L, Phys Rev, 41, 721, (1932).
115. Varshni, V P, Rev Mod Phys, 29, 664, (1957).
116. Scarborough, J B, "Numerical Mathematical Analysis", J Hopkins Press, Baltimore, (1958).
117. Roberts, A, B.Sc. Third Year Report, Southampton University, 1977.
118. Leach, S, J Chem Soc Farad Disc, 54, 68, (1972).
119. Cooley, J W, Math Computation, 15, 363, (1961).
120. Zare, R N, and Cashion, J K, University of California Radiation Laboratory, Report, UCRL-10881, July 1963.
121. Zare, R N, J Chem Phys, 40, 1934, (1964).

Chapter III
Instrumental Details

Contents

Introduction

III-1 Vacuum System

III-2 Ultra-violet Photon Source

III-3 Electron Energy Analyser

III-4 Electron Detector and Counting Electronics

III-5 Inlet System

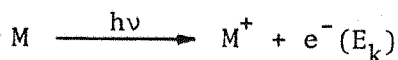
III-6 Factors Contributing to Instrument Performance

III-7 Calibration of Recorded Spectra

III-8 Experimental problems associated with the use of Fluorine

Introduction

The basic photoionization process in PES can be represented by:



The experimental requirements in UV PES are, a UV photon source, an electron energy analyser and an electron detector, with an inlet system to introduce the sample gas. The photoelectron spectrometer used for the work described in this thesis has been specifically developed for the detection of transient species [1], and is outlined schematically in Figure 1. Each of the major components of the instrument will be discussed in turn along with some of the experimental techniques developed during this work. General experimental details can be obtained from the text books [2-4].

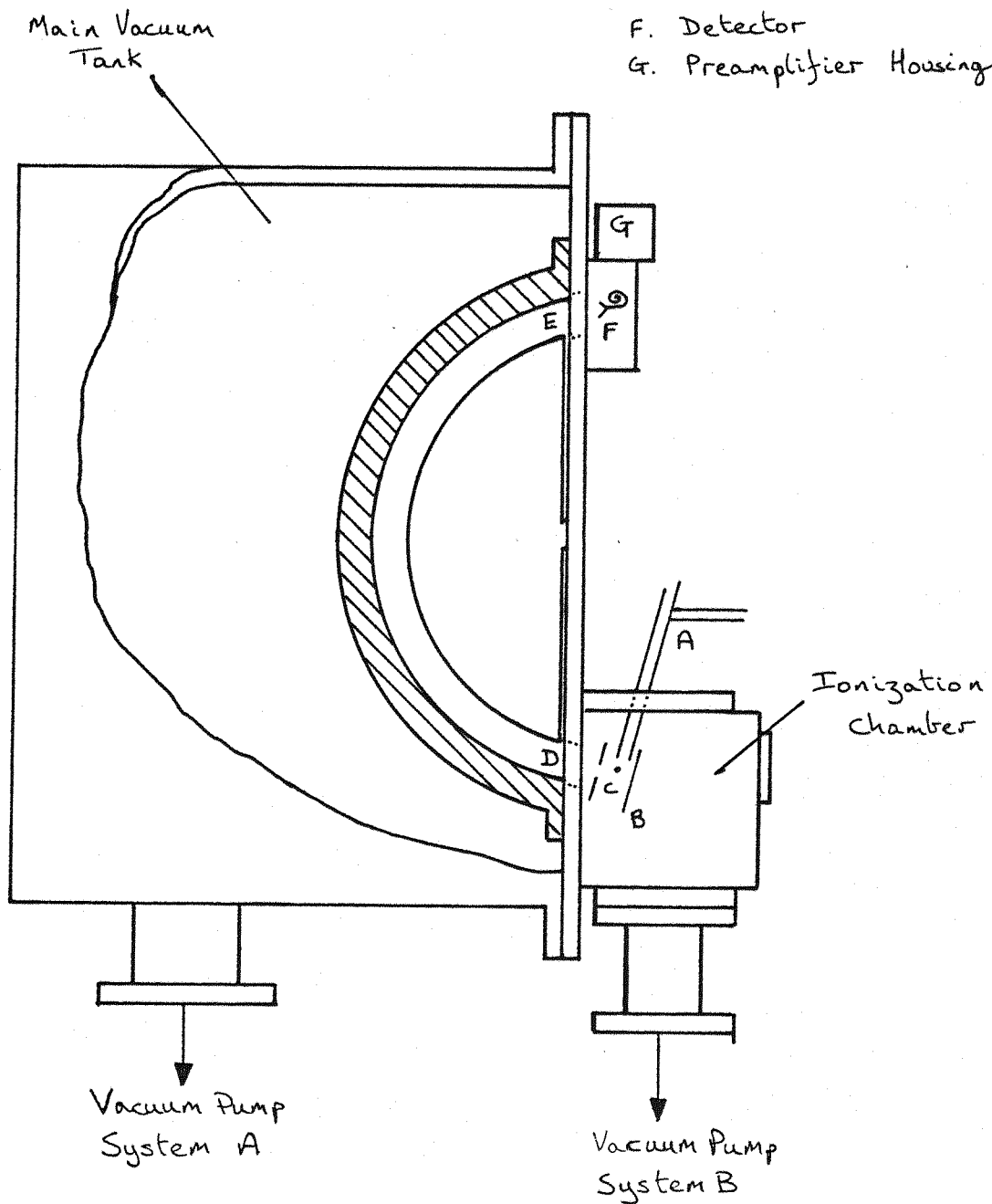
III-1 Vacuum System

The spectrometer is pumped by two pumping systems as shown in Figure 1.

System A consists of a 4 inch diffusion pump, charged with 704 silicone oil (175 ml), backed by a single stage rotary pump (33.3 m³/h). This system maintains a background pressure of <10⁻⁵ torr in the main vacuum chamber. In order to achieve better ultimate pressures and reduce backstreaming the diffusion pump is fitted with a liquid nitrogen cold trap and can be isolated by a butterfly valve. The overall pumping speed above the diffusion pump is of the order of 150 ls⁻¹ for air [5] at 10⁻⁶ torr. Roughing out of the main vacuum tank is achieved via an alternative pumping line direct to the tank, which can be roughed down to 10⁻² torr in approximately ten minutes from atmospheric pressure. Rotary Pump 1 also provides differential pumping for the helium discharge lamp, via an independent pumping line. Under operational conditions system A pumps very little gas, hence pumping speed is not essential except in the time required to pump down to operational pressures.

The second system, System B, consists of a 6 inch vapour diffusion pump, charged with 704 silicone oil (300 ml), backed by a single

- A. Inlet System
- B. Grid System
- C. Photon Beam
- D. Entrance Slits.
- E. Exit Slits
- F. Detector
- G. Preamplifier Housing



stage rotary pump (33.3 l/h). This system functions to pump away the sample gas, and maintain the vacuum in the ionization chamber. A liquid nitrogen trap is fitted to trap condensable gases, and a quarter swing butterfly valve is fitted to enable isolation of the pump. The overall pumping speed at 10^{-6} torr is approximately 410 l/sec for air [5]. Pressures on the backing lines are measured with separate Pirani gauge heads and the main vacuum chamber pressure is measured by an ionization gauge.

III-2 The Ultra-violet Photon Source

The photon source used on the instrument is a cold cathode dc discharge lamp. It consists of a quartz capillary positioned between two stainless steel electrodes supported on a machined boron nitride rod. The discharge region is water cooled and differentially pumped, by a rotary pump, to remove the discharge gas before entry into the ionization chamber. The power supply for the lamp is a $0 \rightarrow 2.5$ kV, 500 mA (max) variable high voltage supply. A stable discharge in Helium, producing the HeI α (21.21 eV) resonance line, requires 0.5 torr of Helium gas. Optimum running conditions require a voltage of 750 volts across the lamp electrodes and a current of 50 mA. The photon output from this type of discharge of helium has been investigated in detail [6] and contains approximately 97% HeI α radiation. Table I contains approximate intensity data for resonance line emission, from discharged helium, in the region 500 Å to 650 Å. Measurement of areas of peaks produced by ionization by one of the secondary lines of the HeI manifold, gives the experimental ratio of the "shadow" lines to the main ionization. This data reproduced the intensity data, recorded using a conventional spectrograph [6], of the output from a similar Helium discharge lamp.

Alternative gases in the discharge lamp can be used to produce other resonance lines. Use has been made of the Neon resonances in some experiments in this thesis. The strongest resonances are the NeI α (16.65 eV) and NeI β (16.83 eV) lines. Using a less energetic ionizing source means that the detection of photoelectrons occurs at lower kinetic energies, than with HeI α radiation hence enhancing the resolution of the instrument (see Section III-6). However the NeI spectrum is complicated by shadow

bands arising from ionization by the $\text{NeI}\beta$ line, which is 0.15 the intensity of the $\text{NeI}\alpha$ resonance line [3].

Table 1

Line	Transition	Wavelength Å	Energy eV	Approx I/I_{max}
$\text{HeI}\alpha$	$1^1\text{S} \rightarrow 2^1\text{P}$	584.3	21.219	1.0
$\text{HeI}\beta$	$1^1\text{S} \rightarrow 3^1\text{P}$	537.0	23.088	0.013
$\text{HeI}\gamma$	$1^1\text{S} \rightarrow 4^1\text{P}$	522.0	23.743	2.5×10^{-3}
$\text{HeI}\delta$	$1^1\text{S} \rightarrow 5^1\text{P}$	516.6	24.047	8.5×10^{-4}

III-3 The Electron Energy Analyser

The electron energy analyser used in the spectrometer is of the hemispherical electrostatic deflection type. Specifically, it has 150° solid sector hemispheres, machined from solid brass, with a mean radius of 10.16 cm and an inter-sphere gap of 1.905 cm. The spheres are mounted on the front plate of the vacuum chamber (see Figure 1) and are electrically isolated by ceramic and perspex spacers.

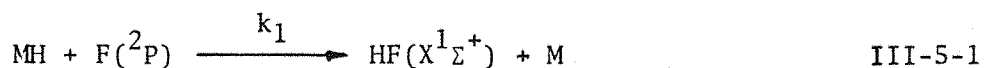
The reduced sector angle was chosen to facilitate the positioning of the entrance slits and exit slits whilst maintaining the object focal point, centre of spheres and image focal point on a line. The entrance and exit slits (D and E on Figure 1) consist of double aperture knife edges for each slit. The knife edge gap was set to 0.04 cm and 0.07 cm for both sets of collimating slits, which gave acceptable resolution without loss of sensitivity. The surfaces of all components of the analyser are coated with graphite (Acheson DAG 580) to eliminate contact potentials and point charges. The analyser including the object and image points are all within a field free region at the centre of 3 pairs of mutually orthogonal Helmholtz coils, set to neutralize the earth's magnetic fields.

III-4 The Electron Detector and Counting Electronics

The detector used in the instrument is a single channel electron multiplier (Mullard B419BL/01) positioned at the image focal point of the analyser. The detector was contained within a housing (F on Figure 1) pumped via the main vacuum chamber and operated at pressures below 10^{-5} torr. Full detailed technical specifications are available from reference 7. The detector was operated in pulse counting mode with an emitter follower preamplifier situated directly above the detector chamber. Pulse signals from the preamplifier are amplified, analysed and counted using standard detection electronics (Nuclear Enterprises "Edinburgh Series", [8]). Signals are recorded on a linear chart recorder, with equal and oppositesweep voltages being supplied to the hemispheres by a motor driven potentiometer.

III-5 The Gas Inlet System

Transient species generated in this work were produced by the rapid atom/molecule reactions of fluorine atoms with a suitable target molecule, i.e.:



or more generally



The conditions necessary for production of detectable quantities of M, from III-5-1 are a primary rate constant of the order of the bimolecular collision frequency, i.e. $10^{-10} - 10^{-11} \text{ cm}^3 \text{ molecule}^{-1} \text{ sec}^{-1}$. Also the secondary reactions removing M should be slow relative to k_1 . The inlet system, as shown in Figure 2, was specifically designed to allow the mixing of two gases at a position that is independently variable during the experiment. This enabled the target molecule to be introduced down the central tube to the point of reaction, which could be varied to alter the time delay before sampling the reaction mixture, with the photon beam. This allows optimization of the concentration of M whilst reducing the

concentration of complicating secondary products. The fluorine atoms were produced by microwave discharge (Electromedical Supplies Mk IV, 2.45 GHz microwave supply) of molecular fluorine, diluted 20:1 with helium (BOC Special Gases) flowing in the outer tube. The presence of fluorine atoms and hydrogen fluoride, in the reaction product mixture, entering the ionization chamber reactively, contaminates the graphite coating of the entrance slits. This alters the conducting properties of the coating, disturbing the constant potential region and leads to rapid deterioration in the sensitivity and resolution of the instrument. The flux of the reactive gas mixture through the slits and into the analyser chamber was greatly reduced by the introduction of a grid system, that facilitates a degree of differential pumping in front of the slits. Figure 2 shows the standard inlet arrangement around the ionization region, which has been developed in the Southampton PES group. The grid is also electrically isolated from earth in order that a bias potential, to pre-accelerate or retard the photoionized electrons, can be applied. This arrangement allowed the instrument to be operated, whilst studying fluorine atom/molecule reactions, for a number of hours before degradation limited the instrument performance.

The efficient pumping of the ionization chamber, by system B in Figure 1, gives, under typical experimental conditions, pumping speeds down the inlet tube of the order of 250 m/sec [9]. This enables the study of species with gas-phase lifetimes down to a few milliseconds provided they can be produced by a collision frequency limited reaction.

III-6 Factors Contributing to Instrumental Performance

The resolution of a electrostatic hemispherical deflection analyser is given by [10]:

$$\frac{\Delta E}{E} = \frac{w}{2r}$$

III-6-1

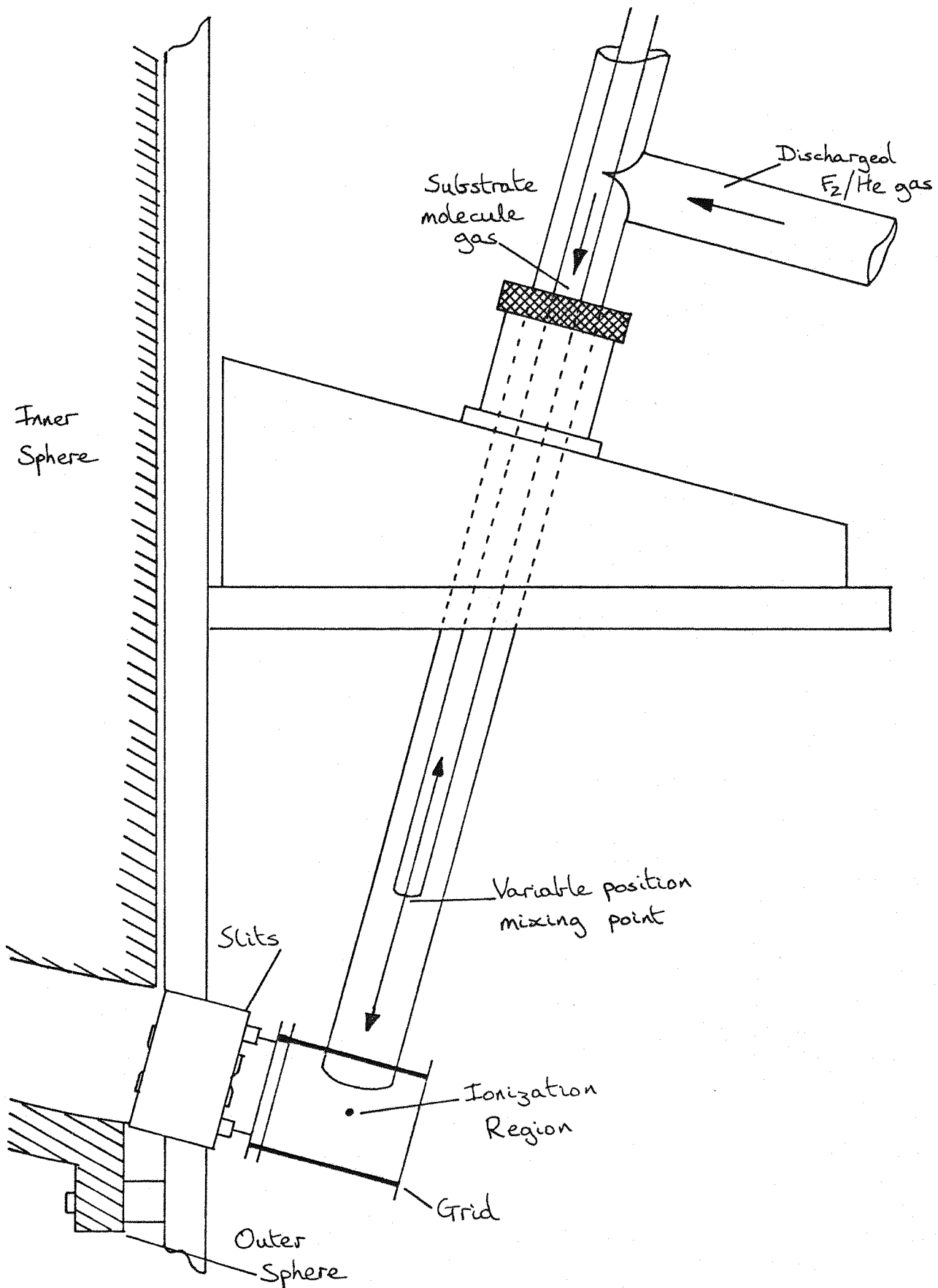
where w is the combined slit width of the entrance and exit slits and r is the mean radius of the hemispheres. This relationship shows that:

(1) The energy uncertainty, for a fixed pass energy, is proportional to

Figure 2

-76-

Diagram of the inlet system



the slit width, w ; (2) The energy uncertainty, for a fixed set of analyser parameters, is proportional to the pass energy, E .

Hence the resolution can be improved if the slit widths are reduced, but this reduces the sensitivity of the instrument by reducing the luminosity of the analyser. Also reducing the analysis energy of the electrons, by applying a retarding potential in the ionization region or by using a less energetic ionizing source (e.g. the NeI resonance lines), will better the resolution.

Other contributions to the overall instrumental resolution arise from thermal motion of the target molecules and from the natural line width of the photoionizing source. There are discussed in greater detail in reference 11. The highest resolution recorded on the instrument used in this work was 14.7 meV, as measured by the FWHM of the $\text{Ar}^+ (^2\text{P}_{3/2})$ peak. This excellent value was never reproduced under experimental conditions during the study of fluorine atom/molecule reactions, due to contamination effects of fluorine atoms and hydrogen fluoride.

The sensitivity of the instrument, to any particular class of electrons of energy E , is mainly governed by the transmission function of the analyser, for fixed analyser parameters. Calibration of the transmission function of the analyser used on this instrument has been carried out [12,13]. For the range of analysis energies 2 → 11 eV the transmission function was found to be linear and directly proportional to the analysis energy. This provides experimental confirmation of the theoretical luminosity of the hemispherical electrostatic analyser, for fixed slit widths [14]. This result is important in the calculation of branching ratios for ionizations to various ionic states, by adjusting experimental peak intensities according to the analysis energy and is useful in aiding assignment of photoelectron bands. This method of correcting peak intensities for the analyser transmission function has been used extensively in this thesis.

III-7 Calibration of Recorded Spectra

The sensitivity of low energy electrons, produced in UV PES, to small local charge variations makes the absolute calibration of spectra, from the analyser constant, inaccurate. Hence all photoelectron spectra

are calibrated by addition of a few commonly occurring molecular species with well characterized ionization potentials. If well known species are not already present in a reaction product mixture, or a particular region needs to be calibrated, then calibrants are introduced to the reaction mixture in the ionization chamber. The calibration of spectra is usually carried out using the ionization potentials recommended by Lloyd [15].

III-8 Experimental Problems Associated with the Use of Fluorine

As mentioned above, the instrument becomes contaminated during fluorine atom/molecule reaction experiments, resulting in the loss of resolution and sensitivity. The exact cause of this degradation is not yet clear, and is probably the result of several factors.

It is found that during the course of an experiment the contamination of the instrument proceeds through two distinct stages. Firstly when the discharge is first switched on, the analyser constant, relating the pass energy of the analyser to the applied potential difference, changes instantaneously to a new constant value. This has little effect on the resolution and linearly affects the whole kinetic energy spectrum. Also during this stage the extinguishing of the discharge returns the instrument to normal operation. However, during the course of the experiment secondary gradual degradation of resolution and sensitivity occurs, until instrument performance becomes sufficiently poor to terminate the experiment. These phenomena can be explained by the presence, in the ionization chamber, of a high density of ions, electrons and metastable atoms produced in the discharge, as well as many reactive atoms and molecular species. The accumulative effect of these species leads to a near instantaneous build up of charge on the exposed surfaces around the ionization region. If the charge density on the surfaces is approximately equal and since all surfaces are a similar distance from the ionization region, then a near uniform field would be generated. This could account for the initial "shift" of the spectra without loss of resolution. The further gradual irreversible degradation of the instrumental performance can be seen as the effect of the spread of contamination on to the surfaces of the slits and the analyser, disturbing the energies and directions of the electrons entering the analyser. Under experimental

conditions the total through-put of gases into the instrument may rise to a maximum, resulting in the ionization chamber pressure and residence time rising to several millitorr and 30 msec respectively [9]. Hence there will be a substantial flux of gas through the slits into the main vacuum chamber and the analyser, leading to contamination of the surfaces. The introduction of the grid system in front of the slits reduces the extent of contamination and slows the gradual degradation process, by directing gas flow away from the analyser entrance slits.

In addition to the contamination effects of fluorine further complications arise from the use of discharged fluorine as a source of fluorine atoms. Other products generated in the discharge are also seen in the PE spectrum. These have been identified as small concentrations of SiF_4 [16], $\text{O}_2(\text{X}^3\Sigma_g^-)$ [17], O Atoms [18] HF [19] and metastable $\text{O}_2(a^1\Delta_g)$ [20]. These all arise from reaction of fluorine atoms with the glass inlet tube around the discharge plasma. Attempts have been made to reduce the production of these species, such as coating the internal glass surfaces with alumina, but these proved unsuccessful. It was found however, that conditioning a new inlet system for several hours, to a F_2/He discharge, resulted in a considerable reduction in the concentration of these species. Recent experiments with inlet tubes fabricated from alumina tube and glass tube resulted in almost complete removal of contaminating products produced in the inlet system [21].

Hence it can be seen that production and detection of transient species present many problems unique to photoelectron spectroscopy. However many of these have been solved, and advances in extending the useful life of the spectrometer under experimental conditions has now resulted in durations of 5-6 hours, which is considered to be sufficient for spectroscopic studies. The advantages of fluorine atom abstraction are that it is often a very efficient way of generating a transient species in detectable concentrations. Also for small molecules the species present in the product mixture, other than the transient species, often have simple spectra (e.g. F, HF, O_2) and are often used for calibration of the spectra.

Chapter III

References

1. Dyke, J M, Jonathan, N B H, and Morris, A, J Elec Spec and Rel Phen, 15, 45, (1979).
2. Rabalais, J W, "Principles of Ultraviolet Photoelectron Spectroscopy", John Wiley and Sons, New York, (1977).
3. Eland, J H D, "Photoelectron Spectroscopy", Butterworth, London, (1970).
4. Turner, D W, Baker, C, Baker, A D, and Brundle, C R, "Molecular Photoelectron Spectroscopy", Wiley-Interscience, (1970).
5. Edwards Catalogue and Handbook, Edwards High Vacuum Ltd, Crawley, Sussex.
6. Samson, J A R, "Techniques of Vacuum Ultraviolet Spectroscopy", John Wiley and Sons, New York and London, (1967).
7. "Single Channel Electron Multipliers", Mullard Technical Information Sheet 16, Mullard Ltd, London, (1975).
8. Nuclear Enterprises: type NE5260 amplifier, type NE5159C analyser and type NE5456 linear ratemeter; Nuclear Enterprises Ltd, Bath Road, Beenham, Reading.
9. Winter, M J, Ph.D. Thesis, Southampton University, (1981).
10. Sevier, K D, "Low Energy Electron Spectroscopy", Wiley-Interscience, New York and London, (1972).
11. Samson, J A R, Rev Sci Instrum, 40, 1174, (1969).
12. Trickle, I R; Ph.D. Thesis, Southampton University, (1980).
13. Fackerell, A D, B.Sc. Project Dissertation, Southampton University, (1978).
14. Klemperer, O, "Electron Optics", Cambridge University Press, Cambridge, (1953).
15. Lloyd, D R, J Phys E, 3, 629, (1970).
16. Jadring, R, Karlson, L, Mattson, L, and Siegbahn K, Chem Phys Letts, 49, 203, (1977).

17. Edquist, D, Lindholm, E, Selin, L E, and Asbrink, L, Physica Scripta, 1, 25, (1970).
18. Jonathan, N, Morris, A, Smith, D J, and Ross, K J, Chem Phys Letts, 7, 497, (1970).
19. Berkowitz, J, Chem Phys Letts, 11, 21, (1971).
20. Jonathan, N, Morris, A, Okuda, M, Ross, K J, and Smith, D, JCS Faraday II, 70, 1810, (1974).
21. Ridha, A M A, Private Communication.

Chapter IV
Photoelectron Spectrum of the
 $\text{FO}(\text{X}^2\Pi_1)$ Radical

Contents

IV-1 Introduction

IV-2 Experimental

IV-3 Computational Details

IV-4 Results and Discussion

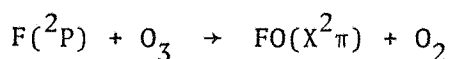
IV-1 Introduction

In spite of being the object of attempted spectroscopic studies by various techniques, the fluorine monoxide radical, FO, defied spectroscopic observation in the gas phase until a very recent laser magnetic resonance (LMR) investigation [1]. Indeed, it was only within the last 15 years that conclusive evidence, derived by matrix isolation [2,3], was obtained for the existence of this molecule. Since that time, the FO radical has been detected in the gas phase mass spectrometrically [4] and this technique has been used to study the kinetics of the gas phase reaction of fluorine atoms with ozone, by monitoring the detector current at $m/e = 35$, corresponding to FO [5,6].

The paucity of available data for fluorine monoxide is all the more surprising in view of the numerous spectroscopic studies which have been made on other halogen monoxides. It was this lack of data and the wish to extend our work on the ClO and BrO radicals [7,8] that stimulated this present study. Also it was after initial results had been derived that the LMR data became known to us. No other photoelectron spectroscopic (PES) results are available for the FO radical and indeed the only estimates of the first adiabatic ionization potential are ones which have been obtained indirectly from photoionization and electron impact mass spectrometric experiments on F_2O [9,10]. The most reliable value obtained from these studies would appear to be (12.79 ± 0.10) eV [9,11]. As far as can be ascertained there are no other data available in the literature pertaining to the various electronic states of the fluorine monoxide positive ion. Also since FO^+ is isoelectronic with molecular oxygen, it is of interest to compare spectroscopic parameters and term values derived for states of FO^+ in a PES study with those known for the corresponding states of O_2 .

IV-2 Experimental

In this study, the FO radical was produced within 5-6 cm of the ionization point of the photoelectron spectrometer by making use of the reaction [5,6].



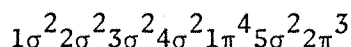
IV-2-1

Ozone was prepared by high voltage discharge of oxygen and stored by trapping on non-indicating silica gel at dry ice temperature. The HeI photoelectron spectrum of ozone has been recorded previously [12], and spectra of samples showed no impurities. Fluorine atoms were produced by microwave discharge (2.45 GHz) of molecular fluorine in helium and introduced into the spectrometer, along with the ozone, using the inlet system described previously (see Chapter III-5).

For the conditions under which FO was observed, the usual resolution was 20-25 meV (FWHM) as measured for argon using HeI α radiation. Calibration of the spectral range was achieved using the HeI α spectrum of argon and oxygen [13], the latter being a product of reaction IV-2-1. Unless otherwise stated, ionization potentials are quoted to an accuracy of ± 0.01 eV and vibrational spacings to ± 30 cm $^{-1}$.

IV-3 Computational Details

The ground state electronic configuration of FO($X^2\pi$) can be written as:



A previous ab initio calculation performed for FO [11] shows that the 2π , 5σ and 1π levels should all be accessible via one-electron ionization with HeI radiation. As has been pointed out for ClO [7], three ionic states ($^3\Sigma^-$, $^1\Delta$, $^1\Sigma^+$) should arise from ionization from the 2π level, two ionic states ($^3\pi$, $^1\pi$) should result from ionization from the 5σ level and six ionic states ($^1\Sigma^-$, $^3\Sigma^-$, $^3\Delta$, $^3\Sigma^+$, $^1\Delta$, $^1\Sigma^+$) should be produced from ionization from the 1π level. In this work, values for the vertical ionization potentials giving rise to these 11 ionic states have been computed using the Δ SCF method. This was achieved by performing ab initio SCF calculations using the ATMOL restricted open-shell method [14] on both the neutral molecule and the ionic states under consideration at the experimental equilibrium bond length of FO($X^2\pi$) of 1.3579 Å [1]. The basis set used was of Gaussian type functions and consisted of a Huzinaga (9s5p) primitive set [15] contracted according to Dunning [16] for each centre. This set was augmented by two d sets on O and one on F each comprising of three Gaussian functions derived from an expansion of

of the Slater type functions, taken from reference [11], according to Stewart [17]. The accuracy of this basis set was confirmed by comparison of total energies and spectroscopic constants, derived from the potential energy/bond length data calculated near the equilibrium bond length, for $\text{FO}(\text{X}^2\pi)$ (see Chapter IIb-1). The results are shown in Table 1.

Table 1

Constant	Ref [11]	This Work	Experimental [1]
Total Energy (AU)	-174.19502	-174.173341	-
r_e (Å)	1.321	1.3155	1.35357
ω_e (cm^{-1})	1211	1251	1043.6
$\omega_e x_e$ (cm^{-1})	5.15	5.16	10.1
D_e (eV)	$3.0^{+0.3}_{-0.8}$	3.0	-
A (cm^{-1})	-	-	-177.36

Calculated and Experimental Constants for $\text{FO}(\text{X}^2\pi)$

Correlation energy contributions were evaluated for each of the ionic states and for $\text{FO}(\text{X}^2\pi)$ using the semiempirical Population Analysis Method [18]. A full configuration interaction study was considered out of the question in view of the large basis set used and the number of configurations necessary to recover a significant proportion of the correlation energy. The calculated energies for FO and the FO^+ ionic states are tabulated in Table 2.

IV-4 Results and Discussion

The HeI photoelectron spectrum obtained from the reaction of fluorine atoms with ozone is shown in Figure 1. Clearly visible in this spectrum are bands attributable to the reactants (fluorine atoms and ozone), molecular oxygen (a reaction product) and bands arising from silicon tetrafluoride and oxygen atoms (obtained from the reaction of fluorine atoms with the glass inlet system). Weak features were also

Table 2

State	E(SCF) Au	-V/T	E(corr) Au	E(Total) Au
$\text{FO}(\text{X}^2\pi)$	-174.172136	2.0001	-0.592	-174.76321
$\text{FO}^+(\text{X}^3\Sigma^-)$	-173.714056	2.0013	-0.550	-174.264056
$\text{FO}^+(\text{a}^1\Delta)$	-173.631313	2.0018	-0.553	-174.184313
$\text{FO}^+(\text{b}^1\Sigma^+)$	-173.55577	2.0024	-0.553	-174.10877
$\text{FO}^+(\text{}^3\pi)$	-173.522487	1.9978	-0.581	-174.103487
$\text{FO}^+(\text{}^1\pi)$	-173.480664	1.9967	-0.542	-174.022664
$\text{FO}^+(\text{}^1\Sigma^+)$	-173.591809	1.9975	-0.541	-174.132809
$\text{FO}^+(\text{}^1\Delta)$	-173.596020	1.9976	-0.541	-174.13702
$\text{FO}^+(\text{}^3\Sigma^+)$	-173.59609	1.9976	-0.541	-174.13709
$\text{FO}^+(\text{}^3\Delta)$	-173.599254	1.9977	-0.541	-174.140254
$\text{FO}^+(\text{}^3\Sigma^-)$	-173.600275	1.9977	-0.541	-174.141275
$\text{FO}^+(\text{}^1\Sigma^-)$	-173.602424	1.9978	-0.541	-174.143424

Calculated total energies for a number of states of FO and FO^+

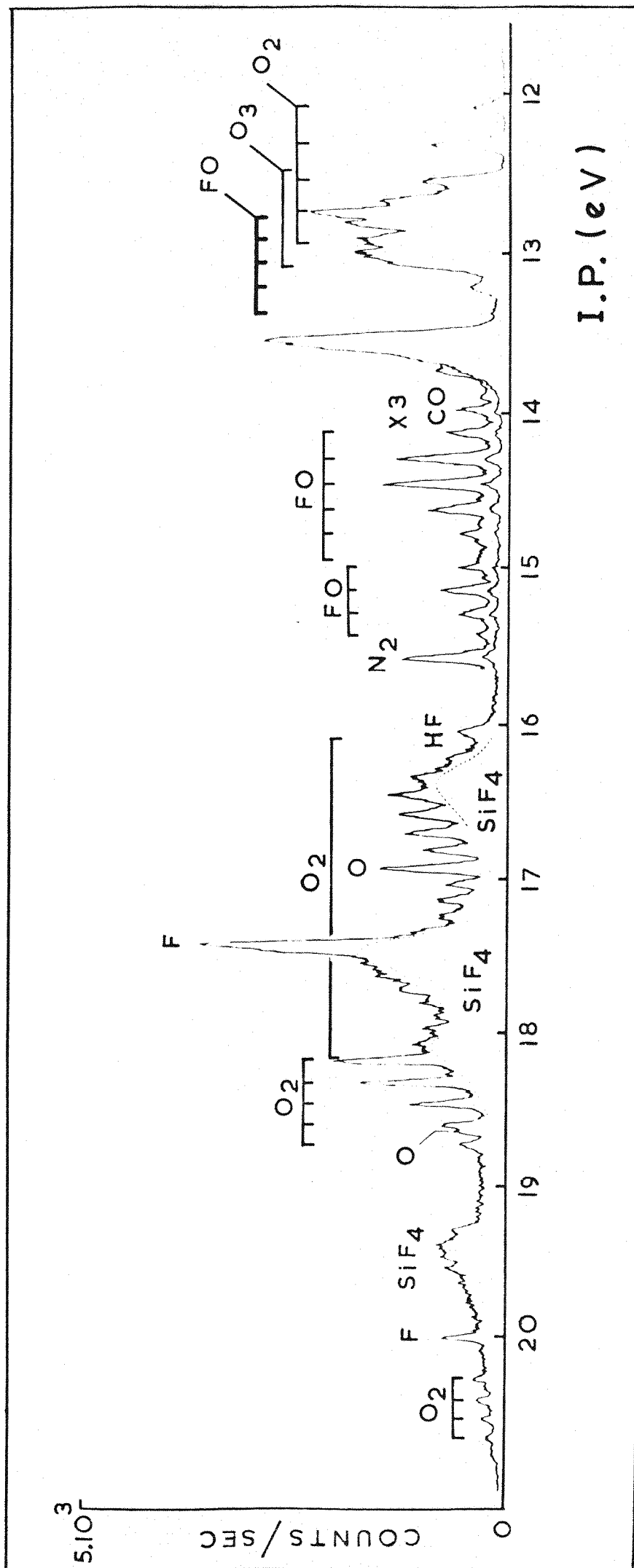


Figure 1

seen attributable to molecular nitrogen (arising for minor leaks in the inlet system) and carbon monoxide, probably arising from reaction of oxygen atoms with the graphite surfaces within the ionization chamber. However, three extra bands showing clear vibrational structure were observed in the ionization energy region 12.0-16.0 eV, and these are shown in Figure 2. The second and third bands both consist of a vibrational series of at least four vibrational components and their vertical ionization potentials were measured as 14.48 and 15.16 eV respectively. The first band was partially overlapped both by the first band of ozone and the fourth and fifth vibrational components of the first band of oxygen. However, by using an excess of fluorine atoms, the ozone contribution could be reduced virtually to zero. The contribution of the first band of oxygen was then subtracted off, revealing a band with five regularly spaced vibrational components, shown in Figure 3. The adiabatic and vertical ionization potentials of this band were measured as 12.77 and 13.08 eV respectively.

The three observed bands were attributable to the same short-lived molecule because their experimental intensity ratios (measured as $3.5 \pm 0.2 : 2.0 : 0.9 \pm 0.2$, after correction for analyser transmission function) remained constant for all experimental conditions and, increasing the product residence time by moving the mixing point backwards to a point some ten centimetres above the photon beam caused a dramatic reduction in their intensities. These bands can only be assigned to FO because all other likely products of the reaction mixture have different photoelectron spectra (e.g. F_2O [19]). In support of this, the observed relative intensities of the three bands agree favourably with the statistically expected ratio of 3:2:1 for the $^3\Sigma^-$, $^1\Delta$ and $^1\Sigma^+$ states, which are formed from the $(2\pi)^{-1}$ ionization of FO. In addition the adiabatic ionization potential measured for the first band, 12.77 eV, is in good agreement with a value of 12.79 ± 0.10 eV determined previously for FO by photoionization mass spectrometry [9]. Also, the overall vibrational envelopes observed here for this ionization process closely resemble the band shapes obtained from laser photodetachment of isoelectronic O_2^- [20].

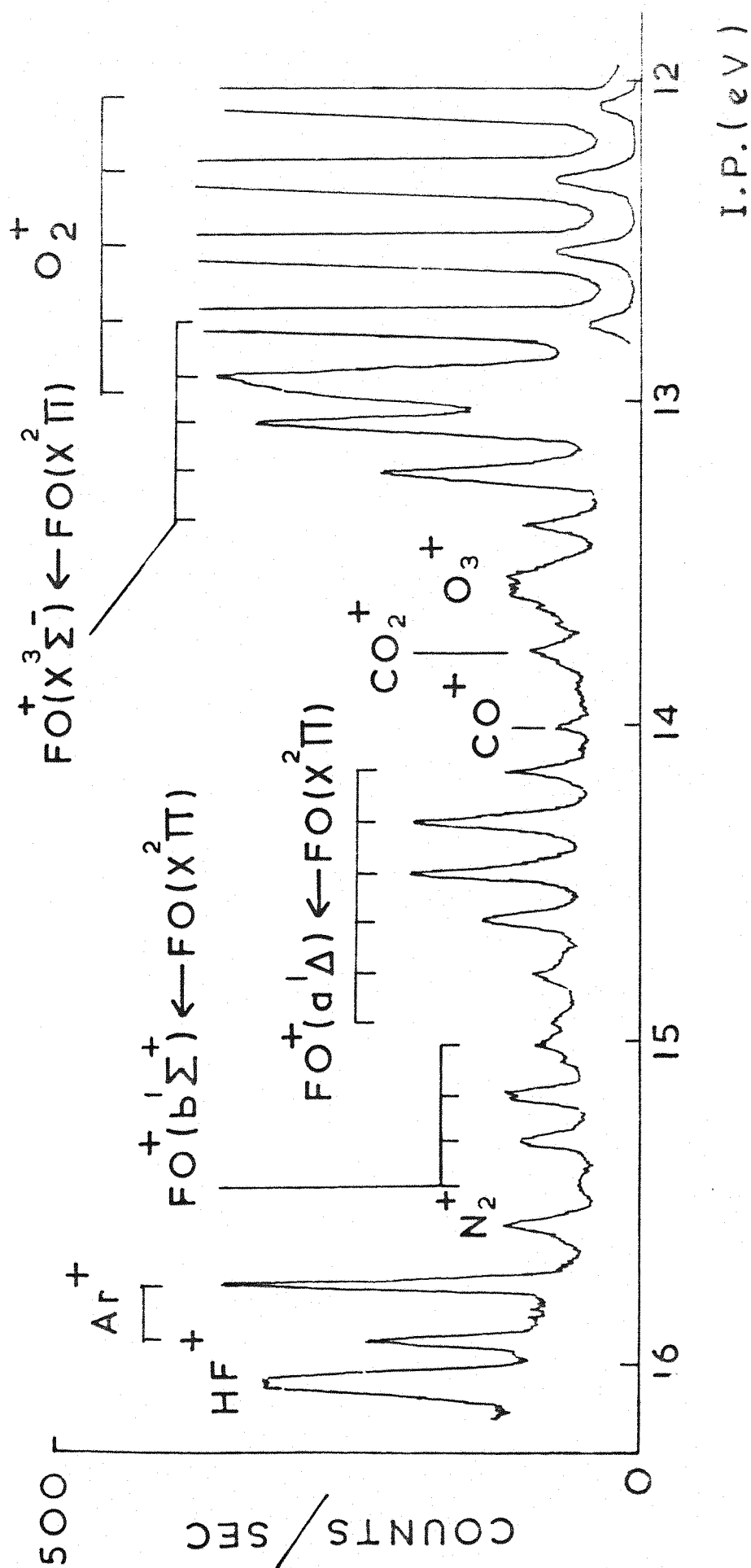


Figure 2

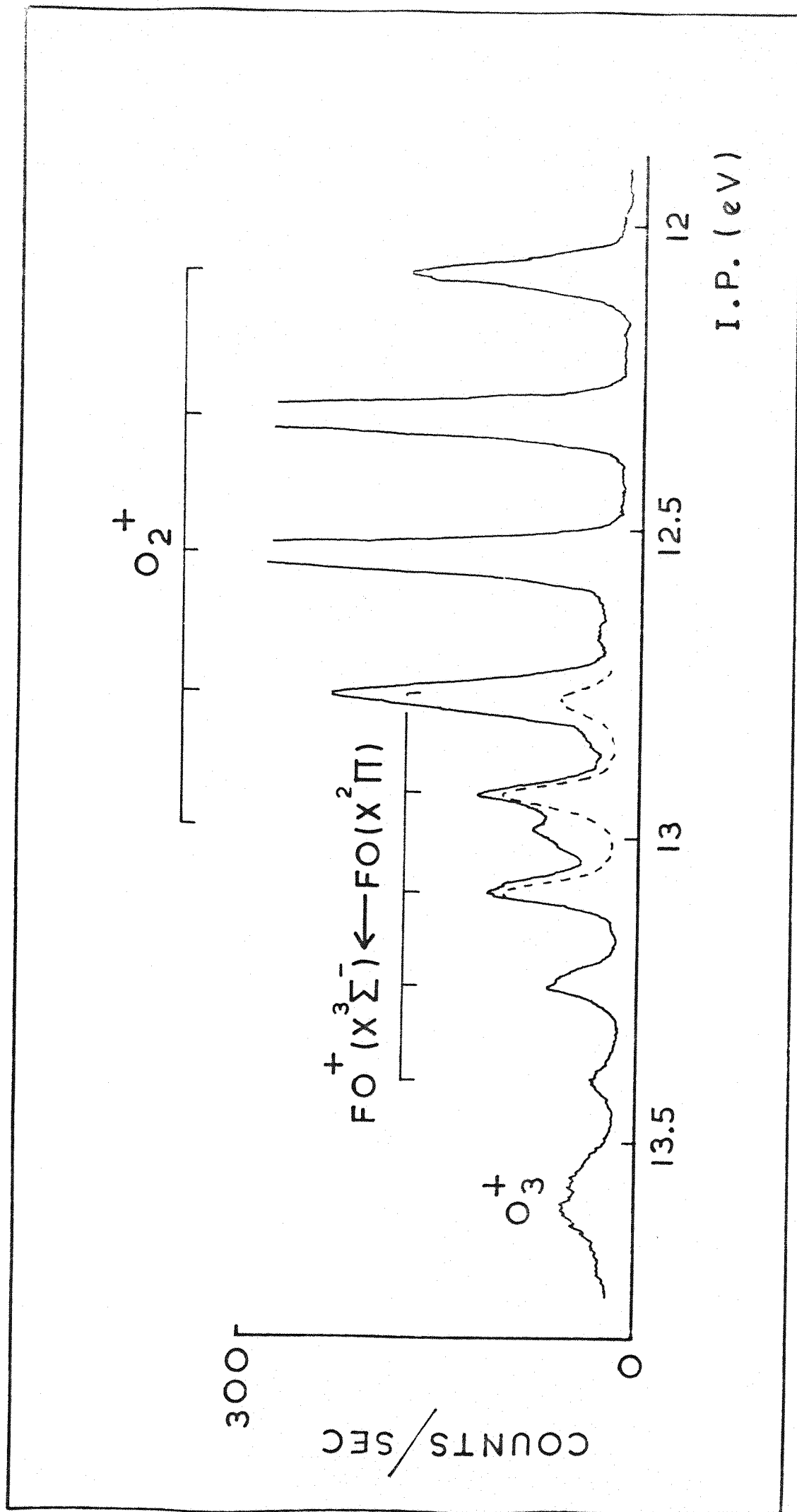


Figure 3

A comparison of the observed and predicted vertical ionization potentials of FO is shown in Table 3.

Table 3^(b)

Ionization	Ionic State	Δ SCF VIp(a)	Δ SCF + E_{corr} VIp(a)	Observed VIp
2 π	$3\Sigma^-$	12.465	13.582	13.08
	1Δ	14.717	15.752	14.48
	$1\Sigma^+$	16.772	17.808	15.16
1 π	$1\Sigma^-$	15.503	16.865	Not observed because of overlapping band problems
	$3\Sigma^-$	15.561	16.923	
	3Δ	15.589	16.951	
	$3\Sigma^+$	15.675	17.037	
	1Δ	15.677	17.039	
	$1\Sigma^+$	15.792	17.154	
5 σ	3π	17.678	17.951	
	1π	18.816	20.151	

Computed and experimental vertical ionization potentials

(a) Calculated at the experimental neutral bond length of $r_e = 1.3579$ [1].

(b) All figures in electron volts (eV).

The comparison of the observed and computed values shows good agreement for the Δ SCF results, but the values obtained using estimated correlation energies are consistently over predicted. The method of Population Analysis to estimate correlation energies has been previously evaluated to give ionization potentials to an accuracy of ± 0.6 eV [21]. However, the wide variation in the results obtained here suggests extensive mixing of ionic states which is not accounted for in the semi-empirical method. As can be seen from this table, at least eight other

bands of FO are expected in the HeI region. However, these were not observed experimentally because the 16.0 eV - 20.0 eV ionization energy region is complicated by strong contributions from molecular oxygen and silicon tetrafluoride.

For the three observed bands of FO, analysis of the vibrational structure led to estimates of the corresponding ionic vibrational frequency (ω_e) and associated anharmonicity ($\omega_e x_e$). The values obtained for ω_e are listed in Table 4, along with derived bond lengths and dissociation energies (derived using methods in Chapter IIb). For each state the anharmonicity constant, $\omega_e x_e$, was estimated as $10 \pm 20 \text{ cm}^{-1}$, due to the limited number of vibrational components resolved in each band. Data for neutral FO is included for comparison.

Table 4

State	Equilibrium bond length, r_e	Vibrational wavenumber $\bar{\omega}_e$	Dissociation energy, D_e
$\text{FO}(X^2\pi)$	1.3579 Å (a)	1044 cm^{-1}	2.31 \pm 0.15 eV(b)
$\text{FO}^+(X^3\Sigma^-)$	1.23 ₄ Å (c)	1300 cm^{-1}	6.96 eV (d)
$\text{FO}^+(a^1\Delta)$	1.23 ₉ Å (c)	1280 cm^{-1}	5.57 eV (d)
$\text{FO}^+(b^1\Sigma^+)$	1.24 ₆ Å (c)	1230 cm^{-1}	4.72 eV (d)

Spectroscopic constants for FO and FO^+

(a) Ref [1]

(b) Ref [4]

(c) Error of $\pm 0.01 \text{ Å}$

(d) Error of $\pm 0.16 \text{ eV}$

As can be seen from Table 4, the values of $\bar{\omega}_e$ obtained for the $X^3\Sigma^-$, $^1\Delta$ and $^1\Sigma^+$ FO^+ states are greater than the corresponding value in $\text{FO}(X^2\pi)$, which is consistent with removal of an electron from the 2π antibonding level. A similar trend has been observed for the first three ionic

states of ClO [7] and is further evidence for assignment of the observed bands to ionization of FO. For these states of FO^+ , it was assumed that ionic dissociation occurs to $\text{F}^+(\text{}^3\text{P})$ and $\text{O}(\text{}^3\text{P})$. Dissociation energies were estimated by subtracting the measured adiabatic ionization potentials from the sum of the known dissociation energy of $\text{FO}(\text{X}^2\pi)$ [4] and the first ionization potential of atomic fluorine [22].

The spectroscopic constants (r_e , D_e and $\bar{\omega}_e$) derived in this work for FO^+ can be compared with those of the corresponding states of O_2 , as shown in Table 5.

Table 5

State	Equilibrium bond length, r_e	Vibrational wavenumber, ω_e	Dissociation energy, D_e
$\text{O}_2^-(\text{X}^2\pi_g)$	$1.341 \pm 0.01 \text{ \AA}^{\text{O}}$ (a)	1089 cm^{-1} (a)	$4.16 \pm 0.01 \text{ eV}$ (a)
$\text{O}_2(\text{X}^3\Sigma_g^-)$	$1.2075 \text{ \AA}^{\text{O}}$ (b)	1580 cm^{-1} (b)	5.21 (c)
$\text{O}_2(\text{a}^1\Delta_g)$	$1.2157 \text{ \AA}^{\text{O}}$ (b)	1509 cm^{-1} (b)	4.23 (b,c)
$\text{O}_2(\text{b}^1\Sigma_g^+)$	$1.2268 \text{ \AA}^{\text{O}}$ (b)	1433 cm^{-1} (b)	3.58 (b,c)

Spectroscopic constants for O_2^- and O_2

(a) Ref [23] and [24].

(b) Ref [25].

(c) Ref [26].

An increase in equilibrium bond length and decrease in vibrational frequency along the series $\text{X}^3\Sigma^-$, $^1\Delta$ and $^1\Sigma^+$ occurs in both cases. Also, the separations of the first three adiabatic ionization potentials of FO have been measured in this work as $(1.39 \pm 0.02) \text{ eV}$ and $(0.85 \pm 0.02) \text{ eV}$. These values compare with the separations of the zeroth vibrational levels in the corresponding states of molecular oxygen of 0.977 eV and 0.649 eV respectively [26].

The observation of the FO radical in this study represents only the

second spectroscopic detection of FO in the gas phase. This is rather surprising in view of the moderate sensitivity of the PES technique (lower limit of detection $\sim 10^{11}$ molecules per cm^3). Also the reasonably long life of FO under our conditions, (typically FO was generated some 5 centimetres above the photon beam, a distance traversed in ~ 5 milliseconds), contradicts previous predictions of the lifetime of FO [2 7], which was largely based on the fact that it remained undetected spectroscopically until recently. McKellar [1] suggests that electronic spectra have not been observed because of predissociation effects and EPR transitions have not been detected because of the small value of the dipole moment of FO.

In this PES investigation, only three of the expected 11 ionic states of FO accessible with HeI radiation have been observed. This is due to problems associated with overlapping bands. Hence, although ionic spectroscopic constants ($\bar{\omega}_e$, r_e and D_e) were derived and adiabatic and vertical ionization potentials were measured for the three observed states, much work remains to be done to locate and characterize the higher ionic states of FO. It is hoped that this present work will encourage further spectroscopic and theoretical work on this problem.

Chapter VI

References

1. McKellar, A R W, Can J Phys, 57, 2106, (1979).
2. (a) Arkell, A, Reinhard, R R, and Larson, L P, J Am Chem Soc, 87, 1016, (1965).
(b) Arkell, A, J Phys Chem, 73, 3877, (1969).
3. (a) Andrews, L, J Chem Phys, 57, 51, (1972).
(b) Andrews, L, and Raymond, J I, J Chem Phys, 55, 3078, (1971).
4. Clyne, M A A, and Watson, R T, Chem Phys Letts, 12, 344, (1971).
5. Clyne, M A A, and Watson, R T, J Chem Soc Farad Trans I, 70, 1109, (1974).
6. (a) Wagner, H G, Zetzsch, C, and Warnatz, J, Berichte Bunsen-Ges Phys Chem, 76, 526, (1972).
(b) Wagner, H G, Warnatz, J, and Zetzsch, C, Angew Chem Int Ed, 10, 564, (1971).
7. (a) Bulgin, D K, Dyke, J M, Jonathan, N, and Morris, A, J Chem Soc Farad Trans II, 75, 456, (1979).
(b) Bulgin, D K, Dyke, J M, Jonathan, N, and Morris, A, Molecular Physics, 32, 1487, (1976).
8. Dunlavey, S J, Dyke, J M, and Morris, A, Chem Phys Letts, 53, 382, (1978).
9. Berkowitz, J, Dehmer, P M, and Chupka, W A, J Chem Phys, 59, 925, (1973).
10. Dibeler, V H, Reese, R M, and Franklin, J L, J Chem Phys, 27, 1296, (1957).
11. O'Hare, P A G, and Wahl, A C, J Chem Phys, 53, 2469, (1970).
12. Dyke, J M, Golob, L, Jonathan, N, Morris, A, and Okuda, M, J Chem Soc Farad Trans II, 70, 1828, (1974).
13. Edqvist, O, Lindholm, E, Selin, L E, and Asbrink, L, Physica Scripta, 1, 25, (1970).
14. (a) Saunders, V R, and Guest, M F, "ATMOL-3 Reference Manual," Atlas Computing Division, Rutherford Laboratory, (1976).
(b) See Chapter IIa-4.
15. Huzinaga, S, J Chem Phys, 42, 1293, (1965).

16. (a) Dunning, T H, J Chem Phys, 53, 2823, (1970).
(b) Dunning, T H, and Hay, P J, "Methods of Electronic Structure Theory", Modern Theoretical Chemistry, Volume 3, Ed: H F Schaefer, Plenum Press, New York and London, (1977).
17. Stewart, R F, J Chem Phys, 52, 431, (1970).
18. Liu, H P D, and Verhaegen, G, J Chem Phys, 53, 735, (1970).
19. (a) Cornford, A B, Frost, D C, Herring, F G, and McDowell, C A, J Chem Phys, 55, 2820, (1971).
(b) Von Niessen, W, J Elec Spec Rel Phen, 17, 197, (1979).
20. Celotta, R J, Bennett, R A, Hall, J L, Siegel, M W, and Levine, J, Phys Rev A, 6, 631, (1972).
21. Verhaegen, G, J Chem Phys, 49, 4696, (1968).
22. Moore, C E, "Ionization Potentials and Ionization Limits Derived from Analysis of Optical Spectra", NSDRDS-NBS, p34, (1970).
23. Schulz, G J, Rev Mod Phys, 45, 423, (1973).
24. Celotta, R J, Bennett, R A, Hall, J L, Siegel, M W, and Levine, J, Phys Rev A, 6, 631, (1972).
25. Herzberg, G, Can J Phys, 30, 185, (1962).
26. Rosen, B, "International Tables of Selected Constants: Data Relative to Diatomic Molecules", Pergamon Press, London, (1970).
27. Turner, J J, Endeavour, 27, 42, (1968).

Chapter V

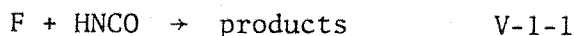
Photoelectron Spectroscopic Study of the Reaction $F + HNC O$

Contents

V-1	Introduction
V-2	Experimental
V-3	Computational Details
V-4	Results and Discussion

V-1 Introduction

A study of the reaction products of reaction V-1-1 was initiated using photoelectron spectroscopy.



The primary aim was to characterize the photoelectron spectrum of the NCO radical.

Although the NCO radical has been the subject of a number of spectroscopic investigations [1-4], it has not previously been studied with photoelectron spectroscopy. Most notable previous studies include analysis of its electronic absorption [1] and EPR spectra [2] recorded in the gas phase and a study of the infrared and ultraviolet spectra of NCO trapped in inert gas matrices [3]. Also, no spectroscopic studies have been performed on the low-lying ionic states of NCO and no estimates are available for the first ionization potential of this radical. However, if the more recent value of (16.66 ± 0.15) eV is assumed for the appearance potential of NCO^+ from HNCO [5] determined from an electron impact mass spectrometric study, and an upper limit of $D(\text{H-NCO})$ is taken as (4.90 ± 0.01) eV [6], obtained from a photodissociation study of HNCO in the vacuum ultraviolet region, a lower limit for the first adiabatic ionization potential of NCO can be estimated as (11.76 ± 0.16) eV. The error in this value is likely, however, to be larger than the quoted figures as no attempt was made to monochromatize the incident electron beam in the mass spectrometric study.

The aim of this work, therefore, was to use vacuum ultraviolet photoelectron spectroscopy to make a direct determination of the first ionization potential and to characterize the accessible ionic states of NCO.

V-2 Experimental

In this study the complete photoelectron spectrum of the products of reaction V-1-1 was recorded for several values of reagent mixing distance, in the range 1 cm - 16.5 cm from the ionization point.

HNCO was prepared by slow addition of concentrated aqueous potassium cyanate to orthophosphoric acid in a vacuum line. The

products of the reaction were passed through two traps at 231 K (diethyl ketone/slush) to remove water vapour and then collected in a third trap held at 77 K. The major impurity in the sample was found from its photoelectron spectrum to be carbon dioxide and this was removed by several slow distillations between slush baths held at 231 K and 195 K (acetone/dry ice eutectic). The sample was admitted to the spectrometer from a slush bath held at 231 K and the spectrum obtained was found to be in good agreement with those published for HNC0 previously [7,8].

The source of fluorine atoms was a microwave discharge (2.45 GHz) of a flowing F_2 /He mixture (5% Fluorine, BOC Special Gases) in a glass tube. Complete dissociation of fluorine into ground state atoms was achieved, and monitored by recording the photoelectron spectrum of the discharge products alone.

The photoelectron spectrometer was of the electrostatic analyser type and has been described elsewhere [9]. For the conditions under which the NCO radical was observed, the usual resolution was 20-25 meV (FWHM) as measured for argon using $HeI\alpha$ radiation. Spectral calibration was achieved using the $HeI\alpha$ spectra of carbon monoxide, nitrogen, hydrogen fluoride and isocyanic acid. Unless otherwise stated, ionization potentials are quoted to an accuracy of ± 0.01 eV and vibrational spacings to ± 30 cm^{-1} .

V-3 Computational Details

To aid analysis of recorded bands attributable to radical products of reaction V-1-1, calculations were performed on the primary radical species, NCO.

NCO($X^2\pi$) has a linear equilibrium geometry with the electronic configuration [1].

$$(1\sigma)^2(2\sigma)^2(3\sigma)^2(4\sigma)^2(5\sigma)^2(6\sigma)^2(1\pi)^4(7\sigma)^2(2\pi)^3$$

where the 2π molecular orbital is composed mainly of a nitrogen $2p_\pi$ atomic orbital with small contributions from C $2p_\pi$ and O $2p_\pi$ atomic orbitals [10]. An ab initio calculation performed for NCO($X^2\pi$) shows that the 2π , 7σ , 1π , and 6σ levels should all be accessible via one-

electron ionization from the neutral molecule with HeI radiation. Three ionic states ($^3\Sigma^-$, $^1\Delta$, $^1\Sigma^+$) will arise from ionization from the 2π level, two ionic states ($^3\pi$, $^1\pi$) result from ionization from the 7σ level, six ionic states ($^1\Sigma^-$, $^3\Sigma^-$, $^3\Delta$, $^3\Sigma^+$, $^1\Delta$, $^1\Sigma^+$) arise from ionization from the 1π level and two ionic states ($^3\pi$, $^1\pi$) will be produced from ionization from the 6σ level. Also, as NCO^- is isoelectronic with CO_2 and N_2O and as the low-lying electronic states of NCO^+ are expected to be linear [11], the known photoelectron spectra of carbon dioxide and nitrous oxide [12,13] can be used to predict the expected band envelopes in the photoelectron spectrum of $\text{NCO}(X^2\pi)$. On this basis, the $(2\pi)^{-1}$, $(7\sigma)^{-1}$ and $(6\sigma)^{-1}$ ionizations should give rise to sharp bands where the adiabatic ionization potential is equal to the vertical ionization potential, whereas the $(1\pi)^{-1}$ ionization is expected to give rise to broad bands characteristic of a large equilibrium geometry change on ionization.

In this work, values for the vertical ionization potentials for ionization to the 13 ionic states arising from the $(2\pi)^{-1}$, $(7\sigma)^{-1}$, $(1\pi)^{-1}$ and $(6\sigma)^{-1}$ processes have been computed using the ΔSCF method. This was achieved by performing ab initio calculations using the ATMOL restricted open-shell method [14] on both the neutral molecule and the ionic state under consideration. These calculations were all performed at a linear NCO geometry with $R(\text{N-C}) = 1.251 \text{ \AA}$ and $R(\text{C-O}) = 1.157 \text{ \AA}$. Since no direct experimental measurement of the equilibrium bond lengths in $\text{NCO}(X^2\pi)$ has been made, the above bond lengths have been estimated from the ab initio minimum energy geometry values of Thomson and Wishart [10] corrected, with the ratio of the N-C and C-O bond lengths held constant, to give a total bond length equal to the upper limit of $R(\text{N-C-O})$, determined experimentally, of 2.408 \AA [1]. Equilibrium bond lengths for $\text{NCO}(X^2\pi)$ obtained in this way are in close agreement with values suggested from the infrared spectrum of NCO and its isotopically substituted variants isolated in an inert gas matrix [3]. The basis set used in these calculations was a large basis of Gaussian functions. For each atom, a (9s5p) basis contracted to (4s3p) was used [15,16]. These functions were augmented by a d polarization STO function on each centre. The exponents used for these functions were taken from reference [17] and

each STO was expanded in terms of three Gaussian functions [18]. The results of these calculations are shown in Table 1.

Table 1

Orbital Ionized	Ionic State Produced	Computed Δ SCF vertical ionization potential (eV)
2 π	$3\Sigma^-$	10.81
	1Δ	12.31
	$1\Sigma^+$	13.65
7 σ	3π	13.73
	1π	16.36
1 π	$1\Sigma^-$	14.34
	3Δ	14.42
	$3\Sigma^+$	14.49
	$3\Sigma^-$	14.72
	1Δ	14.91
	$1\Sigma^+$	15.09
6 σ	3π	17.27
	1π	17.69

Calculated Δ SCF vertical ionization potentials
for the NCO($X^2\pi$) radical.

V-4 Results and Discussion

The HeI photoelectron spectrum of the products of reaction V-1-1 is shown in Figure 1(a). Clearly visible in this spectrum are bands attributable to HNCO (Figure 1(b)) and F atoms (the reactants), and HF, CO, CO₂ and N₂, which were found to be products of the reaction. Also observed are weaker bands due to molecular oxygen and oxygen atoms,

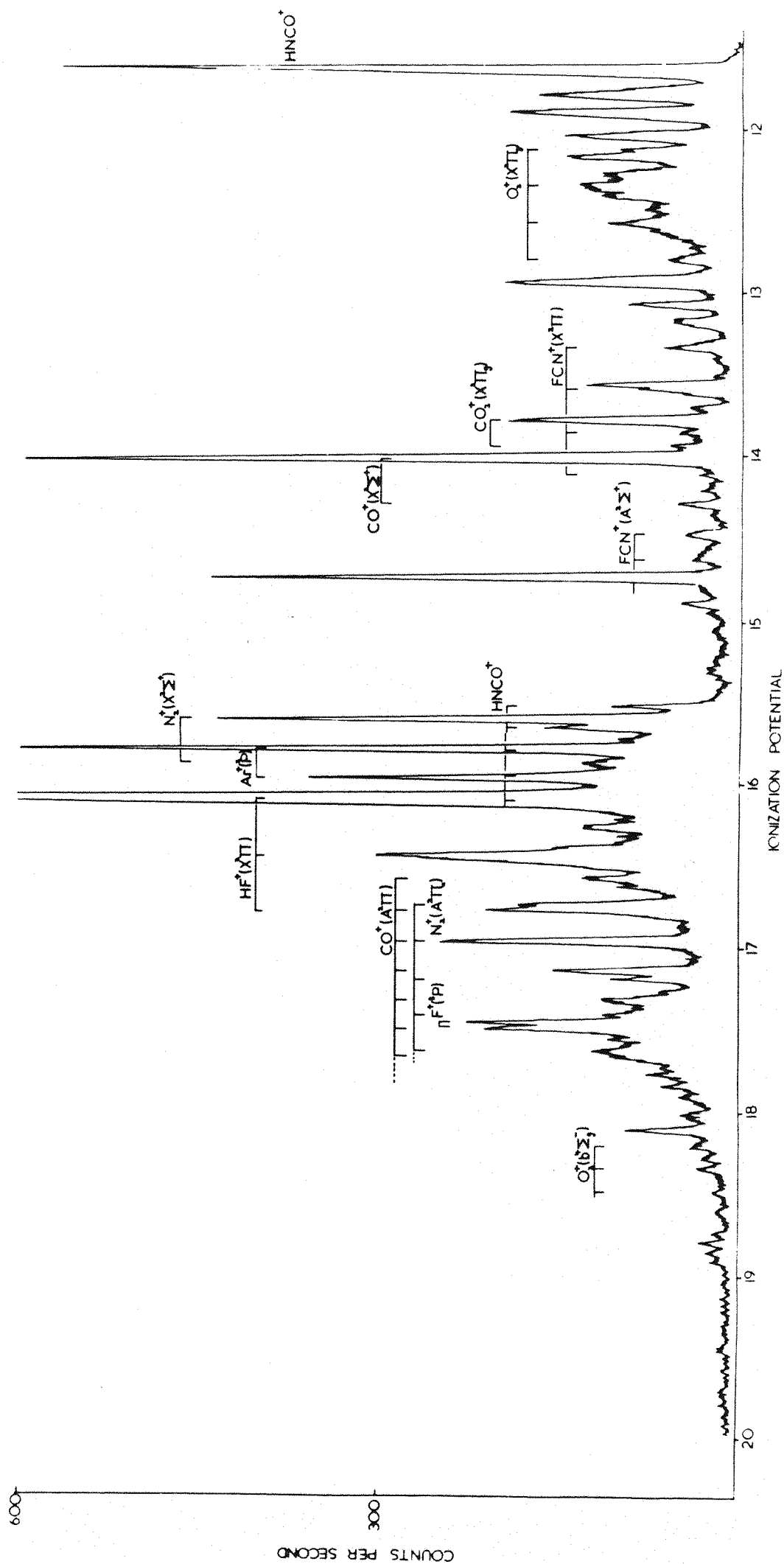


Figure 1a

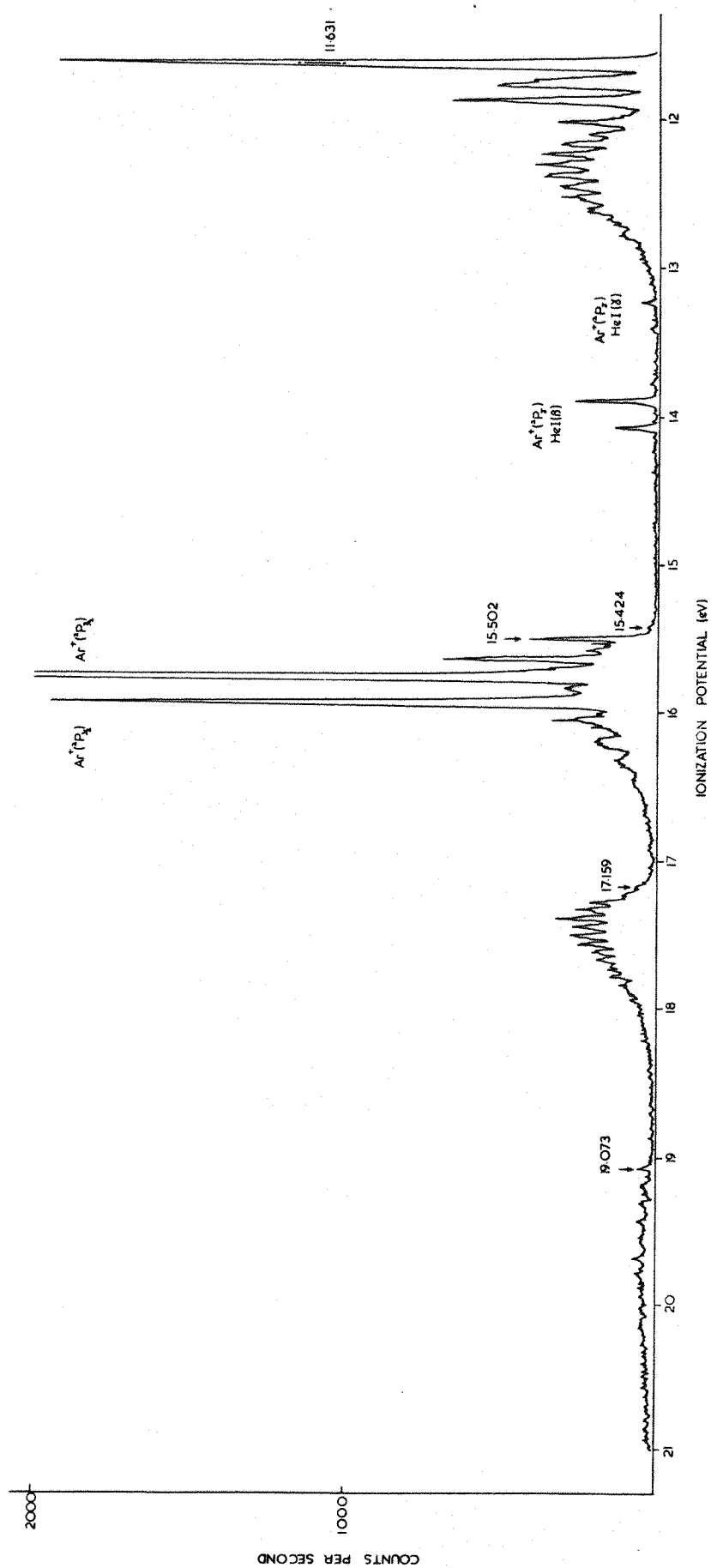


Figure 1b

obtained from the reaction of fluorine atoms with the glass inlet system. However, extra structure was seen in the 12.9-13.8 eV, 14.0-15.0 eV and 18.7-19.0 eV ionization energy regions. The most obvious new features were sharp bands at 12.92 and 14.73 eV. By varying the distance at which the reactant gases were mixed from the photon beam, it was found that these two bands decreased markedly in intensity at large mixing distances (>7 cm from the photon beam) with a corresponding increase in the bands associated with CO₂, N₂ and CO. Also observed at larger mixing distances were bands attributable to FCN [19]. It was also found that the relative intensities of the bands at 12.92 and 14.73 eV remained constant over a wide range of experimental conditions, and on this basis the bands were assigned to ionization of the same short-lived molecule. An expanded view of the 12.8 to 14.5 eV ionization energy region is shown in Figure 2. Clearly, for the sharp band at 12.92 eV the adiabatic and vertical ionization potentials are coincident and the band envelope is consistent with ionization from a non-bonding orbital, as expected for the band associated with the first ionization potential of NCO. Vibrational structure associated with this band has been analysed to give $\nu_1 = 1130 \pm 30 \text{ cm}^{-1}$ and $\nu_3 = 1890 \pm 50 \text{ cm}^{-1}$ (Figure 2). These values are slightly lower than the known values of $\nu_1 = 1275 \text{ cm}^{-1}$ and $\nu_3 = 1922 \text{ cm}^{-1}$ [3,4] in NCO($X^2\pi$). A slight reduction in the vibrational frequencies ν_1 and ν_3 on ionization is also observed in the first bands of the HeI photoelectron spectra of N₂O and CO₂ [12,13] and is supporting evidence for the possible assignment of the band at 12.92 eV to ionization of NCO. However, the $(2\pi)^{-1}$ NCO ionization leads to three possible ionic states (see Table 1) and if the band at 12.92 eV is assigned to the ionization $\text{NCO}^+(X^3\Sigma^-) \leftarrow \text{NCO}(X^2\pi)$ then bands associated with $\text{NCO}^+(^1\Delta)$ and $\text{NCO}^+(^1\Sigma^+)$ should also be observed. Figure 2 also shows a sharp band at 13.56 eV whose experimental intensity was found to be proportional to that of the first band. Although this band was overlapped by a very small contribution arising from the first band of oxygen atoms, the relative intensity of the adiabatic vibrational component of the first band relative to the band at 13.56 eV has been measured as $(3.4 \pm 0.3 : 2)$ (after correcting for the transmission function of the analyser), in good agreement with the expected 3:2 intensity ratio

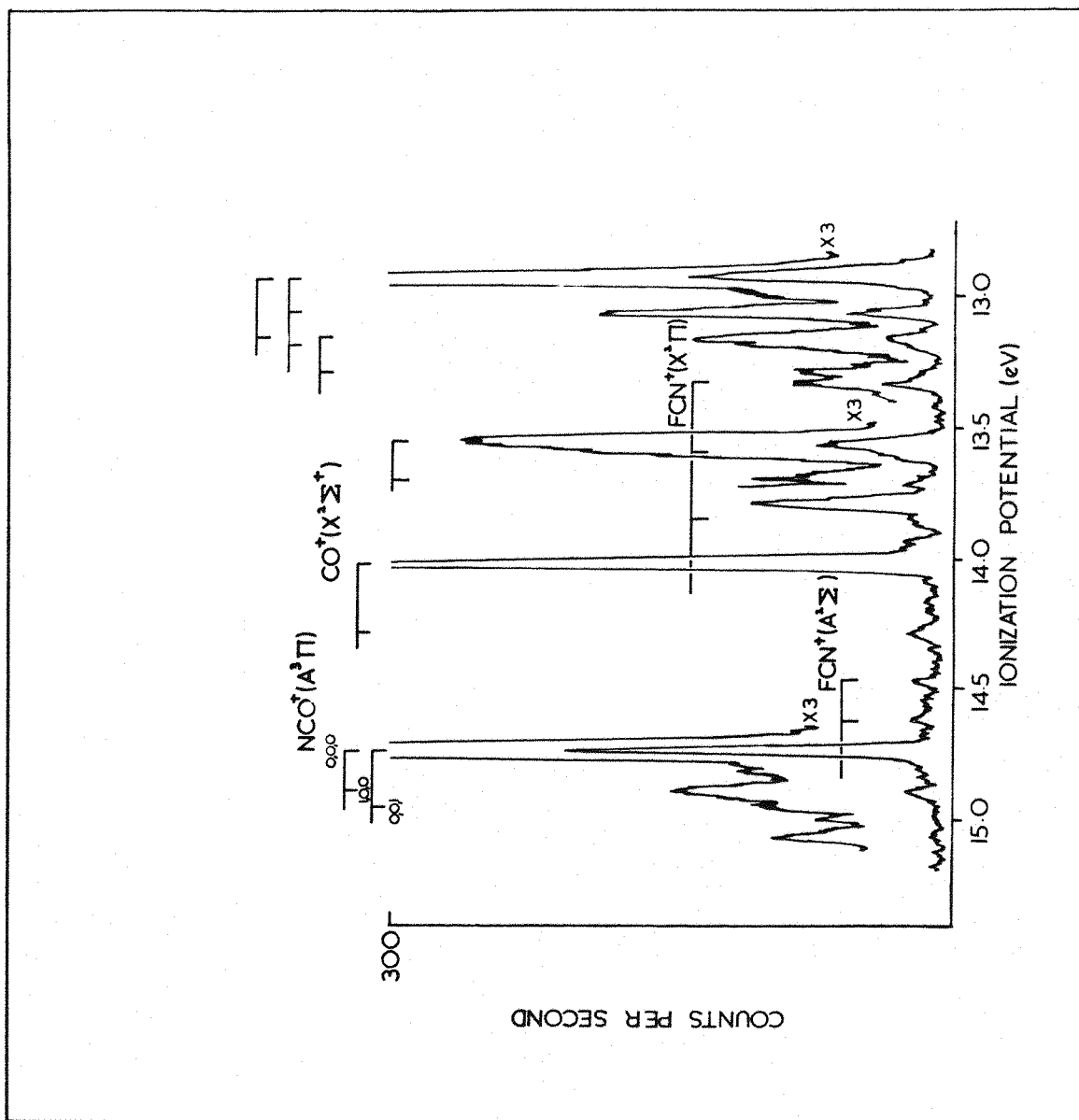


Figure 2

for the first two bands of NCO. One weak vibrational component was resolved associated with the second band, separated from the adiabatic component by $(1150 \pm 40) \text{ cm}^{-1}$. This is in agreement with the corresponding value observed in the first band and is assigned to excitation of the symmetric stretching vibration in the ionic state.

The ionization energy region above 13.5 eV gave no obvious evidence of a band associated with ionization to the $\text{NCO}^+(\text{}^1\Sigma^+)$ state arising from the $(2\pi)^{-1}$ ionization. Such a band would be half the intensity of the band at 13.56 eV, with a similar band envelope, at slightly higher ionization potential.

The lack of evidence for the expected third band arising from the first ionization of NCO as well as the large disparity between the notional first ionizational potential (12.92 eV) and the ΔSCF calculated value, and the value obtained from the appearance potential [5], led to further investigation of the ionization energy region 10 eV - 12 eV. However, no band with a similar envelope to the band at 12.92 eV ionization energy could be resolved; the sharp structure and the gain in intensity for this band (relative to the band at 12.92 eV) would have made identification relatively trivial. No peaks remained unassigned in the region up to 12.92 eV, that were more intense than the peak at 12.92 eV. In the light of the absent third component of an ionization from $\text{NCO}(\text{X}^2\pi)$, $2\pi^{-1}$, the assignment of the peaks at 12.92 eV and 13.56 eV to ionization of $\text{NCO}(\text{X}^2\pi)$ can not be made with certainty.

Further investigation of the extra structure observed in the spectrum of the product mixture revealed that additional broad band contributions are present in the regions 11.0 to 13.0 eV and 15.0 to 18.0 eV ionization energy regions.

Inspection of the 15.0-18.0 eV ionization energy region (Figure 3) revealed a broad band extending from 15.8 to 17.0 eV. After allowing for other contributions in this region from HF, HNC, CO and N_2 , the intensity of this broad feature was found to be approximately proportional to the bands at 12.92 eV and 14.73 eV. The vertical ionization potential of this band is placed at $(15.90 \pm 0.10) \text{ eV}$.

Inspection of the 11.0 to 13.0 eV region revealed a weak structured band with adiabatic ionization potential at 11.77 eV. This band was

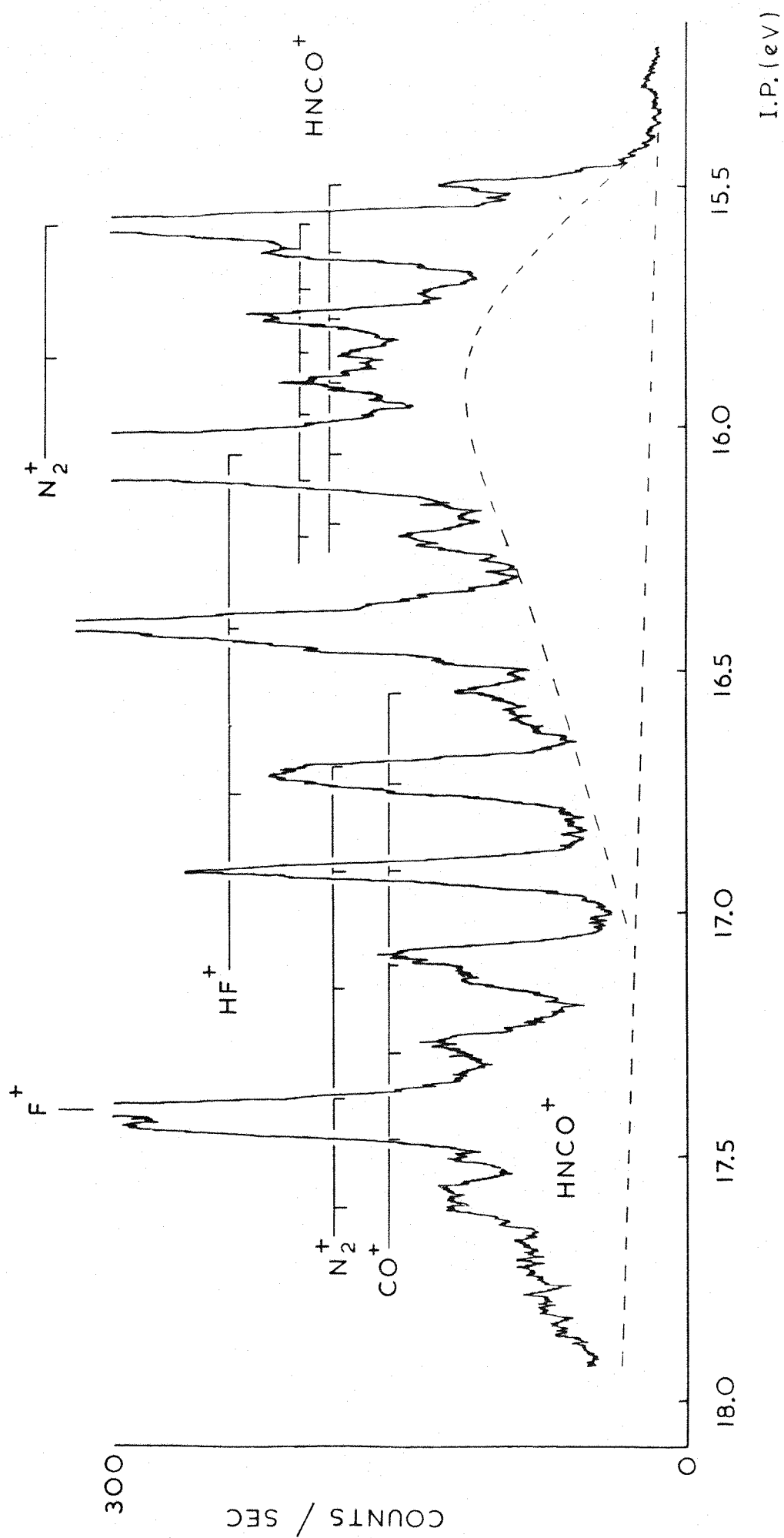


Figure 3

strongly overlapped by contributions from HNC and $O_2(X^3\Sigma_g^-)$ and $O_2(a^1\Delta)$ (Figure 4). The band could only be observed under conditions when there was little or no HNC remaining in the product mixture. Studies with variations in the mixing distance and with initial reagent partial pressures revealed that the intensity of this band was proportional to the intensity of the band at 12.92 eV, and hence arises from ionization of the same species.

The photoelectron spectrum of the products of reaction V-1-1 in the ionization energy range 18.0-21.0 eV is shown in Figure 5. Bands attributable to CO_2 , CO, N_2 , HF and F atoms could be readily identified in this spectrum. A weak band at an apparent ionization energy of 19.17 eV was attributed to autoionization of oxygen atoms in the ionization chamber arising from a small oxygen impurity in the HeI photon source [20]. Another weak band was also observed at 18.57 eV which, although found to be a product of reaction V-1-1, could not be assigned to any known species. However, by varying the mixing distance of the reactants above the photon beam and the partial pressures of the reactants this band was shown to be independent of the other bands at lower ionization energy. In fact, only three bands, at 18.69, 18.82 and 18.86 eV were found to vary linearly with the bands at lower ionization potential.

The identification of the short lived species that gives rise to all the additional features observed in the product mixture spectrum that are unassigned is still uncertain. It can, however, be concluded that the species is not NCO. Comparison with recent results obtained for N_3 give the first VIP of 11.06 ± 0.01 eV [21]. Therefore it would be expected that the first VIP of NCO, which is isoelectronic to N_3 , would have a lower IP than the derived value from the appearance potential, of 11.76 ± 0.15 eV [5]. Also it can be concluded that the observed band at 11.77 eV, with vibrational separations of 990 ± 30 cm^{-1} , is not the first IP of NCO. The observed band is weak and broad compared with the second band at 12.92 eV, and does not maintain the expected 3:2 intensity ratio or band envelope for ionization to states derived from the $\pi^4\pi^2$ configuration (i.e. $NCO(X^2\Pi)(2\Pi)^{-1} \rightarrow NCO^+(^3\Sigma^-, ^1\Delta, ^1\Sigma^+)$).

The multitude of species recognized in the product mixture, illustrated by the occurrence of FCN and NO as well as the observation

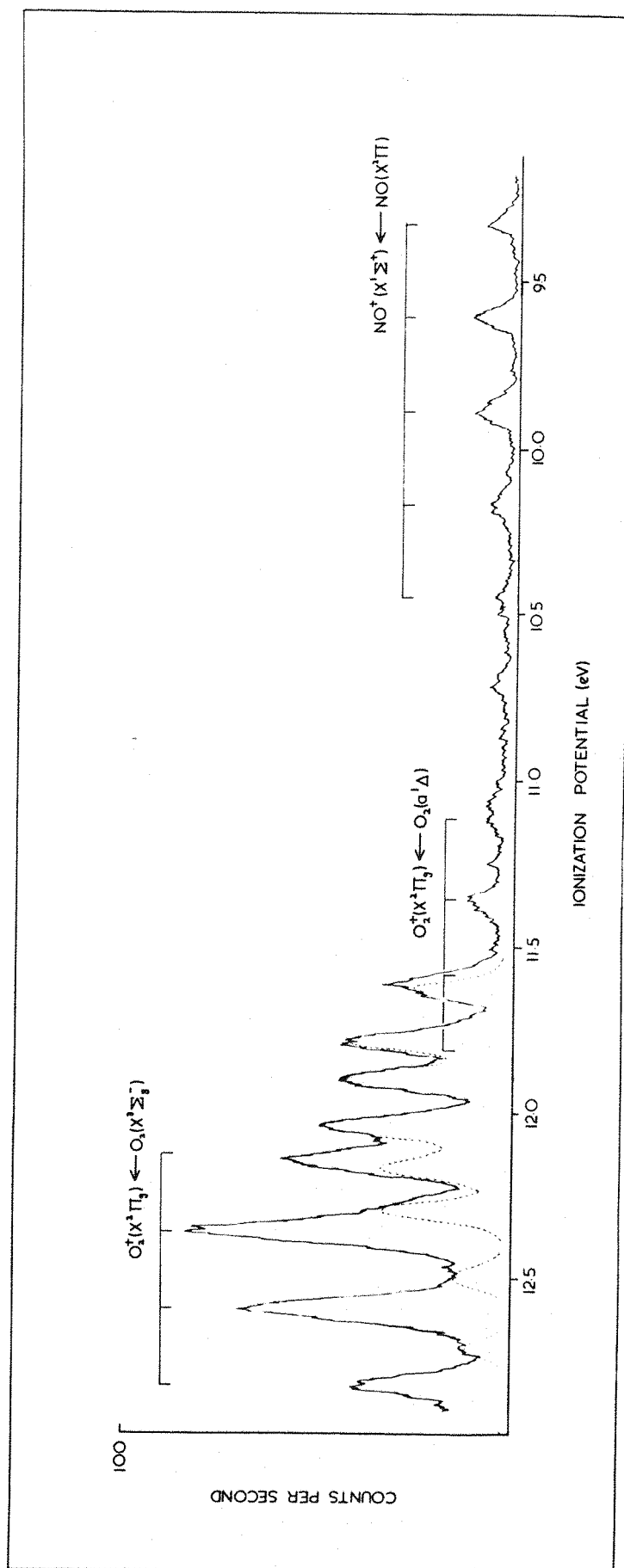


Figure 4



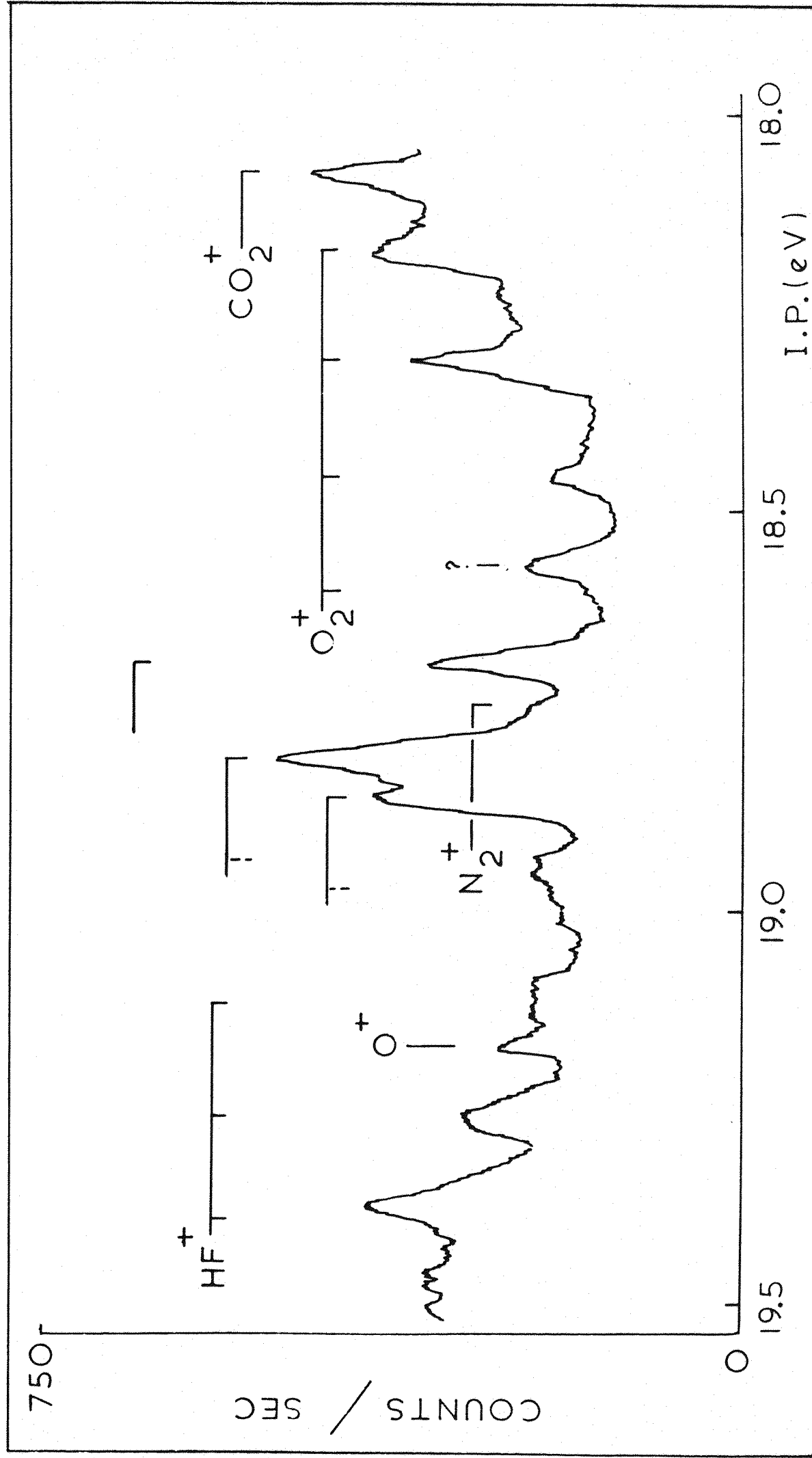


Figure 5

of the characteristic CN blue glow discharge from the region of reagent mixing, suggests that the reaction V-1-1 is highly complex. Slone et al [22] have studied the reaction by observing infrared emission from the vibrationally excited HF molecules produced via:



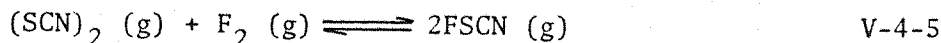
and suggest that the following series of reactions are occurring:



They conclude that the observed HF infrared emission is consistent with a long-lived HNF_2 intermediate for reaction V-4-3. The occurrence of FCN (as observed in the pes experiments) suggests considerable rearrangement of the basic HNCO geometry, and clearly does not arise directly but must occur either after, or in parallel to, the breaking of a C-O bond. The exact mechanism for the formation of FCN is not well understood, however estimates can be made of the heat of reaction of:

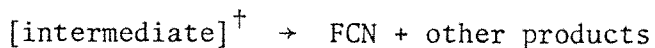


as $+(51.8 \pm 34.3) \text{ kJ mole}^{-1}$ indicating that V-4-4 is the likely origin of FCN. The observation of FCN at longer mixing distances suggests that it is not the primary radical terminator for the NCO/F system. This suggests that a closed shell short lived molecule could be the primary product of secondary reactions. This view is supported by results published on a study of the reaction:



where FCN was also seen in the Photoelectron Spectrum of the products of reaction V-4-5 [23]. Jonkers et al did not suggest a mechanism for the production of FCN in the related system NCS/F. Hence reaction V-4-4 could be written:





V-4-7

The nature of the intermediate proposed is uncertain, but the unassigned spectrum recorded could arise from such a species, since it is seen in addition to FCN.

Comparison of the recorded spectrum with those of XNCO [24], where X = Cl, Br and I shows little similarity. This would suggest that any NCO fragment of the intermediate is not bonded through the nitrogen.

Comparison of the recorded spectrum with the recently published PES of FSCN shows several elements of similarity.

Firstly the first ionization shows considerable structure in the S-F stretching mode ($840 \pm 50 \text{ cm}^{-1}$). This compares with the recorded band at 11.77 eV, showing a vibrational series of 990 cm^{-1} . Secondly there is a group of three sharp bands in the IP range 13.5-13.9 eV for FSCN. This would correspond to the observed bands at 12.92, 13.56 and 14.73.

Hence the spectrum can be tentatively assigned to the species FOCN. This species is at present uncharacterized by any technique but an approximate value for the O-F stretching frequency can be obtained by comparison with the related FOX molecule OF_2 . From the published data ν_1 in OF_2 [25] is 928 cm^{-1} and in $\text{OF}_2^+ (^2\text{B}_1)$ [26] is $1032 \pm 40 \text{ cm}^{-1}$ and the first VIP is 13.36 eV [26]. This compares favourably with the structure, position and separation of the recorded band at 11.77 eV. The shift in first ionization potential can be explained by the substitution of an F atom in OF_2 with the pseudo-halogen group CN in FOCN, as reflected by the reduced electronegativity of the CN group.

The tentative assignment of the recorded spectrum to the species FOCN is supported by general considerations of related molecules. Work is at present being conducted [27] to support the assignment with the aid of molecular orbital calculations and further experimental measurements.

Chapter V

References

1. (a) Dixon, R N, Can J Phys, 38, 10, (1960).
(b) Dixon, R N, Phil Trans Roy Soc, A252, 165, (1960).
2. Carrington, A, Fabris, A R, Howard, B J, and Lucas, N J D, Molec Phys, 20, 961, (1971).
3. Milligan, D E, and Jacox, M E, J Chem Phys, 47, 5157, (1967).
4. Bondybey, V E, and English, J H, J Chem Phys, 67, 2868, (1977).
5. (a) Rowland, C G, Eland, J H D, and Danby, C, J Chem Soc Chem Commun, 1535, (1968).
(b) Bogan, D J, and Hand, C W, J Phys Chem, 75, 1532, (1971).
6. Okabe, H, J Chem Phys, 53, 3507, (1970).
7. Cradock, S, Ebsworth, E A V, and Murdoch, J D, JCS Faraday II, 86, (1972).
8. Eland, J H D, Phil Trans Roy Soc, A268, 87, (1970).
9. Dyke, J M, Jonathan, N, and Morris, A, Electron Spectroscopy: Theory, Techniques and Applications, 1979, Volume 3, 189, (Academic Press, London).
10. Thomson, C, and Wishart, B J, Theor Chim Acta, 35, 261, (1974).
11. Walsh, A D, J Chem Soc, 2266, (1953).
12. Brundle, C R, and Turner, D W, Int J Mass Spec Ion Phys, 2, 195, (1969).
13. Eland, J H D, and Danby, C J, Int J Mass Spec Ion Phys, 1, 111, (1968).
14. Saunders, V R, and Guest, M F, ATMOL 3 Reference Manuals, Atlas Computing Division, Rutherford Laboratory, 1976.
15. Huzinaga, S, J Chem Phys, 42, 1293, (1965).
16. (a) Dunning, T H, J Chem Phys, 53, 2823, (1970).
(b) Dunning, T H, and Hay, P J, Modern Theoretical Chemistry, Volume 3, Applications of Electronic Structure Theory, Editor: Schaefer, H F, (Plenum Press).

17. Cade, P E, and Huo, W M, J Chem Phys, 47, 614, (1967).
18. Stewart, R F, J Chem Phys, 52, 431, (1970).
19. Bieri, G, Chem Phys Letts, 46, 107, (1977).
20. de Leeuw, D M, and de Lange, C A, Chem Phys, 54, 123, (1980).
21. Dyke, J M, Jonathan, N, Lewis, A E, and Morris, A, unpublished data.
22. Sloan, J J, Watson, D G, and Wright, J S, Chem Phys, to be published.
23. Jonkers, G, Grabandt, O, Mooyman, R, and de Lange, C A, J Elec Spec and Rel Phen, to be published.
24. Frost, D C, Macdonald, C B, Mcdowell, C A, and Westwood, N P C, Chem Phys, 47, 111, (1980).
25. Brundle, C R, Robin, M B, Kuebler, N A, and Bosch, H, J Amer Chem Soc, 94, 1451, (1972).
26. (a) Cornford, A B, Frost, D C, Herring, F G, and Mcdowell, C A, J Chem Phys, 55, 2820, (1971).
(b) Niessen, W Von, J Elec Spec and Rel Phen, 17, 197, (1979).
27. Lewis, A E, Private Communication.

Chapter VI

Theoretical Study of the Complete HeI
Photoelectron Spectrum of
Hydrogen Fluoride

Contents

- VI-1 Introduction
- VI-2 Computational Details
- VI-3 Results and Discussion
- VI-4 Conclusion

VI-1 Introduction

The hydrogen fluoride molecule (HF) has been the subject of a great many theoretical studies. Most of these studies have dealt with the evaluation of ab initio SCF total energies and dipole moment for $\text{HF}(X^1\Sigma^+)$, but also numerous papers have been published which treat HF within the framework of alternative theoretical approaches. A full bibliography of papers will not be given here but is available in references [1-3].

This study has been undertaken with the aim of calculating potential curves, and evaluating spectroscopic constants, for $\text{HF}(X^1\Sigma^+)$ and the two ionic states accessible to HeI radiation. The two ionic states, formed by one electron ionization of HF are, $\text{HF}^+(X^2\Pi_1)$ and $\text{HF}^+(A^2\Sigma^+)$. The evaluated spectroscopic constants are then used to calculate Frank Condon Factors (FCF's) between the neutral and ionic vibrational state energy levels. This data is then used, along with relative population distribution data for the neutral vibrational levels to compute photoelectron band envelopes for the two ionization processes. The ultimate aim is to predict the HeI photoelectron band envelopes using the $\text{HF}(X^1\Sigma^+)$ Boltzmannized room temperature distribution. In addition both the initial and intermediate non Boltzmann vibrational distributions, obtained via measured relaxation infrared chemiluminescence, for the $\text{F} + \text{H}_2$ and $\text{H} + \text{F}_2$ reactions will be used. These predictions would then be useful in analysing band envelopes of vibrationally excited HF, when they are observed by PES.

It is necessary that the theoretical model chosen should have an accuracy within the experimental accuracy of the PES experiment. The method chosen, because of its availability and generality, is the HFR-SCF method with correlation energy effects being accounted for through CI (these methods are explained in Chapter IIa).

Previous HFR-SCF calculations, performed at the Hartree-Fock limit, have been published by Cade and Huo [4] and Clementi [5]. Both papers used a Slater type orbital basis set with optimisation of orbital exponents. Potential energy curves have also been computed for $\text{HF}(X^1\Sigma^+)$. No optimised basis set has been published for the ionic states,

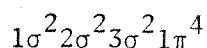
but SCF potential curves have been evaluated using a number of basis sets, using optimised atom exponents [5-8]. Beyond the Hartree-Fock limit, HF and its ion states have received much attention. Correlation energy contributions have been evaluated by several approaches including:

- (1) Many Body Perturbation Theory (MBPT) calculations on $\text{HF}(\text{X}^1\Sigma^+)$ at the experimental bond length [9-14] and a series of internuclear separations [15].
- (2) Pair Natural Orbital Configuration Interaction (PNO-CI) and Coupled Electron Pair Approach (CEPA) pair theories have been applied to $\text{HF}(\text{X}^1\Sigma^+)$ at the experimental geometry [16]. Also potential curves and spectroscopic constants have been computed for both the ground state $\text{HF}(\text{X}^1\Sigma^+)$ [17] and the ground ionic state $\text{HF}^+(\text{X}^2\Pi)$ [18].
- (3) Multiconfiguration SCF (MC-SCF) calculations have been performed on $\text{HF}(\text{X}^1\Sigma^+)$ at the experimental bond length [19] and for a series of internuclear separations [20-22].
- (4) Ab initio SCF-Configuration Interaction Studies (SCF-CI) have been performed at the experimental bond length [23] of $\text{HF}(\text{X}^1\Sigma^+)$. Potential energy curves of $\text{HF}(\text{X}^1\Sigma^+)$ [2,25] and $\text{HF}^+(\text{X}^2\Pi)$ [25] have been computed with this approach.

The study presented here is also of the ab initio SCF-CI type. However, it differs from previous studies of this type in that $\text{HF}^+(\text{A}^2\Sigma^+)$ is included in the investigation. Also it has the general aim of treating $\text{HF}(\text{X}^1\Sigma^+)$, $\text{HF}^+(\text{X}^2\Pi)$ and $\text{HF}^+(\text{A}^2\Sigma^+)$ to the same degree of sophistication within the ab initio SCF-CI method.

VI-2 Computational Details

The electronic configuration of $\text{HF}(\text{X}^1\Sigma^+)$ can be written as:



The 1π and 3σ levels are accessible to HeI radiation and are characterised as fluorine non bonding and sigma bonding orbitals respectively.

The $(1\pi)^{-1}$ ionization gives the $\text{HF}^+(\text{X}^2\Pi)$ state whereas the $(3\sigma)^{-1}$ ionization gives the $\text{HF}^+(\text{A}^2\Sigma^+)$ state (see Figure 1).

This study consists of four distinct computational stages, the SCF step, the CI step, the potential curve analysis and the FCF calculations. These stages will be discussed in turn.

SCF Step: SCF calculations were carried out on each of the states under consideration to find stationary energies for the configurations in Figure 1, for a series of fixed internuclear distances. Calculations were performed using modules from the ATMOL-3 suite of programs [26] implemented on the dual IBM 360/195 facility, at SERC Rutherford Lab. The basis set used for all states was basically that of Cade and Huo [4], modified to satisfy the restrictions of the ATMOL integral evaluation program. The modified basis set used is tabulated in Table 1. Bond lengths were chosen within $\pm 0.2 \text{ \AA}$ of the known equilibrium bond length in increments of 0.05 \AA , for all the states. No attempt was made to investigate regions of the potential curves outside these limits.

CI Step: The CI expansion for each of the states were performed using the SPLICE bonded function CI program [27], implemented at Rutherford Laboratory. The orbital space in each case was a transformed set of SCF molecular orbitals, but with the 1σ molecular orbital (essentially fluorine $1s$ in character) kept doubly occupied, and the 4 highest virtual orbitals excluded from consideration. The configuration space treated consisted of all single and double excitation species generated from a single root function comprising the SCF configuration. The initial configuration list for the ion states proved too extensive for practical computation and selection of configurations had to be utilized. Selection of configurations was achieved by a perturbative procedure (as outlined in Chapter 2) using cumulative selection for the $\text{HF}^+(\text{X}^2\Pi_i)$ state and a single threshold level for the $\text{HF}^+(\text{A}^2\Sigma^+)$ state. This led to 3205 bonded functions being considered for $\text{HF}(\text{X}^1\Sigma^+)$, 2500 bonded functions for $\text{HF}^+(\text{X}^2\Pi)$ and 2500 bonded functions for $\text{HF}^+(\text{A}^2\Sigma^+)$. CI energies were calculated, from the final configuration list, for each of the SCF data points for all 3 states.

Potential energy curve analysis: The computed CI energy curves for all three states were fitted to a Dunham five constant fourth order

Figure 1

Electronic configurations of HF and HF⁺

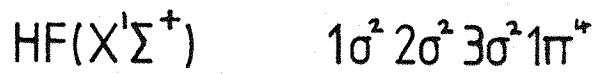


Table 1

Orbital Type	Centre	Exponent, ξ
1s	F	14.10946
1s'	F	7.94374
2s	F	1.93465
2s'	F	3.25633
3s	F	9.92540
2p	F	1.40701
2p'	F	2.37325
2p''	F	4.27843
2p'''	F	8.97251
3d	F	1.83539
3d'	F	3.36796
4d	F	2.70010
1s	H	1.37261
1s'	H	2.46048
2s	H	2.46147
2p	H	2.92262

Basis set used in all SCF calculations,
modified from reference [4].

polynomial. The resultant coefficients were used to derive values for the standard spectroscopic constants (see Chapter IIb). This procedure was achieved by use of the program VIBROT implemented at Rutherford.

Calculation of Frank Condon Factors: Frank Condon Factors (FCF's) were calculated between 10 vibrational levels of the neutral state and 10 vibrational levels in each of the ion states. These values are then used, along with initial state vibrational level relative populations, to calculate relative intensities of each vibrational component. The position of each of the vibrational components is also computed, in eV ionization energy, from the input adiabatic ionization potential, and vibrational term values between the states. These results were calculated using the program FCF (see Chapter IIb) implemented at Rutherford.

VI-3 Results and Discussion

The calculated SCF and CI energies, for each value of the bond length, are given in Tables 2-4, for each state. Also the spectroscopic constants derived from the results of the Dunham analysis of the SCF and CI potential curves, are tabulated in Tables 5-7, along with previously published calculated and experimental values.

Examination of the SCF + CI data, for each state, reveals that the calculated values for ω_e , $\omega_e x_e$, r_e , α_e and B_e are in good agreement with the experimental values. The total energies calculated are consistently higher than the experimental values, showing that the CI treatment has not recovered all the correlation energy. For the neutral $\text{HF}(X^1\Sigma^+)$ and ground ionic state $\text{HF}^+(X^2\Pi)$ more accurate results have been obtained by Rosmus and Meyer [17,18] using PNO-CI and CEPA methods. It should be noted however that pair methods are not variational calculations and do not give an upper bound energy, as does the CI calculation. Estimates of the proportion of the total correlation energy recovered by the CI calculations are not possible because Hartree Fock SCF energies have not been evaluated for the ion states. However, for the neutral 59% of the total correlation energy has been recovered. This is restricted by the quality of the AO basis set used and the

Table 2

R	E(SCF)	-V/T	E(Pair) ^(b)	E(CI) ^(c)
1.6328	-100.0665754	1.99907	-0.24090	-100.307464
1.6828	-100.0680338	1.999737	-0.24184	-100.309858
1.7328	-100.0675980	2.00033	-0.24728	-100.310367
1.7828	-100.0656003	2.00085	-0.24374	-100.309328
1.8328	-100.0623186	2.00131	-0.24471	-100.307015

Energy vs Bond Length Data for $\text{HF}(X^1\Sigma^+)$ ^(a)

(a) All figures in atomic units.

(b) Pair energy calculated from a full configuration space of single and double replacement functions.

(c) $E(\text{CI}) = E(\text{SCF}) + E(\text{Pair})$.

Table 3

R	E(SCF)	-V/T	E(Pair) ^(b)	E(CI) ^(c)
1.7828	-99.53691314	1.99931	-0.19146	-99.7283741
1.8328	-99.53778021	1.99937	-0.19217	-99.7299408
1.8828	-99.53757955	2.00010	-0.19270	-99.7302808
1.9328	-99.53650970	2.00042	-0.19328	-99.7297843
1.9828	-99.53473196	1.99932	-0.19385	-99.7285794

Energy vs Bond Length Data for $\text{HF}^+(X^2\Pi)$ ^(a)

(a) All figures in atomic units.

(b) Pair energy calculated from a selected set of 2500 configurations.

(c) $E(\text{CI}) = E(\text{Pair}) + E(\text{SCF})$.

Table 4

R	E(SCF)	-V/T	E(Pair) ^(b)	E(CI) ^(c)
2.0828	-99.4157705	2.00070	-0.192180	-99.6079448
2.1328	-99.4169448	2.00053	-0.192198	-99.6091304
2.1828	-99.4177359	2.00038	-0.192205	-99.6099354
2.2328	-99.4182096	2.00025	-0.192204	-99.6104083
2.2828	-99.4184224	2.00014	-0.192192	-99.6106092
2.3328	-99.4184224	2.00004	-0.192171	-99.6105881
2.3828	-99.4182506	1.99996	-0.192145	-99.6103905
2.4328	-99.4179418	1.99990	-0.192111	-99.6100485
2.4828	-99.4175267	1.99984	-0.192067	-99.6095872

Energy vs Bond Length Data for $\text{HF}^+(\text{A}^2\Sigma^+)$ (a)

(a) All figures in atomic units.

(b) Pair energy calculated from a selected set of configurations consisting of an average 2500 configurations.

(c) $E(\text{CI}) = E(\text{SCF}) + E(\text{Pair})$.

truncated configuration space considered, where no excitations higher than double replacements were constructed.

It should be noted that the dissociation energies listed in Tables 5-7 for the SCF + CI data have been derived from the energy difference between the potential minimum energy and the total energy of the dissociated products, i.e.

$$D_e = E(r = \infty) - E(r = r_e) \quad \text{VI-3-1}$$

For the SCF data, energies of the dissociated atoms were evaluated using the separated atomic basis sets. This principle could not be applied to include CI because the configuration generation program of SPLICE considers orbitals with symmetry of one of the molecular point groups. In this case the energies of the atoms were taken as the experimental energies, and the energy of the dissociation products evaluated accordingly.

The discrepancy between calculated SCF + CI spectroscopic constants and the accepted experimental values are summarized in Table 8, with the absolute difference and % difference tabulated.

The differences for r_e and ω_e are all within 2% of the experimental values except for the anharmonic term ($\omega_e x_e$) and rotational constants (α_e, B_e) the discrepancy is often larger (the computed value of α_e in $\text{HF}^+(\text{X}^2\Pi)$ is obviously in error and not considered for comparison). In general these results are highly satisfactory, particularly in view of the fact that the dominant factors in determining the photoelectron FCF's are ω_e , and the change in bond length on ionization, both of which are calculated to give small differences from experimental data. Assuming a Morse potential in each state the calculated values of ω_e , $\omega_e x_e$, and r_e , for each state, were used as input to calculate FCF's between ten vibrational levels of $\text{HF}(\text{X}^1\Sigma^+)$ and ten vibrational levels of $\text{HF}^+(\text{X}^2\Pi)$. The same procedure was also adopted for the same ten levels in $\text{HF}(\text{X}^1\Sigma^+)$ and the seven lowest levels of $\text{HF}^+(\text{A}^2\Sigma^+)$. Only seven vibrational levels of $\text{HF}(\text{A}^2\Sigma^+)$ were found to be below the dissociation limit, reflecting the low dissociation energy of that state.

The FCF's calculated for the two bands, arising from $\text{HF}(\text{X}^1\Sigma^+) \rightarrow \text{HF}^+(\text{X}^2\Pi) (2\pi)^{-1}$ and $\text{HF}(\text{X}^1\Sigma^+) \rightarrow \text{HF}^+(\text{A}^2\Sigma^+) (2\sigma)^{-1}$ ionizations, are tabulated

Table 5

Source of Data & Method	Molecular Parameter					
	$E_{\min}/\text{Au}^{(a)}$	D/eV	ω_e/cm^{-1}	r_e/Au	$\omega_e x_e/\text{cm}^{-1}$	α_e/cm^{-1} B_e/cm^{-1}
This Work						
SCF	-100.06808	4.518	4464.4	1.6950	98.34	0.754 21.90
Cade & Huo [4]						
SCF	-100.07077	4.38	4469	1.696	80.34	0.7693 21.87
Lie & Clementi						
[21] MC-SCF	-100.0915 ^(c)	4.95	4128.3	1.730	97.78	0.904 21.06
Bondybey et al						
[25] SCF-CI	-100.1274	5.88	4210	1.7385	-	- 20.8
Dunning [24]						
GVB + CI(d)	-100.27436	5.72	4158	1.7387	113	0.859 20.81
Amos [22]						
MC-SCF	-100.11606	-	4102.0	1.7328	93.2	0.812 20.84
Meyer & Rosmus						
[17] PNO-CI	-100.3274 ^(c)	5.69	4251.5	1.7234	85.9	0.762 21.15
Meyer & Rosmus						
[17] CEPA	-100.3392 ^(c)	5.83	4169.3	1.7328	90.4	0.787 20.95
Wilson [15]						
MBPT(e)	-100.3727	-	4261.0	1.7158	89.97	0.788 21.35
This Work						
SCF + CI	-100.31039	6.11 ^(b)	4213.3	1.7228	87.50	0.809 21.20
Experimental						
[28]	-100.4770 ^(f)	6.395	4138.7	1.7328	90.1	0.795 20.95

Theoretical and Experimental Molecular Constants for $\text{HF}(X^1\Sigma^+)^{\dagger}$

[†] For definition of superscripts see Table 7.

Table 6

Source of Data & Method	Molecular Parameter						
	$E_{\min}/\text{Au (a)}$	D_e/eV	ω_e/cm^{-1}	$r_e/\text{Å}$	$\omega_e x_e/\text{cm}^{-1}$	α_e/cm^{-1}	B_e/cm^{-1}
This work SCF	-99.53783	3.503	3330.7	1.8472	105.12	0.939	18.44
Julienne et al [6] SCF	-	3.56 ^(b)	3492	-	95.23	0.580	17.91
Raftery & Richards [8] SCF	-	-	3453	1.8519	-	-	-
Bondybey et al [25] SCF + CI	-99.5881	3.70	3230	1.8897	-	-	17.6
Rosmus & Meyer [18] PNO-CI	-99.751423	-	3165.7	1.8841	92.1	0.859	17.7
Rosmus & Meyer [18] CEPA	-99.759145	3.45 ^(b)	3116.4	1.8935	92.0	0.864	17.54
This work SCF + CI	-99.73029	3.588 ^(b)	3074.2	1.8755	81.62	2.09	17.88
Experimental [30]	-99.94168 ^(f)	3.420	3090.5	1.8922	88.996	0.8863	17.577
Experimental [31]	as above	-	3016	1.939	75.0	-	-

Experimental and theoretical molecular constants for $\text{HF}^+ (X^2\Pi)^+$

[†] For definition of superscripts see Table 7.

Table 7

Source of Data & Method	Molecular Parameter						
	$E_{\min}/\text{Au (a)}$	D_e/eV	ω_e/cm^{-1}	r_e/Au	$\omega_e x_e/\text{cm}^{-1}$	α_e/cm^{-1}	B_e/cm^{-1}
This Work							
SCF	-99.41845	0.2553	1454.2	2.3074	139.63	1.3223	11.819
Julienne et al [6] SCF	-	0.34	1550	-	136.5	1.308	-
Raftery & Richards [8] SCF	-	-	1387	2.3054	-	-	-
This Work							
SCF + CI	-99.610624	0.333 (b)	1492.6	2.3023	96.352	1.3287	11.871
Experimental [30]	-99.82905 (f)	0.3971	1496.1	2.3140	88.423	1.0261	11.754
Experimental [31]	as above	-	1516	2.268	113	-	-

Experimental and Theoretical Molecular Constants for $\text{HF}^+ (\text{A}^2\Sigma^+)$

- (a) Energy at derived potential minimum.
- (b) Dissociation energy calculated from difference of potential minimum energy and energy of dissociation products.
- (c) Interpolated data from published values.
- (d) General Valence Bond Configuration Interaction.
- (e) Values derived using the Pade Approximation.
- (f) Non relativistic total energy (sum of atomic energies and the dissociation energy), see ref [29].

Table 8

Species	Spectroscopic Constant				
	$r_e/\text{\AA}$	ω_e/cm^{-1}	$\omega_e x_e/\text{cm}^{-1}$	α_e/cm^{-1}	B_e/cm^{-1}
$\text{HF}(X^1\Sigma^+)$	$\Delta x^{(a)}$	74.6	-2.6	1.4×10^{-2}	0.25
	$\Delta x\%^{(b)}$	1.8	-2.89	1.76	1.19
$\text{HF}^+(X^2\Pi)$	$\Delta x^{(a)}$	-16.275	7.38	-	0.31
	$\Delta x\%^{(b)}$	-0.53	8.29	-	1.76
$\text{HF}^+(A^2\Sigma^+)$	$\Delta x^{(a)}$	-3.466	7.93	0.30	0.12
	$\Delta x\%^{(b)}$	-0.23	8.97	29.5	1.0

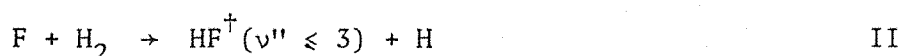
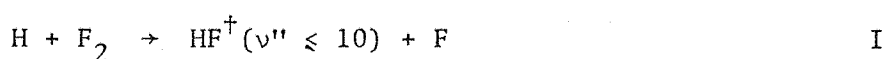
Comparison of Calculated and Experimental Spectroscopic Constants for SCF + CI Data

(a) Differences given as $x(\text{calc}) - x(\text{exptl})$.

(b) Percentages expressed as a ratio of the experimental value.

in Tables 9 and 10. The component positions are determined using published experimental adiabatic ionization potentials [30,31] and the term values derived from input spectroscopic constants. Experimental component intensities are obtained from the FCF's via the relative populations of the initial vibrational state.

In this work relative vibrational level populations for a range of vibrational temperatures, assuming a Boltzmann distribution were used. In addition initial and intermediate non-Boltzmann relative vibrational distributions produced in the reactions:



were used. Intermediate data was used to gain an insight into the experimentally detectable intensities, since the initial population distribution is an instantaneous quantity and is probably not directly observable by PES. The partition of vibrational energy between vibrational levels in HF, formed in reactions I and II, has been investigated using the method of Infra-Red Chemiluminescence [32,33]. By measured relaxation the primary rate constants ($k_{\nu'}$) for the formation of HF in vibrational state ν' can be obtained. This depends on measuring the relative intensity of IR emission from each Rotational-Vibrational transition, and knowing the corresponding Einstein A coefficients. The primary rate constants are directly proportional to the number density for the Vib-Rot state, hence initial relative population distributions can be obtained. Table 11 contains a summary of the relative vibrational level populations of neutral HF, for a range of vibrational temperatures, for the non-Boltzmann initial distributions from reactions I and II and for the intermediate case. Data for the intermediate distribution was obtained from the results of IR Chemiluminescence [32,33] studies, using intensity data after a dwell time of 0.8 milliseconds. This period was chosen because it would not be experimentally feasible under PES conditions to monitor at shorter dwell times, and 0.8 msec is significantly less than the radiative lifetime of HF, which is 2-5 msec [34].

Table 9

Computed Vibrational Component Intensities (PCF's) and Positions for $\text{HF}^+ \text{X}^2_{\pi} \leftarrow \text{HF} \text{X}^1_{\Sigma^+}$

v'/v''	0	1	2	3	4	5	6	7	8	9
0	0.69744 (16.044) [†]	0.25449 (15.5433)	0.04425 (15.0643)	0.00367 (14.6070)	0.00015 (14.1714)	0.00031 (13.7575)	0.0 (12.9948)	0.0 (12.9948)	0.0 (12.6460)	0.0 (12.3189)
1	0.23929 (16.4051)	0.26503 (15.9044)	0.36090 (15.4254)	0.11882 (14.9681)	0.01509 (14.5325)	0.12433 (14.1186)	0.00002 (13.7264)	0.00002 (13.3559)	0.0 (13.0071)	0.0 (12.6800)
2	0.05255 (16.7461)	0.30742 (16.2454)	0.04937 (15.7664)	0.34559 (15.3091)	0.20414 (14.8735)	0.03797 (14.4596)	0.00288 (14.0674)	0.00956 (13.6969)	0.0 (13.3481)	0.0 (13.0210)
3	0.00922 (17.067)	0.12698 (16.5663)	0.24967 (16.0873)	0.00004 (15.6230)	0.25310 (15.1944)	0.27817 (14.7805)	0.07464 (14.3883)	0.00736 (14.0178)	0.00021 (13.6690)	0.0 (13.3419)
4	0.00134 (17.3678)	0.03603 (16.8671)	0.18178 (16.3881)	0.13723 (15.9308)	0.04504 (15.4952)	0.13618 (15.0813)	0.32102 (14.6891)	0.12492 (14.9698)	0.01590 (13.9698)	0.00056 (13.6427)
5	0.0005 (17.6485)	0.00823 (17.1478)	0.07827 (16.6688)	0.18619 (16.2155)	0.04017 (15.7759)	0.10740 (15.3620)	0.04245 (14.9698)	0.32018 (14.5993)	0.18524 (14.2505)	0.03043 (13.9234)
6	0.00001 (17.9091)	0.00155 (17.4085)	0.02609 (16.9295)	0.11909 (16.4722)	0.13805 (16.0366)	0.00048 (15.6227)	0.13466 (15.2305)	0.00121 (14.8600)	0.27468 (14.5112)	0.2484 (14.1840)
7	0.0 (18.1497)	0.00022 (17.6490)	0.00738 (17.1700)	0.05554 (16.7127)	0.13456 (16.2771)	0.06606 (15.8632)	0.01798 (15.4710)	0.11107 (15.1005)	0.01540 (14.7517)	0.19653 (14.4246)
8	0.0 (18.3702)	0.00002 (17.8695)	0.00181 (17.3905)	0.02184 (16.9332)	0.08628 (16.4976)	0.11098 (16.0837)	0.01197 (15.6915)	0.05805 (15.3210)	0.05711 (14.9722)	0.06305 (14.6451)
9	0.0 (18.5706)	0.0 (18.0699)	0.00037 (17.5909)	0.00772 (17.1336)	0.04522 (16.6980)	0.09929 (16.2841)	0.05973 (15.8919)	0.00170 (15.5214)	0.07873 (15.1726)	0.1102 (14.8455)

[†] Fitted to the adiabatic ionization potential [31].

Table 10

Vibrational component Frank-Condon Factors and positions (in brackets) for the band $\text{HF}^+ 2_{\Sigma}^+ \leftarrow \text{HF } X^1_{\Sigma}^+$

v'/v''	0	1	2	3	4	5	6	7	8	9
0	0.02600 (19.118) [†]	0.09599 (18.617)	0.18084 (18.138)	0.22555 (17.681)	0.20528 (17.245)	0.14258 (16.832)	0.07709 (16.439)	0.03262 (16.069)	0.01074 (15.720)	0.00272 (15.393)
1	0.05741 (19.279)	0.12929 (18.779)	0.11407 (18.390)	0.03093 (17.842)	0.00344 (17.407)	0.07583 (16.993)	0.16494 (16.601)	0.18436 (16.230)	0.13492 (15.881)	0.06985 (15.554)
2	0.07472 (19.416)	0.10036 (18.916)	0.02854 (18.437)	0.00547 (17.980)	0.06812 (17.554)	0.08111 (17.130)	0.01895 (16.738)	0.00979 (16.367)	0.09761 (16.019)	0.17886 (15.691)
3	0.07496 (19.530)	0.05898 (19.029)	0.00105 (18.550)	0.03338 (18.093)	0.05682 (17.657)	0.01018 (17.243)	0.01492 (16.851)	0.07229 (16.481)	0.05593 (16.132)	0.00169 (15.805)
4	0.06338 (19.619)	0.02917 (19.119)	0.00224 (18.640)	0.03832 (18.182)	0.02258 (17.747)	0.00137 (17.333)	0.03884 (16.941)	0.03597 (16.570)	0.00023 (16.221)	0.03669 (15.894)
5	0.04574 (19.685)	0.01279 (19.184)	0.00615 (18.705)	0.02725 (18.248)	0.00553 (17.812)	0.00869 (17.398)	0.02933 (17.006)	0.00676 (16.636)	0.00906 (16.287)	0.03937 (15.960)
6	0.02575 (19.727)	0.00487 (19.226)	0.00548 (18.747)	0.01401 (18.290)	0.00087 (17.854)	0.00833 (17.440)	0.01376 (17.048)	0.00040 (16.678)	0.01121 (16.329)	0.01786 (16.002)
7	Dissociation limit									
8										
9										

[†] Fitted to the adiabatic ionization potential [30].

Table 11

Vibrational level	$T_{\text{vib}} = 300\text{K}$	$T_{\text{vib}} = 1000\text{K}$	$T_{\text{vib}} = 5000\text{K}$	$T_{\text{vib}} = 10,000\text{K}$	Reaction I, Initial	Reaction II, Initial(a)	Reaction I Intermediate(b)	Reaction I Intermediate(a)	Reaction II Intermediate(b)
0	1.0	0.997	0.679	0.424	0.016 [†]	0.046 [†]	0.092 [†]		0.217 [†]
1		0.003	0.212	0.237	0.026	0.136	0.069		0.287
2			0.070	0.136	0.032	0.464	0.051		0.361
3			0.024	0.080	0.038	0.353	0.076		0.136
4			0.009	0.048	0.131	0.0	0.184		
5			0.003	0.030	0.259		0.23		
6			0.001	0.019	0.291		0.20		
7				0.012	0.131		0.074		
8				0.008	0.058		0.023		
9				0.006	0.016 [†]		0.0 [†]		

Relative population distribution of the vibrational levels of $\text{HF}(X^1\Sigma^+)$ used for the calculation of experimental component intensities.

[†] Interpolated Data.

(a) From reference [32].

(b) From reference [33].

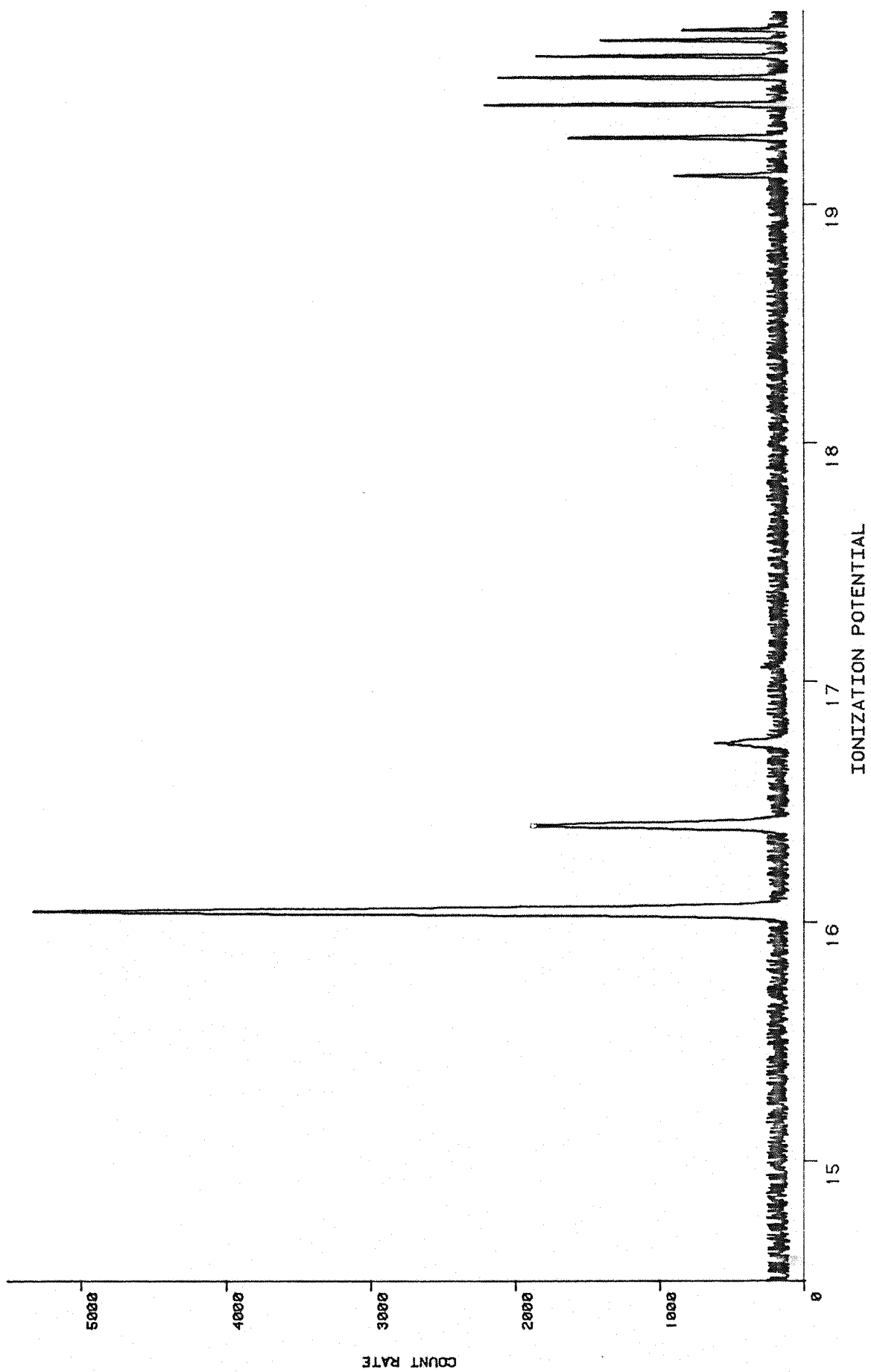


Figure 2

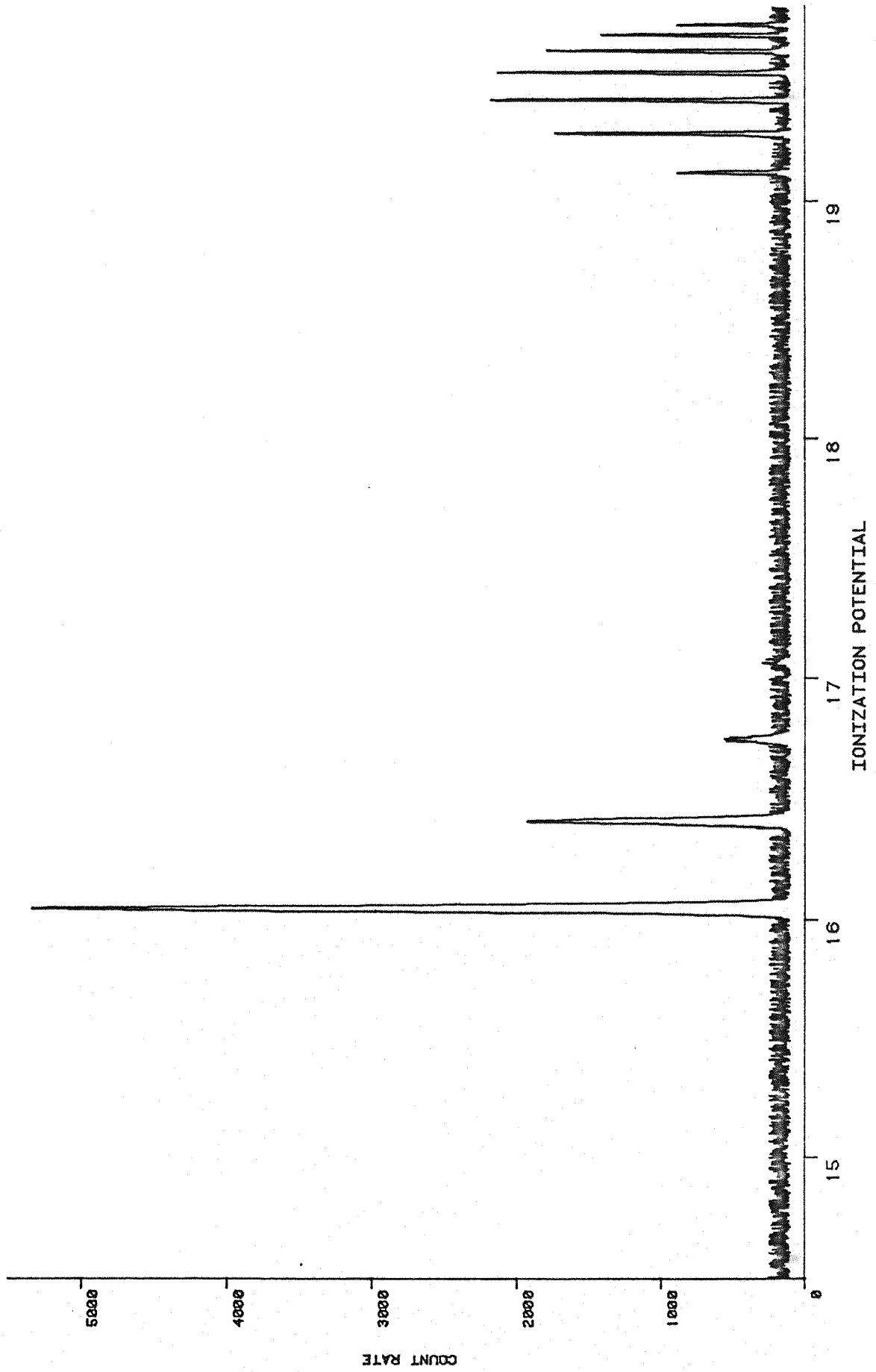


Figure 3

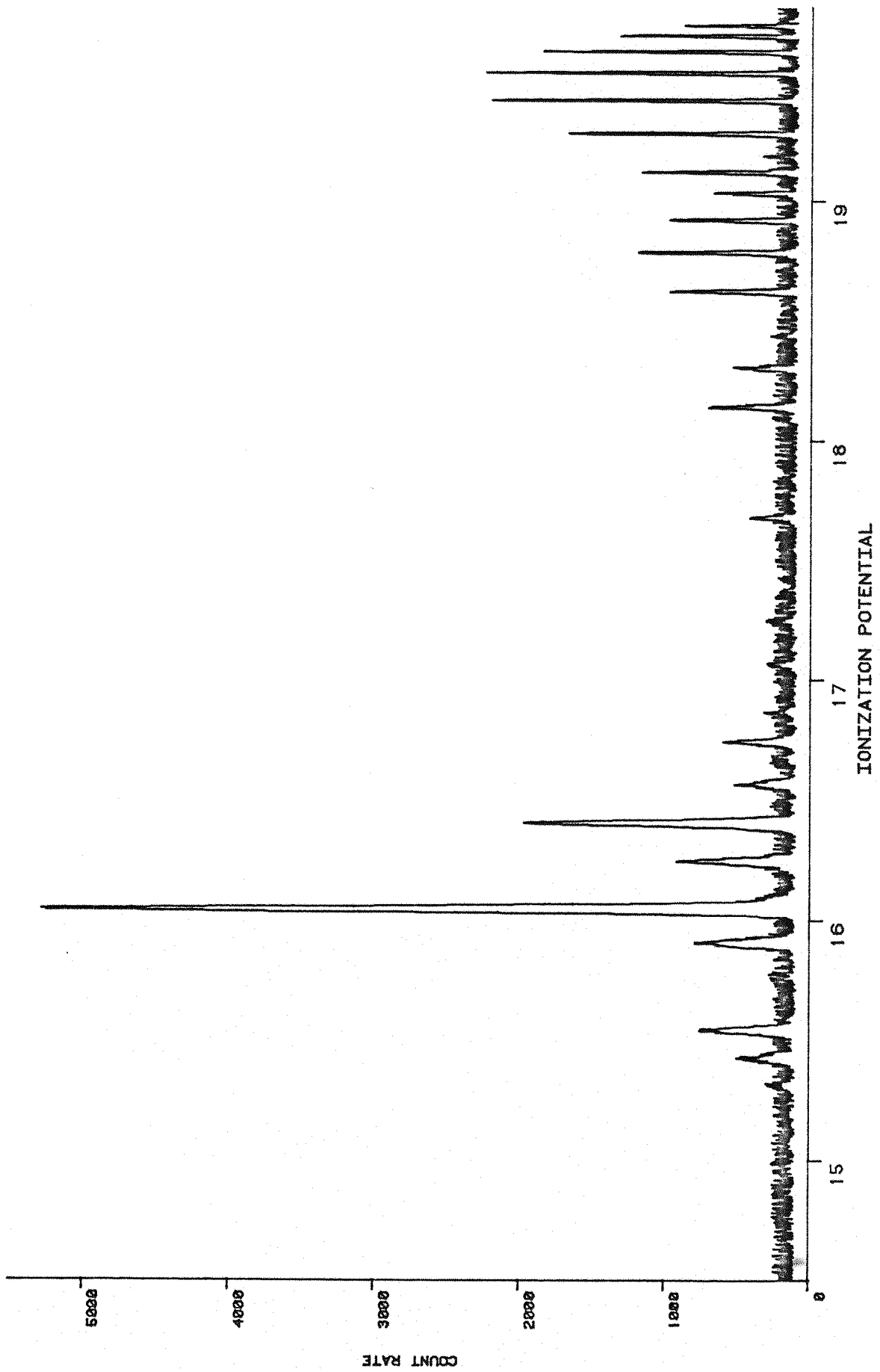


Figure 4

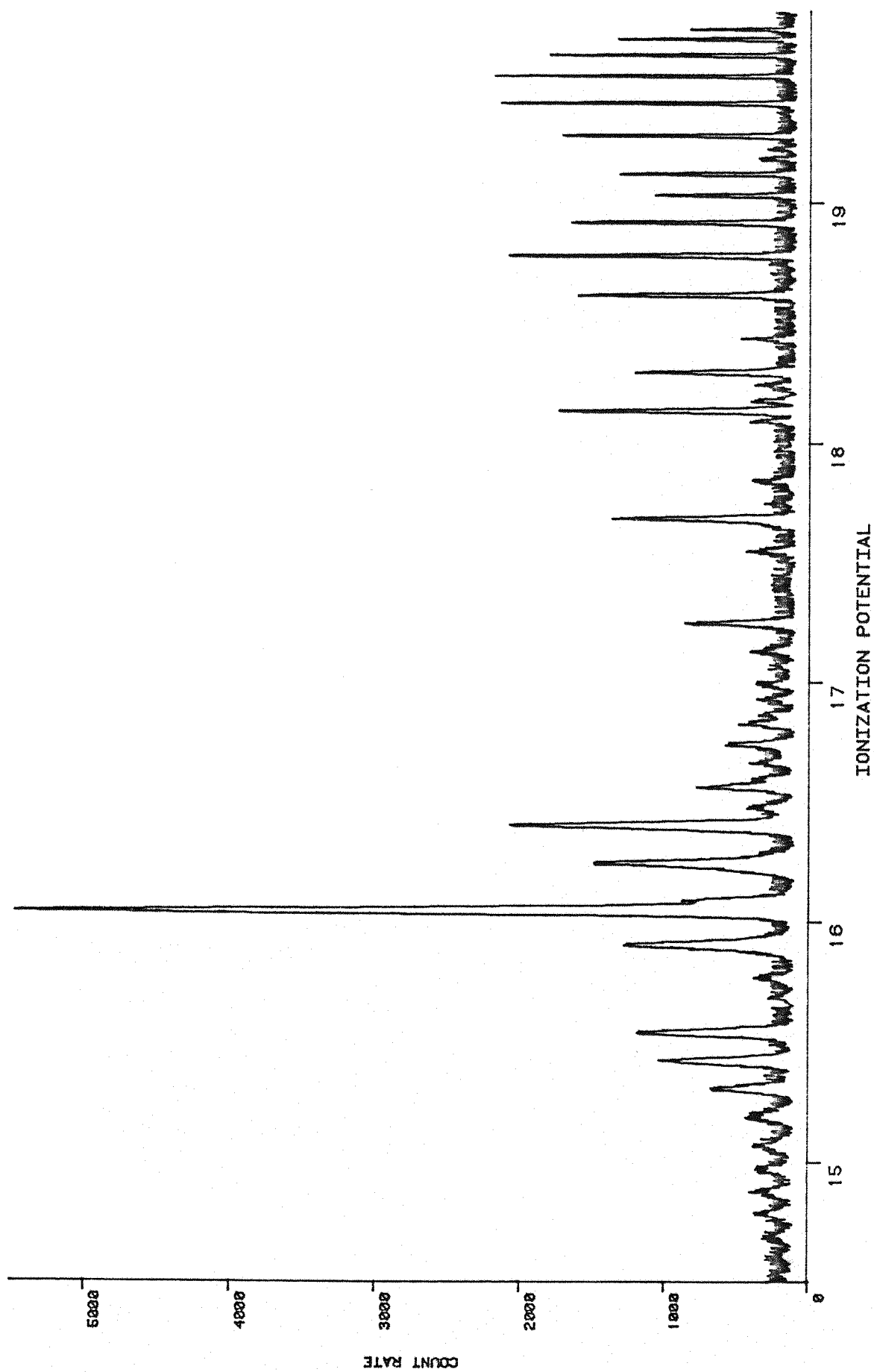


Figure 5

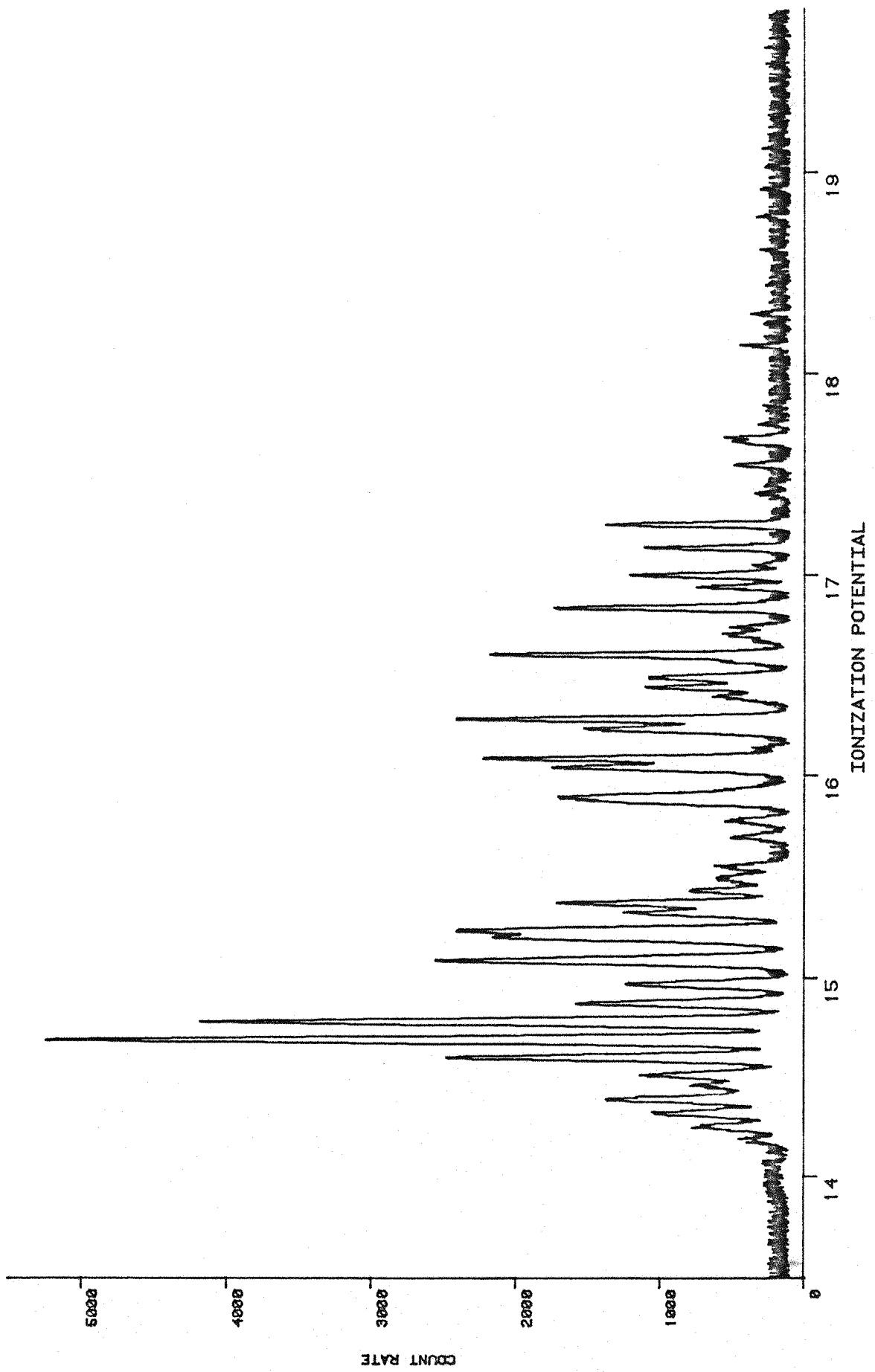


Figure 6

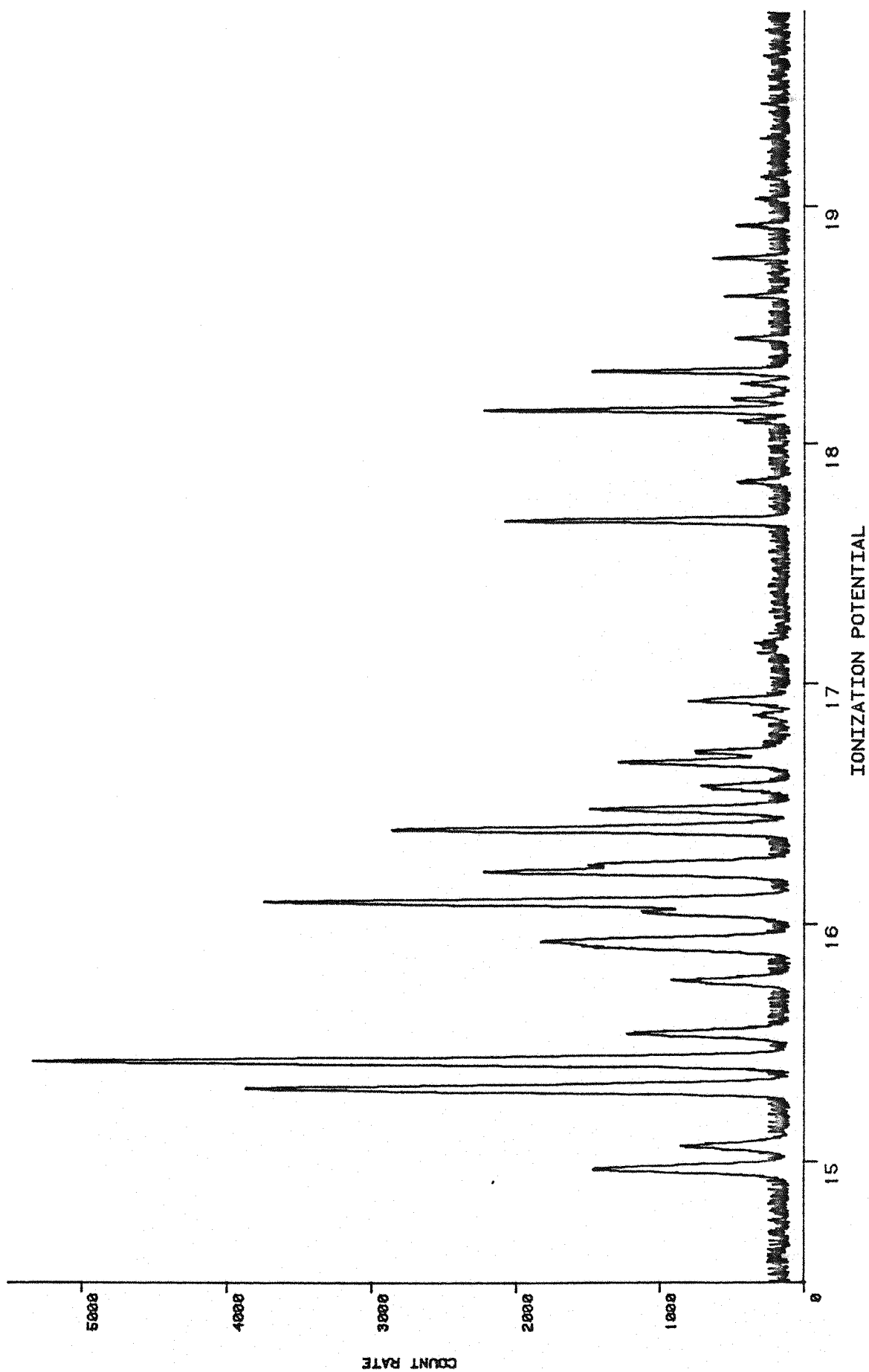


Figure 7

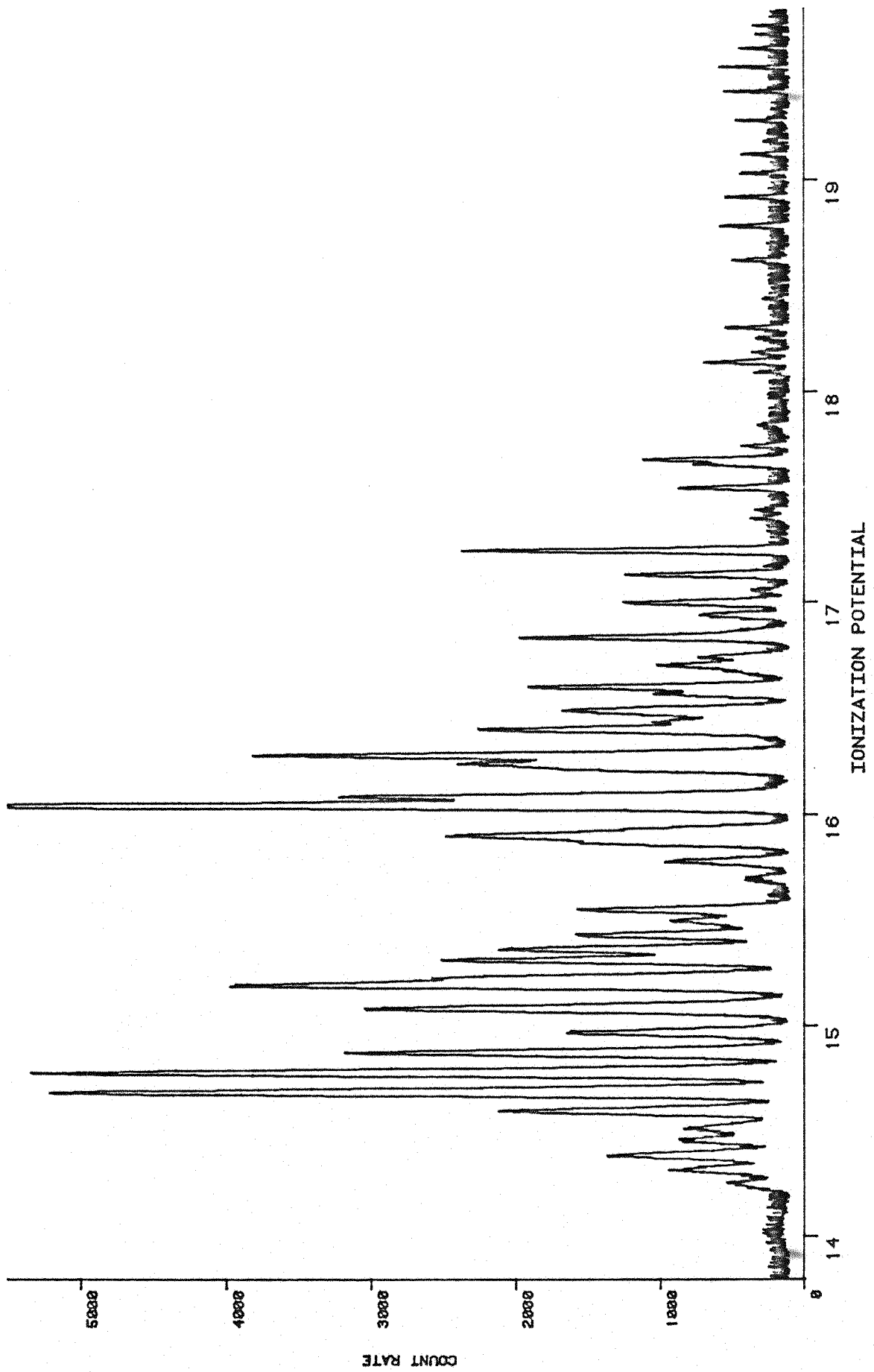


Figure 8

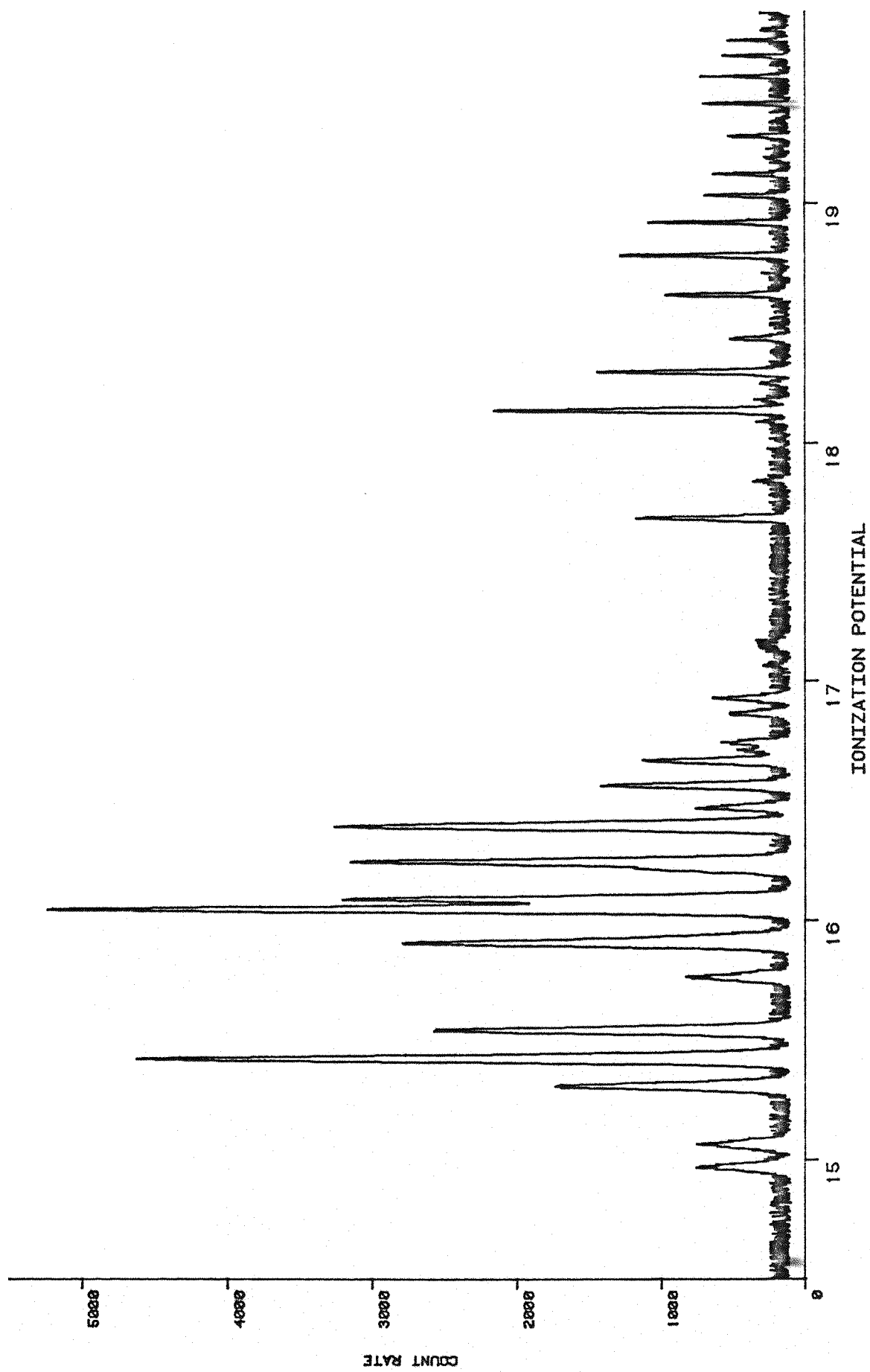


Figure 9

Experimental intensities for the PES vibrational components for both ionizations of HF, using the population distributions in Table 11, were calculated assuming a transmission function with an inverse kinetic energy dependence [35]. Also the electronic transmission moment over a band was assumed to be constant for each of the ionizations, for all vibrational transitions. Plots of calculated spectra were made using computer graphics facilities. The peaks were plotted assuming a Gaussian profile, with half height widths calculated assuming a 25 meV $\text{Ar}^+(^2\text{P}_{3/2})$ peak width. The resulting simulated PE spectra are presented in Figures 2-9.

As can be seen there is a startling change in the band shape, for the various vibrational populations considered. The band shape, for both ionizations, for the room temperature distribution show a remarkable resemblance to the only experimentally recorded PES spectrum [31]. This result arises from the close agreement obtained between the calculated and experimental spectroscopic constants, used in calculating component intensities for the simulated spectra. The band shapes obtained for the intermediate distribution represent the probable PES experimentally detectable band shapes for vibrationally excited HF ($\text{X}^1\Sigma^+$).

VI-4 Conclusions

This work has enabled the complete prediction of the, as yet, unrecorded experimentally, PE spectrum of vibrationally excited HF. The possibility of detecting vibrationally excited HF requires an improvement in sensitivity and pumping speed of the present photoelectron spectrometer. This may become feasible with the advent of sensitive multichannel photoelectron spectrometers, using continuous signal averaging data acquisition techniques. However the detection of vibrationally excited HF has already been reported using mass spectrometry [36], but no resolution of vibrational structure was possible. It is hoped that this work will stimulate research effort into experimental verification of the computed component intensities and positions, by PES.

Chapter VI

References

1. "A Bibliography of ab-initio Molecular Wavefunctions", Richards, W G, Walker, T E H, and Hinkley, R K, Oxford University Press, (1971).
2. "Bibliography of ab-initio Molecular Wavefunctions, Supplement for 1970-1973", Richards, W G, Walker, T E H, Farnell, L, and Scott, P R, Oxford University Press, (1974).
3. "Bibliography of ab-initio Molecular Wavefunctions, Supplement for 1974-1977", Richards, W G, Scott, P R, Colbourn, E A, and Marchington, A, Oxford University Press, (1978).
4. Cade, P E, and Huo, W H, J Chem Phys, 47, 649, (1967).
5. Clementi, E, J Chem Phys, 36, 33, (1962).
6. Julienne, P S, Krauss, M K, and Wahl, A C, Chem Phys Letts, 11, 16, (1971).
7. Lathan, W A, Hehre, W J, Curtis, L A, and Pople, J A, J Amer Chem Soc, 93, 6377, (1971).
8. Raftery, J, and Richards, W G, J Phys B, Atoms and Molecules, 5, 425, (1972).
9. Bartlett, R J, and Silver, D M, Chem Phys Letts, 29, 199, (1974).
10. Bartlett, R J, and Silver, D M, J Chem Phys, 62, 3258, (1975).
11. Wilson, S, Silver, D M, and Bartlett, R J, Mol Phys, 33, 1177, (1977).
12. Urban, M, Kello, V, and Hubac, I, Chem Phys Letts, 51, 170, (1977).
13. Urban, M, Kello, V, Noga, J, and Hubac, I, J Chem Phys, 72, 3378, (1980).
14. Silver, D M, Wilson, S, and Bartlett, R J, Phys Rev A, 16, 477, (1977).
15. Wilson, S, Mol Phys, 35, 1, (1978).
16. Ahlrichs, R, Driessler, F, Lisehka, H, and Staemmler, V, J Chem Phys, 62, 1235, (1975).
17. Meyer, W, and Rosmus, P, J Chem Phys, 63, 2356, (1975).

18. Meyer, W, and Rosmus, P, J Chem Phys, 66, 13, (1977).
19. Krauss, M, and Neumann, D, Mol Phys, 27, 917, (1974).
20. Golebiewski, A, and Nawak-Broctawisk, E, Mol Phys, 28, 1283, (1974).
21. Lie, G C, and Clementi, E, J Chem Phys, 60, 1275, (1974).
22. Amos, R D, Mol Phys, 35, 1765, (1978).
23. Dunning Jr, T H, Chem Phys, 42, 249, (1979).
24. Dunning Jr, T H, J Chem Phys, 65, 3854, (1976).
25. Bondybey, V, Pearson, P K, and Schaefer, H F (III), J Chem Phys, 57, 1123, (1972).
26. ATMOL-3 Users Manual, Atlas Computing Division, Rutherford Laboratory, Oxon.
27. SPLICE Users Reference Manual, Atlas Computing Division, Rutherford Laboratory, Oxon, (1977).
28. Herzberg G, and Huber, K P, "Constants of Diatomic Molecules", Van Nostrand Reinhold, New York, 1979.
29. Hopkinson, A C, Holbrook, N K, Yates, K, and Csizmadia, I G, J Chem Phys, 49, 3596, (1968).
30. Walker, T E H, Dehmer, P M, and Berkowitz, J, J Chem Phys, 59, 4292, (1973).
31. Berkowitz, J, Chem Phys Letts, 11, 21, (1971).
32. Jonathan, N B H, Okuda, S, and Timlin, D, Mol Phys, 24, 1143, (1972).
33. Jonathan, N B H, Mellior-Smith, C M, and Slater, D H, Mol Phys, 20, 93, (1971).
34. Anlauf, K G, Kuntz, P J, Maytotte, D H, Pacey, P D, and Polanyi, J C, Disc Faraday Soc, 44, 183, (1967).
35. Fackerell, A, B.Sc. Third Year Thesis, Southampton University, Chemistry Department.
36. Foner, S N, and Hudson, R L, J Chem Phys, 68, 2987, (1978).

PART II

Chapter I
Basic Principles of Multidetector
Spectroscopy

Contents

- I.1 Introduction
- I.2 Multidetector Spectroscopy
- I.3 Multidetector Techniques Applied to PES

I.1 Introduction

The underlying principle of all spectroscopic experiments is to measure the intensity of photons or charged particles as a function of energy or mass. This traditionally involves using an energy or mass analyser which disperses the incident energy or particle beam on to a detector (Figure 1). By scanning the analyser a small part of the spectrum can be detected at any one time. The resolving power of the analyser is a function of the slit widths employed. Reducing the slit widths of an analyser will increase the resolution of the analyser. However the sensitivity of the analyser will be reduced as the slit width is narrowed. The interrelationship between resolution and sensitivity is the controlling factor in determining experimentally acceptable slit widths.

To remedy this situation and to make use of the whole dispersed image, or a greater part of it, a multichannel system is needed. Such a system will detect all, or a considerable part of, the dispersed image (Figure 2).

I.2 Multidetector Spectroscopy

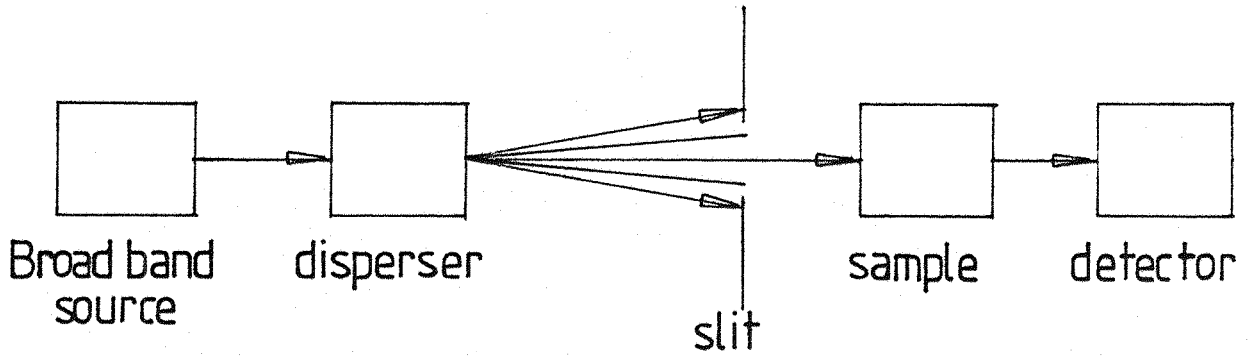
Multichannel spectrometers can be sub-divided into multidetector spectrometers and single detector spectrometers. Multichannel-single detector spectrometers employ a multiplexing scheme to evaluate the intensity in each channel. Two such multiplexing schemes are the Fourier Transform and Hadamard Mask methods. The former has found extensive application in radio frequency and infrared spectroscopy.

Multichannel-multidetector spectroscopy is a direct and obvious extension to the traditional single channel spectrometer. A multi-detector spectrometer would have a large slit width such that intensity in several channels in the spectrum would be detected simultaneously with a separate detector for each channel. The number of detectors required is related to the number of channels in the whole spectrum by:

$$N_D = N_C / N_B$$

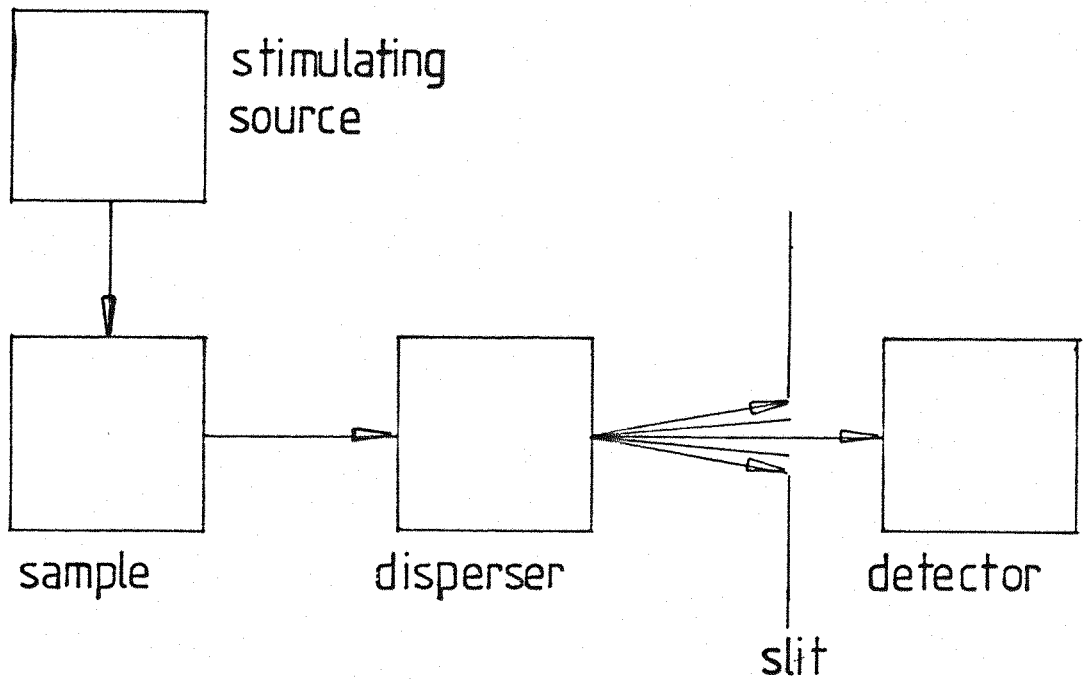
I-2-1

Figure 1a



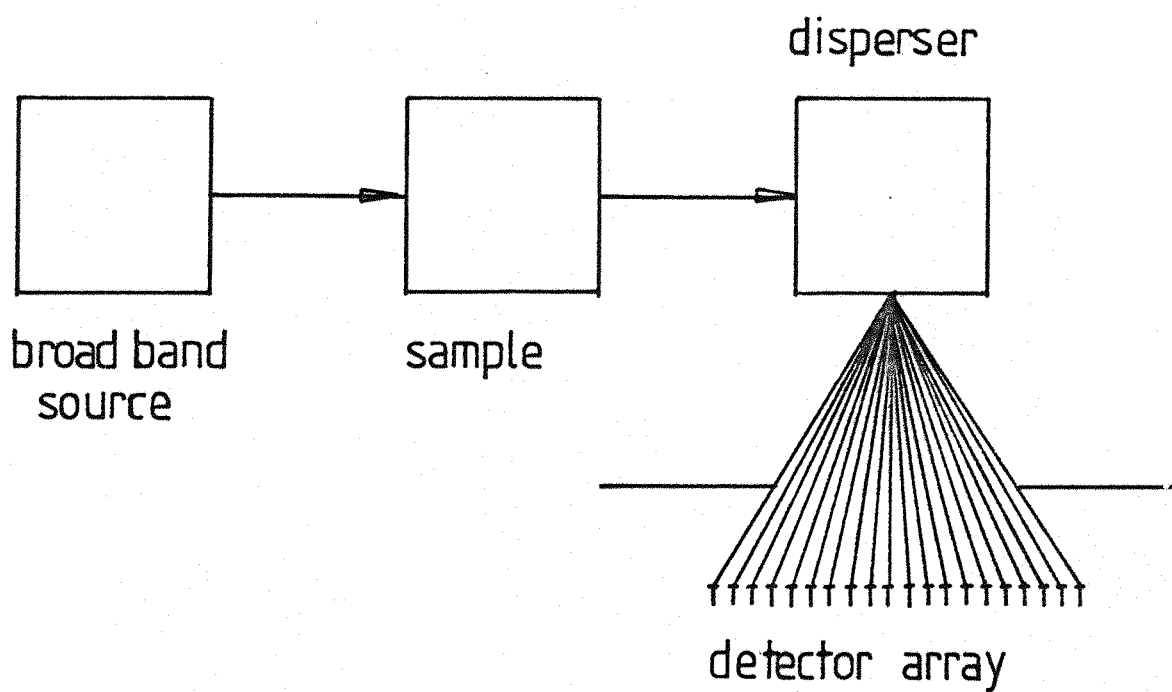
Schematic single channel absorption spectrometer

Figure 1b



Schematic single channel dispersion spectrometer

Figure 2



Schematic multidetector spectrometer

Where N_C is the number of channels in the complete spectrum and a channel of a spectrum is defined as a specified narrow energy range, usually less than the width of a single line. N_B is the number of spectral bins where a bin is a specified wide energy range that can be detected simultaneously. The number of bins in a spectrum is determined by experimental design of the disperser. For uv PES the complete kinetic energy spectrum spans 10 eV and the narrowest recorded width of 1 line is approximately 10 meV. Hence the maximum number of channels required is essentially 1000. For complete peak characterization the number of channels required could be of the order of 10^4 . Hence 100 bins would require 100 detectors, where each bin would comprise of 100 channels, i.e. 1 meV per channel.

The advantages of multichannel-multidetector spectroscopy extends beyond the immediate gain in experimental sensitivity arising from using larger slit widths. There arises two further, interrelated factors when a multidetector spectrometer (N_D detectors) is used to scan a spectrum consisting of N_C channels spanned by N_B bins.

Firstly there is a time factor. Since data for 1 bin can be accumulated in the same time as data for 1 channel, in a single channel spectrometer, then the entire spectrum will be acquired N_D times faster. If T_S is the acquisition time for the entire spectrum, for a single channel spectrometer, and T_M for a multidetector spectrometer, for the same spectrum, then:

$$T_M = \frac{1}{N_D} T_S = \frac{N_B}{N_C} T_S \quad \text{I-2-2}$$

Secondly there is the signal to noise enhancement factor. It follows that if the whole spectrum can be accumulated N_D times faster using a multidetector, then the measurement can be repeated N_D times for each bin, resulting in the spectrum being accumulated over the same period of time as using a single detector.

For noise proportional to the square root of the signal strength (Source Limited Noise) then for N_D repeated measurements the signal to noise ratio will be improved. If S_S is the signal strength for a single measurement and N_S is the noise, and K_S the proportionality

constant. Then:

$$N_S = K_S \sqrt{S_S} \quad \text{I-2-3}$$

If S_M is the signal accumulated over N_D measurements, i.e.

$$S_M = N_D S_S \quad \text{I-2-4}$$

Therefore, the noise observed for the repeated measurement, N_M , will be:

$$N_M = K_M \sqrt{S_M} = K_M \sqrt{N_D} \sqrt{S_S} \quad \text{I-2-5}$$

Hence the signal to noise ratio will improve by a factor of $\sqrt{N_D}$, for N_D repeated measurements.

Source Limited noise is not the only component in an observed noise profile. For weak signals the major noise contribution is proportional to the signal strength (Fluctuational or Scintillation Noise). Hence repeated measurements in this case will not improve the recorded signal to noise ratio.

The two factors considered above are dynamically interrelated, and can be traded off against one-another in a variety of intermediate ways in any one single experiment.

Hence for a typical PES application with $N_D = 100$ and $N_C = 10^4$, a spectrum can be accumulated 100 times faster using a multidetector instrument for the same experimental signal to noise ratio as that for a single channel instrument under the same conditions. Conversely an improvement of 10 in the signal to noise ratio would be found if the spectrum is acquired over the same period of time as in the single channel case.

I.3 Multidetector Techniques Applied to PES

Early multidetector electron spectrometers were just a simple extension of the single channel instrument, where the extended electron image was detected by an array of individual detectors. Such an instrument, as constructed by Nilsson et al [1] had severe limitations

on spatial resolution imposed by the size of each detector in the array. Also a major disadvantage was the large quantity of electronic equipment needed to process the output from each detector. Individual channel electron multipliers have been successfully used for a number of years for the detection of charged particles and ionizing radiation. They are however limited in their usefulness in a multidetector array because of their physical size. However most of the electrical performance characteristics of channel multipliers are not a function of channel length or diameter, but only a function of the ratio:

$$\alpha = \text{length/diameter}$$

I-3-1

This enables an almost arbitrary size reduction possible, with no loss of performance, to form a micro channel plate (MCP) for use as an imaging high gain electron detector. The first operational MCP's were built between 1959 and 1961 [2], but it has not been until recent years that the reliable manufacture of MCP arrays has been possible. The MCP provides an area capable of electron multiplication by independent channels such that spatially separate simultaneous events can be resolved. The channel size can be as small as a few tens of microns with channel densities of the order of 10^5 channels per square cm.

The MCP array is used as an extended electron multiplier with the output being imaged on a suitable position sensitive detector.

Two major techniques have been developed to determine the position of individual electron events over the extended image. These are charge division techniques and image scanning techniques, which will be discussed separately.

In charge division techniques the extended electron image is multiplied by an MCP, and subsequently impinged on an anode. Anodes that have been used are high resistance carbon coated silica filament wires [3] for one dimensional position analysis. Also resistive anodes have been developed and used in imaging devices [4-6] with two dimensional positional sensitivity. With resistive anodes the incident charge divides and the arrival position is determined from the current measured at each end, or at the corners, of the device. Electron

imaging devices using the resistive anode for position sensitive detection are limited by the relatively large dead time characteristic of the devices and the associated electronics. Whole device event rates in excess of 10^4 events/sec will lead to saturation and loss of data. However such devices are very sensitive, enabling detection of single primary events, also they are event driven, i.e. the arrival of an individual primary electron, in the extended image, will trigger detection of the arrival position.

In image scanning techniques the multiplied secondary electrons from the MCP are impinged on to a photosensitive area, usually a phosphor screen, to convert the charged particles to photons. The positional information is then retained by the photon output and is detected by an image sensing element. Commonly used image sensing devices are discrete photodiode arrays (Charge coupled devices) or scanning optical pick-up tubes (television cameras). There have been many implementations of both types of image scanning devices.

The first operational PES multidetector spectrometer, used a TV camera pick-up tube for optical sensing [7]. Weeks et al [8] have also used a TV camera for parallel detection, angle resolved electron spectroscopy, where the angular dependence of ionization provides the primary electron image.

A CCD imaging device has been chosen by Hicks et al for their multidetector, electron energy loss spectrometer [9].

The two devices have their relative merits. TV pick-up tubes are more sensitive. However CCD devices are small light-weight devices and offer in particular notable low noise performance. Also CCD devices have no high voltage and magnetic components to possibly disturb the field free region around the spectrometer.

The instrument developed by the PES group in Southampton uses a MCP array to intensify the extended electron image produced by the photoelectron spectrometer analyser. The position sensitive detector is the optical image scanning type with a TV camera pick up tube monitoring optical output from a phosphor screen.

The instrument is described fully in Chapter II.

Chapter I

References

1. Nilsson, O, Jadrny R, and Siegbahn, K, Proc Int Conf Spectroscopy, Calif, USA, ed, D A Shirley, North Holland, Amsterdam, 141-9, (1972).
2. Wiley, W C, and Hendee, C F, IEE Trans Nucl Sci, NS9, 103, (1962).
3. Hansson, G V, Goldberg, B, and Bachrach, R Z, Rev Sci Instrum, 52, 517, (1981).
4. Lampton, M, and Carlson, C W, Rev Sci Instrum, 50, 1093, (1979).
5. Rees, D, McWhirter, I, Rounce, P A, Barlow, F E, and Kellock, S J, J Phys E Sci Instrum, 13, 763, (1980).
6. Rees, D, McWhirter, I, Rounce, P A, and Barlow, F E, J Phys E Sci Instrum, 14, 229, (1981).
7. Karlsson, L, Mattsson, L, Jadrny, R, Bergmark, T, and Siegbahn, K, Physica Scripta, 14, 230, (1976).
8. Weeks, S P, Rowe, J E, Christman, S B, and Chaban, E E, Rev Sci Instrum, 50, 1249, (1979).
9. Hicks, P J, David, S, Wallbank, B, and Comer, J, J Phys E Sci Instrum, 13, 713, (1980).

Chapter II
Multidetector Instrument
Design Details

Contents

- II.1 Introduction
- II.2 Vacuum System
- II.3 Electron Energy Analyser
- II.4 Multichannel Detector and Phosphor Screen
- II.5 Video Signal Preprocessor
- II.6 Data Handling and Analysis

II.1 Introduction

The design philosophy for the multichannel instrument is basically that of the earlier instruments, with specific additions and refinements for the multichannel detector.

The major features of the instrument are outlined in Figure 1, showing similarities with the instrument described in Part I, Chapter 3. The discussion in this chapter will cover the features of the multichannel instrument which represent enhancements over the previous generation of instruments.

II.2 Vacuum System

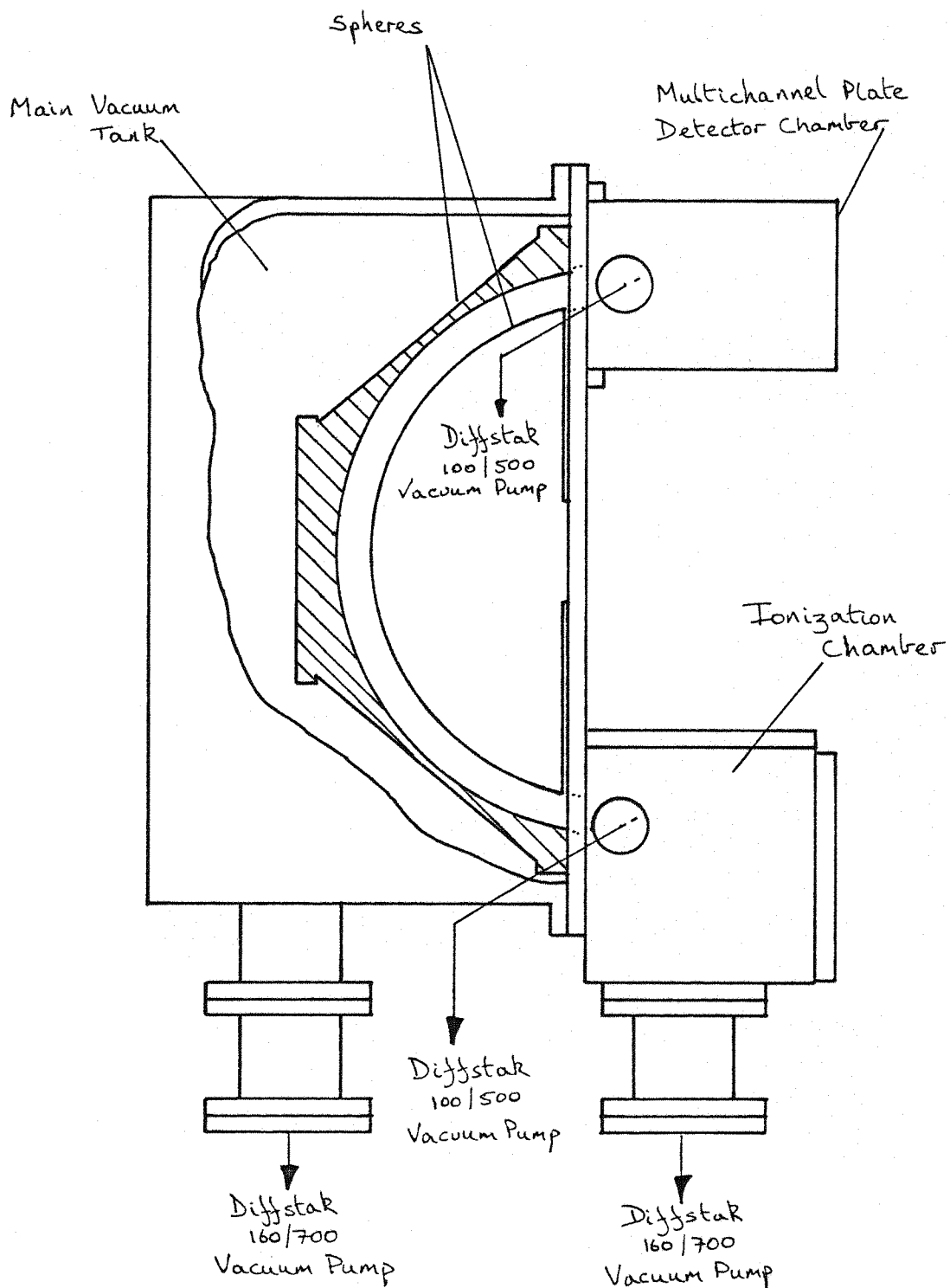
As shown in Figure 1 the instrument is comprised of three vacuum chambers, namely the ionization chamber, the analyser chamber and the detector chamber, each of which will be described in turn. The vacuum system was designed to allow instrument operation with high throughput of sample gas whilst reducing contamination of the analyser and detector surfaces.

The ionization chamber is pumped by two separate vacuum systems. Bulk pumping of the chamber is facilitated by an Edwards Diffstak 160/700 vapour diffusion pump with integral butterfly valve, backed by an EDM20 direct drive dual stage rotary pump. No cryotrap was included, because of the minimal backstreaming characteristic of the Diffstak. The primary function of this system is to pump gas samples directly, maintaining a gross chamber pressure of less than 10^{-5} mbar. Differential pumping of a region directly in-front of the slits (~ 10 cm³ volume) is facilitated by a second vacuum system consisting of an Edwards Diffstak 100/300 backed by an EDM6 direct drive rotary pump. This pumping is achieved by a vacuum duct introduced through the side of the ionization chamber. The differentially pumped volume has a set of slits to allow free passage of photoelectrons to the analyser slits. This system serves to reduce the flux of sample gas entering the analyser chamber, from the ionization region.

The analyser chamber is pumped by an Edwards Diffstak 160/700, backed by an ED660 36 m³/hour rotary pump. The large volume rotary

Figure 1

Diagram of the multidetector spectrometer



pump was chosen to enable fast pump-down time, when roughing out the instrument, which has a total volume of approximately 0.5 m^3 , from atmospheric pressure. The vacuum system maintains a chamber pressure, as measured by an ionization gauge, of less than 10^{-6} mbar under operational conditions.

The detector chamber was fitted with a separate pumping system to ensure complete degassing of the detector. The sensitive surfaces of the multichannel plate and the close proximity of high voltage and earthed components makes the operation of the detector in a high vacuum essential. Safe detector operation is only possible at pressures less than 10^{-5} mbar, above which spark discharges occur. The vacuum system consists of an Edwards Diffstak 100/300 backed by an EDM6 rotary pump. This is in addition to pumping via the analyser chamber which has an opening to the detector chamber at the analyser exit point. An ionization gauge was used to directly measure the detector chamber pressure. It was found that out-gassing of pockets of gas from the intricate structure of the detector and its mounting, necessitated extended pump down periods (typically ~ 3 hours) for safe operation.

Backing line pressures on all vacuum systems were measured by Pirani gauge heads, Edwards PR10S, controlled by an Edwards Pirani 10 control box (1 for 2 heads). The entire vacuum system is controlled through a relay activated switch gear, which ensures logical operation of rotary pumps and diffusion pumps. Also fail safe alarm circuits were incorporated to facilitate safe shut down, and alarm alert in the event of loss of vacuum or failure of the coolant water supply. In the event of such a failure the Diffstak heater current, detector supply voltage and ionization gauge head supplies are switched off, and an alarm sounded.

II.3 Electron Energy Analyser

The electron energy analyser used in the instrument is of the same type as the previous generation of instrument, namely a 150° solid sector hemispherical electrostatic analyser. To improve the dispersion and resolution a mean sphere radius of 20 cm was implemented, with a 4 cm intersphere gap. The hemispheres were machined from solid

aluminium by Leisk Engineering Limited [1].

The DC voltages for each hemisphere could either be supplied from a mechanical ramp generator, for manual control, or be output from two channels of an eight channel digital to analogue converter, for automated control.

An area electron detector samples the entire electron image from the analyser at the image plane. The dispersion of the electron image determines the energy range of any one spectral bin, which is analysed as a number of equally spaced channels. The dispersion of the electron image over the detector can be deduced using the method of Purcell [2], using the analyser parameters for the analyser used.

Consider an electron travelling on the trajectory A to F in Figure 2, traversing through regions I, III and II. In region I an electron will travel in a straight line, on a divergent path until an abrupt I/III boundary is reached (no fringe effects will be considered in this analysis). The electron path subtends an angle, α , radians with the x axis, with a velocity in region I given as:

$$v = v_0(1 + \beta) \quad \text{II-3-1}$$

where v_0 is the mean pass velocity, for the given potential difference between the hemispheres, ΔV_0 , and for an electron entering region III perpendicular to the boundary. The radius of the trajectory of such an electron in region III will be:

$$r_0 = \frac{(R_1 + R_2)}{2} \quad \text{II-3-2}$$

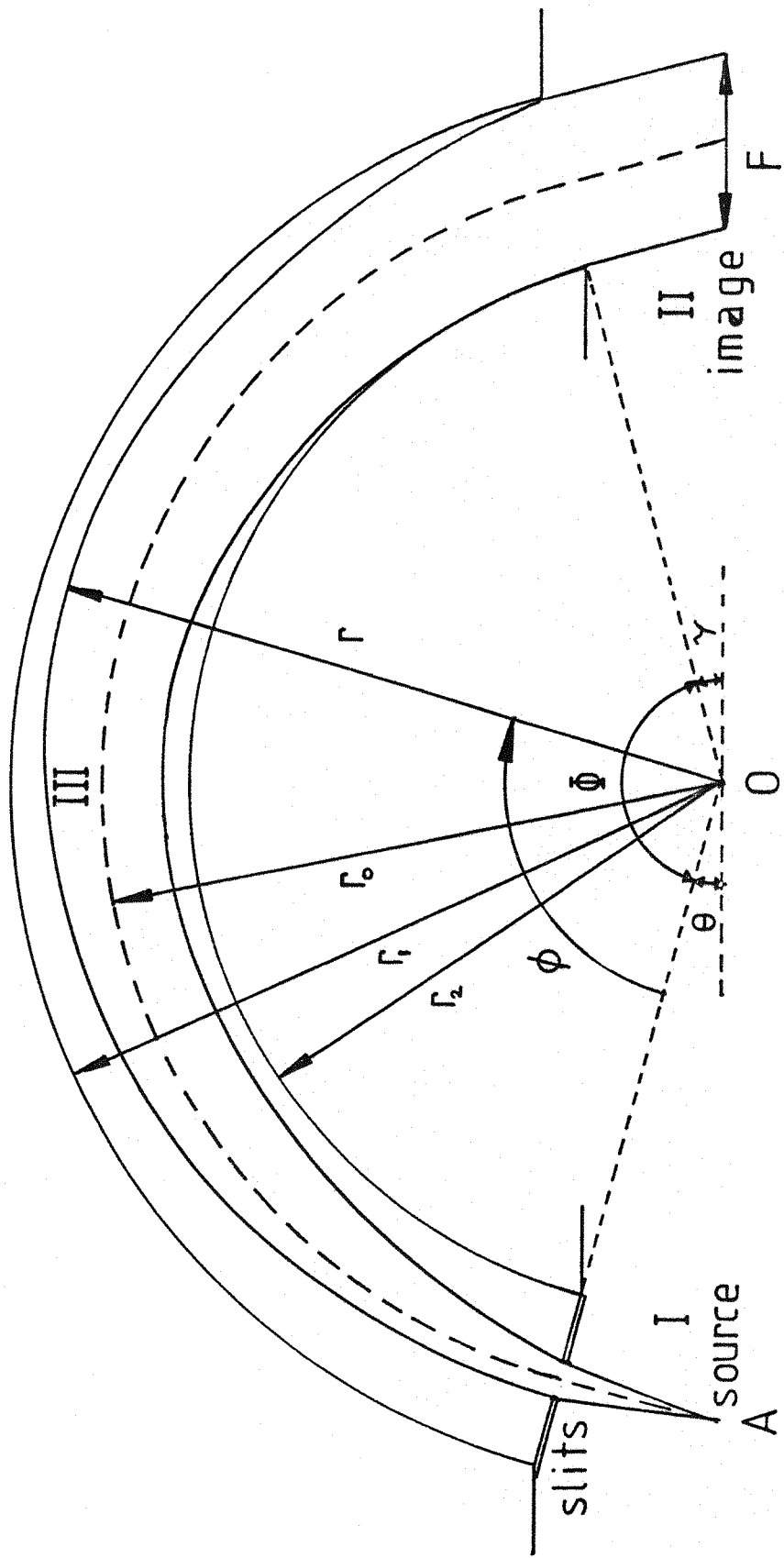
β in II-3-1 represents a possible spread in velocity of the incident electrons.

In region III the electron experiences the radial inverse square electric field given by:

$$\mathcal{E}(r) = \frac{R_1 R_2}{(R_2 - R_1)r^2} \Delta V_0 \quad \text{II-3-4}$$

and assumes an orbit throughout region III and exits abruptly at the

Figure 2
Electron energy analyser parameters



II/III boundary, into the field free region, region II. The problem is to evaluate the path DF and hence optimise parameters α and β for the maximum luminosity and resolution of the analyser. This would enable an expression to be obtained for the energy of electrons across the dispersed electron image as a function of position along axis OF.

Using the coordinates in Figure 3, the trajectory of an electron of velocity v in region I is:

$$y_1 = \alpha_1(x_{10} - x_1) \quad \text{II-3-5}$$

In region III the generalized trajectory is found from the equations of motion and is:

$$\frac{1}{r} = P \cos\phi + Q \sin\phi + \frac{1}{r_0(1 + \beta)^2} \quad \text{II-3-6}$$

with $r = r_0(1 + z)$, where z is small and represents the proportional displacement of the trajectory from the mean path, r_0 .

Substituting, rearranging and dropping powers of β we obtain:

$$z = 2\beta - r_0 P \cos\phi - r_0 Q \sin\phi \quad \text{II-3-7}$$

The constants P and Q are determined from the boundary conditions on the I/III boundary, i.e. when $\phi = 0$. This gives:

$$z = \alpha_1 \sin\phi + \left(\frac{\alpha_1 x_{10}}{r_0} - 2\beta\right) \cos\phi + 2\beta \quad \text{II-3-8}$$

On entering region II, the y_{20} displacement is given as:

$$y_{20} = r_0 z \quad \text{II-3-9}$$

This occurs when $\phi = \phi$, hence substituting II-3-8, for z , II-3-9 becomes:

$$y_{20} = r_0 \left[\alpha_1 \sin\phi + \left(\frac{\alpha_1 x_{10}}{r_0} - 2\beta\right) \cos\phi + 2\beta \right] \quad \text{II-3-10}$$

In region II the electron travels in a straight path, given by:

$$y_2 = y_{20} - \alpha_2 x_2 \quad \text{II-3-11}$$

where the divergence on crossing the III/II boundary, α_2 , is given as:

$$\alpha_2 = \frac{-dz}{d\phi} \quad \text{at} \quad \phi = \phi \quad \text{II-3-12}$$

i.e.

$$\alpha_2 = -\alpha_1 \cos\phi + \left(\frac{\alpha_1 x_{10}}{r_o} - 2\beta\right) \sin\phi \quad \text{II-3-13}$$

hence y_2 becomes:

$$\begin{aligned} y_2 = & r_o \left[\alpha_1 \sin\phi + \left(\frac{\alpha_1 x_{10}}{r_o} - 2\beta\right) \cos\phi + 2\beta \right] \\ & + x_2 \left[\alpha_1 \cos\phi - \left(\frac{\alpha_1 x_{10}}{r_o} - 2\beta\right) \sin\phi \right] \end{aligned} \quad \text{II-3-14}$$

Using the identities

$$\tan\theta = \frac{x_{10}}{r_o} \quad \text{II-3-15}$$

$$\tan\tau = \frac{x_{20}}{r_o} \quad \text{II-3-16}$$

$$\tan(\theta+\tau) = \frac{r_o(x_{10} + x_{20})}{(r_o^2 - x_{10}x_{20})} = -\tan\phi \quad \text{II-3-17}$$

and rearranging II-3-14, for $x_2 = x_{20}$ then the dispersion at x_{20} is given as:

$$Y_2 = 2\beta r_o \left(1 - \cos\phi + \left(\frac{x_{20}}{r_o}\right) \sin\phi\right) \quad \text{II-3-18}$$

Where Y_2 is the distance y_2 at $x_2 = x_{20}$. The dispersion along axis OF, denoted Y_D , would be a simple projection of the distance, i.e.:

$$Y_D = Y_2 \cos\tau \quad \text{II-3-19}$$

To evaluate optimized parameters, α_1 and β_1 for the greatest dispersion at F, equation II-3-8 is used with $r = r_o(1 + z)$, i.e.:

$$r = r_o \left[\alpha_1 \sin \phi + \left(\frac{\alpha_1 x_{10}}{r_o} - 2\beta \right) \cos \phi + 2\beta + 1 \right] \quad \text{II-3-20}$$

Differentiating with respect to ϕ , with α_1 , x_{10} , r_o and β constants gives:

$$\left(\frac{dr}{d\phi} \right)_{\alpha_1, \beta, x_{10}, r_o} = r_o \alpha_1 \cos \phi - r_o \left(\frac{\alpha_1 x_{10}}{r_o} - 2\beta \right) \sin \phi \quad \text{II-3-21}$$

The radial dispersion in region III will be at a maximum, or minimum, when II-3-21 is zero. Putting II-3-21 equal to zero and rearranging gives:

$$r_o \alpha_1 \cos \phi = r_o \left(\frac{\alpha_1 x_{10}}{r_o} - 2\beta \right) \sin \phi \quad \text{II-3-22}$$

or:

$$\tan \phi = \frac{\alpha_1}{\left(\frac{\alpha_1 x_{10}}{r_o} - 2\beta \right)} \quad \text{II-3-23}$$

The largest dispersed image should be obtained at the III/II boundary, i.e. when $\phi = \Phi$. Hence II-3-23 becomes:

$$\alpha_1 \left(\frac{x_{10}}{r_o} \tan \Phi - 1 \right) = 2\beta \tan \Phi \quad \text{II-3-24}$$

Using II-3-15 this becomes:

$$\alpha_1 (\tan \theta \tan \Phi - 1) = 2\beta \tan \Phi \quad \text{II-3-25}$$

Rearranging II-3-24, using trigonometric identities we obtain:

$$\frac{\beta}{\alpha_1} = 2 \sin 2\theta \quad \text{II-3-26}$$

For the analyser used, $\theta = 15^\circ$ hence

$$\beta = \alpha_1 \quad \text{II-3-27}$$

This equality is a property of a symmetrically placed 150° solid sector sphere.

Using equation II-3-20 with the values:

$$\begin{aligned} R_1 &= 22 \text{ cm} \\ R_2 &= 18 \text{ cm} \\ \phi &= \Phi = 150^\circ \\ r_o &= 20 \text{ cm} \\ x_{10} &= r_o \tan \theta \end{aligned} \quad \text{II-3-28}$$

α_1 and β can be evaluated as:

$$\alpha_1 = \beta = 2.5 \times 10^{-2} \quad \text{II-3-29}$$

Using this value of β , the range of velocities of electrons in the entire extended image, for a set mean pass energy can be evaluated.

α_1 is used to calculate the minimum collimating slit widths for electrons entering the analyser that would ensure all electrons in the specified energy range would be focused on to the dispersed image.

From II-3-1 the maximum and minimum velocities over the extended image at the III/II boundary are given as:

$$\begin{aligned} v_{\max} &= v_o(1 + \beta) \\ v_{\min} &= v_o(1 - \beta) \end{aligned} \quad \text{II-3-30}$$

Hence the velocity range covered by the extended image is:

$$\frac{\Delta v}{v} = 2\beta = 5 \times 10^{-2} \quad \text{II-3-31}$$

This represents an energy range of:

$$\frac{\Delta E}{E} = 4\beta = 0.1 \quad \text{II-3-32}$$

Hence the range of energies of electrons comprising the extended image is 10% of the mean pass energy. All electrons leaving region III travel in a straight line through field free region II to strike the detector positioned on plane OF centred on F. The energy of the electrons detected, as function of the position from the centre of the detector, can be evaluated. Also the range of energies detected, for a given mean pass energy, can be evaluated to give the width of the spectral bin. Figure 3ashows the coordinates systems in region II.

Using equation II-3-18, and rearranging using trigonometric identities we obtain:

$$Y_2 = 4r_o\beta \quad \text{II-3-33}$$

Transferred to detector centered coordinates:

$$\begin{aligned} Y_D &= Y_2 \cos \tau \\ &= 4r_o\beta \cos \tau \end{aligned} \quad \text{II-3-34}$$

Rearranging for β gives:

$$\beta = \frac{Y_D}{4r_o \cos \tau} \quad \text{II-3-35}$$

And substituting in:

$$E = E_o(1 + \beta)^2 \quad \text{II-3-36}$$

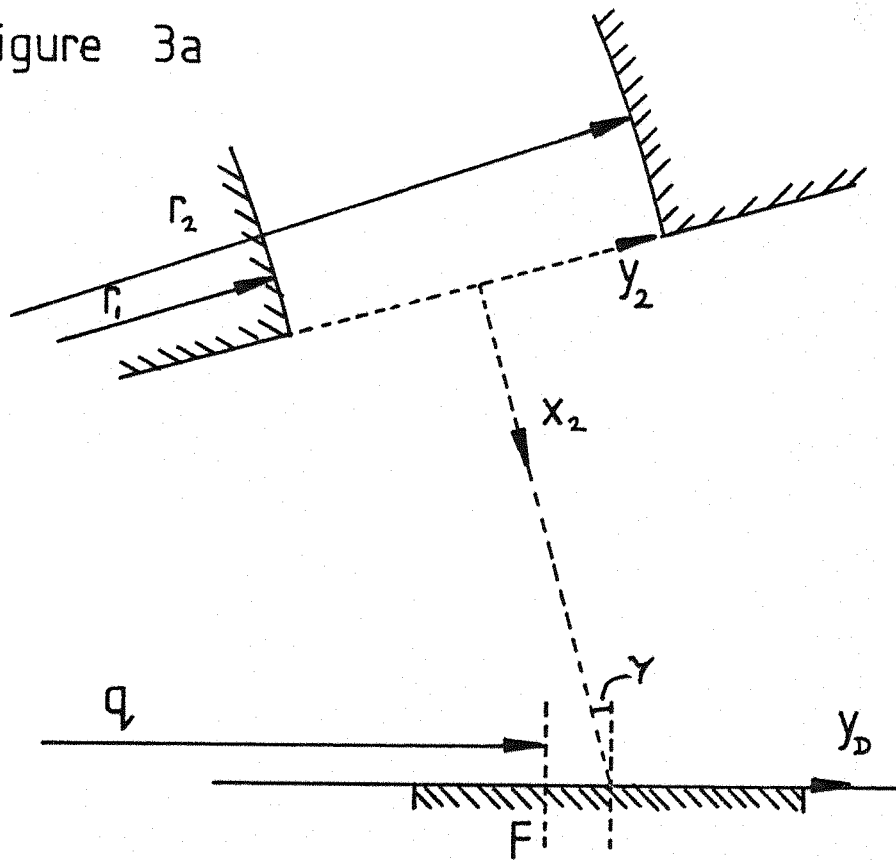
Gives:

$$E = E_o \left(1 + \frac{Y_D}{4r_o \cos \tau}\right)^2 \quad \text{II-3-37}$$

Equation II-3-37 gives the energy of a particle striking the detector along the Y_D axis, centred on the detector, as a function of mean pass energy. Using the values:

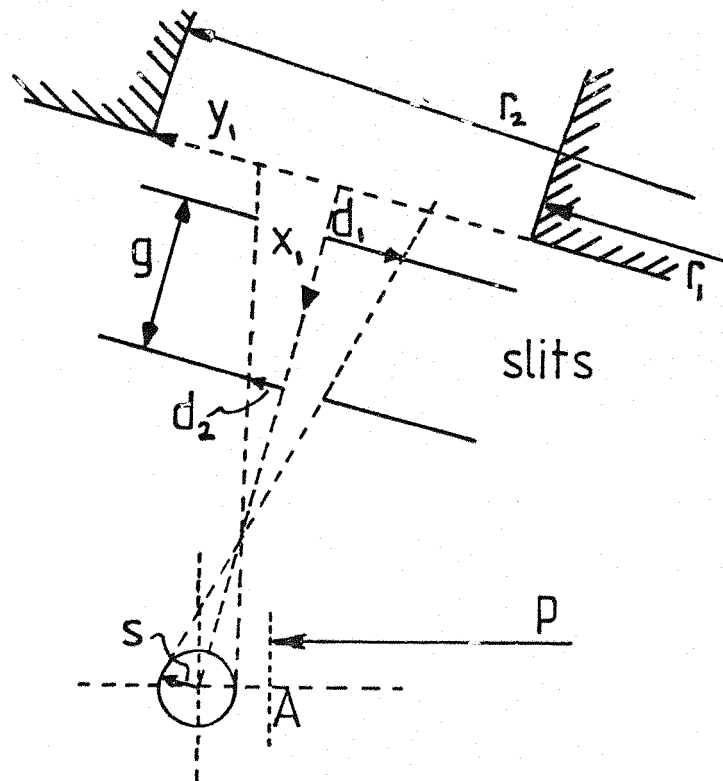
$$\begin{aligned} r_o &= 20 \text{ cm} \\ \tau &= 15^\circ \end{aligned}$$

Figure 3a



Analyser exit region coordinates

Figure 3b



Analyser source region coordinates

II-3-37 simplifies to:

$$E = E_0(1 + 1.294 \times 10^{-2} Y_D)^2 \quad \text{II-3-38}$$

For a detector of radius 1.1 cm Figure 4 is a plot of function II-3-38. The spectral bin width as a function of the mean pass energy is given as:

$$E_B = E_0 1.294 \times 10^{-2} 2D_W$$

Where D_W is the detector width, $D_W = 2.2$ cm. Figure 5 is a plot of E_B as a function of E_0 .

The optimized value of α_1 can now be used to calculate entrance slit widths, which would allow electrons with an energy spread of 4β to pass to the exit region of the analyser. The value of α_1 is limited by the intersphere gap with the ratio α_1/β constant for any one analyser arrangement. Figure 3b is a diagram of the entrance slit region, showing the axis systems, and the double collimating slits.

For a finite width source, Browne et al [3] used the equation:

$$\alpha_1 = \frac{(d_1 + s)}{x_{10}} \quad \text{II-3-40}$$

Where d_1 is the primary slit offset, s is the finite source width (throat of the ionizing radiation beam) and α_1 and x_{10} are defined as before.

Rearranging for d_1 gives:

$$d_1 = x_{10}\alpha_1 - s \quad \text{II-3-41}$$

The secondary slit offset is given by:

$$d_2 = \alpha_1(x_{10} - g) - s \quad \text{II-3-42}$$

where g is the inter-slit gap.

Using the values:

$$\begin{aligned} \alpha_1 &= 2.5 \times 10^{-2} \\ s &= 0.05 \text{ cm} \\ x_{10} &= r_0 \tan \theta = 5.359 \text{ cm} \\ g &= 2.4856 \text{ cm} \end{aligned}$$

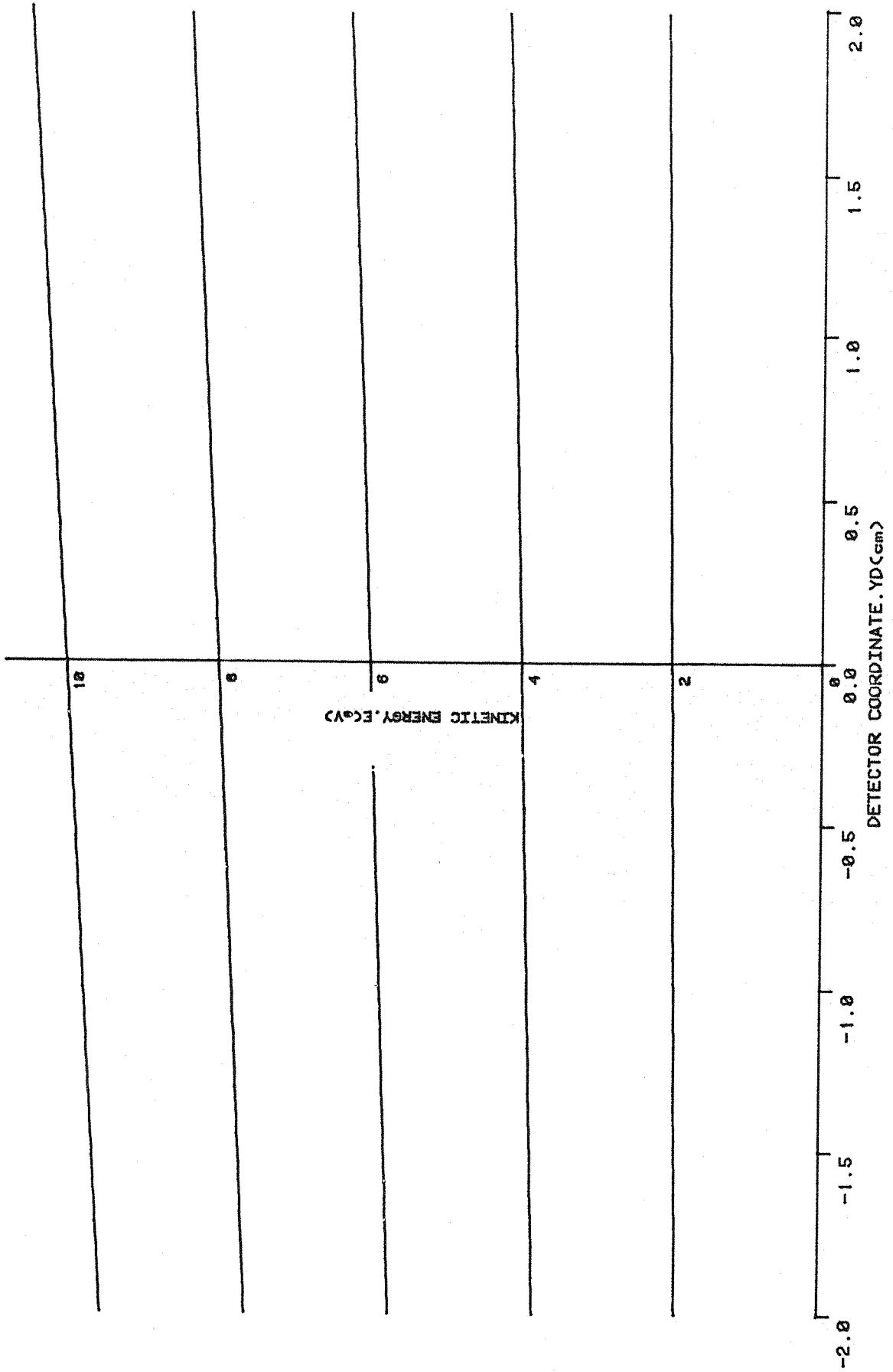


Figure 4

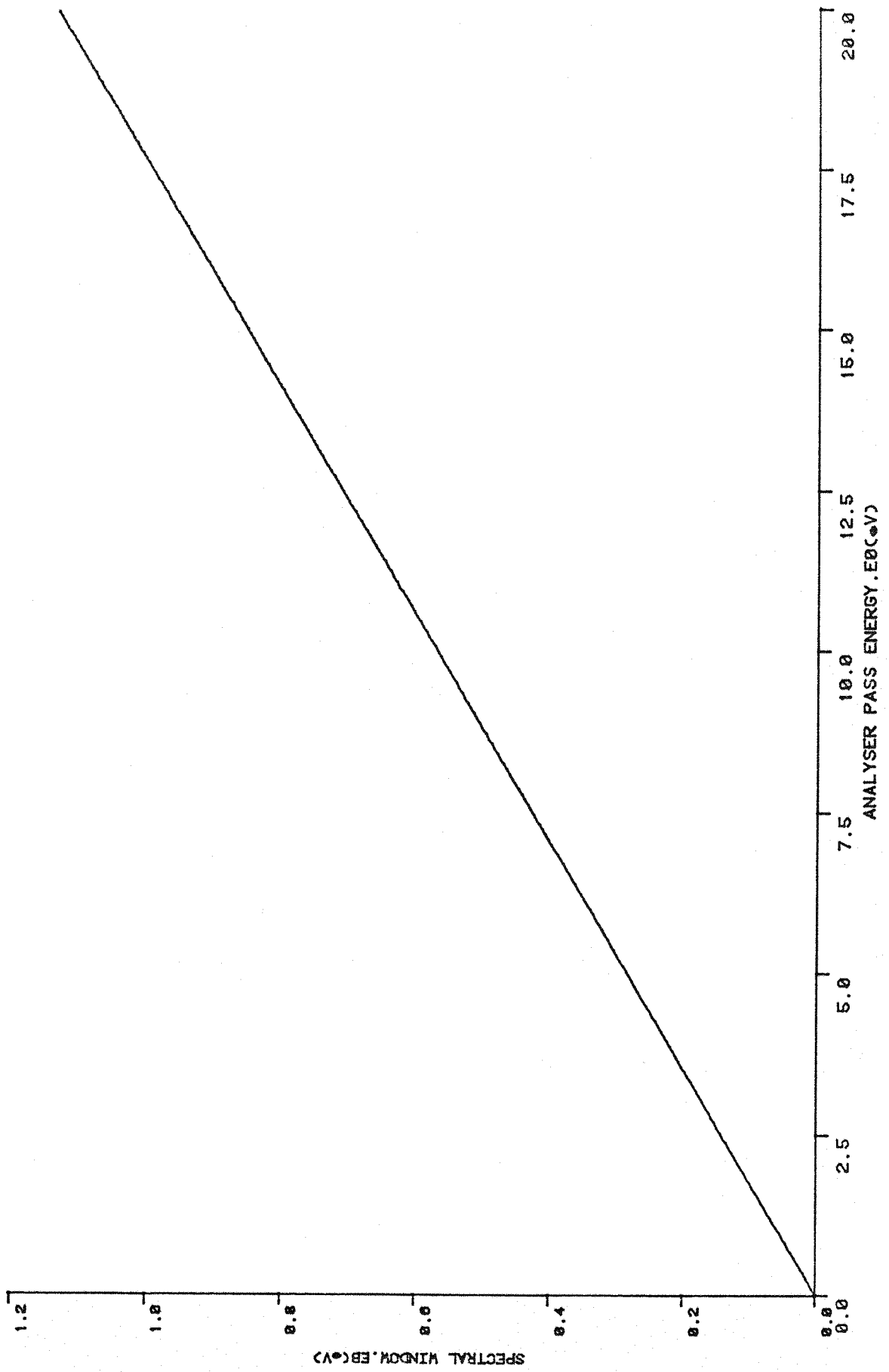


Figure 5

The slit offsets are found to be:

$$\begin{aligned}d_1 &= 0.84 \text{ mm} \\d_2 &= 0.22 \text{ mm}\end{aligned}$$

Hence the optimized entrance slit widths, for centered slits are:

$$\begin{aligned}\text{Front slit width} &= 0.44 \text{ mm} \\ \text{Rear slit width} &= 1.68 \text{ mm}\end{aligned}$$

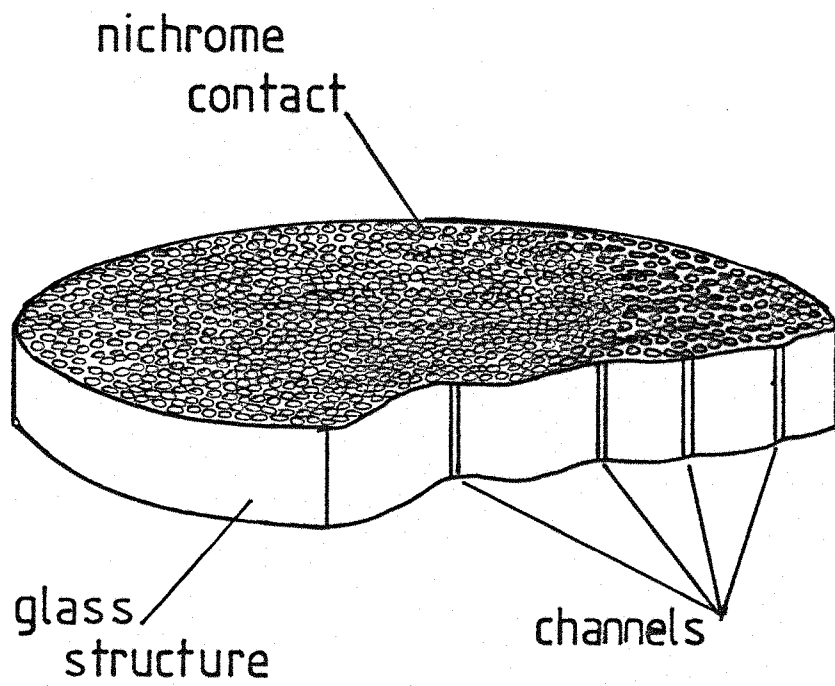
Exceeding those widths will not increase the luminosity of the analyser since electrons will collide with the analyser surfaces, if they are within the specified velocity range. However electrons beyond the derived energy range could follow a trajectory to the detector, hence resulting in loss of focus in the extended image.

The treatment used here has considered electron trajectories in three defined regions, two of which are field free. The boundaries between the regions have been considered instantaneous, and no fringe effects have been considered. However the values calculated are reasonable and subsequent experiments have demonstrated that the treatment is essentially correct.

II.4 Multichannel Detector and Phosphor Screen

The microchannel plate (MCP) Detector used is an array of approximately 10^6 miniature electron multipliers. Figure 6 is an exploded diagram of the MCP. The channel diameter is $25 \mu\text{m}$ and length, extending through the entire thickness of the plate, is 1.0 mm . The plates used initially were Mullard G25-25 plates of 27.1 mm diameter with a channel pitch of $31 \mu\text{m}$. The principle of operation of each of the channels in the MCP is analogous to that of a continuous dynode, as in a single channel multiplier. Parallel electrical contact to each channel is provided by deposited Nichrome layers at both the front and the rear. The total resistance across the plate is approximately 5×10^7 ohms. Under typical operating conditions an MCP provides a current gain of approximately 10^3 coupled with ultra short time characteristics (FWHM output peak width of $<100 \text{ psecs}$) and high spatial resolution.

Figure 6



Schematic diagram of a microchannel plate

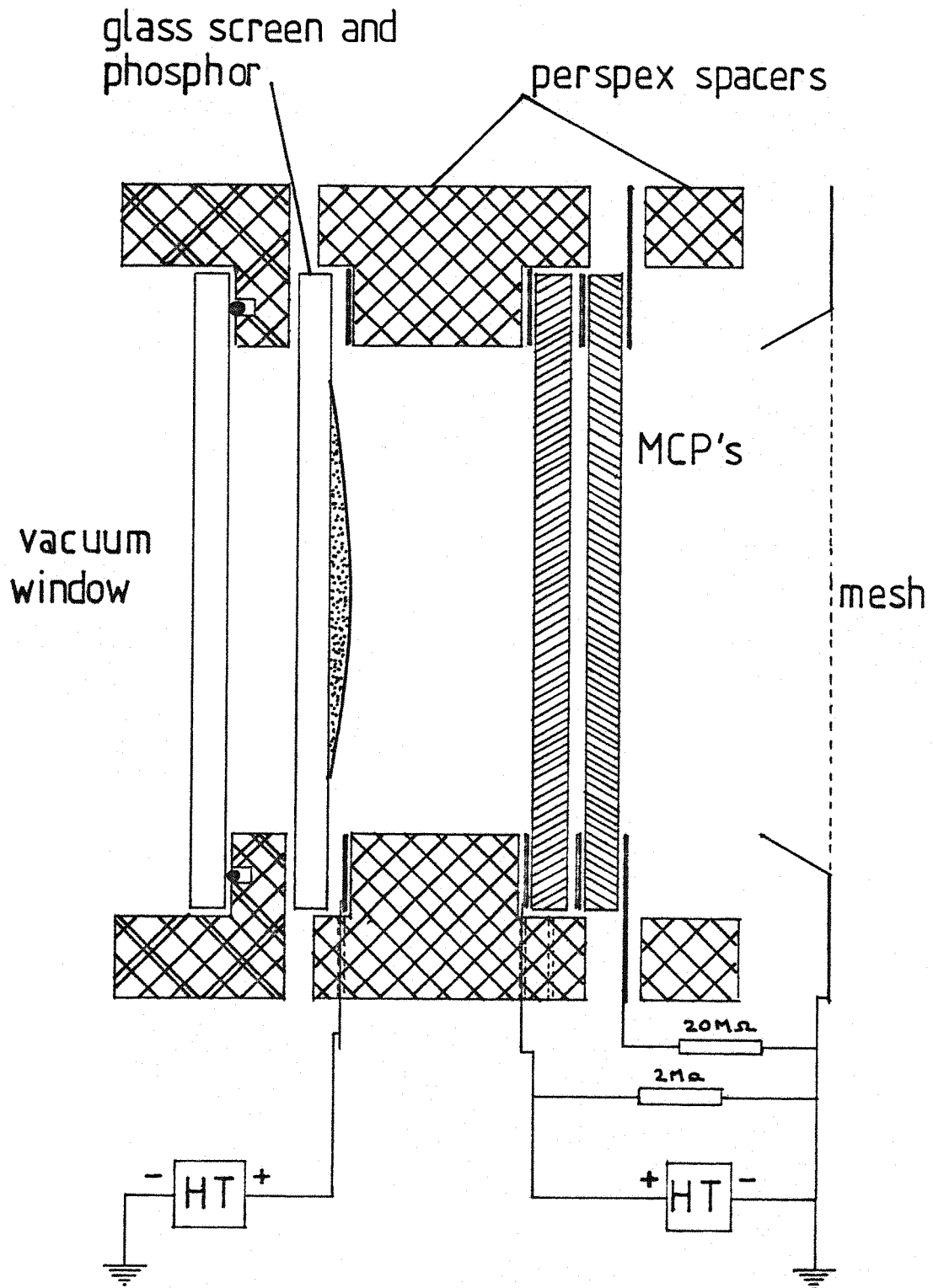
The detector arrangement implemented on the instrument is a pair of MCP's in a Chevron configuration, with a phosphor screen acting as the output target. The assembly is shown in Figure 7. In this arrangement total current gains in excess of 10^6 are achieved with detector voltage of 900 volts on each MCP. The phosphor target screens used were deposited on glass discs, by Instrument Technology Limited [4]. The choice of phosphor for the screen is very crucial. Consideration was given to the phosphor efficiency, the temporal decay characteristics and the peak wavelength for optical output. Characteristics for the common commercial phosphors were obtained from references [5-7]. Phosphor P20 was chosen for initial trials because it met most of our specifications. P20 has the following major characteristics [5].

- (1) Efficient Quantum Yield (0.063 photons per eV).
- (2) Medium Persistence (the exact persistence time depends on many variable parameters such as the exact chemical composition, particle size and deposition method, hence is not a constant for any one phosphor).
- (3) Peak optical output in center of visible region (5660 Å).

The design of the detector assembly proved a time consuming task. The major difficulty was to satisfy the requirement to bias the front MCP face to 200 volts, whilst maintaining the region up to the detector completely field free. The problem was identified when distorted electron images were detected, resulting in randomization of spatial information. Further investigation proved that the extended electron image was in fact inverted and condensed.

These problems were overcome with the detector configuration shown in Figure 7. The field generated by the MCP faceplate voltage was restricted by a 200 cpi mesh adhered to an annular ring positioned in front of the detector. This was effective in limiting the field effects but unfortunately reduced the sensitivity of the overall detector by obscuring the electron flux of the extended electron image in front of the detector. This was compensated for by the increased charge multiplication of the MCP with a biased surface. The increased gain of the MCP is because secondary electron emission is at a maximum for surface

Figure 7



Exploded diagram of the detector assembly

collisions in excess of 150 eV for primary electrons. Throughout development the MCP's were kept in clean dry atmospheres, in dessicators, because the secondary emitting surfaces are highly sensitive to contaminants, particularly hydrocarbons. The high voltage components of the detector required careful attention to minimise arcing. This was achieved by insulating all conductor wires with quartz glass tubing. Spark discharges are catastrophic for the delicate MCP arrays and result in vapourization of the aluminized phosphor. It was found that prolonged use, particularly with high electron fluxes, lead to voltage breakdown and sparking, within the detector. This was due to the MCP's getting hot resulting in a significant drop in their resistance, and a proportional increase in the current drawn from the power supply. Finally voltage breakdown would occur, with its damaging effects. This problem was overcome by placing a safety resistor in series with the detector, to protect it from excessive dissipation.

The phosphor screen target serves to convert electron particle events on the MCP faceplate into light photon events on the output phosphor screen, with retention of spatial information. The light output from the screen is encoded into serial form by the scanning image of a TV optical pick up tube. A TV camera is set up so that an individual line, of a composite frame, represents one spectral channel. All events occurring on a single line originate from the same energy electrons, since they occur at the same offset along a detector centred axis (axis Y_D in section II.3) Output from the TV camera is a video signal which, between line synchronization pulses, is an analogue representation of the photon flux illuminating the camera faceplate along the path of a particular line. Thus the screen is constantly scanned with photon events occurring on the screen being detected over an integration period, which is the duration of 1 line scan, of 64 μ secs. The persistence time of the phosphor must therefore be greater than a line scan time but less than a frame cycle time, 40 msecs.

The optical pick up tube must also be sufficiently sensitive to detect all optical events occurring on the phosphor screen. The light output from the phosphor screen can be calculated approximately from the characteristics of the phosphor and the output from the MCP arrays.

Output from the MCP's is in the form of a secondary electron charge cloud which is accelerated along a potential gradient into the phosphor screen. The charge cloud is sufficiently small and energetic to stimulate optical output from a single phosphor crystal. Given that for a single incident primary electron the MCP output is described by the following characteristics:

- t = temporal width of the MCP output pulse = 0.5 ns
- n_e = number of output secondary electrons = 10^5
- r_e = radius of secondary electron cloud at the phosphor = 50 μm
- J = current density of the secondary electron cloud =
$$\frac{n_e e}{t \pi r_e^2} \text{ Am}^{-2}$$
- V = voltage of the secondary electrons = 4×10^3 Volts
- V_k = voltage offset needed to penetrate aluminium layer on the phosphor = 1×10^3 Volts
- f = integrated event frequency, in the range $10 - 10^4$ Hz

For P20 phosphor the following parameters are typical:

- ϵ_L = luminous equivalent = $67.2 (\text{lumens ster}^{-1})\text{m}^{-2}$
- t_p = persistence time for the phosphor = 100 μsecs
- r_p = radius of a single phosphor crystal = 50 μm
- A_p = area of optical output on phosphor = πr_p^2
- A_s = area of whole phosphor screen = $2 \times 10^{-3} \text{m}^2$

For a phosphor screen radiating according to Lamberts Cosine Law, the luminance in lumens per steradian per metre squared is given by [5]:

$$B_L = \frac{\epsilon_L}{\pi} J(V - V_k) \quad \text{II-4-1}$$

$$= \frac{\epsilon_L}{\pi} \frac{n_e e}{t \pi r_e^2} (V - V_k) \quad \text{II-4-2}$$

The luminous flux, in lumens per steradian per single event would be given by:

$$B = B_L A_p t_p \quad \text{II-4-3}$$

$$= \frac{\epsilon_L}{\pi} \frac{n_e e}{t \pi r_e^2} (V - V_k) \pi r_p^2 t_p \quad \text{II-4-4}$$

The light from the single event is seen by the camera within the entire scene. The light entering the camera is given by the scene brightness which is related to the luminous flux, for a single event, by:

$$B_S = \frac{B}{A_S} \quad \text{II-4-5}$$

$$= \frac{\epsilon_L}{\pi} \frac{n_e e}{t \pi r_e^2} (V - V_k) \frac{\pi r_p^2 t_p}{A_S} \quad \text{II-4-6}$$

Using the values assigned above, equation II-4-6 is evaluated as:

$$B_S = 2.05 \times 10^{-4} \text{ candela per square metre (Nits)} \quad \text{II-4-7}$$

B_S is the scene brightness for each individual event, and represents the minimum light detectable. Hence a TV pick up tube must be able to operate within such low light levels. The scene brightness for operational optical output from the phosphor screen will be given by:

$$B_{out} = B_S f \quad \text{II-4-8}$$

Hence the operational scene brightness will vary with the integrated event frequency on the MCP faceplate. Typical photoelectron integrated peak areas vary over at least three orders of magnitude, which represents the range of scene brightness that can be anticipated. Consideration must also be given to optical losses through the vacuum window and through the lens, for a set aperture (f number). The performance of several TV optical pick up tubes were evaluated for each of the above considerations, under experimental conditions. Among those tested were Vidicon [8], Newvicon [9], Chalnicon [10] and Silicon Intensified Target (SIT) [11] pick up tubes. The best performance was found for the SIT tube, implemented in a JAl 731 Low Level Light TV camera [11] (RCA 4804/H pick up tube). The camera has the sensitivity to detect single events, well within its operational range, and has

sufficient dynamic range to monitor intense light without overloading and blooming. The camera did not show any picture lag, as experienced with many of the other cameras. This occurs when the response of the optically sensitive coating of the pick up tube is sufficiently slow such that it doesn't record the movement of the image. This time response factor was a serious limitation on the performance of many tubes evaluated. The high sensitivity of the SIT tube requires that the camera is not miss handled. After being set up for low level light detection the camera must not be exposed to bright light (even diffuse day light), this arises from our request not to incorporate automatic aperture control with the camera, which is the standard safety feature.

II.5 Video Signal Preprocessor

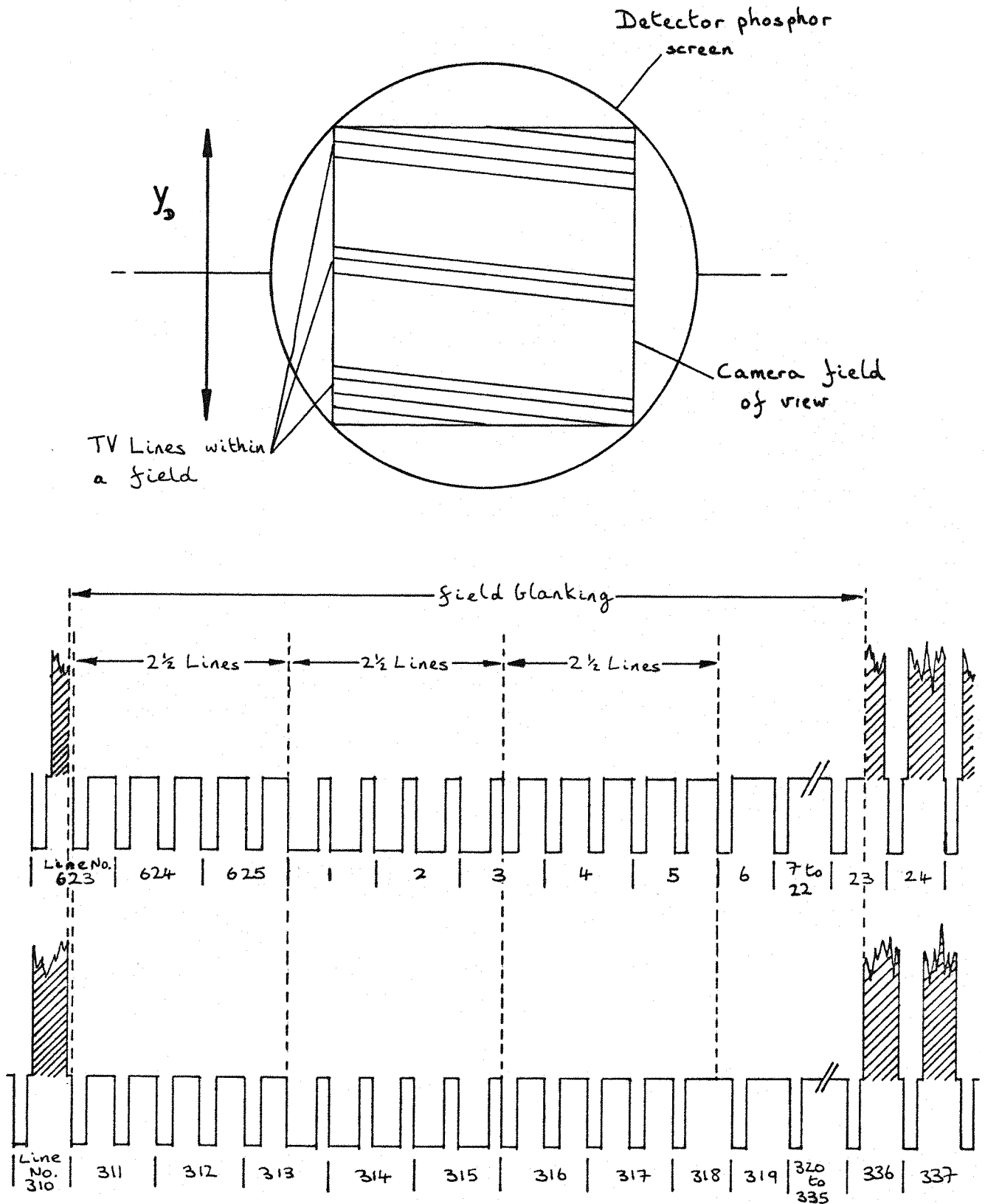
The optical pick up tube used to record the scintillations on the detector phosphor screen produces a standard CCIR 625 line monochrome composite video signal waveform. The video preprocessor is used to decode the serial video signal into separate logical channels. Each logical channel will correspond to a TV line which make up the fields of the TV frame. Each channel corresponds to a specific offset on the detector, hence defines a specific energy for the incident electrons producing the scintillations on the detector.

Figure 8 shows the composition of a TV frame as a number of lines, superimposed over the detector phosphor screen. The TV frame is built up, as two interlaced fields, by each line being scanned and measuring the optical intensity along the line. The composite video waveform is shown for a representative detector picture during operation. The video preprocessor serves to decode one dimensional positional information by counting line synchronization pulses, to give the line offset from the top of the frame. As shown in section II.3, positional information in the second dimension is not required. Thus the light level for a particular line is integrated along its length, and is proportional to the intensity of electrons of the associated energy.

The video preprocessor was designed by Mr P D Francis [12] to meet the following requirements in the three functional areas below:

Figure 8

Camera field of view and video waveform



(i) Video Analyser

The video analyser will decode the composite video output signal from the TV camera and accumulate integrated light intensities for user defined logical channels. Logical channels define the data acquisition window which is a sub set of the physical window (i.e. the full TV field of view). Data acquisition continues for a user defined number of TV fields, with data being accumulated for all frames. The data acquisition rate will enable the integration of line light levels in real time (i.e. 64 μ secs for each line) with totals for separate logical lines being stored in separate accumulator locations.

(ii) User Interface

The User Interface will enable the interactive specification of the logical window (as a number of lines each of which is a number of data points) in a position relative to the physical window. In addition, in a scan the number of fields to be used in the accumulative procedure will be specified. User output will include a display of the acquired data, for the specified logical window, in histogram form. The display will be continually refreshed, on completion of each scan. In addition as a maintenance aid a number of test programs will be initiated via the user interface.

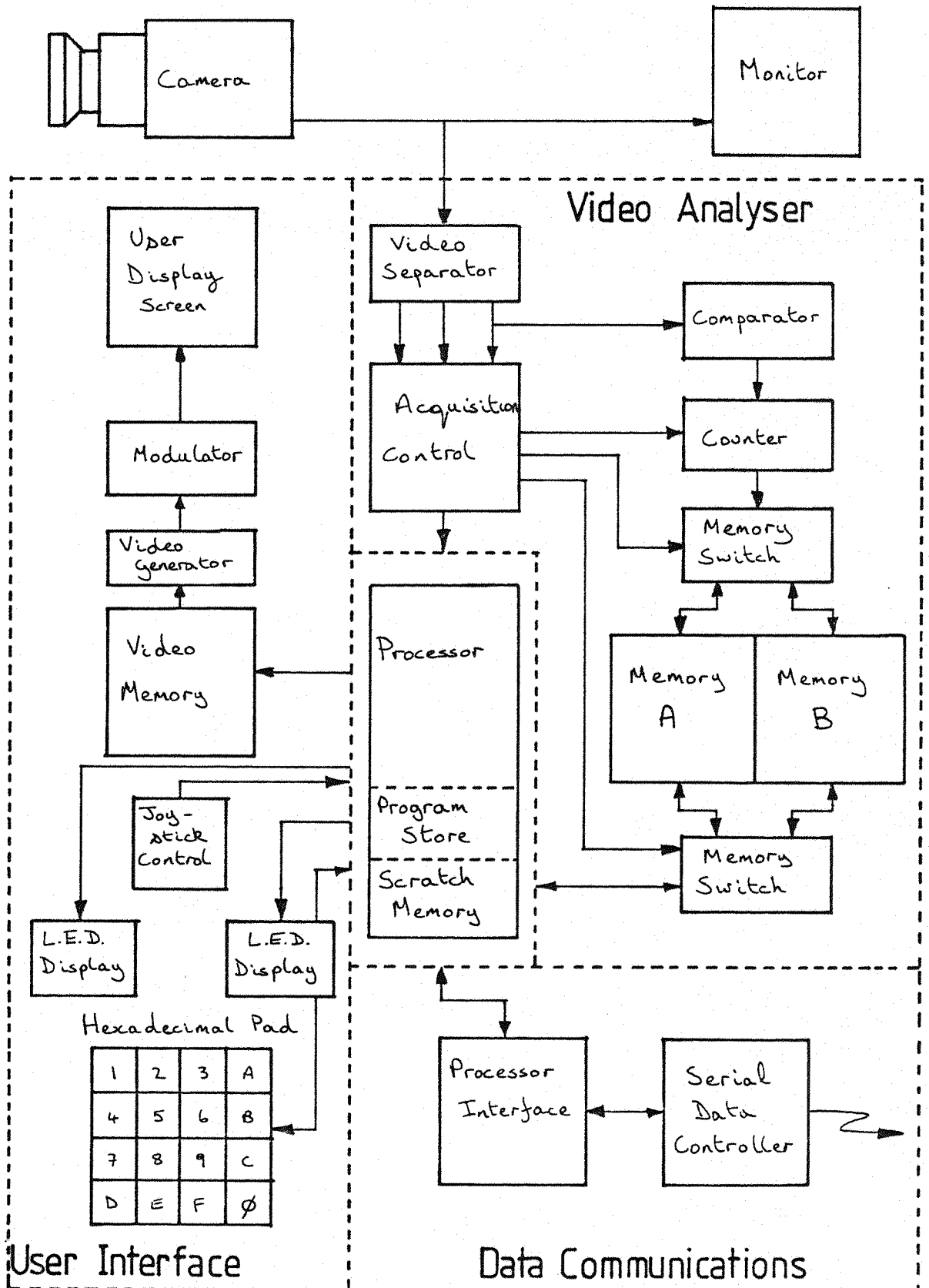
(iii) Data Communications

Data communications will allow data transfers to take place between the video preprocessor and a downstream computer system. Complete bidirectional communications will be defined for the computer control of the preprocessor, via a command stream, and for off-loading of data for further analysis.

The functional areas identified above are shown in Figure 9, along with the major components arising from the design implementation. The video preprocessor uses a Z80 microprocessor [13] to perform many operations required by each of the three functional areas, and to enable communication between the functional areas. The microprocessor is controlled by a software executive stored in non volatile memory (Erasable Programmable Read Only Memory, EPROM). In addition temporary storage of data is possible using a random access memory (RAM) for

Figure 9

Block diagram of the video preprocessor



program use. The implementation design for each of the three functional areas will be briefly described below.

(i) Video Analyser

For real time acquisition of data from the video signal the design implements an acquisition algorithm using hard wired logic circuits. This is because the data sampling rate was chosen as 4 MHz, which exceeds the microprocessors' instruction cycle time, of 1.5 MHz.

The input CCIR composite video signal is first split into separate field synchronization, line synchronization and video signals. The synchronization signals are used, along with the user defined logical window size and position, to generate horizontal and vertical gate logic signals. Figures 10a, 10b and 10c show the logic signals used to produce the block acquire logic signal (BLOCKAQ). The video signal is passed through a fast voltage comparator, with a preset threshold reference voltage. This produces a logic signal (VIDAT) which becomes true (logic level 1) during periods when the video signal is above the threshold voltage. The analyser operates by counting the number of clock pulses that occur when the VIDAT signal is logic level 1, and when BLOCKAQ is true. Figure 10d shows the major logic signals used for video data acquisition. The design incorporates a fast 16 bit (one binary digit represents a bit) counter and two sets of 16 bit registers. The registers buffer the transfer of data to and from the counter and memory locations, used to store accumulated counter values for each channel. Two sets of registers are used to enable synchronous transfer of data and counter accumulation. The accumulated counter values are stored in locations in a block of memory. Two blocks are used which define two distinct address spaces. These can be interchanged when the analyser is inactive, by an address switch. This allows synchronous running of two tasks, one of which is acquiring data in one memory block, while the other task is performing data transmission from the other block. No two tasks can access the same memory block.

(ii) User Interface

The user interface is implemented as two custom built devices,

Figure 10a
Vertical gate logic signals

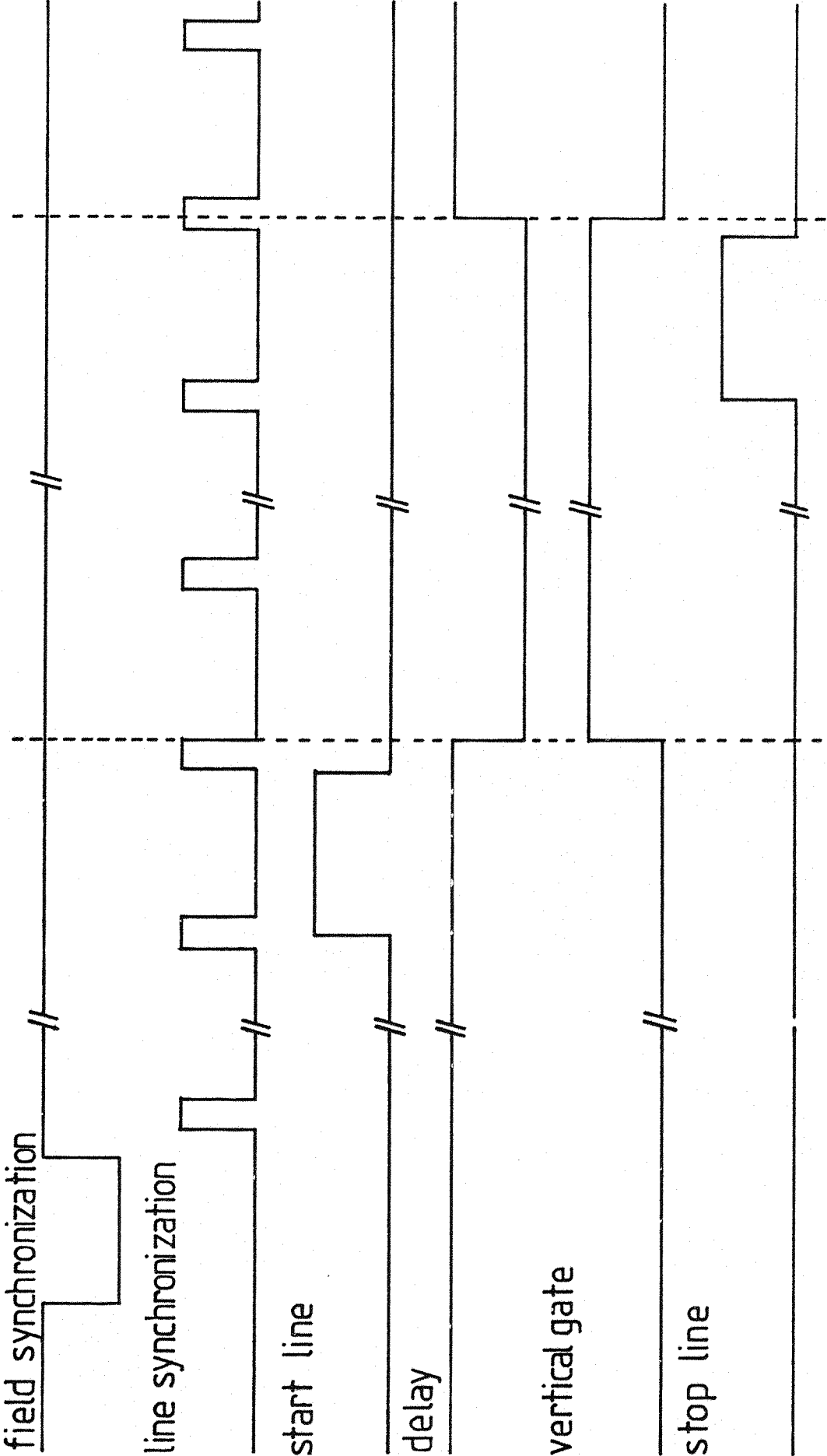


Figure 10b
Horizontal gate logic signals

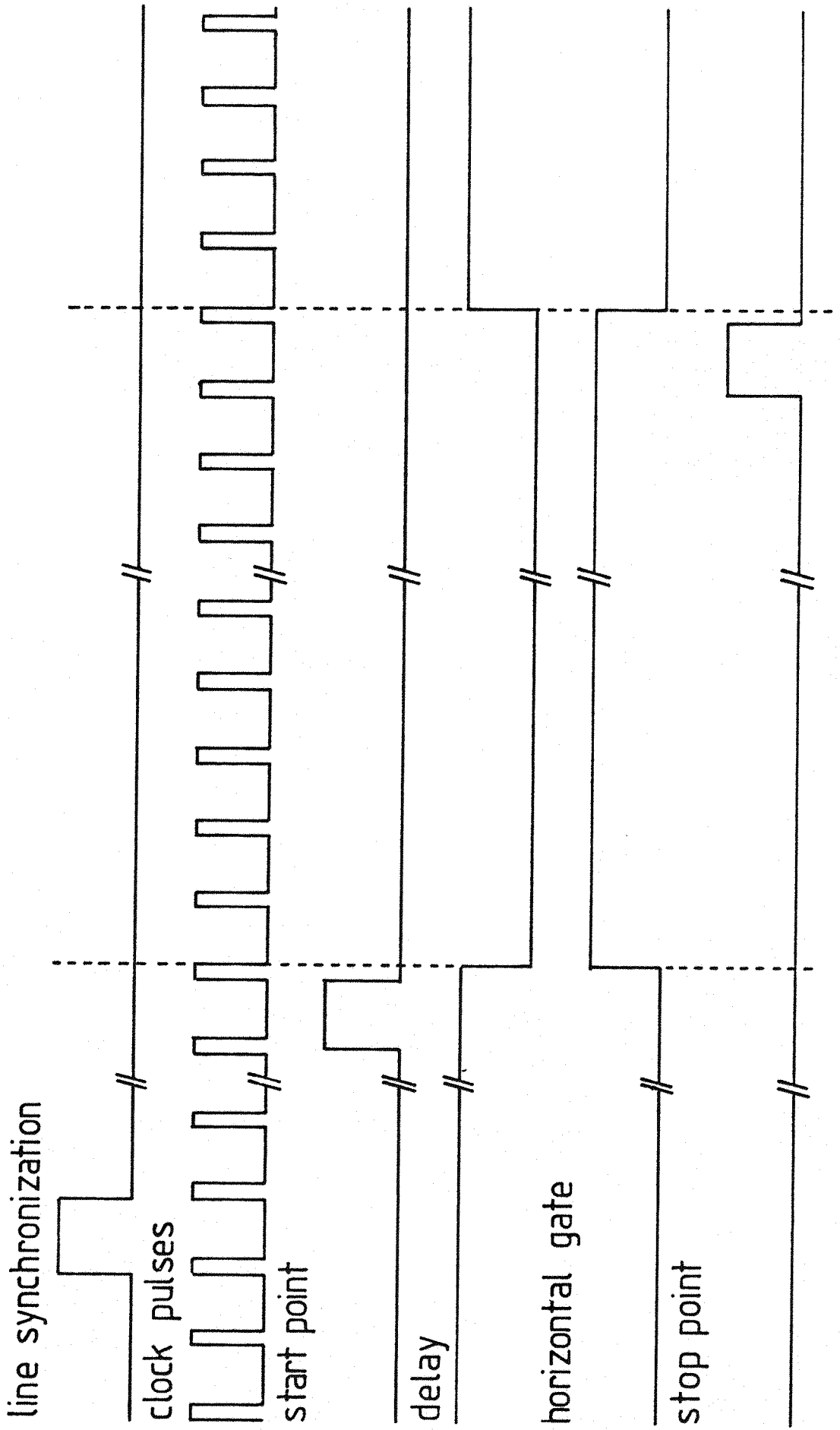


Figure 10c
Acquisition gate logic signals

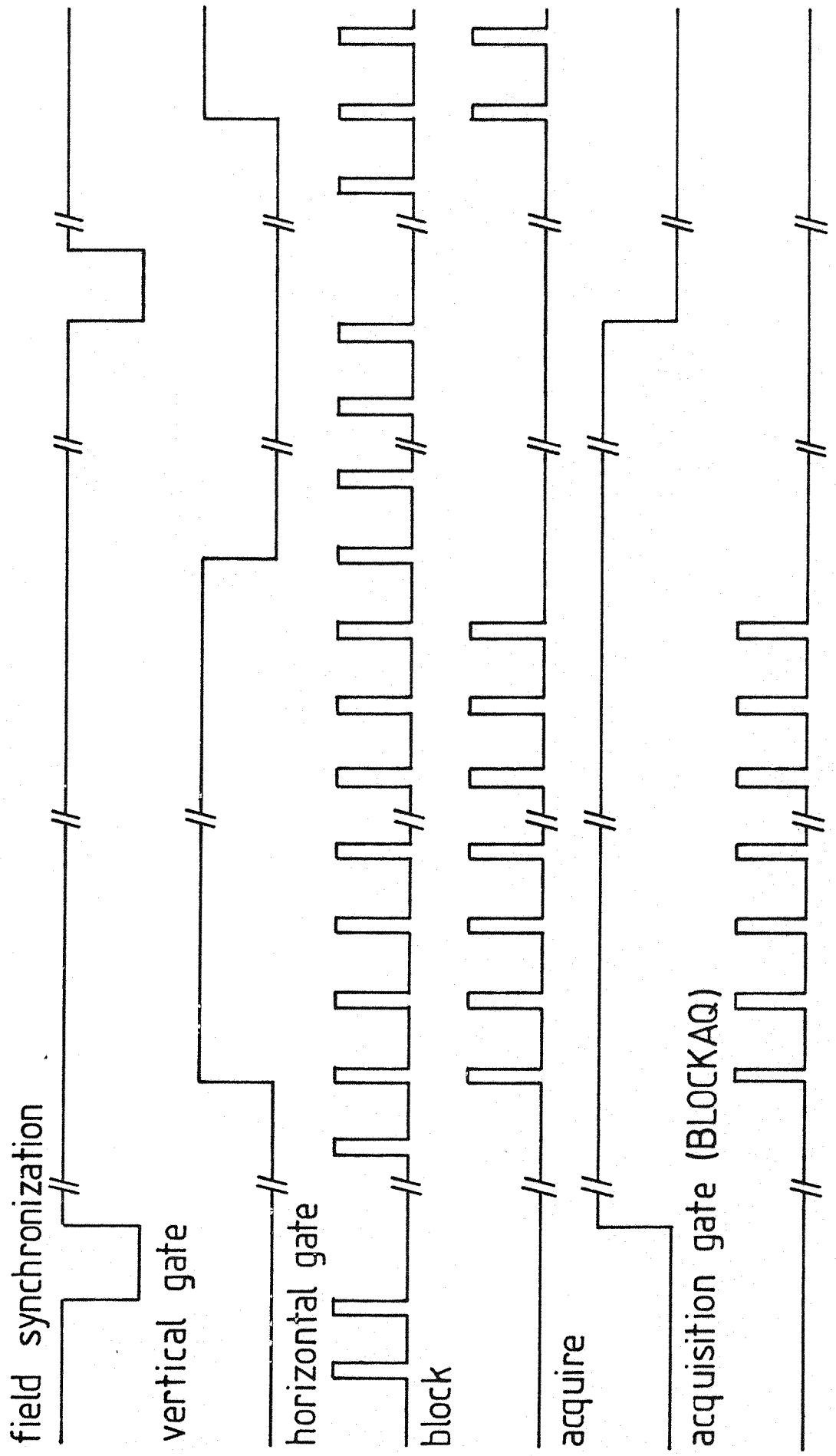
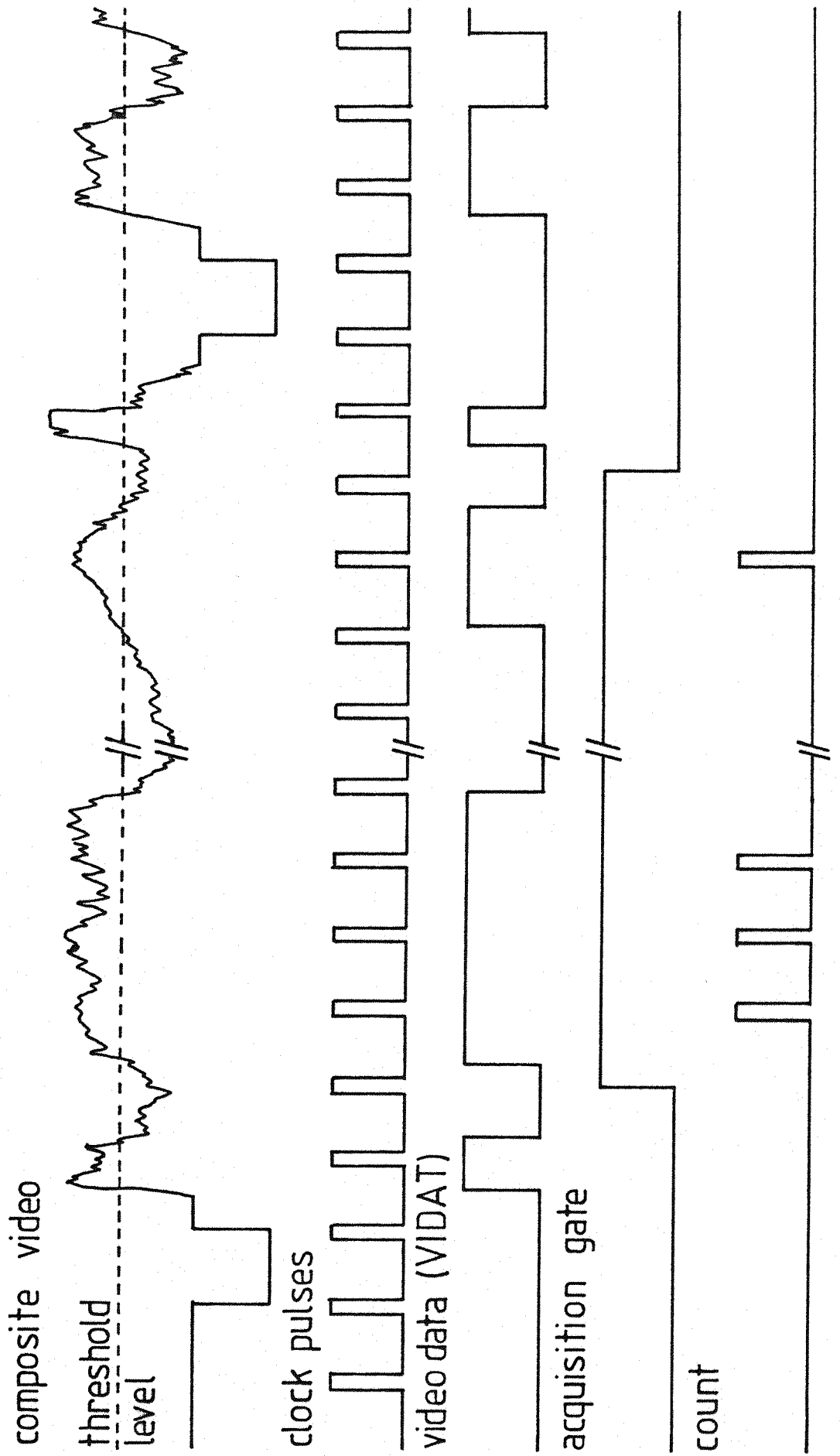


Figure 10d
Logic signals for encoding video data



serving as input and output devices for the Z80 microprocessor executing the software executive. Firstly, all user input is received from an operator console. The device contains a hexadecimal keyboard, a joystick control and ten push button switches for data entry. The control station hardware encodes data from the input sources. The data is passed to the processor via one of the input/output (I/O) ports. The input data is used by the executive software to action responses to the entered command or data. Secondly for output there are two display devices. Primarily there is a user display screen, produced on a standard TV monitor. This is implemented using a dual port memory block. Each memory location can define alphanumeric display characters and graphics characters. The video display circuits generate output video and synchronization pulses, to drive the display monitor, by encoding each character as a 5 x 10 dot matrix for display. This uses one of the dual read/write ports, the other is available for use by the Z80 microprocessor. The Z80 is able to define the characters and symbols for display by writing to specific locations in the display memory. In addition numeric information can be output using the two four-digit Light Emitting Diodes (LED's) on the control console. Each digit is a seven segment display with a decimal point. These are implemented at specific locations in the Z80 address space (i.e. memory mapped).

(ii) Data Communications

The video preprocessor interfaces to the host computer via a high speed (9600 bits per second) standard RS232 serial data link. The video preprocessor implements the interface by passing data from the processor to an 8 bit register via one of the I/O ports. Hard wired logic circuits generate handshake signals for the data transfer. Conversion of the data byte to serial representation and transmission of the data is entirely controlled by the interface handshake logic circuits. The software executive controls I/O for the serial link to the host computer and actions responses to all received commands.

The hardware defined above operates with a software executive. The executive is initiated on power up and controls the preprocessor

operation as well as defining the user and data communications interfaces. The actions defined for each command received, as programmed in the current executive, will be described in turn for each of the two interfaces.

Interactive User Commands

These commands are entered by the user via the control console and perform four major functions. These are:

(i) Logical Window Definition

The executive generates a chequered mask for output on the user display screen, to represent the extent of the logical window. Separate commands exist to display the logical window alone, or superimposed on the TV camera field of view. This allows assessment of the logical window in relationship to the physical window, comprising of the TV frame. Manipulation of the logical window is achieved by two further commands. One command allows the position of the logical window to be dynamically altered under joystick control. A second command allows dynamic alteration of the logical window size, by use of the joystick control. The minimum and maximum logical window sizes are one line of one data point and 256 lines of 208 data points respectively. The joystick control directly maps the horizontal and vertical axes defined for the TV frame. The control allows change, in either direction, for the two major axes, as well as for the two axes bisecting the major axes (represented as symmetric vectors). The logical window parameters can be output, in response to another command, as two decimal numbers displayed on the control panel LED's. These define the starting line number of the logical window, with respect to the physical window, and the width of the logical window as a number of lines.

(ii) Scan Parameter Definition

A single command is used to initiate a dialogue requesting the specification of the number of TV fields to be used in the iterative data accumulation process. This enables data for weak signals to be acquired by summing the integrated count for each logical channel, for repetitively acquired logical windows. The user is prompted, by a message output on the user display screen, to input the number of TV

fields to be repetitively acquired. The number is input using the hexadecimal keypad, and can be in the range, 1 to 256.

(iii) Acquired Data Display

Two primary commands exist to display the acquired data either as a histogram graph or as a list of numbers. For histogram display a column is generated for each line, which is proportional to the acquired total count for the scan. The display is repeatedly refreshed on completion of each acquisition scan. This provides continuous feedback to allow tuning of instrument parameters, to set up the best operating conditions. Before display of the histogram, the user is prompted, by a message output on the user display screen, to enter a scale factor in the range 1 to 255, for the histogram display. This enables a range of intensities to be displayed conveniently. The alternative display command simply lists the accumulated count for each of the lines of the defined logical window. The numbers are output on the user display screen as decimal numbers representing the exact contents of each logical channel accumulator.

(iv) Test Program Initiation

A command can be entered to initiate a test program session. Several test programs exist to check the operation of various components of the device. The test program to be run is selected by entering a two digit code on the hexadecimal keyboard.

Computer Control Commands

These commands are initiated by the host computer and are transmitted via the data communications link. The commands are in three functional areas, these are:

(i) Operational Mode Control

The software executive has been designed to operate in two mutually exclusive modes. These are Local Mode and Remote Mode. In Local Mode the User Interface is activated and the operating parameters can be defined using the commands described above. In Remote Mode the Data Communications interface is utilized allowing the device to be controlled by commands that are described below. Two commands exist that simply allow the interchange between the two modes of operation. Before trans-

mission of a command stream to the device, Remote Mode must first be successfully entered. Local Mode must be re-entered before any interactive user commands can be used. The software executive initiates local mode on power up or reset.

(ii) Initiate a Data Acquisition Scan

This command is used to initiate a data acquisition scan for the defined logical window, using the input video signal. Prior to initiation the analyser status is checked to ensure that it is not still busy servicing a previous request. If the analyser is busy an error code is returned to the host computer. If the analyser is inactive the acquisition memory block is switched, the new block initialized to zero and the analyser started. The previously used memory block then becomes free for use by another task.

(iii) Transmit Data Block to Host

This command is used to initiate the Transmission of a data block to the host computer. The data transmitted consists of up to 259 numbers formatted into variable length records terminated by control characters. Each number of the data block is represented as 6 decimal digits (each digit is transmitted as its standard ASCII code byte). The first three numbers define the number of logical lines, the starting line number of the logical window and the number of frame cycles used for the scan. The following numbers are the acquired data for the logical window, with one number for each logical line.

In conclusion the video preprocessor described here provides a flexible and powerful interface to enable real time data acquisition and data reduction prior to transmission to the host computer. The preprocessor is the primary input device for the data handling and analysis system during instrument operation. The control of the preprocessor, and its operational aspects will be discussed in the next section.

II.6 Data Handling and Analysis

Operational control of the instrument and final data output are performed by a Data Handling and Analysis Computer System.

The Computer System will be composed of five functional areas,

these are: Analogue Output, Preprocessor Interface, Graphics Output, User/Operator Interface and Central Control. Figure 11 shows the relationships between the functional areas of the computer system. The major functions performed by each of the functional areas will be described in turn below.

(i) Analogue Output

Analogue Output is required for control of the instrument electron energy analyser sphere voltages. The output will consist of two voltages, of equal but opposite potential, the positive voltage will be used for the inner sphere and the negative voltage for the outer sphere. The potential difference between the spheres defines the mean pass energy for the analyser and hence defines the energy window (see this chapter, section II.3 for further details). Central control will interface to Analogue Output to specify the output voltage.

(ii) Preprocessor Interface

The Preprocessor Interface is required to accept data blocks from the preprocessor and to send command sequences to control its operation. Various routine functions such as data deblocking, conversion to internal format and appending control characters will also be performed. Central control will link to the Preprocessor Interface to define the command stream and to utilise the input data.

(iii) User/Operator Interface

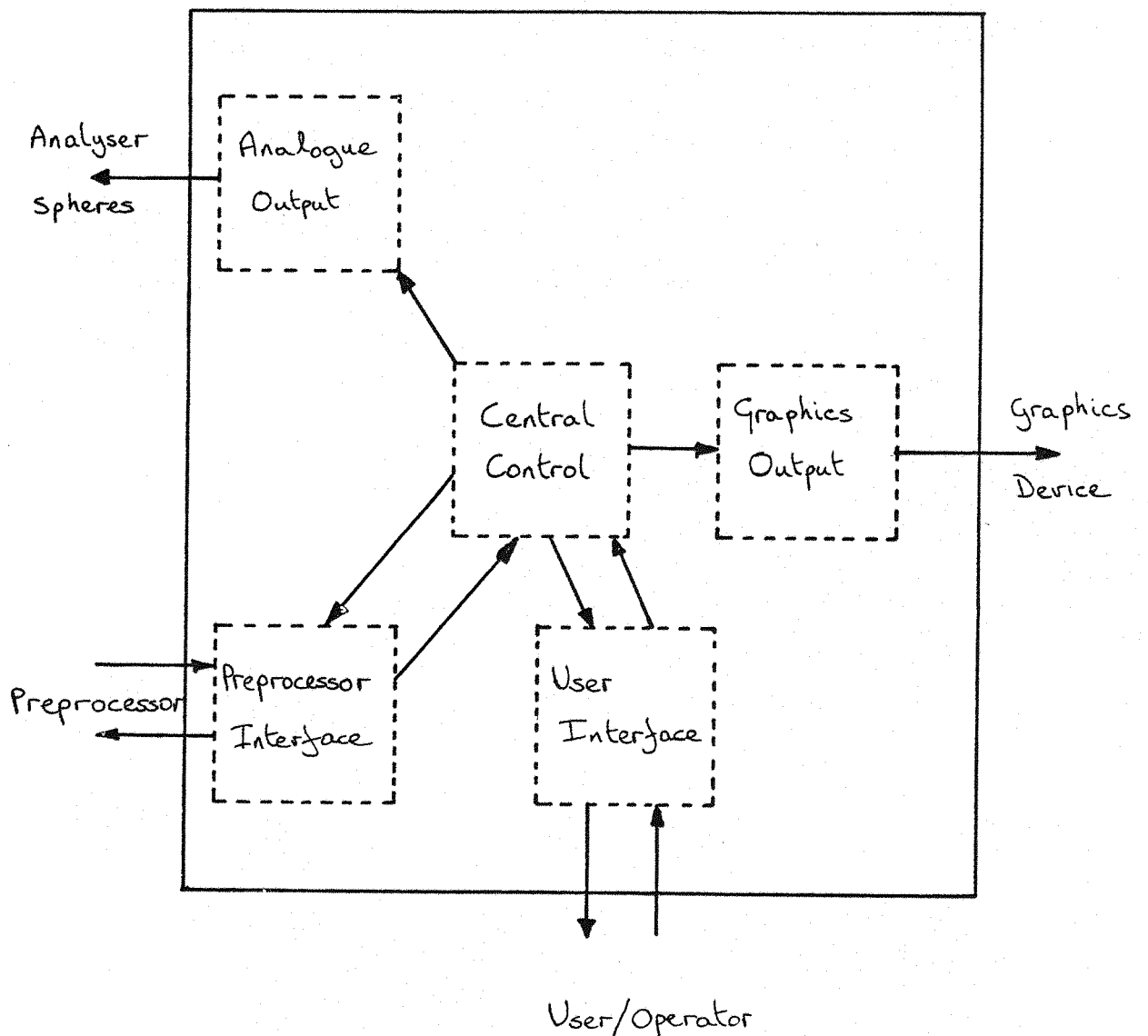
The User/Operator Interface functions to conduct an interrogative dialogue with the instrument user/operator. The dialogue is conducted via a standard computer console display screen and keyboard. Central Control defines the output messages and actions the user/operator response.

(iv) Graphics Output

Graphics Output functions to allow output of final and intermediate data to one of two graphics output devices. This enables data to be presented in the familiar spectral form, i.e. as standard intensity versus electron kinetic energy plots. Central Control links to the Graphics Output to specify the destination graphics device, and the data to be output.

Figure 11

Functional diagram of the Data Handling and Analysis System



(v) Central Control

Central Control functions to manage the operation of each of the subordinate functional areas, to conduct an experiment. Central Control ensures logical operation of activity of each of the functional areas, and oversees data flow during an on line session, maintaining consistency and performing validation checks.

The functional areas identified above have been implemented as an integrated "stand alone" dedicated computer system. The computer system is an association of hardware and software components, which will be described in two sections below.

Hardware Components

The Data Handling and Analysis Computer System is implemented using Digital Equipment Corporation (DEC) [14] kit. Figure 12 shows the hardware configuration of the system. Each major component will be briefly described below:

(i) Backplane, Data Bus and Power Supply

The backplane provides for each component of the hardware configuration a standard data-way and power supplies. Each component of the system is a circuit board that locates into a slot in the backplane, with metal strips ensuring electrical contact. The data way (called Q Bus by the manufacturers) enables communication between each resident board via data and control signals. The backplane used is a H9270 module with a H780 power supply providing dc voltages and a system 50 Hz real time clock.

(ii) Processor

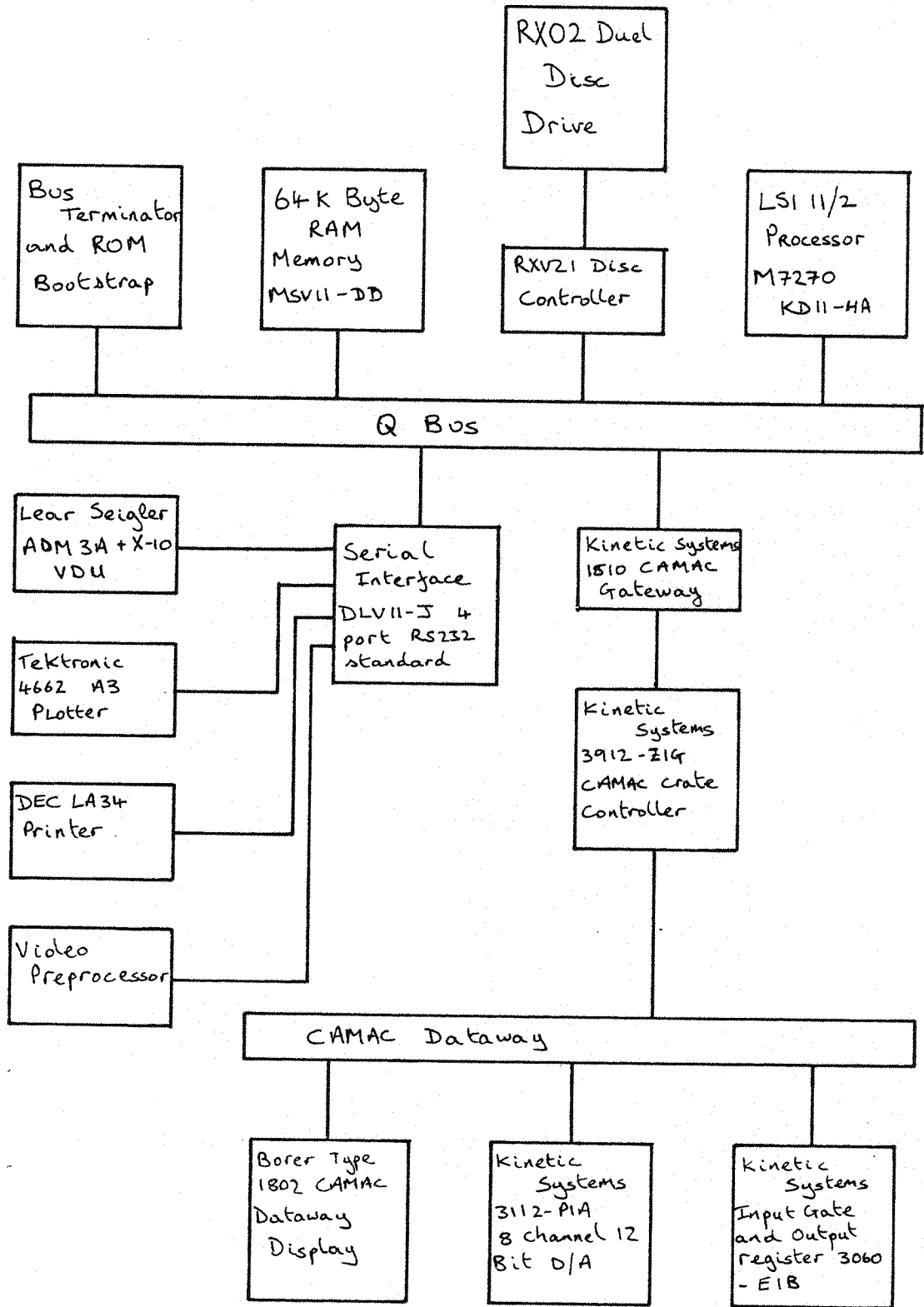
The system central processor unit (CPU) is a LSI 11/2 16 bit processor (M7270 KD 11-HA). The powerful CPU has an extensive instruction set which is upward compatible with more powerful LSI 11 and PDP 11 processors. This ensures minimum software changes if system expansion is required.

(iii) Mass Storage Device

Mass Storage for the system is provided by an RX02 double density dual 8 inch floppy diskette drive. Each disk drive contains an interchangeable platter that can store up to 512K bytes (1K = 1024). The

Figure 12

Components of the Data Handling and Analysis System



total device storage is 1 M byte online, and has essentially unlimited off line storage, by using many interchangeable disks. The device is controlled via a bus resident controller (RXV21), which performs fast data transfers via Direct Memory Access (DMA).

(iv) Main Memory

The main memory for the system is semiconductor random access memory (RAM) (MSV11-DD). The full complement of the 16 bit address space is used, i.e. 64K bytes. The CPU executes programs stored in memory, which must occupy no more than the low 56K bytes of memory. This is because the high 8K bytes of the address space is assigned to device registers.

(v) Communications Port

The communications port for the system is a 4 channel RS232C serial transmission device (DLV11-J). The 4 channels are used to communicate with various peripheral devices attached to the system (see Figure 12). Each channel has a switch selectable data transmission rate, between 150 and 38400 bits per second. The device controls data transmission and reception via handshaking signals exchanged with the peripheral device.

(vi) Bootstrap

The system bootstrap is a program contained in non volatile memory to initiate system operation automatically when the power is switched on. The Bootstrap is encoded in Read Only Memory (ROM) on a bus terminator device (REV11-A). The bus terminator is necessary because the Q bus passes signals in turn from device to device resident in backplane slots (daisy chain) and these must be terminated by 128 ohm resistors.

(vii) CAMAC Gateway and Crate Controller

The CAMAC (Computer Applications on Measurement and Control) Gateway decodes Q bus data and address signals, which are then transmitted to the CAMAC crate. The CAMAC crate is an industry standard flexible interfacing device which can accommodate a variety of interface modules. The CAMAC crate (Kinetic Systems Model 1510) is controlled by the control module (Kinetic Systems 3912-ZIG) which decodes commands received from the host computer. The controller communicates with the

other modules in the crate via an internal dataway. The CAMAC crate implements completely independent module control via a suite of commands and internal module addressing. The internal CAMAC address space maps on to a region of the host computer address space. This enables CAMAC modules to be addressed as if they were resident directly on the Q Bus. In addition the controller decodes attention signals (Look At Me, LAM, signals) from modules to generate an interrupt of the host CPU to invoke a service routine via a specified vector. This enables separate modules to be serviced by separate interrupt service routines.

(viii) Digital to Analogue Converter CAMAC Module

The Digital to Analogue (D/A) CAMAC module (Kinetic systems 3112-PlA) is an 8 channel 12 bit D/A. Two of the channels are used to provide analogue output to the analyser spheres.

(ix) CAMAC Dataway Display Module

The Dataway Display module (Borer Type 1802) monitors CAMAC dataway activity and shows the latest dataway operation. The module is primarily used to find hardware and system faults for the CAMAC crate and the resident modules.

(x) CAMAC Input Gate and Output Register Module

The Input Gate and Output Register (IGOR) module (Kinetic Systems 3060-E1B) is used for parallel transfer of 16 bit data words between the module and an attached device. Full handshaking is implemented, as well as LAM generation on input. The module is not used at present and is intended for an upgraded video preprocessor.

(xi) System Console

The System Console (Lear Siegler ADM-3A VDU) peripheral device communicates with the system via serial port 3 operating at 4800 bits per second. The VDU is a 24 line by 80 character display, with a full QWERTY keyboard. The VDU also incorporates a Lambert RG-512 with X-10 option Retro-Graphics board. This enhances the data display capabilities of the terminal to enable graphics displays to be output. The graphics facilities allow point and vector generation on a 250 x 512 raster of data points, as well as alphanumeric character generation at any point.

(xii) Hard Copy Graphics Plotter

The Hard Copy Graphics Plotter (Tektronic 4662 A3 Plotter) peripheral is attached via serial port 0 operating at 300 bits per second. The device incorporates high resolution (2723 x 4096) graphics with automatic vector generation from vector end points. In addition flexible alphanumeric character generation is incorporated with a choice of character font type, printing angle, size and aspect ratio.

(xiii) Line Printer

The Line Printer (DEC LA34 Decwriter IV) peripheral is attached via serial port 2 operating at 300 bits per second. The printer is capable of writing 30 characters per second using dot matrix character generation.

(xiv) Video Preprocessor

The Video Preprocessor (see section II.5) is attached via serial port 1 operating at 9600 bits per second. The peripheral performs primary data acquisition and data blocking from the detector video signal.

The system hardware defines a powerful 16 bit mini computer that is configured with a mass storage device and a serial peripheral interface. In addition a CAMAC crate provides a basis for implementation of a number of modules for interfacing to non standard devices for I/O of both analogue and digital data. The video preprocessor has been designed to interface via a serial data link for ease of implementation. However this can be redesigned and easily reconfigured to take advantage of faster more efficient data transfer devices present in the system. The hardware configuration fulfills the specifications of the major functional areas described above.

Software Components

The Data Handling and Analysis System is implemented using a number of software components from a variety of sources. Three major sources of software have been exploited, these are: Manufactures Proprietary Software, Third Party Software and PES Group Software. The software from each of these sources will now be described in turn.

(i) Manufactures Proprietary Software

System software was obtained from DEC [14]. Operating system and

language processors were purchased to enable application program development and to perform the major functions required by the run time environment. In summary the major products comprising system software are:

RT-11: a real time disk operating system that enables interactive program development and dedicated on line applications. The operating system includes a number of system utility programs that actually perform many of the systems functions.

EDIT: a text editor that creates or modifies ASCII text source files for use as input to other system programs such as the MACRO-11 assembler or the FORTRAN compiler.

FORTRAN: a FORTRAN language compiler and run time system implementing ANS FORTRAN 66 with some enhancements.

MACRO-11: a powerful assembly language processor that produces relocatable object code. MACRO-11 has extensive macro features and enables direct access to hardware features of the system.

(ii) Third Party Software

Extensive use has been made of two third party software products. These are:

UCSD Pascal System [14]

This product is a complete software development environment written entirely in PASCAL. The system includes FORTRAN 77, BASIC and Assembler language compilers. The major use of the system has been to develop programs written in the Z80 assembler language for the video preprocessor software executive. The system assembler is a single pass flexible cross assembler, and was configured to produce Z80 object code from programs written in Z80 assembler language. This enabled the software executive to be programmed on the LSI-11 computer for assembly into Z80 object code. The program could then be stored on EPROM, by manual entry on an EPROM encoder, for inclusion in the video pre-processor.

SIMPLEPLOT Graphics Software [16]

This product is a suite of subprogram modules written in FORTRAN

and accessed via FORTRAN CALL statements, to implement device independent plotting of graphs. Facilities are included for a wide variety of graphs with automatic scaling, graduating and location of graphs. The graphics output produced by the system used SIMPLEPLOT software to generate VDU display graphs and hard copy plots.

(iii) PES Group Software

Software components from this source include all system programs and utilities written personally and by other members of the PES Group. The programs were written mainly in FORTRAN with the remainder written in MACRO-11 assembly language. A brief description of the major software components written will be given below:

DC:

This is a low level program, written in MACRO-11, to control the D/A CAMAC module. The program is incorporated into the RT-11 operating system, and performs data transfers between the system and the CAMAC device registers. The program is more specifically called a device handler, and forms the software component for the Analogue Output functional area.

IT:

This program is the device handler for the Video Preprocessor, and is written in MACRO-11. The handler is incorporated into the RT-11 operating system and performs I/O with the Video Preprocessor, via the serial communications link. The program fulfils software requirements for the preprocessor interface functional area of the system.

PESDAT:

This program performs spectral data acquisition via the Preprocessor interface whilst controlling the instrument operation via Analogue Output. The program is written in FORTRAN and conducts a dialogue with the user, via the system console, to set up various parameters. Functionally the program fulfils the software requirements of both the Central Control and the User Interface Functional Areas. Data is acquired using the following algorithm:

```

Accept Spectra start and end Points
Put Preprocessor In Local Mode
Wait until prompted to proceed
Put Preprocessor in Remote Mode
Set sphere voltages for first window
Start Preprocessor acquisition
Repeat - While window is within spectral range
    Wait until current acquisition is ended
    Set sphere voltages for next window
    Start Preprocessor acquisition
    Request preprocessor to transmit previous data
    Read previous window data
    Store data on data set
End iterative loop

```

The acquired data is stored on a disk data set in unformatted data records. The voltage required to cycle the next adjacent energy window, for a defined logical window, is calculated using the generation formula [17]:

$$E_{\text{CENTRE}}(I) = E_{\text{START}} \frac{(1 - \text{RATIO})^{I-1}}{(1 + \text{RATIO})^I} \quad \text{II-6-1}$$

Where $E_{\text{CENTRE}}(I)$ is the kinetic energy of the centre of the window for the I^{th} window. E_{START} is the spectrum region start point (on the kinetic energy scale) and RATIO is the ratio of the energy width of the logical window to the energy at the centre. For a logical window, defined for an acquisition scan, RATIO will depend on the width and position of the logical window relative to the physical window, i.e.

$$\text{RATIO} = \frac{1}{2} \frac{\text{NLINES} + 1}{\text{CONST}(287 + \frac{\text{OFFSET}}{\text{CONST}})} \quad \text{II-6-2}$$

Where NLINES is the number of lines composing the logical window, CONST is the inverse of the proportionality constant relating the physical window energy width to the mean pass energy (derived in section II.3 as 0.05694) and OFFSET is defined as the number of lines the logical window

centre is offset from the physical window. This is given by the expression:

$$\text{OFFSET} = 143.5 - (\text{STARTLINE} + 1 + \frac{1}{2}(\text{NLINES} + 1)) \quad \text{II-6-3}$$

where STARTLINE is the starting line of the logical window relative to the physical window. Figure 13 shows the juxtaposition of a logical window within a physical window.

Finally the output potential difference required for the I^{th} window is given as:

$$\Delta V(I) = k \times \frac{E_{\text{CENTRE}}(I)}{(1 + \frac{\text{OFFSET}}{287 \text{ CONST}})} \quad \text{II-6-4}$$

where $E_{\text{CENTRE}}(I)$, OFFSET and CONST are defined above and the constant k is the spectrometer constant relating the mean pass energy of the analyser to the potential difference. Notionally this is 2.475, but point charges will influence the electron trajectories and alter the observed proportionality constant.

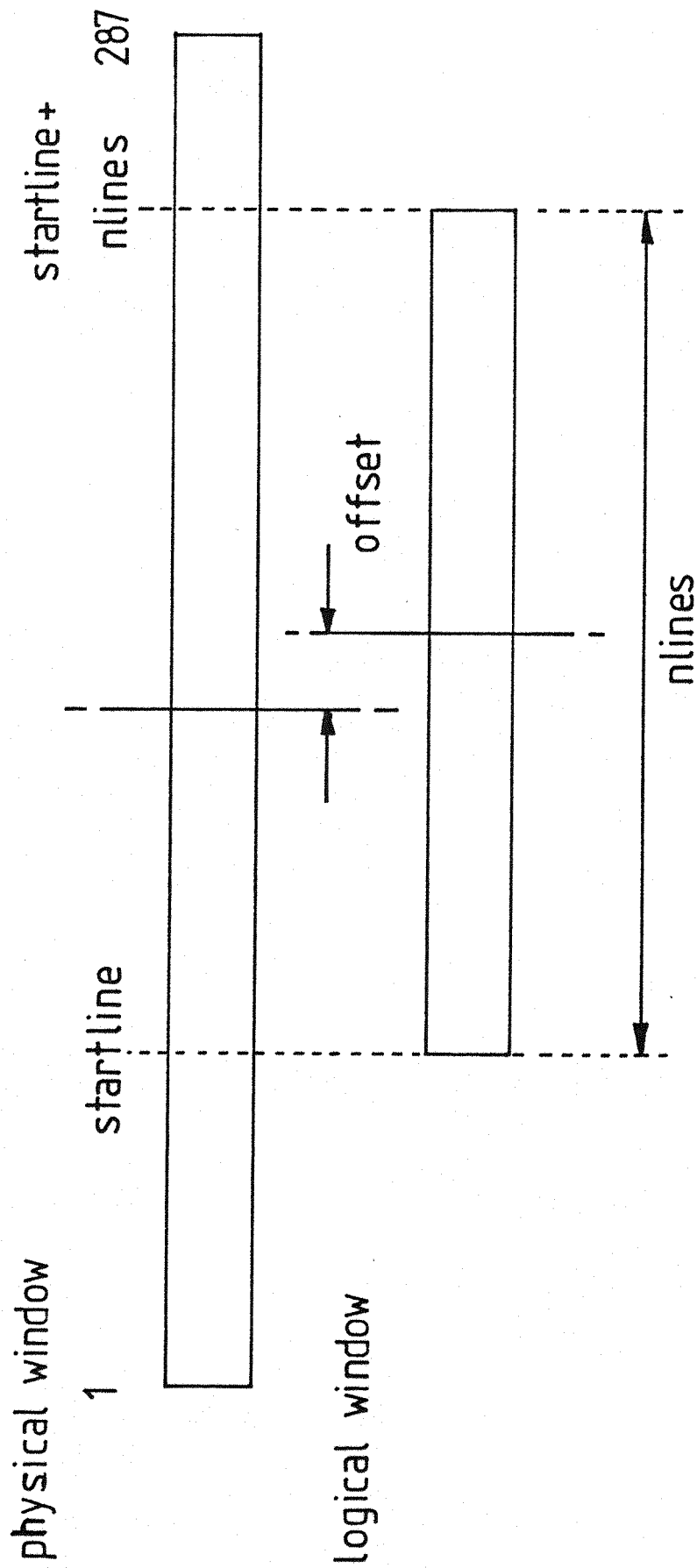
PESPLT

This program is used to produce graphics output, from acquired spectral data. The program is written in FORTRAN and defines the software in the User Interface and Central Control functional areas, for Graphics output. The program utilises data previously acquired by PESDAT, and stored on a disk data set. The data set is first scanned to identify the maximum intensity to be plotted for scaling. Secondly the graphics plot of the acquired spectrum is generated by calculating energy axis data values for each line acquired for each window in the range. The program incorporates an N point smoothing routine [18] which can be optionally applied to the data prior to plotting.

PESSYN

This software is a set of programs to synthesise PES spectra from molecular data. Complete peak construction is implemented using Gaussian peak shapes. Peak positions and intensities and half height widths are calculated from input Frank Condon Data, neutral molecule

Figure 13
Acquisition physical and logical windows



vibrational level population data and instrumental resolution factors. The constructed spectra are output on graphics devices. These programs have been used to produce the simulated spectra for HF in Chapter 6 of Part I.

The equipment described in this chapter has been developed over a period of approximately 14 months, and is able to acquire data from the multidetector and produce for output in standard form.

Chapter II

References

1. Leisk Engineering Limited, 76 Livingstone Road, Burgess Hill, Sussex, RH15 8QP.
2. Purcell, E M, Phys Rev, 54, 818, (1938).
3. Browne, C P, Craig, D S, and Williamson, R M, Rev Sci Instrum, 22, 952, (1951).
4. Instrument Technology Limited, 29 Castleham Road, St Leonards-on-Sea, East Sussex, TN38 9NS.
5. Reference Data for Radio Engineers, Howard W Sams and Co Inc, New York, (1969).
6. Leverenz, H W, "Introduction to Luminescence of Solids", John Wiley and Sons, New York, (1950).
7. "Optical Characteristics of Cathode Ray Tube Screens", JEDEC Publication No 16 (J6-C3-1).
8. Grundig FAH 125, Supplied by: J O Grant and Taylor (London) Limited, Arlingham House, South Mimms, Potters Bar.
9. Grundig FA 70 H, Supplied by: J O Grant and Taylor (London) Limited, address as above.
10. Hamamatsu C1000-01 (N1453) Supplied by: Hakuto International (UK) Limited, Hakuto House, 159a Chase Side, Enfield, Middlesex.
11. JAI 731 Supplied by: JAI (UK), 18A Bridge Street, Caversham, Reading, Berkshire.
12. Francis, P D, Instrumentation Section, Department of Chemistry, Southampton University.
13. Zilog Model Z-80A. Manufactured by: Zilog Inc, 10460 Bubb Road, Cupertino, California 95014.
14. Digital Equipment Corporation, P O Box 85, Stadium Way, Reading, RG1 3EE.
15. UCSD Pascal System, Supplied by: Dicoll Data Systems Limited, Bond Close, Kingsland Estate, Basingstoke, Hants.
16. Butland, J, "SIMPLEPLOT Users Handbook", Report No 253, University of Bradford, Postgraduate School of Electrical and Electronic Engineering.

17. Dr N Keddar, personal communication.
18. Savitzky, A, and Golay, M J E, Anal Chem, 36, 1624, (1964).

Chapter III

Initial Results and Conclusions

Contents

1. Initial Results
2. Conclusions

III.1 Initial Results

The acquisition of data from the multidetector, via the video preprocessor, using automated instrument control has been achieved. At present the PES spectrum of Argon has been used as an example.

Figures 1 and 2 show the output graphics plot of the Argon doublet produced using directly acquired data and smoothed data. The data was acquired using a logical window starting at line 42 and consisting of 248 lines. Data for each window was accumulated over 20 TV fields. The smoothed data was calculated using a 16 point smoothing function.

From the spectral plot the measured full width half maximum for the main $\text{Ar}^2\text{P}_{3/2}$ peak is 0.038 eV and the ratio of the peak intensities is 1:2.4. The main peak maximum intensity of 650 counts was acquired over a period of 1.28 mseconds. This therefore represents a single channel count rate of 5×10^5 counts per second and reflects the much improved sensitivity of the multichannel instrument. The measured intensity ratio is not in agreement with the expected 2:1 result and could result from nonlinear performance of the data acquisition system. However encouragement can be gained from the fact that the peaks are wholly resolved and that a basic Gaussian peak shape is found. It can also be noted that the base width across the doublet is in fact spanned by several adjacent windows. Each acquired window is treated directly and no account has been taken to eliminate possible discontinuities at window boundaries.

III.2 Conclusions

The initial results outlined in the previous section are proving extremely valuable in the further development of the multidetector system. Instrumental design improvements can be implemented and the effects directly assessed in terms of improved data quality. A number of design changes and operational improvements have been identified, these are:

- (i) The diameter of the detector plates needs to be increased. This will enable the detected energy window to be increased to span the

Figure 1

Argon PES spectrum

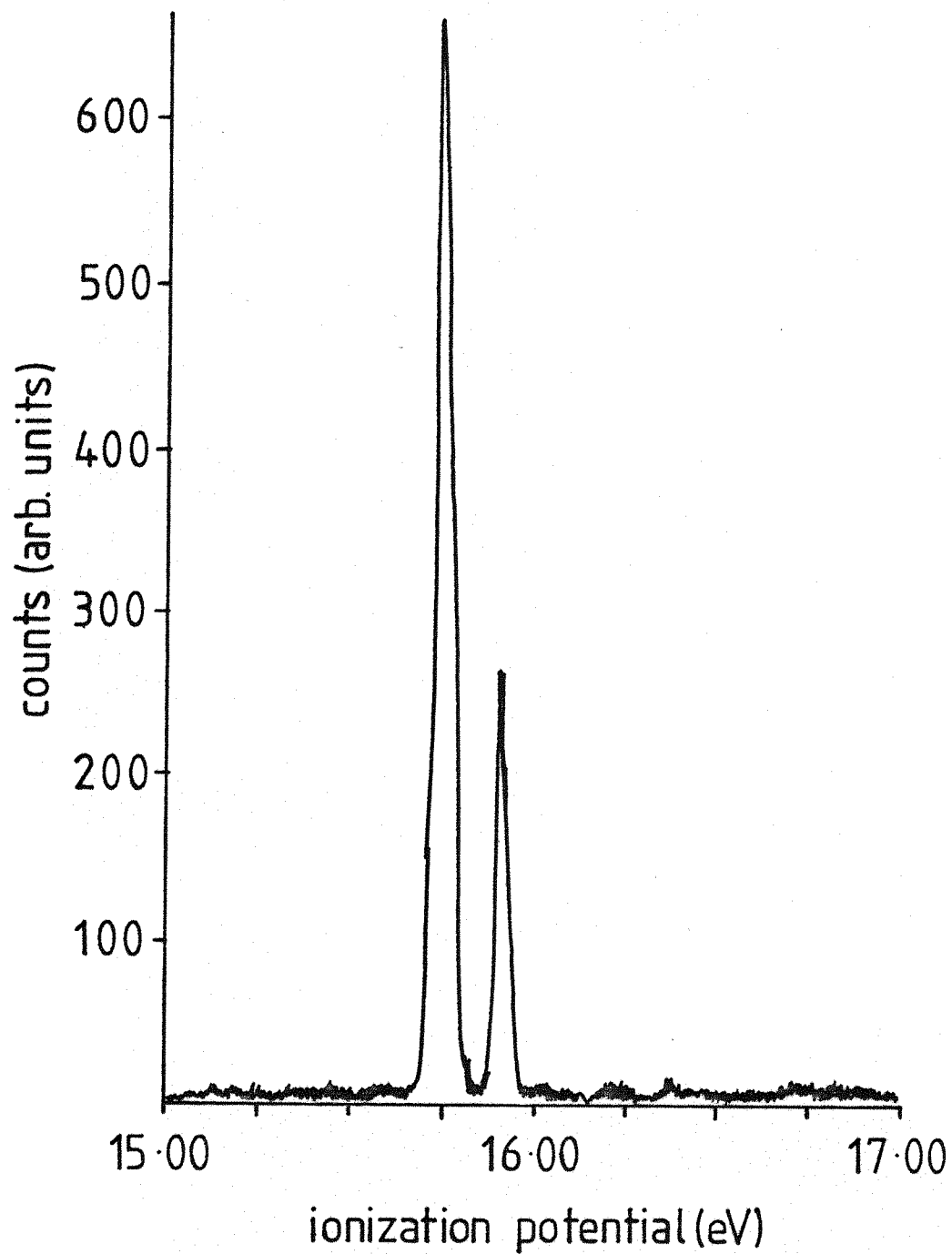
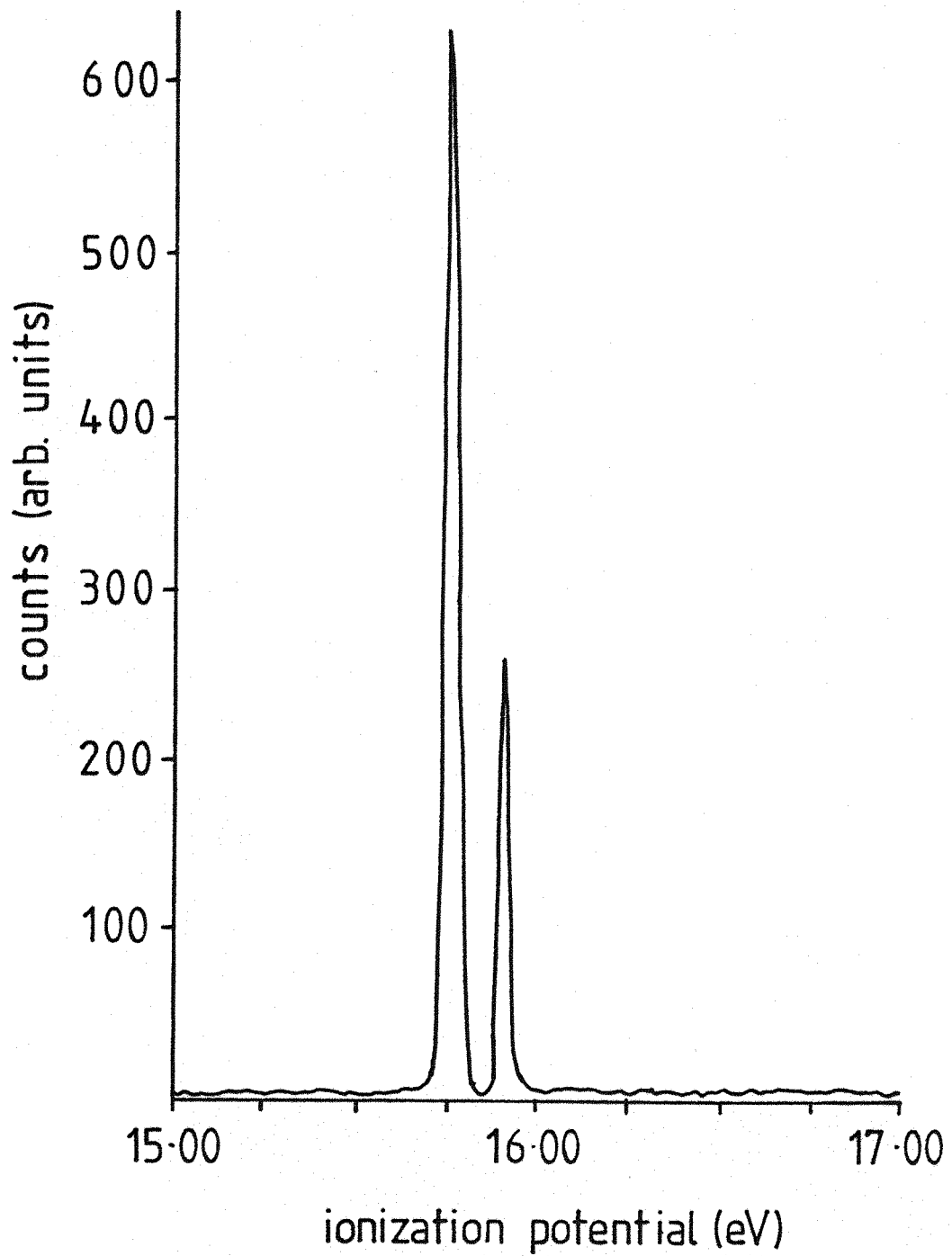


Figure 2
Smoothed Argon PES spectrum



base width of the Argon ion doublet. Using data from a single window the sensitivity of the detector, as a function of detection position in the window, can be calibrated.

(ii) There is a need to implement more sophisticated data acquisition techniques, to allow noise reduction and extend the maximum range of the line accumulators.

(iii) There is a need to implement data acquisition via overlapping windows, to eliminate localised inefficiencies of the detector.

Finally in summary, although some work still needs to be done, the major problems associated with multidetector parallel detection have been overcome, and encouraging initial results have been obtained. The development of the system will continue with the aim of establishing operating procedures for the routine use of the instrument in transient studies. The advantages of multidetection such as greater sensitivity, faster spectral acquisition time and signal averaging to reduce noise will enable the study of shorter lived radicals that are produced in much lower concentrations. Thus the detection of vibrationally excited HF, produced in fluorine atom abstraction reactions, should become experimentally feasible, and will test the band shapes predicted earlier in this thesis (see Part I, Chapter VI).